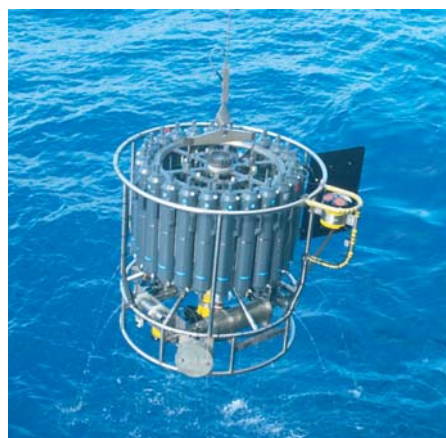




# **Evaluation of Stochastic Kinetic Energy Backscatter** in the GME Ensemble Prediction System

Jaison Ambadan Thomas



## Hinweis

Die Berichte zur Erdsystemforschung werden vom Max-Planck-Institut für Meteorologie in Hamburg in unregelmäßiger Abfolge herausgegeben.

Sie enthalten wissenschaftliche und technische Beiträge, inklusive Dissertationen.

Die Beiträge geben nicht notwendigerweise die Auffassung des Instituts wieder.

Die "Berichte zur Erdsystemforschung" führen die vorherigen Reihen "Reports" und "Examensarbeiten" weiter.



## Notice

*The Reports on Earth System Science are published by the Max Planck Institute for Meteorology in Hamburg. They appear in irregular intervals.*

*They contain scientific and technical contributions, including Ph. D. theses.*

*The Reports do not necessarily reflect the opinion of the Institute.*

*The "Reports on Earth System Science" continue the former "Reports" and "Examensarbeiten" of the Max Planck Institute.*

## Anschrift / Address

Max-Planck-Institut für Meteorologie  
Bundesstrasse 53  
20146 Hamburg  
Deutschland

Tel.: +49-(0)40-4 11 73-0  
Fax: +49-(0)40-4 11 73-298  
Web: [www.mpimet.mpg.de](http://www.mpimet.mpg.de)

## Layout:

Bettina Diallo, PR & Grafik

Titelfotos:

vorne:

Christian Klepp - Jochem Marotzke - Christian Klepp

hinten:

Clotilde Dubois - Christian Klepp - Katsumasa Tanaka

Evaluation of Stochastic Kinetic  
Energy Backscatter  
in the GME Ensemble Prediction System

Jaison Ambadan Thomas

aus Puthiyakavu (Kochi), Indien

Hamburg 2012

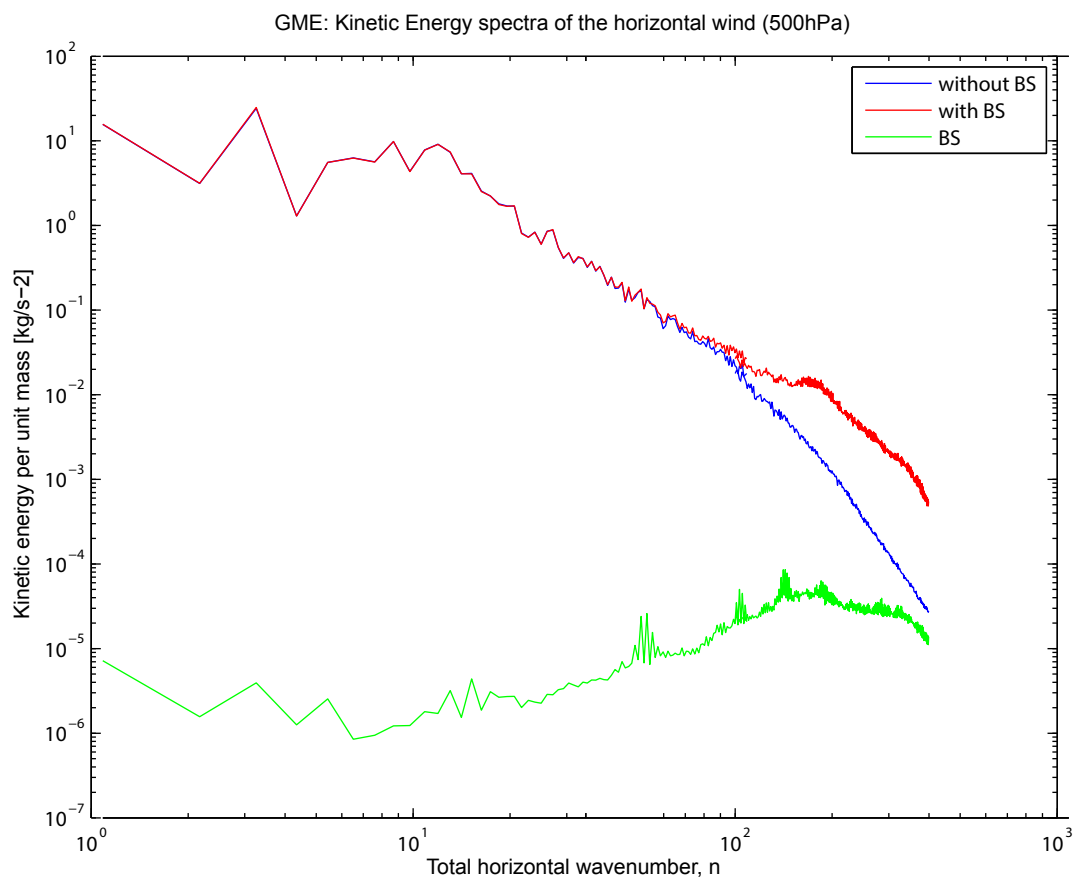
Jaison Ambadan Thomas  
Max-Planck-Institut für Meteorologie  
Bundesstrasse 53  
20146 Hamburg

Als Dissertation angenommen  
vom Department Geowissenschaften der Universität Hamburg

auf Grund der Gutachten von  
Prof. Dr. Björn Stevens  
und  
Dr. Andreas Rhodin

Hamburg, den 19. November 2012  
Prof. Dr. Jürgen Oßenbrügge  
Leiter des Departments für Geowissenschaften

# Evaluation of Stochastic Kinetic Energy Backscatter in the GME Ensemble Prediction System



Jaison Ambadan Thomas

Hamburg 2012

*To my dearest Hamburg ...*

# Abstract

The model error has significant effect on the quality of numerical weather forecasts, in addition to the initial and boundary conditions. Ensemble forecast and ensemble analysis systems provide an assessment of the uncertainty of the system and thus rely on an appropriate representation of model error. However, due to theoretical and computational limitations model error estimation remains an unchallenged issue in operational ensemble forecasting and data assimilation. This study addresses the importance of estimating the model uncertainties associated with kinetic energy (KE) dissipations in a Numerical Weather Prediction (NWP) model and incorporating the same in an ensemble data assimilation (EDA) system. A stochastic kinetic energy backscatter (SKEB) scheme is used to represent the flow-dependent model errors in an Ensemble Prediction System (EPS). The backscatter scheme also serves as an alternative to represent the model errors in the EDA system, since it reflects the errors due to dissipation or damping on the small scales by numerical diffusion and parameterization schemes.

The operational global weather forecast model GME of the *Deutscher Wetterdienst* (DWD) and a coupled 3D VAR - Local Ensemble Transform Kalman Filter (LETKF) assimilation system were used as test-bed for the experiments. The experiments were performed in a pre-operational global ensemble prediction test suit. Three sets of experiments were performed in order to study the impact of the SKEB scheme: i) Deterministic forecasts, ii) Ensemble forecasts using initial conditions from the deterministic analysis and iii) Ensemble forecasts using initial conditions from the EDA cycle. In all the experiments, a Cellular Automated (CA) scheme was used to introduce stochasticity into the backscatter scheme. Kinetic energy spectra of the horizontal wind of the GME forecast shows the observed double cascade, which indicates that the backscatter in fact compensates for the reduced energy up-scaling due to over-dissipation, and also seems to compensate for the absence of the inverse cascade.

In the forecast experiments without the EDA cycle the results show that the SKEB scheme significantly improves the medium-range forecast. For example, the temperature forecast significantly improves over ten days period at all pressure levels. Incorporating a stochastic backscatter scheme produces significantly better results compared to random perturbations. The forecast which incorporates all the dissipation components performs best in most cases and generates the highest ensemble spread. The backscatter also has a significant positive effect on the precipitation forecast, especially

in the Tropics.

In the GME-EPS experiments, overall the backscatter scheme increases the LETKF analysis ensemble spread thereby inflating the covariance implicitly. However, the increase in ensemble spread due to backscatter has an overall negative impact on the analysis. Since the SKEB scheme has a positive impact on the ensemble spread which implies the inflation of covariance, we expected a significant positive impact on the LETKF analysis and the EPS forecast. However, the combined effect of the initial uncertainty and of the other mechanisms in the EDA cycle have negative impacts on the backscatter contributions deteriorating the analysis and thereby the EPS forecast quality.

We also studied a *worst-case scenario* using the backscatter scheme, which violate the basic assumptions in the Kalman filter based data assimilation, using simple toy models. We considered the backscatter scheme as a multiplicative noise model, and explored the challenges of the multiplicative noise to the current EnKF schemes. The classic Lorenz '63 model and a higher dimensional Lorenz '96 model were used as testbeds for this data assimilation experiments. A hybrid Kalman-Particle filter called Sigma-point Particle Filter (SPPF) is presented as an alternative to solve the issues associated with multiplicative noise.

We also introduced a simple stochastic pattern generator for the SKEB scheme based on a power-law, which can overcome some of the drawbacks of the CA stochastic pattern generator. The main advantage of using the new pattern generator is that there is only one tuning parameter compared to the CA and there is no need of complicated automation rules. The scheme is computationally simpler as it does not require any spin-up runs.

In summary, we showed that the SKEB scheme is effective in representing the kinetic energy dissipations and flow-dependent uncertainty in the GME model, and incorporating the same in the model has significant positive impact on short-to-medium range forecast.



# Contents

|  |           |
|--|-----------|
| <b>Abstract</b>  | <b>i</b>  |
| <b>1 Introduction</b>  | <b>1</b>  |
| 1.1 Probabilistic Weather Forecasting: A Historical Overview . . . . . | 1         |
| 1.2 Background: Model Errors and Ensemble Forecasting . . . . .        | 2         |
| 1.2.1 Role of Model Errors in Ensemble Data Assimilation . . . . .     | 3         |
| 1.3 Research Objectives . . . . .                                      | 6         |
| 1.4 Contribution of this Research Work . . . . .                       | 7         |
| 1.5 Thesis Overview . . . . .  | 7         |
| <b>2 Tools and Methods</b>   | <b>9</b>  |
| 2.1 GME Model . . . . .  | 9         |
| 2.2 The GME Data Assimilation . . . . .                                | 9         |
| 2.3 Overview of Verification Methods and Diagnostics . . . . .         | 15        |
| <b>3 Stochastic Backscatter in the GME Model</b>                       | <b>23</b> |
| 3.1 Parameterizing stochasticity: Role of Backscatter . . . . .        | 23        |
| 3.2 Stochastic Kinetic Energy Backscatter in GME . . . . .             | 23        |
| 3.2.1 Stochastic Pattern Generators . . . . .                          | 24        |
| 3.2.3 Calculation of Total Dissipation in GME . . . . .                | 26        |
| 3.3 Role of Stochastic Backscatter in the GME forecast . . . . .       | 29        |

|          |   |            |
|----------|---|------------|
| 3.3.1    | SKEB: Experimental setup . . . . .                                  | 30         |
| 3.3.2    | SKEB: Impact on Kinetic Energy Spectra . . . . .                    | 31         |
| 3.3.3    | SKEB: Impact on the Medium-Range Forecast . . . . .                 | 32         |
| 3.3.5    | SKEB: Impact on the Precipitation Forecast . . . . .                | 63         |
| <b>4</b> | <b>Stochastic Backscatter in the LETKF</b>                          | <b>69</b>  |
| 4.1      | Covariance Inflation in LETKF . . . . .                             | 69         |
| 4.1.1    | Incorporating Flow-Dependent Model Errors in LETKF . . . . .        | 70         |
| 4.2      | Impact of the SKEB Scheme on the LETKF Assimilation . . . . .       | 71         |
| <b>5</b> | <b>Non-Gaussianity in Ensemble Kalman Filters</b>                   | <b>87</b>  |
| 5.1      | Multiplicative Noise and Non-Gaussian statistics in EnKFs . . . . . | 87         |
| 5.2      | The Sigma-Point Particle Filter . . . . .                           | 89         |
| 5.3      | Parameter estimation experiments . . . . .                          | 94         |
| 5.4      | Discussion and Conclusions . . . . .                                | 101        |
| <b>6</b> | <b>Conclusions</b>  | <b>105</b> |
| 6.1      | Summary of Results and Conclusions . . . . .                        | 105        |
| 6.2      | Outlook . . . . .   | 107        |
| <b>A</b> | <b>The LETKF Algorithm</b>  | <b>111</b> |
| <b>B</b> | <b>Least square formulation of Kalman gain</b>                      | <b>113</b> |
| <b>C</b> | <b>Additional Supporting Figures</b>                                | <b>117</b> |
| <b>D</b> | <b>List of Acronyms</b>   | <b>133</b> |
|          | <b>Bibliography</b>   | <b>135</b> |
|          | <b>Acknowledgments</b>  | <b>149</b> |

# Introduction

## 1.1 Probabilistic Weather Forecasting: A Historical Overview

The existence of uncertainty in weather forecast and the ways to tackle it have been subjects of interest for more than a century [Cooke, 1906; Murphy and Winkler, 1971, 1984; Ehrendorfer, 1997]. In the early 20<sup>th</sup> century there were many successful attempts applying probabilistic techniques to weather forecasting. However those attempts were focused on probabilistic verification of observed data (mostly temperature and precipitation) rather than probabilistic modelling. On the other hand probabilistic forecasting in those days was subjective, meaning that the uncertainties of the forecasts mostly depended on the forecasters ability to issue the likelihood occurrence of a weather event. The process of issuing categorical forecasts was improved since the introduction of confidence intervals and probability scores such as the Brier score. For example, in the case of a temperature forecast, there were mainly five categories of departure from the average temperature: near normal, above normal, below normal, much above, and much below normal. This categorization permitted the users to *subjectively interpret* the forecasts and allowed them to make their own decision [Leight, 1953].

During the second half of the 20<sup>th</sup> century the focus shifted towards probabilistic modelling. On one hand the main challenge was the limit on prediction primarily due to the errors in the initial states, which were reconstructed from discrete observations from finite number of points (incomplete data coverage) [Thompson, 1957]. On the other hand the models themselves are based on incomplete knowledge. It was clear that even if we assume no errors in the observed data, the reconstruction of the initial state from such data (finite number of points) will not be same as the true state, and it was therefore useless to perform long-range (longer than several days) forecasts in detail. Practically, expanding the observation network thereby increasing the data density is economically infeasible. Since the pioneering works by Edward N Lorenz on the theoretical limit on prediction, it was necessary to establish the maximum range of predictability, beyond which the details of the atmospheric state is essentially unpredictable. However, it has been proposed that certain statistical characteristics of the atmosphere might be inherently more predictable than its details [e.g., Namias, 1947; Namias and Clapp, 1949], which lead to the conceptual development of *stochastic approaches*, and eventually of *ensemble forecasting*. See Lewis [2005] and Murphy [1998] for complete historical reviews of probabilistic forecasting in the context of Numerical

Weather Prediction (NWP).

## 1.2 Background: Model Errors and Ensemble Forecasting

In general one can divide the errors which cause the uncertainties in a forecast into three classes: i) initial condition errors, ii) boundary condition errors, and the so-called iii) model errors. Initial condition errors are the errors in specifying the initial state of the model. Similarly, boundary condition errors are errors in specifying the boundary conditions of the model. However, the role of boundary condition errors is small in a global Numerical Weather Prediction (NWP) system compared to the initial condition errors, but its impacts may be significant in regional NWP and climate models. The term *model errors* broadly refers to errors in the formulation of the whole model itself that include errors in modelling the dynamics as well as errors in representing subgrid scale physical processes (physical parameterizations).

Estimating the uncertainty can be thought of as a process which quantifies the extent of the incomplete knowledge of the output quantity of a model (which is in fact an approximation of reality) to incomplete knowledge of its input quantities [Cox and Harris, 2006]. Theoretically, it is possible to precisely quantify the uncertainty of the future state by propagating the associated Probability Density Function (*pdf*) in time by solving the continuous state evolution of the associated *pdf* in time described by the Fokker-Plank Equation (FPE) or the corresponding Louville Equation (LE). However, analytical solutions to the FPE have been found only in rare cases. Since the pioneering works by Epstein [1969] and Fleming [1971a,b], many successful efforts have been made to quantify and incorporate the uncertainties in NWP models. The most popular concepts are: stochastic-dynamics prediction and the Monte-Carlo (MC) approach. The *stochastic-dynamic* approach to uncertainty, developed by Epstein, is inherently probabilistic, and involves approximating probability informations of the posterior distribution of the variables of interest by making use of the statistical moments of the prior distribution. However, direct application of this approach is computationally intractable in the case of global forecast models. The MC approach first proposed by Leith [1974, 1978, 1980], involves integration of the forecast model starting from different initial condition. The MC approach is the basis of all the ensemble techniques (including the ensemble data assimilation) which in fact mimics the time evolution of the *pdf*. There also exist a third approach known as the Lagged-Average Forecasting (LAF) proposed by Hoffman and Kalnay [1983], where the initial states are generated from different but regularly *lagged* analysis time steps.

The main purpose of ensemble forecasting is to describe the uncertainty of the forecast in terms of the statistical properties of the ensemble, and these statistical properties depends on the representation of the model error, in addition to the initial and boundary conditions. Appropriate representation of model error is very important especially in the first hours of the integration. In the framework of an Ensemble Prediction System (EPS), the initialization uncertainty can be tackled by integrating the model using a set of possible initial states generated using techniques such as breeding vectors (BVs) [Patil et al., 2001; Keller et al., 2010], singular vectors (SVs) [Ehrendorfer and Tribbia, 1997; Palmer et al., 1998; Gelaro et al., 1998], LAF [Dalcher

et al., 1988; Toth and Kalnay, 1993] etc. or an analysis ensemble derived from an ensemble data assimilation [Molteni et al., 1996; Houtekamer and Mitchell, 1998, 2001; Kalnay, 2003]. For example, at the European Center for Medium-range Weather Forecasts (ECMWF), the initial ensembles are generated by perturbing the analysis using a linear combination of SVs from an adjoint model and ensemble data assimilation (EDA) perturbations. The use of SVs for the perturbation is based on the intuition that SVs represent the error growth along the directions of most rapid amplification. In the United States, the National Center for Environmental Prediction (NCEP) use BVs, which show similar error growth characteristics as SVs, for the EPS initialization [Toth and Kalnay, 1993, 1997]. One advantage of the BV approach is that it does not need an adjoint model and is thus computationally attractive. Furthermore, the model uncertainties can be brought down to some extent by introducing *stochasticity* within the forecast model.

There have been numerous discussions in the literature regarding the role of model errors in NWP [e.g., Tribbia and Baumhefner, 1988; Saha, 1992; Dee, 1995; Ehrendorfer, 1997]. The physical parameterization error is one of the major contributors to the uncertainties associated with a model since the errors in the unresolved scales inevitably amplify the errors in the resolved scales through the nonlinear scale interaction, also known as inverse error-cascade [Lorenz, 1969; Leith, 1971; Ehrendorfer, 1997]. The concept of stochastic parameterization is originated from the fact that incorporating the uncertainties associated with the smaller scales may in turn helps a better estimation of model errors, hence of forecast uncertainty, as well as a better representation of atmospheric processes. This in fact turns out to be true in many operational EPS.

Apart from the model uncertainties caused by the parameterization schemes, almost all numerical weather prediction models generally tend to over-dissipate energy near the truncation scale; few examples are: i) the Kinetic Energy (KE) released in deep convection, which is assumed to be dissipated within the model grid; ii) Parameterization of the mountain and gravity wave drag, and iii) the vertical diffusion, which generates turbulent energy dissipation. Shutts [2005] argued that a fraction of the dissipated kinetic energy should be backscattered into the model. Shutts [2005] proposed the use of a stochastic kinetic energy backscatter (SKEB) scheme in NWP models, which was originally developed in the context of large eddy simulation [Leith, 1978; Mason and Thomson, 1992; Frederiksen and Davies, 1997], to compensate for the reduced energy up-scaling due to the over-dissipation. It has been shown that, random injection of backscatter near the model truncation scale compensates for the absence of inverse cascade coming from the unresolved and highly dissipated scales [Shutts, 2005; Berner et al., 2009; Charron et al., 2010; Tennant et al., 2011].

In the following sections we will discuss the role of model errors in data assimilation, the motivation of this thesis, and the research questions. We will also provide a summary of research contributions and the outline of this thesis work.

### 1.2.1 Role of Model Errors in Ensemble Data Assimilation

In meteorology and physical oceanography, data assimilation is a procedure for *optimal estimation* of the state of the atmosphere or the ocean by combining all available ob-

servations along with the model forecast states as well as the corresponding estimated uncertainties, which include both forecast and observation errors. In a broad sense data assimilation is equivalent to a recursive Bayesian optimal estimation. Generally, a data assimilation system consists of three major components: a set of observations, a dynamical model, and an assimilation scheme which is equivalent to an optimal estimation method. The most popular data assimilation methods are variational methods such as 3-Dimensional Variational (3D VAR) and 4-Dimensional Variational (4D VAR) methods, sequential methods such as Ensemble Kalman Filter (EnKF), and *hybrid* methods which make use of the advantages of both variational methods and Kalman Filter (KF) methods. Variational methods are based on Maximum-Likelihood Estimate (MLE) and KFs are based on minimum mean-squared estimate. It can be shown that both 4D VAR and KFs are equivalent in the case of linear Gaussian systems.

The goal of deterministic data assimilation systems (such as 3D VAR, 4D VAR) is to provide an estimate of the most probable state of the atmosphere which then can be used as the initial condition for a weather forecast. In NWP, this is achieved by deriving an optimal analysis state using a short range forecast or *background*, the *background errors*, actual observations, and *observation errors*. The short range forecast is usually initialized from a previous optimal analysis. The *background* and *observation* errors are usually prescribed quantities based on long term statistics, and also based on other assumptions. Almost all operational data assimilation systems except nudging are *cycled data assimilation* schemes, which consists of repeated sequences of short range forecasts and analysis steps. One of the main goals of an EDA system is to provide an estimate not only of the most probable state of the atmosphere but also an estimate of its time-evolved uncertainties. The time-evolved uncertainty associated with the analysis is also known as the *analysis error* or simply the *error of the day*. Since an explicit description of the time-evolved *pdf* is not achievable, the uncertainty is represented by an ensemble of model states for both the analysis and the background. Another goal of the EDA is to use more sophisticated knowledge on the situation and the state depending on the uncertainty of the background (background error) in order to provide an improved deterministic analysis and analysis error. Thus the uncertainty estimates provided by the EDA are background error and analysis error. These estimates depend on the history of the cycled analysis system and on the uncertainties introduced, mainly the observation and model errors.

The analysis error is derived during the analysis step by making use of the information from the background error provided by the forecast ensemble and from the observational error. Depending on the formulation, the observational errors is either explicitly taken into account (as in ensemble square root filters) or must be introduced by randomization of the observations (independent analysis approach at the ECMWF). In order to account for the shortcomings of the analysis system itself (limited ensemble size, linearity assumptions etc.) an *inflation* mechanism is used for the analysis ensemble. More details regarding the formulation of the analysis step and inflation mechanism can be found in section (2.2) and (4.1) respectively.

As mentioned previously, in a cycled data assimilation system the *background* is derived from a short range ensemble forecast started from the previous analysis ensemble. Consequently its uncertainty (background error) depends on the prior analysis

error and also errors introduced by the forecast model, i.e., the *model error*. In contrast to the observation error the model error has to be introduced by incorporating stochasticity during the model integration or randomly perturb the background state at the end of the short-range forecast. Formulating suitable approaches to represent the model error is an essential component of ensemble data assimilation systems and currently subject of intensive research. The evaluation of the stochastic kinetic energy backscatter scheme in the above context is the main contribution to this research.

Several strategies have been proposed and are extensively studied for incorporating model errors into ensemble data assimilation schemes [e.g., Daley, 1992; Stensrud et al., 2000; Evensen, 2003; Hamill and Whitaker, 2005; Hamill, 2006; Zupanski and Zupanski, 2006; Houtekamer et al., 2009]. The most popular methods include: i) adding zero mean Gaussian noise with a small amplitude during the assimilation cycle, which in fact mimics the forecast uncertainty [Evensen, 2003]; (ii) additive and multiplicative inflation, i.e., inflating the “underestimated” background error covariance matrix before the analysis step [Anderson and Anderson, 1999; Anderson, 2001]; iii) perturbing the model physics (stochastic physics) [Buizza et al., 1999] or perturbing the model dynamics using techniques such as SKEB [Shutts, 2005] which in fact corrects or inflates the background covariance matrix; iv) combination of the above three methods [Palmer et al., 2009; Berner et al., 2011; Bonavita et al., 2012]. There is no clear indication of the out-performance of one particular method over the others since the performance of the above mentioned techniques also depends on the model formulation and on the data assimilation scheme.

From the data assimilation point of view, the forecast errors are treated as the sum of the model errors<sup>1</sup>, and of the system errors. As described in the previous section, the *background errors* are the sum of the errors due to the imperfections in the knowledge of initial atmospheric state, imperfections in the model formulations such as the adiabatic framework (spectral or grid-point etc.), imperfections in using different vertical co-ordinate systems, and errors due to the representativeness of physical processes. On the other hand the so-called *system errors* are mostly due to numerics, i.e., numerical approximation, errors due to truncation and computing precision. Theoretically, in contrast to the sequential data assimilation methods such as the KFs, variational methods assume that there is no *system errors*, i.e., the numerical model is perfect. However, in practice, a *weak constraint* formulation is used in order to incorporate the system errors in variational methods [Gauthier and Thépaut, 2001; Trèmolet, 2003]. In general, system errors are unavoidable in virtually any computer simulations involving numerical models. In data assimilation it is assumed that their contribution to the total uncertainty is only a tiny fraction of the forecast errors, and does not introduce any significant impact on the short-term forecasts within the assimilation window. Also, it is assumed that the model and the observations are unbiased. In the framework of operational EPS, both background and initial errors are inexplicably linked through the data assimilation system. Any underestimation of one leads to the underestimation of the other, which may lead to huge forecast uncertainty in subsequent cycles, and unrealistic forecasts especially over longer time scales. It has also been shown that minor analysis differences can cause major forecast differences [Rabier et al., 1996]. In

---

<sup>1</sup>In the data assimilation community, a more generic name for model error is *background error*

this sense estimating precisely the forecast uncertainty and incorporating it into the data assimilation scheme is of extreme importance in NWP.

The motivation of this research stems from the fact that, in the context of global NWP, quantitative precipitation forecast (QPF<sup>2</sup>) is inherently probabilistic. The main reasons for the inherent probabilistic nature are: i) the time scale of the physical processes related to precipitation formation are much shorter than the model time step or the forecast lead-time, and ii) the inherent uncertainties in the representation of subgrid scale physical processes, i.e. the model error associated with physical parameterization. Therefore the only feasible method for QPF is to characterize the uncertainty and propagate the underlying *pdf* through MC approach. In practice, this is achieved through ensemble simulations, i.e. applying stochastic techniques to a state-of-the-art global EPS so that it can capture the forecast uncertainty. Simple stochastic approaches such as random perturbation of physical tendencies are quite unsatisfactory at least in its current state. On the other hand novel stochastic methods such as SKEB are promising but are still in their infancy. Thus a great deal of scientific underpinning is needed in order to evaluate its effectiveness in representing the model error in an ensemble prediction system.

### 1.3 Research Objectives

This thesis is primarily focused on evaluating the uncertainties associated with model error and the ways to using them to improve the model error representation in an ensemble data assimilation and prediction system. The chosen model for this study is the operational global weather forecast model GME of the *Deutscher Wetterdienst* (DWD) and the data assimilation system is a 3D VAR - Local Ensemble Transform Kalman Filter (LETKF) [Hunt et al., 2007]. The GME model is an icosahedral-hexagonal grid-point model [Majewski et al., 2002], and is ideally suited for an independent evaluation of forecast uncertainty because of its unique design features in comparison to other operational weather forecast models (e.g., ECMWF, NCEP, CMC). On the other hand, currently there are no stochastic parameterization or stochastic physics schemes available for the operational GME model.

Until now, the first and only work referring to a stochastic parameterization of a full-scale weather forecast model was performed by Theis [2005]. Theis [2005] used the perturbed physics approach developed at the ECMWF [Buizza et al., 1999] in the COSMO model (at that time, it was called LM, Local model), a high resolution regional model further developed by the COSMO (Consortium for Small scale Modeling) consortium COSMO [2003].

The chosen stochastic approach to study and characterize the forecast uncertainty is the recently developed stochastic kinetic energy backscatter technique [Shutts, 2005; Berner et al., 2009]. Generally speaking, the Kinetic energy backscatter is a *concept*, which was developed during the early 90's by [Leith, 1990; Mason and Thomson, 1992] and was further developed to the SKEB scheme by Shutts [2005] at the ECMWF. In

---

<sup>2</sup>Funding of this PhD was provided by the DFG project, Quantitative Precipitation Forecast (QPF Phase III - SPP 1167)

the late 2010, ECMWF implemented a Spectral Stochastic Backscatter, which is based on a spectral autoregressive model, for their operational Integrated Forecasting System. Other operational forecasting centers, such as Canadian Meteorological Center (CMC), and UK Met. Office (UKMO) are working on their own SKEB schemes. However, the stochastic backscatter approach has not been yet used and studied in conjunction with a coupled 3D VAR - LETKF data assimilation system.

This study aims to:

- Investigate the sources of kinetic energy dissipation and develop a Stochastic Kinetic Energy Backscatter (SKEB) scheme for the operational global weather forecast model GME of the DWD;
- Study the impact of SKEB scheme on the medium range weather forecasts;
- Investigate the nature of flow-dependent background errors in GME, and study their impacts on the coupled 3D VAR - LETKF assimilation scheme, i.e. assessing the contribution of SKEB to the background error covariance;
- Explore the possibilities to overcome the drawbacks or constraints of the SKEB scheme on the GME-EPS, if any.

## 1.4 Contribution of this Research Work

During the course of this thesis, most of the research objectives stated in the previous section were successfully completed. The following concrete contributions were made to the development of a stochastic parameterization scheme for the GME Ensemble Prediction System (EPS) of the DWD.

### Summary of Research Contributions:

- Developed and implemented a Stochastic Kinetic Energy Backscatter (SKEB) scheme for the GME-EPS in a pre-operational setting.
- Demonstrated that the SKEB scheme is capable of improving the GME probabilistic forecast.
- Proposed and investigated a new power-law based random stream-function forcing pattern generator for SKEB scheme for GME model, which is computationally less-intensive than the cellular automated scheme and can overcome some of the drawbacks associated with the Cellular Automation.

## 1.5 Thesis Overview

This thesis describes the successful implementation of the stochastic kinetic energy backscatter scheme in the GME-EPS for improving quantitative precipitation forecasts.

Chapter 1 (*Introduction*) gives a brief general introduction to probabilistic ensemble forecasting in a historical context, followed by an overview of uncertainty problems in

NWP models, and possible solutions to it by using *stochastic approaches*. The key issues in approximating model (background) errors are discussed along with their impact on data assimilation schemes.

Chapter 2 (*Tools and Methods*) introduces the global Ensemble Prediction System (EPS) based on the global model GME of the Deutscher Wetterdienst (DWD). This chapter gives an overview of the GME model, and of the coupled 3D VAR - Local Ensemble Transform Kalman Filter assimilation system used in the GME-EPS experiments, as well as the existing issues and challenges associated with them. It also gives a short overview of the ensemble verification tools used to evaluate the experiments.

Chapter 3 (*Stochastic Backscatter in the GME Model*) introduces the general concept of Kinetic energy backscatter, and details the Stochastic Kinetic Energy Backscatter (SKEB) scheme used in the GME forecast model. The impact of the SKEB scheme on the forecast is evaluated in detail based on an ad-hoc set of EPS experiments. The impact of backscatter on the precipitation forecast is analyzed in detail.

Chapter 4 (*Stochastic Backscatter in the LETKF*) gives a detailed picture of how the background errors are represented in LETKF in general. This chapter also gives a detailed analysis of the LETKF assimilation, in particular of the impacts of incorporating the flow-dependent background errors in the LETKF using the backscatter scheme.

Chapter 5 (*Non-Gaussianity in Ensemble Kalman Filters*) provides a different perspective on the role of stochastic kinetic energy backscatter as a multiplicative (*state-dependant*) noise, and on its impact on both model forecast and LETKF assimilation. The potential issues regarding the possible deviation from Gaussianity due to multiplicative noise are also discussed in detail. This chapter also introduces the hybrid Kalman filter - Particle filter known as Sigma-Point Particle Filter. It is shown that it can handle non-Gaussianity due to multiplicative noise while overcoming the drawbacks of standard ensemble based Kalman filters. This Chapter has been published in the *Journal of Advances in Modelling the Earth System* (JAMES), as Ambadan and Tang [2011], and reproduced in this thesis with editorial modifications.

Chapter 6 (*Conclusions*) consolidates this thesis with a detailed discussion of the presented research topics, and provides some suggestions for future research.

Appendix A, and B, give a summary of the LETKF algorithm and the least square approach to Kalman gain; Appendix C gives additional figures supporting the main results.

## Tools and Methods

### 2.1 GME Model

The GME model is an icosahedral-hexagonal grid-point model developed by the DWD [Majewski et al., 2002]. The GME model has a primitive equation based dynamical core, and uses second order accurate semi-implicit numerical scheme. The current operational version of the GME uses a grid spacing of 20 km and 60 layers, and the forecast is deterministic (i.e., no ensemble forecast). All ensemble experiments described in this chapter use the GME model with a resolution of 40 km and 40 layers (with a cell area of  $1384\text{km}^2$ ), which was operational from 27<sup>th</sup> September 2004 till 2<sup>nd</sup> February 2010. The GME grid is generated by inscribing an icosahedron with 20 triangles of equal size into the sphere. The spacing of the GME grid is determined by the number of intervals  $n_i$  on a main triangle side (of a length of about 7054 km). The vertical discretization of GME is based on hybrid sigma-pressure coordinates [Simmons and Burridge, 1981]. Combining all grid points of two adjacent large triangles to a square matrix the global GME grid consists of 10 diamonds or sub-domains. For a better load balance the  $(n_i + 1)^2$  grid points of each diamond are distributed to  $n1 \times n2$  processors (processing elements, PEs). The sub-domains are surrounded by a halo of two rows and columns, and are exchanged at each time step between adjacent sub-domains. The parallel communication between PEs are based on Message Passing Interface (MPI) routines, and all the diamonds are synchronized after each forecast step.

### 2.2 The GME Data Assimilation

In this section we will briefly review the concepts of the 3D VAR and of the LETKF assimilation algorithms, which are used in our investigations. Initial conditions are either taken from the operational 3D VAR data assimilation cycle (interpolated to the resolution of the experiments) or from the pre-operational LETKF. In the latter context the 3D VAR is still used for quality control of the observations. The theory and derivations presented in this section are mainly based on the works by, Daley [1992]; da Silva et al. [1995]; da Silva and Guo [1996]; Courtier [1997]; Cohn [1997]; Cohn et al. [1998]; Courtier et al. [1998]; Kalnay [2003]; Tippett et al. [2003]; Hamill [2006]; Hunt et al. [2007], and the references therein.

### 2.2.1 3D VAR Assimilation

Variational methods such as 3D VAR, are Maximum-Likelihood Estimators (MLE); i.e., they seek an estimate which maximizes the probability of occurrence of the state.. Since variational methods seek a conditional *mode* they can be thought of as *model-trajectory estimators*. On the contrary, sequential methods such as KFs are conditional *mean* estimators or Minimum Mean-Squared Error (MMSE) estimators, i.e., they seek an estimate which minimizes the mean squared error. In general both MLE and MMSE estimators are equivalent in the case of a linear Gaussian system while they are different for nonlinear systems.

To formulate the 3D VAR estimator, consider an  $L$  dimensional dynamical system represented by a set of discretized state space equations,

$$\boldsymbol{\theta}_k = \mathbf{f}(\boldsymbol{\theta}_{k-1}, \mathbf{q}_{k-1}) \quad (2.1)$$

$$\boldsymbol{\psi}_k = \mathbf{h}(\boldsymbol{\theta}_k, \mathbf{r}_k) \quad (2.2)$$

where  $\boldsymbol{\theta}_k$  represents the system state vector at time  $k$ ,  $\mathbf{f}(\cdot)$  is the nonlinear function of the state,  $\mathbf{q}_k$  is the random model errors,  $\boldsymbol{\psi}_k$  is the measured state,  $\mathbf{h}(\cdot)$  is the measurement function, and  $\mathbf{r}_k$  is the zero-mean random measurement noise. Assuming that the state, observation and noise terms are Gaussian processes, the probability of the maximum likelihood state of  $\boldsymbol{\theta}$  is proportional to  $e^{-\mathbf{J}}$ , where  $\mathbf{J}$  is a *cost function*, given by,

$$\begin{aligned} \mathbf{J}(\boldsymbol{\theta}) = & \frac{1}{2} [\boldsymbol{\theta} - \boldsymbol{\theta}_k^b]^\top (\mathbf{P}_k^b)^{-1} [\boldsymbol{\theta} - \boldsymbol{\theta}_k^b] \\ & + [\boldsymbol{\psi}_k^o - \mathbf{h}(\boldsymbol{\theta})]^\top (\mathbf{R}^{-1}) [\boldsymbol{\psi}_k^o - \mathbf{h}(\boldsymbol{\theta})] \end{aligned} \quad (2.3)$$

where  $\boldsymbol{\theta}_k^b$  is the background,  $\mathbf{P}_k^b$  is the background state covariance matrix, also known as the *B matrix*,  $\boldsymbol{\psi}_k^o$  is the observations, and  $\mathbf{R}$  is the observation error covariance matrix. Assuming that  $(\boldsymbol{\theta} - \boldsymbol{\theta}_k^b)$  is small and analysis is close to the truth, we can linearize the observation function  $\mathbf{h}(\cdot)$  as follows:

$$[\boldsymbol{\psi}_k^o - \mathbf{h}(\boldsymbol{\theta})] = \boldsymbol{\psi}_k^o - \mathbf{h}(\boldsymbol{\theta}_k^b + (\boldsymbol{\theta} - \boldsymbol{\theta}_k^b)) \quad (2.4)$$

$$\approx \{\boldsymbol{\psi}_k^o - \mathbf{h}(\boldsymbol{\theta}_k^b)\} - \mathbf{H}(\boldsymbol{\theta} - \boldsymbol{\theta}_k^b) \quad (2.5)$$

Substituting (2.5) in (2.3), we obtain the quadratic cost function,

$$\begin{aligned} \mathbf{J}(\boldsymbol{\theta}) \approx & \frac{1}{2} [\boldsymbol{\theta} - \boldsymbol{\theta}_k^b]^\top (\mathbf{P}_k^b)^{-1} [\boldsymbol{\theta} - \boldsymbol{\theta}_k^b] \\ & + [\{\boldsymbol{\psi}_k^o - \mathbf{h}(\boldsymbol{\theta}_k^b)\} - \mathbf{H}(\boldsymbol{\theta} - \boldsymbol{\theta}_k^b)]^\top (\mathbf{R}^{-1}) [\{\boldsymbol{\psi}_k^o - \mathbf{h}(\boldsymbol{\theta}_k^b)\} - \mathbf{H}(\boldsymbol{\theta} - \boldsymbol{\theta}_k^b)] \end{aligned} \quad (2.6)$$

For the analysis  $\boldsymbol{\theta} = \boldsymbol{\theta}_k^a$ , we set the gradient of  $\mathbf{J}(\boldsymbol{\theta}) = 0$ , which minimizes the *cost function* (2.3), i.e.,

$$\left. \frac{\partial \mathbf{J}}{\partial \boldsymbol{\theta}} \right|_{\boldsymbol{\theta}=\boldsymbol{\theta}_k^a} = \nabla_{\boldsymbol{\theta}} \mathbf{J}(\boldsymbol{\theta}_k^a) = 0 \quad (2.7)$$

Its solution gives the 3D VAR analysis equation,

$$\boldsymbol{\theta}_k^a = \boldsymbol{\theta}_k^b + \left[ (\mathbf{P}_k^b)^{-1} + \mathbf{H}^T \mathbf{R}^{-1} \mathbf{H} \right]^{-1} \mathbf{H}^T \mathbf{R}^{-1} (\boldsymbol{\psi}_k^o - \mathbf{h}(\boldsymbol{\theta}_k^b)) \quad (2.8)$$

Equation (2.8) can be re-written in many forms. The most common form is,

$$\boldsymbol{\theta}_k^a = \boldsymbol{\theta}_k^b + \mathbf{K} (\boldsymbol{\psi}_k^o - \mathbf{h}(\boldsymbol{\theta}_k^b)) \quad (2.9)$$

where  $\mathbf{K}$  is known as the *gain*<sup>1</sup> matrix, given by,

$$\mathbf{K} = \mathbf{P}_k^b \mathbf{H}^T [\mathbf{H}^T \mathbf{P}_k^b \mathbf{H} + \mathbf{R}]^{-1} \quad (2.10)$$

In practice the solution is obtained through iterative minimization algorithms, such as *conjugate-gradient* algorithm, since direct inversion of the matrix term in (2.8) is impractical because of its large dimensionality ( $L \approx 10^8$ ).

The GME-EPS uses a variant of 3D VAR, known as Physical Space Assimilation System (PSAS) [Courtier, 1997]. which computes the analysis equation in the physical space (or observation space) rather than in the model space. The main advantages of PSAS are: i) most of the calculations are in observation space, which reduces the size of the problem, ii) efficient preconditioning of the iterative solver (see below) is possible, and iii) most parts of the algorithm are fairly independent from the model formulation.

The PSAS algorithm solve the following equation for the quantity  $\mathbf{w}$

$$\mathbf{M}\mathbf{w} = \boldsymbol{\psi}_k^o - \mathbf{h}(\boldsymbol{\theta}_k^b) \quad (2.11)$$

where  $\mathbf{M}$  is the innovation matrix given by,

$$\mathbf{M} = (\mathbf{H}\mathbf{P}_k^b\mathbf{H}^T + \mathbf{R}) \quad (2.12)$$

and the quantity  $\mathbf{w}$  is known as *partially weighted innovations*. The corresponding analysis is given by,

$$\boldsymbol{\theta}_k^a = \boldsymbol{\theta}_k^b + \mathbf{P}_k^b \mathbf{H}^T \mathbf{w} \quad (2.13)$$

The innovation matrix  $\mathbf{M}$  is usually not sparse and too big to be specified explicitly. It must also be a symmetric positive definite matrix. Equation (2.11) is solved by a standard pre-conditioned conjugate gradient algorithm [Golub and van Loan., 1989]. The pre-conditioner uses the block-diagonal of the matrix,  $\mathbf{M}$  given by Eq. (2.12). Each block consists of about 500-1000 nearby observations as matrices of this size can easily be inverted explicitly.

Solving equations (2.11) to (2.13) is equivalent to minimizing the cost function (2.6). In order to account for the nonlinearities in  $\mathbf{h}$ , the linearization (2.5) is repeated in an outer loop and (2.11) to (2.13) solved for adjusted  $\mathbf{H}$  and right hand side of (2.11). More details can be found in the GME 3D VAR documentation [Fischer et al., 2012].

---

<sup>1</sup>commonly known as *Kalman gain*

In the GME 3D VAR, the background error covariance matrix  $\mathbf{P}_k^b$  is currently derived by using the NMC method, i.e. by calculating the covariances of differences of forecasts  $\boldsymbol{\theta}_{24h}$ , and  $\boldsymbol{\theta}_{48h}$  with different lead time but valid at the same time, i.e.,

$$\mathbf{P}_k^b \approx \frac{1}{\gamma} \mathbb{E} \left[ (\boldsymbol{\theta}_{48h} - \boldsymbol{\theta}_{24h}) (\boldsymbol{\theta}_{48h} - \boldsymbol{\theta}_{24h})^T \right] \quad (2.14)$$

where  $\mathbb{E}$  is the mathematical expectation, and  $\gamma$  is a scaling factor. The NMC method is a commonly used procedure to estimate balanced correlation patterns for background error covariances. The covariances are derived according to a seasonal climatological basis using statistics from three consecutive months. Zonal averaging is used which implicitly increases the size of the ensemble. A weak localization is applied in order to suppress spurious correlations between the Northern and the Southern hemisphere. The factor  $\gamma$  is derived from the previous analysis error estimate and a simple model for the increase of forecast error with time. Covariances are stored in form of wavelet coefficients on a Gaussian grid. Currently separability of horizontal and vertical correlations is assumed. See the DWD 3D VAR documentation for more details [Fischer et al., 2012].

### 2.2.2 LETKF Assimilation

Among sequential data assimilation methods, EnKF based methods have attracted broad attention in meteorology and physical oceanography because of their simplicity as well as ease of implementation [e.g., Evensen, 1992; Houtekamer and Mitchell, 1998; Evensen, 2003; Zhang and Snyder, 2007]. In a broad sense, the EnKF is an MC approximation to the standard KF which is in turn a simplification of Bayesian estimation that provides sequential, unbiased, minimum error variance estimates based upon a linear combination of all past measurements and dynamics [Welch and Bishop, 1995]. The main concept behind the formulation of the EnKF is that the prediction error statistics described by the Fokker-Plank equation can be approximated using ensemble integrations [Evensen, 1994, 1997]; i.e., the error covariance matrices can be calculated using an ensemble of model states. The major strengths of the EnKF include: i) there is no need to calculate the tangent linear or adjoint of forecast models, which is quite difficult for General Circulation Models (GCMs), ii) the background error covariance matrix is propagated in time via the full nonlinear model (no linear approximation), and iii) it suits modern parallel computing [Keppenne, 2000]. However, there are also some disadvantages of using EnKF data assimilation which limit the direct use of the standard EnKF for many real world problems. They are: i) a finite ensemble size has major effects on the performance of the EnKF. A small ensemble size increases the residual errors while a large ensemble is computationally infeasible in NWP; ii) linear assumptions in the assimilation step (linearized measurement or observation operator); and iii) computing limitations due to size of the error covariance matrix.

Several EnKF based methods have been proposed over the last couple of decades, some of which have shown to overcome most of the drawbacks associated with the standard EnKF assimilation. Among them, the most popular include Ensemble Adjustment Kalman Filter (EAKF), the Ensemble Square Root Kalman Filter (EnSRKF), the Lo-

cal Ensemble Transform Kalman Filter (LETKF), and their variants [e.g. Anderson, 2001, 2002; Tippett et al., 2003; Hamill, 2006; Hunt et al., 2007].

For the purpose of presentation, consider an ensemble of size  $N$  of the  $L$  dimensional state space model given by (2.1)-(2.2). The approximated mean and covariance of the background state in model space represented by the ensemble are given by,

$$\bar{\boldsymbol{\theta}}_k^b \approx \frac{1}{N} \sum_{n=1}^N \boldsymbol{\theta}_{k-1,n}^b \quad (2.15)$$

$$\mathbf{P}_k^b \approx \frac{1}{N-1} \sum_{n=1}^N \left[ \left( \boldsymbol{\theta}_{k,n}^b - \bar{\boldsymbol{\theta}}_k^b \right) \left( \boldsymbol{\theta}_{k,n}^b - \bar{\boldsymbol{\theta}}_k^b \right)^T \right] \quad (2.16)$$

$$= \frac{1}{N-1} \sum_{n=1}^N \boldsymbol{\Theta}_k \left( \boldsymbol{\Theta}_k \right)^T \quad (2.17)$$

where  $(\bar{\cdot})$  denotes the statistical average over the ensemble, and  $\boldsymbol{\Theta}_k$  is a  $L \times N$  matrix whose  $n^{\text{th}}$  column is  $\boldsymbol{\theta}_{k,n}^b - \bar{\boldsymbol{\theta}}_k^b$ . The EnKF algorithm also derives an analysis that minimizes the cost function (2.3) by solving equation (2.8). Calculating the inverse term in (2.8) becomes feasible only by restricting the solution to the subspace of the ensemble.

Let  $\mathbf{w}$  be a Gaussian random vector defined in the ensemble sub-space with mean zero, and covariance  $(N-1)^{-1} \mathbf{I}$ , then the model state with covariance (2.17) can be re-written as,

$$\boldsymbol{\theta} = \bar{\boldsymbol{\theta}}_k^b + \boldsymbol{\Theta}_k \mathbf{w} \quad (2.18)$$

Therefore the cost-function (2.3) in the ensemble sub-space is given by,

$$\tilde{\mathcal{J}}(\mathbf{w}) = (N-1) \mathbf{w}^T \mathbf{w} + \left[ \boldsymbol{\psi}_k^o - \mathbf{h} \left( \bar{\boldsymbol{\theta}}_k^b + \boldsymbol{\Theta}_k \mathbf{w} \right) \right]^T \mathbf{R}^{-1} \left[ \boldsymbol{\psi}_k^o - \mathbf{h} \left( \bar{\boldsymbol{\theta}}_k^b + \boldsymbol{\Theta}_k \mathbf{w} \right) \right] \quad (2.19)$$

A quadratic cost-function similar to (2.6) can be obtained by linear approximation of the observation function  $\mathbf{h}(\cdot)$  given by,

$$\mathbf{h} \left( \bar{\boldsymbol{\theta}}_k^b + \boldsymbol{\Theta}_k \mathbf{w} \right) \approx \bar{\boldsymbol{\psi}}_k^b + \boldsymbol{\Psi}_k \mathbf{w} \quad (2.20)$$

where,

$$\bar{\boldsymbol{\psi}}_k^b \approx \frac{1}{N} \sum_{n=1}^N \mathbf{h} \left( \boldsymbol{\theta}_{k,n}^b \right) \quad (2.21)$$

$$\boldsymbol{\Psi}_k = \boldsymbol{\psi}_k^o - \bar{\boldsymbol{\psi}}_k^b \quad (2.22)$$

Thus we can re-write (2.19) as,

$$\tilde{\mathcal{J}}(\mathbf{w}) = (N-1) \mathbf{w}^T \mathbf{w} + \left[ \boldsymbol{\psi}_k^o - \bar{\boldsymbol{\psi}}_k^b - \boldsymbol{\Psi}_k \mathbf{w} \right]^T \mathbf{R}^{-1} \left[ \boldsymbol{\psi}_k^o - \bar{\boldsymbol{\psi}}_k^b - \boldsymbol{\Psi}_k \mathbf{w} \right]^T \quad (2.23)$$

It is assumed that if  $\mathbf{w}^a$  minimizes (2.23), then the analysis  $\boldsymbol{\theta}_k^a$  is optimal. The analysis equations are given by,

$$\bar{\boldsymbol{\theta}}_k^a = \bar{\boldsymbol{\theta}}_k^b + \boldsymbol{\Theta}_k \mathbf{w}^a \quad (2.24)$$

where,

$$\mathbf{w}^a = \tilde{\mathbf{P}}_k^a (\boldsymbol{\Psi}_k)^T \mathbf{R}^{-1} (\boldsymbol{\psi}_k^o - \bar{\boldsymbol{\psi}}_k^b) \quad (2.25)$$

$$\tilde{\mathbf{P}}_k^a = \left[ (\mathbf{N} - 1) \mathbf{I} + (\boldsymbol{\Psi}_k)^T \mathbf{R}^{-1} \boldsymbol{\Psi}_k \right]^{-1} \quad (2.26)$$

The initial background ensemble at the next analysis time is generated by integrating the model forward and adding some model error  $\boldsymbol{\epsilon}$ :

$$\boldsymbol{\theta}_k^b = \mathbf{f} (\boldsymbol{\theta}_{k-1,n}^a + \boldsymbol{\epsilon}) \quad (2.27)$$

Accounting for model error is an essential part of any Kalman filter algorithm. Without that, the ensemble spread would always decrease due to the additional information added to the system by the observations. Currently we represent the model error by random errors  $\boldsymbol{\epsilon}$  whose spatial correlations are consistent with the dynamical balances accounted by the 3D VAR  $\mathbf{B}$  matrix. Technically we add a vector of normally distributed random variables multiplied by a fraction of the square-root of the 3D VAR  $\mathbf{B}$  matrix<sup>2</sup>. Another method to keep the ensemble spread at a finite value is inflation; i.e., the ensemble deviations  $\boldsymbol{\Theta}$  are multiplied by a number slightly larger than 1. This can be implemented within the LETKF algorithm itself without explicitly modifying the model state [Hunt et al., 2007].

Analysis increments  $\mathbf{w}^a$  are restricted to the subspace spanned by the ensemble members. For practical reasons the ensemble size  $\mathbf{N}$  is about 100 or well beyond in atmospheric applications. This is much too low to represent all the degrees of freedom of the atmospheric state. Representation of the background error covariance matrix by an ensemble of limited size leads to spurious large correlations. This is especially true for locations separated by large distances. On the contrary the true correlations are actually small due to the limited statistical basis. To cure this problem the ensemble background error covariance matrix is generally multiplied element by element (Schur product) by another (localization) matrix which has the same property of the covariance matrix, i.e., positive definite, one on the diagonal, zero for off-diagonals for large separation distances.

The EnKF algorithm described above is computationally cheaper because calculations are performed in the subspace of the ensemble. Straightforward application of the Schur product localization leads to full rank background error covariance matrices and thus lead to expensive numerical algorithm.

In the GME-EPS implementation we use the LETKF algorithm of Hunt et al. [2007]. Hunt et al. [2007] use another localization procedure in order to keep the algorithm efficient. At each grid-point of the model the EnKF equations (2.15)-(2.26)

---

<sup>2</sup>More details regarding the inflation techniques can be found in Chapter (4)

are solved using only the observations within a given distance to this point. In order to get analysis varying smoothly from grid-point to grid-point, observations are weighted with a smooth function [Gaspari et al., 1998; Gaspari and Cohn, 1999]. Basically the terms  $R^{-1}$  in Eqs. (2.25) and (2.26) are multiplied with this factor. This function is very similar to a Gaussian being 1 for small distances and zero for  $\sigma \approx 3$  just at the boundary of the area containing the used observations. For in-situ observations the effect of Hunt et al. [2007] algorithm is very close to that of the original Schur product.

In LETKF implementation, an inflation of the covariance is necessary in most cases due to the underestimation of  $\tilde{\mathbf{P}}_k^a$ . The underestimation of covariance is due to: i) the lack of enough spread in the forecast ensemble; ii) sampling errors; and iii) approximation of nonlinearities. Two most popular ways of introducing covariance inflation are additive inflation and multiplicative inflation. Additive inflation is equivalent to adding perturbation  $\epsilon$  as in (2.27). More details regarding the covariance inflation and the role of backscatter are described in Chapter 4. Appendix A summarizes the complete LETKF algorithm.

### 2.2.3 Observation Processing

Observation processing is performed by the same code as used in the operational 3D VAR system at the DWD. In the experiments the LETKF is preceded by a 3D VAR step which performs the first guess check and quality control of observations. It then passes the observations to the LETKF module. Conceptually, a hybrid 3D VAR - LETKF uses a weighted  $\mathbf{P}_k^b$  matrix derived from both the 3D VAR and the LETKF for the minimization of the cost-function. The main role of the 3D VAR module in GME-EPS is to perform first guess checks and a quality control of observations. It then passes the observations to the LETKF module. Before the assimilation step all available observations are monitored, quality controlled, bias corrected and thinned. Only a fraction of the available observations is used for the assimilation. Afterwards the statistics on the data is stored and used in subsequent assimilation cycles. The main task of *monitoring* the observations is to apply the observation operator to the background model states and gather statistics which can later be used to assess the errors and the biases. The *quality control* step includes blacklisting and removing the outliers. The *bias correction* step removes any systematic error in the radiance observations. The *bias correction* also gather the *innovation statistics* and derive the mean bias of the observations w.r.t. the first-guess. The *thinning* step accounts for correlation in the observations. If the correlations are not accounted for, too much weight is given to that particular data which deteriorate the assimilation. The spatially correlated data may be thinned until the remaining data is un-correlated. The *thinning* step also helps to reduce the computational burden in the assimilation step. In almost all experiments the role of 3D VAR in the actual assimilation step is minimal (other than preprocessing observations). An overview of the hybrid system in GME-EPS is illustrated in Fig. (2.1). In a later stage the 3D VAR - LETKF will be extended to a truly hybrid system where the localized ensemble background is directly used in the variational scheme, following the approach of extended control variables [Buehner, 2005; Buehner and Charron, 2007].

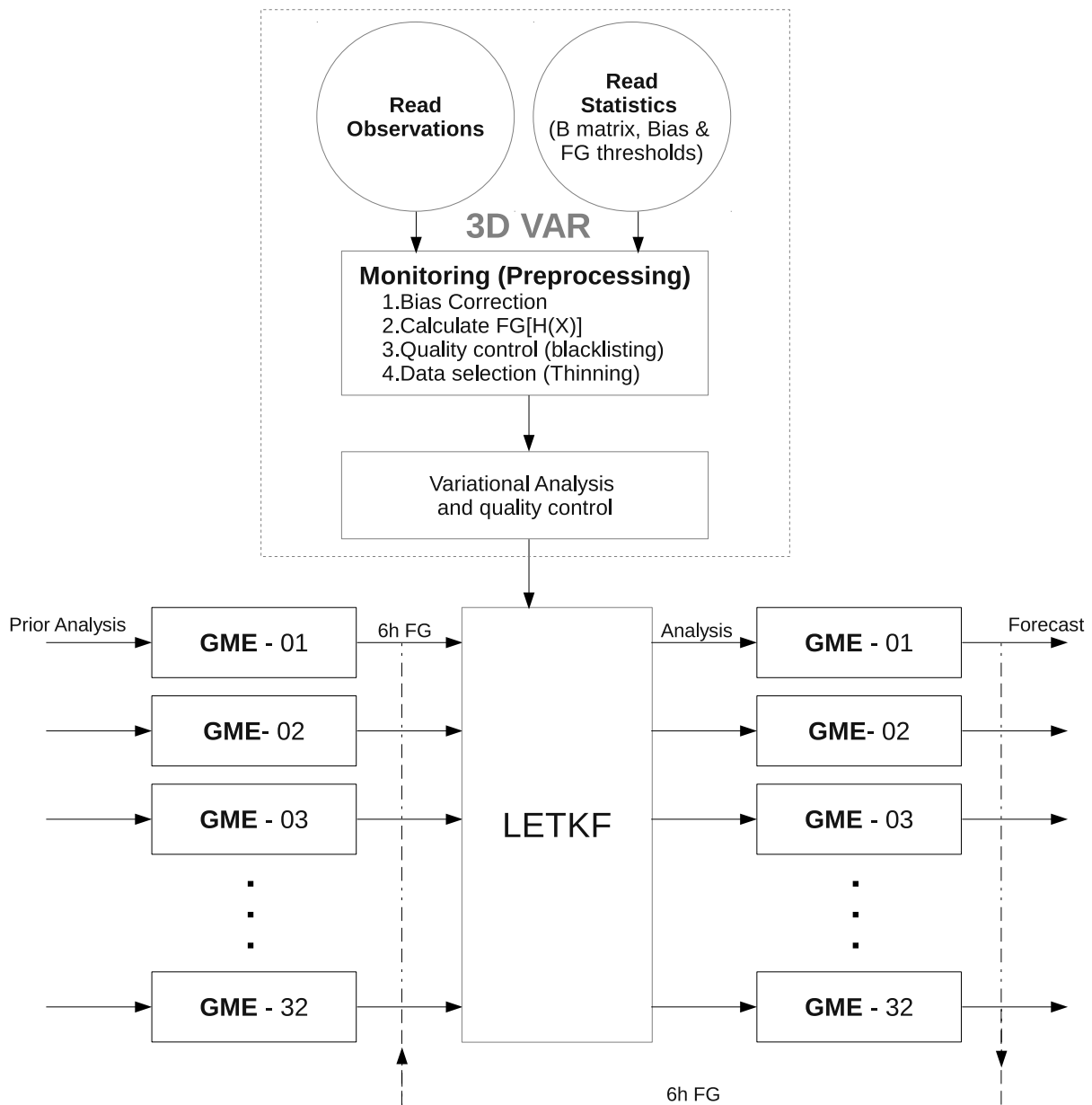


**Figure 2.1:** Schematics of the 3D VAR - LETKF assimilation system

## 2.3 Overview of Verification Methods and Diagnostics

Several verification methodologies have been developed to evaluate forecast and analysis ensemble products from an EPS [e.g., Casati et al., 2008]. Generally speaking, there is no well established way of comparing and evaluating ensemble data from two different NWP systems, and there is no clear indication of the superiority of one statistical measure over the others in evaluating an ensemble forecast. Many research suggests that verification and validation methodology for EPS need to be developed further. However, the most commonly used statistics in evaluating ensemble forecasts, which we have also used, are: i) the ensemble spread, and the root mean squared error

(RMSE) against observation or reference analysis, ii) the continuous ranked probability score (CRPS) and its components, iii) the Ranked histograms iv) the Brier score and its components, and v) the receiver (relative) operating characteristics (ROC) curve and its area. The following subsections will give a brief overview of the statistical measures used in this thesis.

### 2.3.1 Ensemble Spread and Root Mean Squared Error

In ensemble forecasting, the most commonly used statistic is the ensemble (sample) standard deviation, commonly known as the ensemble spread. The ensemble spread measures the distance of an ensemble (sample) distribution from its mean (the sample mean). For the purpose of presentation, we use the common term SPREAD for representing the ensemble spread, i.e.,

$$\text{SPREAD} = \sqrt{\left(\frac{1}{N-1} \sum_{i=1}^N (\theta_i - \bar{\theta})^2\right)} \quad (2.28)$$

where  $\bar{\theta}$  is the ensemble (sample) mean.

In theory, the quantity root mean squared error (RMSE) is the measure of the distance between the ensemble (sample) distribution from the truth (population mean). In general, it is the population standard deviation, i.e.,

$$\text{RMSE}_e = \sqrt{\left(\frac{1}{N-1} \sum_{i=1}^N (\theta_i - \mathbf{o}_i)^2\right)} \quad (2.29)$$

where  $\mathbf{o}_i$  is usually either a set of accurate observations or an analysis from the same or an independent analysis system representing the unknown truth.

In this thesis, instead of the standard RMSE we use the RMSE of the ensemble mean as a metric to measure the accuracy of the forecast, i.e., a measure to evaluate the ensemble mean compared to the truth. Here the operational analysis from DWD is taken as the reference or truth. The RMSE the mean can be obtained from Eq. (2.28) and (2.29) as follows:

$$\text{RMSE} = \sqrt{(\text{RMSE}_e^2 - \text{SPREAD}^2)} \quad (2.30)$$

The RMSE is not a probabilistic but a deterministic score. Thus it can be used to compare a deterministic forecast with (some product from) a probabilistic forecast system, i.e., the mean of the forecast ensemble or a deterministic forecast started from the ensemble mean analysis. For long forecast ranges, there the forecast becomes uncertain, the mean of the forecast ensemble in general is better than a deterministic forecast as it takes advantage from the fact that it is close to climatology. In order to compare the RMSE of two forecasts in situations where the overall forecast quality varies considerably in different situations (periods of different general weather situations) normalized RMSE differences are used, i.e. statistics of the RMSE differences

normalized by the mean RMSE in a given subset, i.e.,

$$\text{Normalized RMSE}_l = \frac{(\text{RMSE}_l - \text{RMSE}_{ref})}{\{\text{RMSE}_{l=1\dots L}, \text{RMSE}_{ref}\}} \quad (2.31)$$

The ensemble spread should provide information of the uncertainty of the forecast. It is not a quality measure by itself but should match the RMSE defined above if forecast uncertainty is assessed appropriately. Descriptions of more sophisticated probabilistic measures are given in subsequent sections.

### 2.3.2 Ranked Histogram

In general the ranked histogram give more detailed information on the actual distribution of the truth (here observation or analysis) compared to the expectation (provided by the ensemble forecast) than just comparing RMSE and SPREAD. For an EPS of  $N$  ensemble members, equal weight is given to each member, i.e., the probability of occurrence of a certain event assigned to be equal for all members. The verifying analysis is such that the members are indistinguishable. The ranked histogram (also known as Talagrand diagram) is a measure of this indistinguishability [Talagrand et al., 1997; Hamill, 2001]. The ranked histogram is generated by plotting the relative frequencies of forecasted events with respect to the observed values as a function of the ensemble distribution. In general the ranked histogram can explain the variability of ensemble spread compared to observed. In a perfect EPS, the probability that the observation falls between any two ensemble members is equal among all member pairs.

The steps to create a ranked histogram are as follows:

1. Sort the ensemble members in ascending order, which represents  $N+1$  possible bins that the observation may falls into (including the outliers)
2. Identify the bin in which the observation fits in.
3. Repeat step 2 for all observations, and calculate the total frequency (sum over)
4. Plot the frequency (on the y-axis) versus the ensemble bins (on the x-axis)

A flat ranked histogram represents a robust ensemble forecast, i.e., the ensemble spread in fact represent the forecast uncertainty. However, a flat ranked histogram does not necessarily indicate a good forecast since it is only an indication that the observation distribution is well represented by the ensemble. A U-shaped ranked histogram indicates that most observations falls outside the ensemble (outliers), which is also an indication of low ensemble spread. A dome-shaped ranked histogram indicates that the ensemble is over-dispersive. A skewed dome-shape or U-shape indicate a bias in the ensemble.

### 2.3.3 Brier Score

The Brier score, first introduced by Brier [1950], measures the mean squared probability error of a forecast. It is also the first proper scoring rule introduced in NWP. The Brier

score is most commonly used for evaluating binary events characterized by a threshold value; for example, forecast events where precipitation is greater than 5 *mm* per day. The Brier score has a negative orientation: the smaller the score the better is the forecast. The Brier score (BS) is defined as,

$$\text{BS}(x_i) = \sum_i w_i (p_i - o_i)^2 \quad (2.32)$$

where  $p_i$  is the forecast probability of an event for the  $i^{\text{th}}$  case (or grid point) characterized by the threshold value  $x_i$ , and  $o_i$  is the observed probability.  $o_i = 1$  if the event is said to have happened, otherwise  $o_i = 0$ , and  $w_i$  is the corresponding weight.

Sanders [1963] partitioned the Brier score into reliability and resolution. Later, Murphy [1973] partitioned it into three terms: (i) reliability, (ii) resolution, and (iii) uncertainty. The reliability component measures the correspondence between forecast probability and observed relative frequencies, while resolution gives a measure of the ability of a forecaster, or forecasting technique to separate, in advance, a set of situations for which the event will occur and the set of situations for which it will not occur. The uncertainty measures the uncertainty of the forecast.

Following Hersbach [2000], the Brier score can be re-written as,

$$\text{BS}(x) = \text{Reliability}(x) - \text{Resolution}(x) + \text{Uncertainty}(x) \quad (2.33)$$

$$= \sum_{i=0}^N \mathbf{g}_i(x) [\mathbf{o}_i(x) - p_i]^2 + \sum_{i=0}^N \mathbf{g}_i(x) [\mathbf{o}_i(x) - \mathbf{o}(x)]^2 + \mathbf{o}(x) [1 - \mathbf{o}(x)] \quad (2.34)$$

where,

$$\mathbf{o}(x) = \sum_{i=0}^N \mathbf{g}_i(x) \mathbf{o}_i(x) \quad (2.35)$$

For an EPS of  $N$  ensemble members of equal weight sorted ascendingly,  $p_i = \frac{i}{N}$ . The quantity  $\mathbf{g}_i$  is the weighted fraction of the cases with  $p_i$  probability of the forecast, and  $\mathbf{o}_i$  is the fraction of cases (with  $p_i$ ) that are actually observed.  $\mathbf{g}_i$ , and  $\mathbf{o}_i$  are calculated as follows.

$$\mathbf{g}_i = \alpha_i + \beta_i \quad (2.36)$$

$$\mathbf{o}_i = \frac{\beta_i}{\alpha_i + \beta_i} \quad (2.37)$$

where,

### 2.3.4 Continuous Ranked Probability Score

In general the Continuous Ranked Probability Score (CRPS) can be interpreted as an integral of the Brier score over all possible thresholds. The CRPS measures the integrated squared difference between the cumulative distribution function of the forecast

| $0 < i < N$           | $\alpha_i$      | $\beta_i$       |
|-----------------------|-----------------|-----------------|
| $x_a > x_{i+1}$       | $x_{i+1} - x_i$ | 0               |
| $x_{i+1} > x_a > x_i$ | $x_a - x_i$     | $x_{i+1} - x_a$ |
| $x_a < x_i$           | 0               | $x_{i+1} - x_i$ |
| Outlier               | $\alpha_i$      | $\beta_i$       |
| $x_a < x_1$           | 0               | $x_1 - x_a$     |
| $x_N < x_a$           | $x_a - x_N$     | 0               |

and that of the observations. Following Hersbach [2000], the CRPS, may be decomposed into *Reliability*, and *Potential CRPS* (CRPS<sub>pot</sub>). It is given by,

$$\text{CRPS} = \text{Reliability} + \text{CRPS}_{\text{pot}} \quad (2.38)$$

$$= \sum_{i=0}^N \bar{\mathbf{g}}_i [(1 - \bar{\mathbf{o}}_i) p_i^2 + \bar{\mathbf{o}}_i (1 - p_i)^2] \quad (2.39)$$

where  $\mathbf{g}_i$ , and  $\mathbf{o}_i$  can be calculated according to (2.36), and (2.37), and the  $(\bar{\quad})$  denotes the statistical average over  $N$  cases or grid points. The Reliability component of CRPS measures the reliability of the EPS in general, while CRPS<sub>pot</sub> measures the CRPS of the EPS if the system would have been perfectly reliable. The CRPS is also a negatively oriented score: the lower the score, the better the system is. In the case of deterministic forecasts the CRPS corresponds to the Mean Absolute Error (MAE), given by

$$\text{MAE} = \frac{1}{N} \sum_{i=i}^N |\boldsymbol{\theta}_i - \mathbf{o}_i| \quad (2.40)$$

where  $\mathbf{o}_i$  is either the observed data or the analysis from a reference EPS depending on the variables.

### 2.3.5 Receiver Operating Characteristics

The Receiver (or Relative) Operating Characteristic curve, commonly known as ROC curve, is a plot of hit rate (HR) vs false alarm rate (FAR). The ROC measures the ability of the forecast to discriminate between two alternative outcomes, and it indicates the usefulness of a forecast. The hit rate is defined as the fraction of forecasted events (with some threshold) which are correctly observed, and the false alarm rate is the fraction of the forecasted events that are not actually observed (simply, the fraction of incorrect forecast). The HR and FAR are computed from the following contingency table.

|                      |                     |                     |
|----------------------|---------------------|---------------------|
| Observed<br>Forecast | Yes                 | No                  |
| Yes                  | True Positive (TP)  | False Positive (FP) |
| No                   | False Negative (FN) | True Negatives (TN) |

$$\text{HR} = \frac{\text{TP}}{\text{TP} + \text{FN}} \quad (2.41)$$

$$\text{FAR} = \frac{\text{FP}}{\text{FP} + \text{TN}} \quad (2.42)$$

The area under the ROC curve is related to the Mann-Whitney U test, a non-parametric statistical hypothesis test, which tests whether positives (HR) are ranked higher than negatives (FAR). For a perfect forecast, the area under the curve equals unity, and the curve travels from the bottom-left to top-left of diagram, then across to the top right of diagram. A diagonal line indicates that there is no forecast skill for the EPS. A more detailed information on ROC can be found in Mason [1982] and Jolliffe and Stephenson [2003].

### 2.3.6 GME-EPS Verification: Specifics, and Assumptions

The following are the specific assumptions made during the verification of the GME-EPS output data.

1. All the above mentioned statistics are performed on the GME model grid. No interpolation to Gaussian or regular lat-lon, or any other grid is performed (unless otherwise stated in the description of the respective figures or results; for example for the zonal average plots).
2. The statistics are computed for global values as well as for three regions of average values, namely the Northern extra-tropics (20N to 90N, 180W to 180E), the Tropics (20S to 20N, 180W to 180E) and the Southern extra-tropics (20S to 90S, 180W to 180E).
3. For the probability scores such as the CRPS, the statistical significance, and confidence intervals are calculated using a bootstrap technique similar to Candille et al. [2007].
4. For the ROC curve a bi-linear fitting is performed using a generalized linear model. The fitting is necessary to avoid any bias as suggested by some researchers [e.g., Wilson, 2000]. The ROC area under the curve (AUC) is calculated using trapezoidal integration.
5. For the probability density plots, the bin size is calculated according to *Freedman-Diaconis* rule, which is one of the standard method for the histograms and probability plots [Freedman and Diaconis, 1981; Birgé and Rozenholc, 2006].



## Stochastic Backscatter in the GME Model

### 3.1 Parameterizing stochasticity: Role of Backscatter

Generally speaking, introducing stochasticity (or stochastic parameterizations) into a NWP model has two purposes: to represent the atmospheric processes stochastically, and to approximate the time evolved *pdf* through a Monte-Carlo (MC) approach such that one can estimate the forecast uncertainty.

In a broad sense, one may classify the stochastic parameterization schemes into two types: i) introduce stochasticity in the existing parameterization schemes. For example, simply multiplying or adding uniform (or Gaussian) random numbers to the parameter of interest [e.g., Buizza et al., 1999; Theis et al., 2005]. ii) introduce the stochasticity as a parameterization scheme, which represents uncertainties in subgrid-scale processes as well as dynamical uncertainties. The SKEB scheme falls into the latter type, where stochasticity is introduced as a separate parameterization scheme rather than perturbing the existing parameters with a random number. The basic idea behind the kinetic energy backscatter (KEB) is to inject a fraction of the dissipated kinetic energy back into the numerical model to compensate the excessive dissipation due to numerical diffusion and parameterized subgrid scale processes such as convection and gravity wave drag. Stochasticity is introduced into the KEB in the form of a random streamfunction forcing modulated with approximated dissipated kinetic energy. Effectively, the stochastic backscatter parameterization represents a nonlinear scale interaction which allows the flow of energy from unresolved to resolved scales by exciting the energy at the unresolved scales. This stochastic forcing is the basis of flow-dependent perturbation for the GME-EPS.

In this chapter we introduce the stochastic forcing generators for GME, and then we introduce the SKEB scheme developed for GME in detail, which serves as the background for the experiments involving SKEB schemes.

### 3.2 Stochastic Kinetic Energy Backscatter in GME

Several SKEB schemes have been developed and implemented at various operational centers over the last few years: Berner et al. [2009] developed a spectral SKEB for the European Center for Medium Range Weather Forecasts (ECWWF) EPS; Charron

et al. [2010] used a modified version of spectral SKEB for the Global Environmental Multiscale Model (GEM) EPS, and Tennant et al. [2011] also used a modified version of spectral SKEB for the Met Office Global and Regional EPS (MOGREPS). However, there is no general way to implement a SKEB scheme since it depends on the particular model and model properties. Motivated by the works of Shutts [2005] and Berner et al. [2009], a modified version of the cellular automated SKEB scheme is used to represent the flow-dependent model errors in the framework of a pre-operational Ensemble Prediction System (EPS) using the global model GME of the Deutscher Wetterdienst (DWD).

In the GME model, the SKEB scheme mainly depends on the kinetic energy dissipations from the horizontal diffusion scheme, and parameterization from deep convection and subgrid-scale orography (SSO) wave drag. In general, the horizontal diffusion scheme is employed to remove small scale noise and also to improve the stability of the numerical scheme. In most cases the scheme is *over-diffusive* which creates the so called *numerical dissipation* or simply the dynamical component of dissipation approximated from the horizontal diffusion scheme. It has been shown that the model diffusive effects usually consume kinetic and available potential energy at an unrealistically excessive rate [Shutts, 2005]. The dissipations from deep convection and gravity wave drag are calculated from the respective parameterization schemes. The parameterization of deep and shallow convection is based on a mass flux approach [Tiedtke, 1989]. The convection scheme distinguishes three different convection types, namely shallow, mid-level and deep. The SSO scheme is based on Lott and Miller [1997]. To save computing time, both the convective parameterization, and SSO scheme are not computed each time step but only every third time step. Also, to remove high frequency initial noise from the forecast GME employs an adiabatic digital filtering initialization (DFI; Lynch et al. [1997]). To reduce the impact of the DFI on the initial state, the filtering is performed in vertical normal mode space, which makes sure that the structure of the atmospheric boundary layer is hardly changed by the DFI. In the following subsections, we describe the implementation details of the SKEB scheme in GME.

### 3.2.1 Stochastic Pattern Generators

Two most popular choices for generating random patterns are spectral auto-regressive models [Weber and Talkner, 1993; Mitchell and Houtekamer, 2000; Berner et al., 2009] and Cellular Automata (CA) models [Palmer, 1997, 2001; Shutts, 2005]. Operational weather forecasting centers such as ECMWF, Canadian Meteorological Center (CMC), and UK Met Office (UKMO) use spectral auto-regressive models for their SKEB scheme [Berner et al., 2009; Charron et al., 2010; Tennant et al., 2011]. In our GME-EPS experiments we have used a modified version of Shutts [2005] CA scheme for generating the random pattern. The choice of Cellular Automata for SKEB scheme is due to the following reasons: i) appropriateness for high resolution global grid-point models such as GME; ii) allow interactions of many nearest neighboring grids or cells; iii) the spatial pattern resembles convective cloud clustering in certain cloud-resolving models; iv) automata rules are easy to configure according to the model properties such as resolution etc.; v) simple random fields may be too noisy (crude spatial and

temporal correlations), which may lead to incorrect error covariance estimation for data assimilation; and vi) automata rules allow the spatial pattern to take arbitrary, size and shape (not regular square cells).

### 3.2.2 Cellular Automated Scheme

In the GME-EPS, CA is implemented globally on the model resolution without any coarse graining. The automation rules are similar to the “Generations” family of CA. Since GME model uses an Arakawa-A grid staggering that places the prognostic variables at the vertices of the triangle, a *cell* evolves according to the values (or lives) of its twelve nearest neighbors as shown in Fig. 3.1. The automation rules used for generating the stochastic pattern in GME is as follows:

1. Initialize the automation by seeding the cells with uniform random numbers or life value between 0 and 100
2. Classify the cell as *fertile* or *non-fertile* according to a critical life value. We set the critical value to 50, i.e. if the life value is greater than 50 then the cell is considered as fertile otherwise non-fertile
3. For each *fertile* cell: if the number of nearest *fertile* neighbors is less than some threshold less than 4, then decrease the life value of the cell by subtracting a small fraction (in our case fraction depends on the resolution of the model). On the other hand, the same rule applies to a fertile cell with “overpopulated” fertile neighbors.
4. Spin-up stage: Repeat step 2 and 3 until we get a reasonable spatial pattern. For spin-up, we used 500 automation steps for the low resolution (ni064) and 1000 steps for high-resolution (ni192)
5. Smooth and filter the final pattern. We have used a  $5 \times 5$  Gaussian filter for smoothing.
6. Finally scale the pattern and remove the bias if there is any. In our case we scale the final pattern to  $-1$  to  $1$

The automation rules are designed in such a way that the final pattern resembles an “eddy vorticity” pattern rather than large scale structures. The automation rules are applied at every model integration step. An example of the random stream-function forcing patterns using CA on the GME model grid is shown in Fig. (3.1).

Temporal correlation is introduced into the CA by adjusting the CA rules accordingly. For example, instead of initializing the automation with a random field at subsequent backscatter steps, the automation is initialized with previously evolved pattern. Also, by reducing and adjusting the spin-up steps it is possible to introduce correlations in both vertical and temporal coordinates. The correlations are introduced in order to study the impact of randomness in GME forecasts, since it may reduce the noise

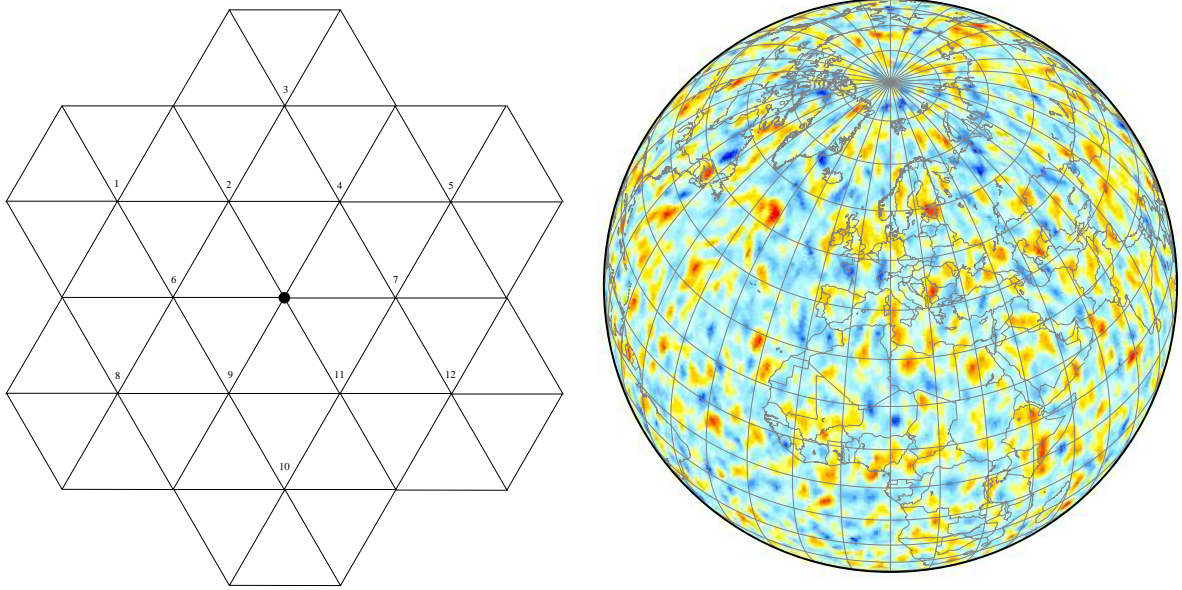


**Figure 3.1:** *Left: Twelve nearest neighbors of a cell (solid black dot) represented in icosahedral-hexagonal grid of the GME model; Right: CA streamfunction forcing in the GME model.*

level in SKEB scheme. In a broad sense the process of introducing correlation can be thought of as a first order auto-regressive model given by,

$$\psi_t = \alpha\psi_{t-1} + w_t \quad (3.1)$$

where  $w_t$  is the zero mean random white noise with a relatively small amplitude,  $\psi_t$  the CA pattern at time  $t$ , and the parameter  $\alpha$  controls the correlation strength.

### 3.2.3 Calculation of Total Dissipation in GME

Dissipative mechanisms such as diffusion schemes in GCMs are in general used to improve the overall numerical stability by removing instabilities associated with numerical and physical causes (for example, due to the parameterization of boundary layer turbulence or mixing). Following Shutts [2005], the total dissipation in GME is calculated as the sum of the dissipations due to horizontal diffusion, the dissipations from deep convection parameterization, and the gravity wave drag due to SSO. [Shutts, 2005] argued that the above three contributions acts as energy sinks and cause excessive dissipations in NWP models. However these dissipations are highly model dependent. For example, GME employs a fourth order hyper-diffusion given by,

$$F_u = -K_4 \nabla^4 u \quad (3.2)$$

$$F_v = -K_4 \nabla^4 v \quad (3.3)$$

where  $\nabla$  is the gradient operator, and  $K_4$  is the fourth order diffusion coefficient given by,

$$K_4 = \frac{1}{2\tau} \left( \frac{\Delta x}{2} \right)^4 \quad (3.4)$$

where  $\Delta x$  is the grid length at the equator. Also, a second order diffusion is applied near the top levels, which acts as a sponge layer to suppress the jets streams and also to increase the overall numerical stability. It has been shown that the diffusion coefficients in the GME model are much higher, and hence the diffusion is much stronger compared to spectral models at the same resolution [Jablonowski and Williamson, 2011]. Hence dissipations due to numerical diffusion are expected to be higher in the GME model. Following Berner et al. [2009] the approximate numerical dissipation is given by:

$$D_n = -k\vec{u} \cdot \vec{u}' \quad (3.5)$$

where  $k$  is a scaling factor,  $\vec{u}$  is the horizontal velocity vector, and  $\vec{u}'$  is the difference between the velocity vector before and after the second order hyper-diffusion. Figure (3.2) shows the numerical dissipation averaged over vertical layers.

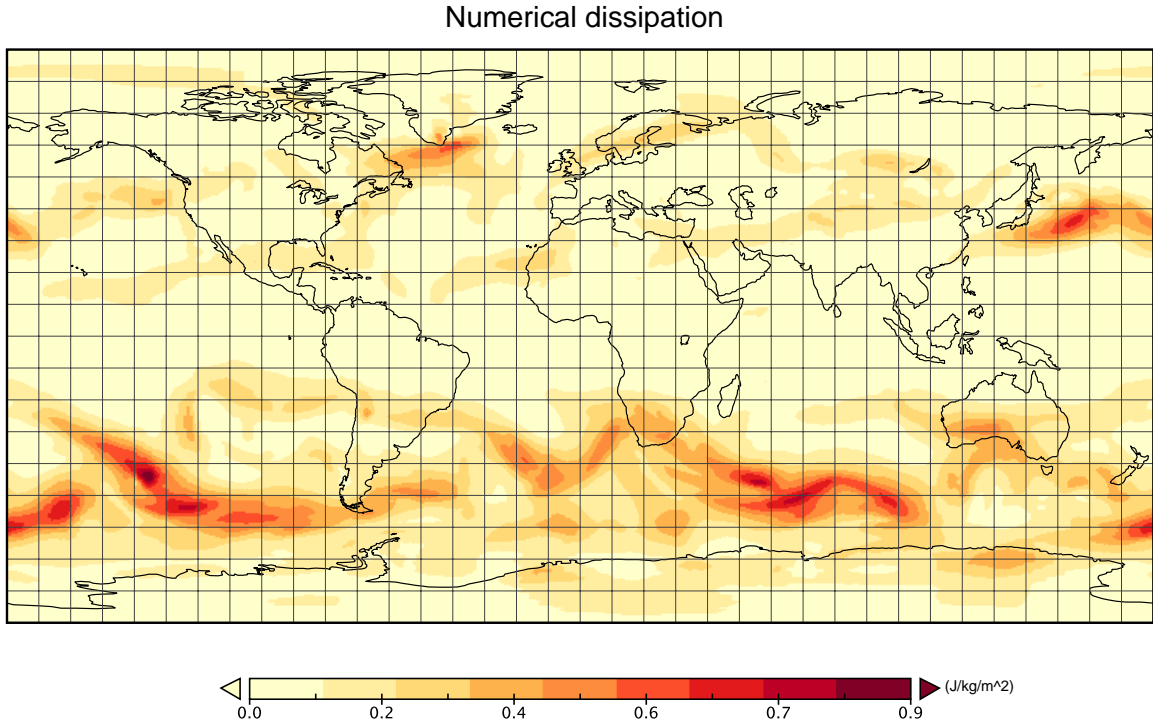


**Figure 3.2:** Numerical dissipation in GME (vertically averaged)

The dissipation rate from deep convection is based on the convective mass-flux

formulation [Berner et al., 2009]:

$$D_c = \frac{\delta M^2}{\rho^3 \beta^2} \quad (3.6)$$

where  $M$  is the updraft convective mass flux rate,  $\delta$  the updraft detrainment rate,  $\rho$  the density. Berner et. al (2009) choose the parameter  $\beta$  in such a way that the global vertically integrated dissipation per unit time and unit area from deep convection is about  $2W/m^2$ , which usually depends on the model and model physics. In our experiments we considered  $\beta$  as an independent scaling parameter. An example for the dissipation from deep convection at 500 hPa is shown in Fig. (3.3: Top)

The computation of dissipation from the SSO wave drag, shown in Fig. (3.3: Bottom), is based on Lott and Miller [1997]. The SSO scheme has a pronounced impact on the mean flow of GME. In general the SSO scheme blocks the flow in the lowest model layers but gives rise to gravity waves which break and dissipate higher up retarding the flow in the middle and upper troposphere.

The final streamfunction forcing is a function of the stochastic pattern, and square-root of the total dissipation given by,

$$F_\psi = \frac{1}{2} \alpha \cdot \Delta s \cdot \psi \cdot \sqrt{\frac{\hat{D}}{\Delta \tau}} \quad (3.7)$$

where  $\alpha$  is a scaling factor which determines the fraction of the back-scattered energy,  $\Delta s$  the CA grid length,  $\psi$  is the stochastic CA pattern,  $\hat{D}$  the total dissipation, and  $\Delta \tau$  is the time step for the automation. The effective streamfunction forcing at 500 hPa is shown in Fig. (3.4).

In the SKEB scheme used in this thesis work, the horizontal velocity tendencies due to backscatter forcing are computed by taking the gradient of the streamfunction with respect to the model co-ordinates. Finally, adding these tendencies to the horizontal wind components gives back a fraction of the dissipated kinetic energy into the model. In our SKEB implementation, the temperature field is kept unperturbed since the KE increments in fact change the temperature field accordingly as they are directly proportional. Others have included the temperature tendencies explicitly in the backscatter scheme by crudely estimating the net loss of available potential energy (APE) [Shutts, 2005; Charron et al., 2010].

### 3.3 Role of Stochastic Backscatter in the GME forecast

This section is primarily focus on the GME medium range forecast in particular the impact of the SKEB scheme on the forecast quality. The role of the SKEB scheme in the LETKF assimilation is discussed in Chapter (4). This section is subdivided into four sub-sections: 1) *SKEB: Experimental setup*, which will give an overview of both the deterministic and ensemble forecast experimental setup involving the SKEB scheme, 2) *SKEB: Impact on Kinetic Energy Spectra*, which will discuss the observed double cascade in GME, 3) *SKEB: Impact on the Medium-Range Forecast*, which will

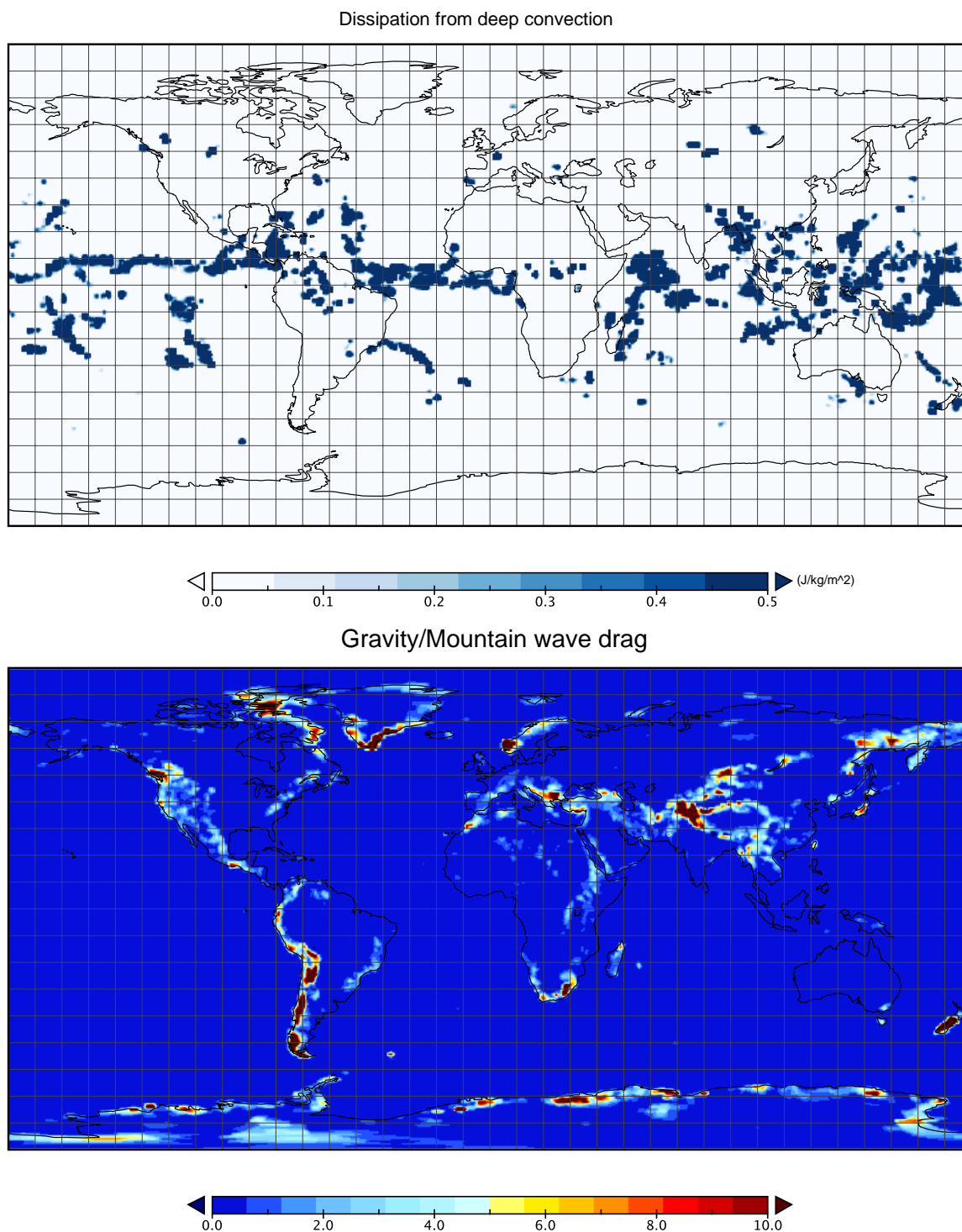


**Figure 3.3:** Top: Dissipation from deep convection at 500 hPa; Bottom: SSO wave drag in GME

describe the impact of SKEB on the medium range (ten days) forecast in detail, and 4) *SKEB: Impact on the Precipitation Forecast*, which will give a detailed analysis of the precipitation forecast.

## Stream function forcing

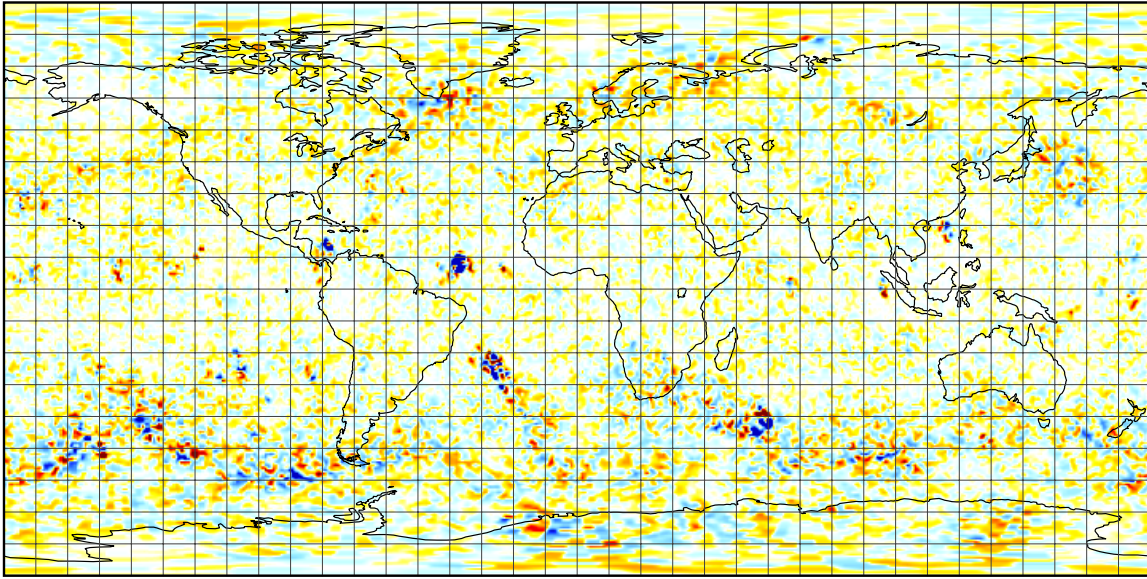


**Figure 3.4:** *Effective streamfunction forcing at 500 hPa*

### 3.3.1 SKEB: Experimental setup

Three sets of experiments were performed in order to study the impact of the SKEB scheme on the GME forecast: i) Deterministic forecasts (hereafter GME-DET), ii) Ensemble forecasts using initial conditions from the deterministic analysis (hereafter GME-ENS), and iii) Ensemble forecasts using initial conditions from the ensemble data assimilation (EDA) cycle (hereafter GME-EPS). For GME-DET and GME-ENS experiments, deterministic analysis from the DWD operational archive for the period starting 2007-05-20, 00:00:00 UTC, are used to initialize the forecasts with a 6-hour interval. The GME-DET forecast experiments were mainly used to study the impact of backscatter on the KE spectra as well as to tune the SKEB scheme for the ensemble experiments.

The GME-ENS experiments were run with GME resolution ni192, and constitute a 32 member ensemble. All the statistical results presented for the GME-ENS experiments use 4 cases (each with different initial condition) of 32 member ensemble, i.e. 128 ensemble members at every 6-hour forecast step (5120 ensemble members for the ten days forecast), for each case study. In total, seven different sensitivity case studies were performed. The GME-ENS case studies were designed to estimate the SKEB contributions from different dissipation mechanisms in the GME to the forecast quality. Therefore, in each case the ensemble members were initialized with identical initial state.

The GME-EPS experiments were performed in a pre-operational LETKF test suite. The observations used for assimilation were monitored and quality controlled in the same way as in the operational 3D-VAR system. The observations used in the assimilation include conventional data such as in-situ radiosonde data (TEMP), aircraft

observations, data from ships, satellite retrievals such as Atmospheric Motion Vectors (AMV; from Eumetsat, GOES, NOAA/NESDIS, MODIS), buoys and scatterometer data, pressure observations derived from satellite (PAOB), and satellite radiances (from AMSU-A). The observation pre-processing include bias correction, thinning, black-listing, and radiative transfer calculation using the RTTOV7 model. The assimilation is performed every 6 hours, followed by a ten days forecast. A total of seven different sensitivity experiments were performed for the low resolution (ni064) GME-EPS. The experiments were started at 2007-05-20, 00:00:00 UTC with 6-hour assimilation cycle in all cases. Each experiment is cycled until 2007-05-25, 18:00:00 UTC. The initial 32-member ensemble is prepared by the 3D VAR system, i.e. by adding a perturbation ensemble to the deterministic analysis. The perturbation ensemble is prepared by multiplying an ensemble of zero mean normally distributed random vectors to the square-root of the  $\mathbf{B}$  matrix (which is initially prepared using the NMC method). To avoid any influence from the initial ensemble spread, all the statistical results presented in this section use only the last 8 cycles, i.e. either 256 ensemble members at every 6 hour forecast step (10240 ensemble members for the 10 days forecast), for each case study<sup>1</sup>.

More specific details regarding the GME-ENS and GME-EPS case-studies can be found in the following subsections concerning the results.

### 3.3.2 SKEB: Impact on Kinetic Energy Spectra

The kinetic energy spectra of the atmospheric fields of an NWP model can be used to study its general statistical features with respect to scale interactions, properties of the dissipating mechanisms such as diffusion filters, as well as atmospheric turbulence. It has been shown that, the KE spectrum of the observed atmosphere obeys a  $k^{-3}$  power-law dependence on the wave number over the synoptic scale (1000-3000 km) and a  $k^{-5/3}$  power-law over the meso-scale (wavelength 2.6-300km) [Nastrom et al., 1984; Nastrom and Gage, 1985; Cho et al., 1999]. The observed  $k^{-3}$  power-law dependence on wavenumber over the synoptic scale is the well known downscale enstrophy cascade and can be associated with geostrophic turbulence [Charney, 1971]. On the other hand there is no globally accepted theory supporting the  $k^{-5/3}$  power-law dependence on the wavelength over the mesoscale. Three most prominent theories for the  $k^{-5/3}$  dependence are that: 1) it may be associated with a reverse energy cascade from high to low wave numbers in quasi-2D-turbulence with a negative energy flux [Kraichnan and Nagarajan, 1967; Gage, 1979; Lilly, 1983]; 2) it may be interpreted as a spectrum of internal gravity waves with direct energy cascade to high wave-numbers, as oceanic spectra [Dewan, 1979; Van Zandt, 1982]; 3) it may be due to baroclinic instability [Tung and Orlando, 2003]. More details can be found in the papers by Lindborg [1999]; Lindborg and Alvelius [2000]; Lindborg [2006].

Most atmospheric general circulation models, including GME, are capable of reproducing the  $k^{-3}$  part of the kinetic energy spectrum but not the  $k^{-5/3}$  part. On the other hand some less complex GCMs are shown to be capable of reproducing observed double cascade without using any additional stochastic parameterization schemes [Koshyk

---

<sup>1</sup>In some cases we've used 16 cycles for statistical analysis.

et al., 1999; Koshyk and Hamilton, 2001; Skamarock, 2004]. Figure (3.5) shows the KE spectra of the horizontal wind at 500 hPa from the GME 6 hour forecast (blue line), which shows the absence of the double cascade. One possible explanation for this absence of the  $k^{-5/3}$  part of the GME spectra is due to the KE dissipations within the model. For example, the strong bi-harmonic diffusion scheme in GME acts as a low-pass filter which removes energy most strongly at high frequencies, which may in-turn suppress the upscale energy transfer from the unresolved to the resolved modes. Recently, ECMWF and UK Met. Office NWP models were able to reproduce the observed double cascade by incorporating a spectral stochastic backscatter scheme [Palmer et al., 2009; Tennant et al., 2011]. In this thesis, we have used the cellular automated SKEB scheme for two main purposes: to account for the dissipated KE to the dissipation mechanisms with in the model, and to account for the model uncertainty which can be incorporated into the LETKF data assimilation system.

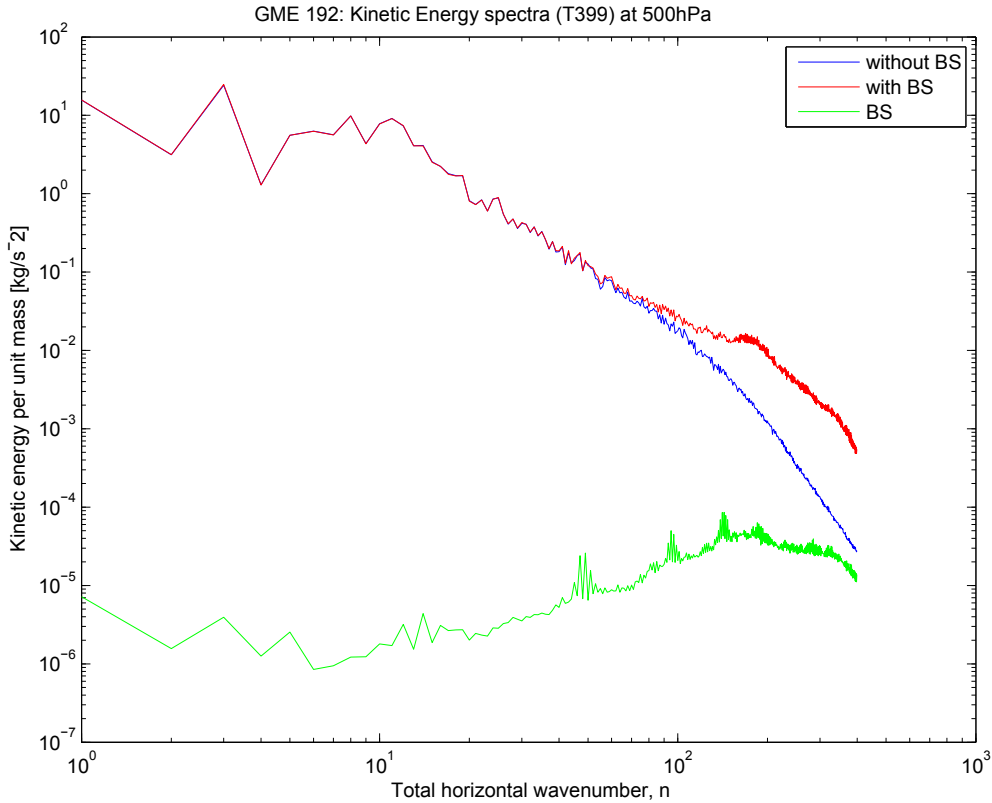


**Figure 3.5:** *SKEB using CA: Kinetic energy spectra of the horizontal wind at 500 hPa*

Figure (3.5) also show the KE spectra of the horizontal wind with the SKEB scheme (red line) and also the spectra of the backscatter forcing (green curve). The spectra (red line) shows that the backscatter in fact inject the energy back into model at mesoscales (green line), effectively contributing to the  $k^{-5/3}$  part of the spectrum. It should be noted that, the  $k^{-5/3}$  part of the Kinetic Energy spectra is usually associated with the kinetic energy of the divergent modes. However, in our SKEB formulation, we assume that the contribution of the divergent mode at the mesoscale is negligible compared

the rotational mode. This may explain the reason for the dampening of the tail of the KE spectrum with SKEB (red line). The lack of proper divergent component in the backscatter forcing at the mesoscales may be one reason for the lack of a clear  $k^{-5/3}$  dependence on wavenumber over the mesoscale, as shown in the GME KE spectra (red line).

### 3.3.3 SKEB: Impact on the Medium-Range Forecast

One of the primary objective of this thesis work is to improve the global medium range (i.e. three-to-five days) forecast by incorporating model uncertainty in the GME-EPS.

| GME-ENS<br>Exp. ID | Dissipation components<br>(in the SKEB scheme)                    | Backscatter<br>forcing       | CA Pattern<br>Correlation |
|--------------------|---|------------------------------|---------------------------|
| nCAP-2a            | None<br>(CA Pattern is taken<br>as the streamfunction<br>forcing) | $\alpha = 2$                 | No                        |
| oCON-2a            | Deep CONvection   | $\alpha = 2$                 | Yes                       |
| oALL-2a            | Numerical diffusion,<br>Deep convection, &<br>Gravity wave drag   | $\alpha = 2$<br>$\alpha = 2$ | Yes<br>Yes                |
| nNAG-2a            | Numerical diffusion, &<br>Gravity wave drag                       | $\alpha = 2$                 | No                        |
| oNAG-2a            | Numerical diffusion, &<br>Gravity wave drag                       | $\alpha = 2$                 | Yes                       |
| oCAP-2a            | None  | $\alpha = 2$                 | Yes                       |
| oNAG-1a            | Numerical diffusion, &<br>Gravity wave drag                       | $\alpha = 1$                 | Yes                       |

**Table 3.1:** *Summary of GME-ENS sensitivity experiments.*

By introducing stochasticity into the model we assume that the model error, which contributes to the forecast uncertainty, can be captured thereby improving the mean forecast quality. This hypothesis is tested in the forecast by incorporating a cellular automated SKEB scheme into the GME model. Two sets of forecast results are presented and analyzed in this section: i) the results from the GME-ENS experiments, and ii)

the results from the GME-EPS experiments. The main difference between GME-ENS and GME-EPS experiments are that the GME-ENS experiments incorporate only the model uncertainty and no initial uncertainty, while the GME-EPS experiments incorporate both. To be more specific, the GME-ENS experiments were started with the same initial condition (no ensemble spread; all initial members are identical) and they do not involve any data assimilation cycle. On the other hand the GME-EPS integrations were started from the LETKF analysis ensemble, and thus are initialized with finite ensemble spread. The model uncertainty is incorporated through the SKEB scheme, and each ensemble member evolves stochastically and may be considered as one of the possible realizations of the atmospheric state.

First we will analyze the forecast results from the GME-ENS experiments. A summary of the GME-ENS sensitivity experiments, and the SKEB parameters used are given in table (3.1). As mentioned in the previous sub-section (3.3.1), the GME-ENS experimental cases were designed to evaluate the SKEB contributions from different dissipation mechanisms in the GME model, on the forecast quality.

Figure (3.6) show the Continuous Ranked Probability Scores (CRPS) for ten day forecast for the 850 hPa temperature, for: Global (Top-Left), the Northern extra-tropics (Top-Right), the Tropics (Bottom-Left), and the Southern extra-tropics (Bottom-Right). The CRPS is a negatively oriented score, which means that a lower score indicates better forecast quality. From a first look at the Fig. (3.6), it can be seen that the black line, which represents the experiment without the SKEB scheme, is above all the others, which in general indicates that the SKEB scheme has a positive impact on the forecast. The improvement is more pronounced in the Tropics compared to the extra-tropics. Although the significance level of improvements vary across different sensitivity experiments, overall the CRPS show remarkable improvements in both short-range and medium-range forecasts. Before analyzing the CRPS score of each individual sensitivity experiments and summing-up the reasons behind the improvements in the forecast, we show other statistical measures such as the Ensemble Spread, the Root-Mean Squared Error (RMSE) of the ensemble mean against operational analysis (which is used as the reference or truth), Normalized RMSE (normalized against the deterministic forecast without the backscatter), the Ranked Histogram etc. This will help to perform an unbiased analysis of the results. In general, the RMSE scores (solid lines) is in good agreement with CRPS scores, i.e., the experiments with SKEB scheme have lower RMSE as shown in Fig. (3.7, top-row). The corresponding SPREAD is shown by the dashed-lines. A general conclusion is that the spread in all GME-ENS experiments is much too low compared to the RMSE due to the lack of spread in the initial conditions. Furthermore the figures show that the RMSE of the GME-ENS ensemble means is considerably smaller than the RMSE of the deterministic run especially for long forecast ranges. This is an expected result as the forecasts become less predictable and the score of any single deterministic forecast will be worse than that of the climatological mean. However the ensemble mean will approach the climatological mean for long forecast lead times.

The normalized RMSE scores, shown in Fig. (3.7, highlight the differences between the experiments during the first forecast hours where RMSE is small and are difficult to assess in general. A negative normalized RMSE indicates that the RMSE in the

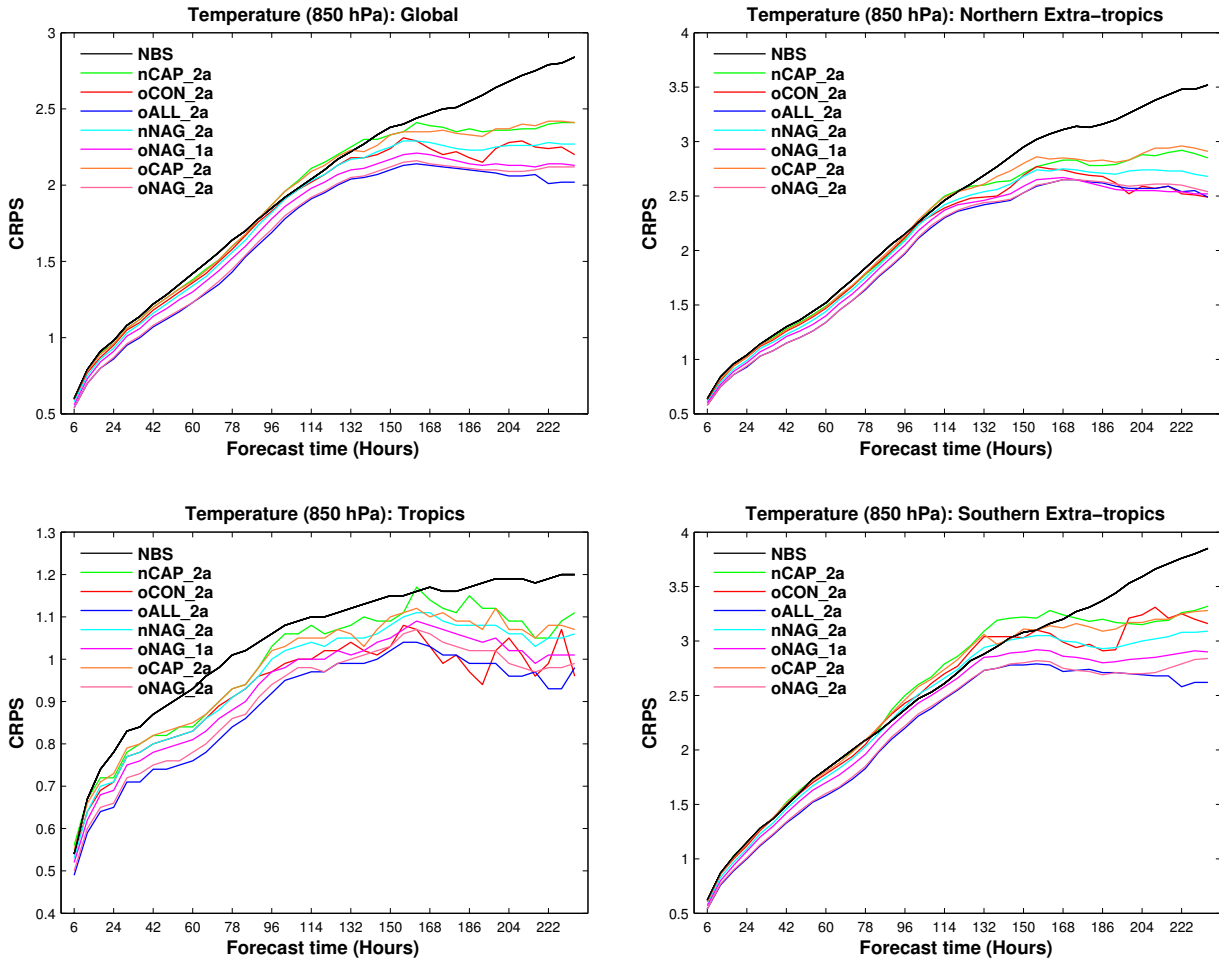


**Figure 3.6:** Continuous Ranked Probability Score (CRPS) for 850 hPa temperature, for ten days forecast: Global (Top-Left), the Northern extra-tropics (Top-Right), the Tropics (Bottom-Left), and the Southern extra-tropics (Bottom-Right).

experiment is lower than in the reference, i.e., that it is better. These figures show that it has an advantage to use the mean of the ensemble instead of the deterministic run even during the first few hours of the forecast, where it is not naturally expected from the above considerations.

The CRPS and RMSE scores confirm the general viewpoint that incorporating model uncertainty can improve the quality of short and medium range forecasts significantly. However, there are some mismatches between the CRPS and RMSE scores of individual SKEB sensitivity experiments. For example, the experiment with no dissipation component in the SKEB scheme (green and orange lines) has a higher CRPS than that of the experiment with all dissipation components in the SKEB (blue line). This indicates that accounting for kinetic energy (KE) dissipations in the model can significantly improve the forecast compared to simple stochastic perturbations of the flow fields, which is in fact consistent with the general idea of incorporating a kinetic energy backscatter. On the other hand the RMSE and Normalized RMSE scores of

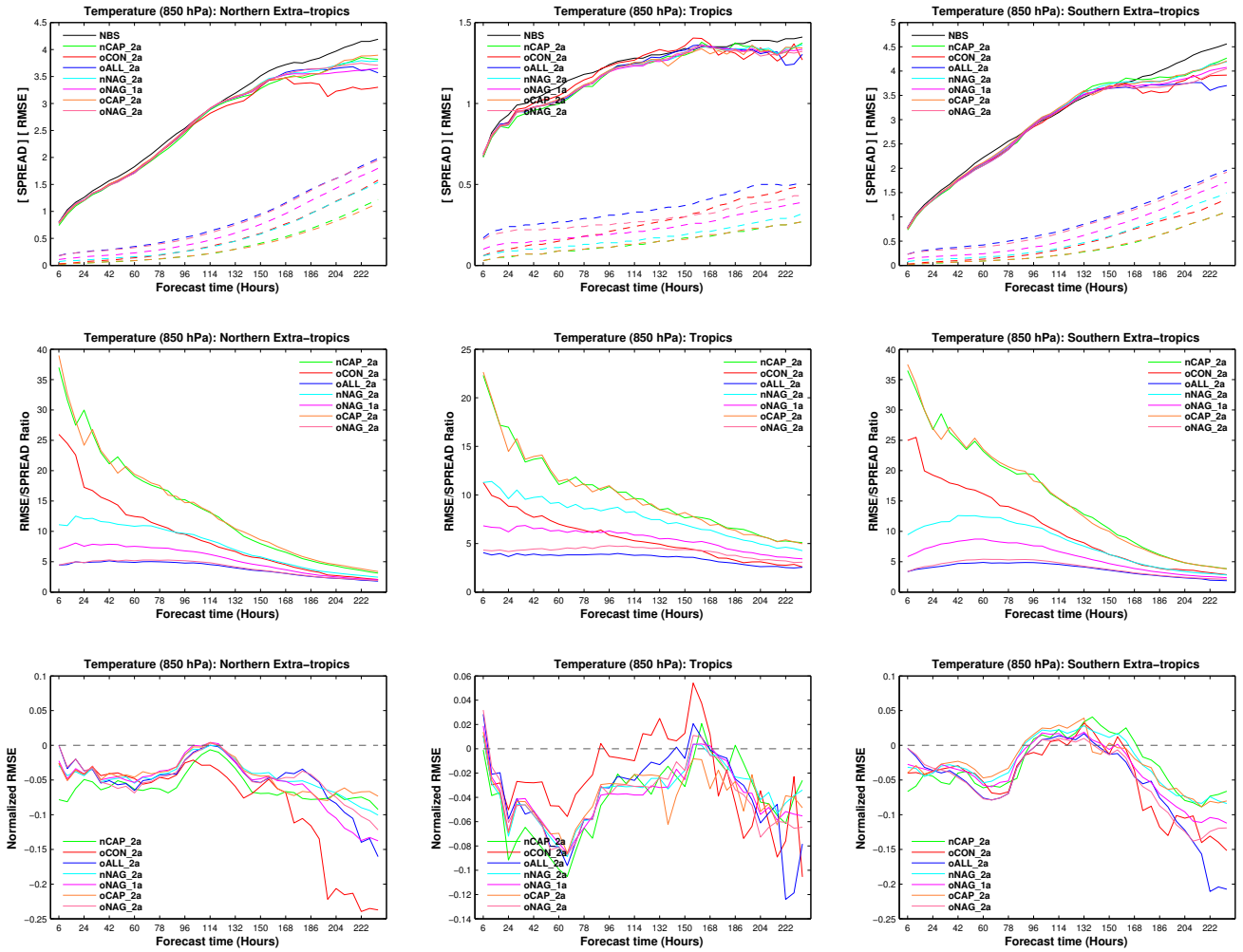


**Figure 3.7:** Ten days forecast statistics for 850 hPa temperature: RMSE (solid) and Ensemble SPREAD (dashed) on the top-row, RMSE/SPREAD Ratio (middle-row), and Normalized RMSE (bottom-row), for the Northern extra-tropics, the Tropics and the Southern extra-tropics respectively (from left to right).

the ensemble mean show the opposite, i.e., the skill scores show better results for random perturbations of the flow fields than for the SKEB scheme which accounts all the KE dissipations. This discrepancy may be due the fact that the RMSE scores are deterministic scores while CRPS is a probabilistic score. By using RMSE, we assume that the data follow a Gaussian distribution, and is based on ensemble mean rather than individual ensemble members. On the contrary the CRPS is independent of such assumptions. For example, Fig. (3.8) shows the probability density distributions of the 850 hPa temperature, and 500 hPa zonal wind fields in the ensemble space, at a particular location (*Hamburg*). It is clear from the figure that the ensemble distribution does not follow an exact normal distribution and that the ensemble mean of the region does not reflect the most probable value especially for temperature. Also, in this case, the limited ensemble size has a strong influence on the ensemble mean, SPREAD and RMSE scores. Thus giving more weight on RMSE may sometimes lead to unjustifiable

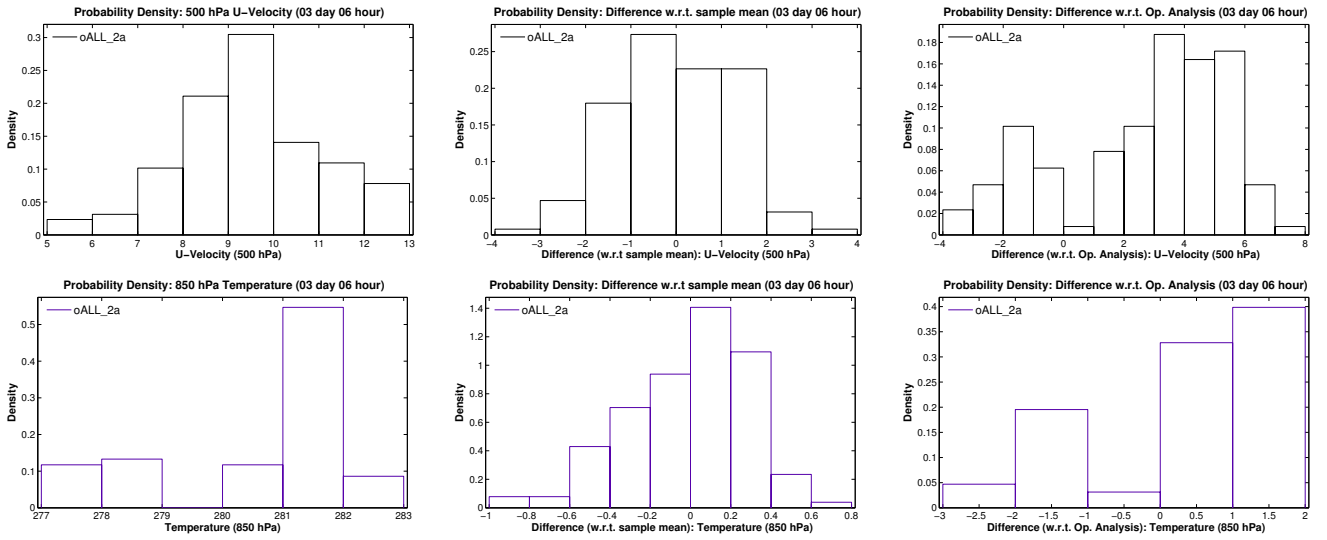


**Figure 3.8:** Probability density of the 500 hPa U-velocity (top-row) and 850 hPa temperature (bottom-row) at a particular location (Hamburg), in ensemble space

conclusions. In this sense the CRPS or other probabilistic verification scores are more trustable than RMSE scores. Although RMSE scores are distribution dependent, they are practically relevant, since the ensemble mean is one of the most common measure for an ensemble of smooth fields such as temperature or wind.

Now, coming back to the GME-ENS results, it is clear from the CRPS and RMSE scores, shown in Fig. (3.6), that accounting for the KE dissipations in the SKEB scheme has significant positive impact on the forecast quality in all the three regions (the Northern extra-tropics, the Tropics, and the Southern extra-tropics). From the CRPS, it can be seen that among all sensitivity experiments, those which use correlated stochastic forcing patterns (legend names starting with **o**) perform better than their random counterparts (legend names starting with **n**). This may be due to the fact that the random forcing reflects the correlation structure of the flow fields to be perturbed (pseudo-random). A completely random forcing may be too noisy and may destroy the existing correlation of the fields. This can also be inferred from the RMSE/SPREAD ratios shown in Fig. (3.7: Middle-row). The RMSE/SPREAD ratio of experiments with correlated stochastic forcing is closer to one than that of the uncorrelated ones. It also implies that completely random forcing may suppress the SPREAD as seen in Fig. (3.7: Middle-row, dashed-lines). Thus introducing correlation in the pattern is necessary and in fact found to enhance the ensemble spread.

In the Northern extra-tropics and the Southern extra-tropics the difference between the experiment which does not account for the KE dissipations from deep convection (e.g. [oNAG\_2a]), and the experiment which accounts for the same (e.g., [oALL\_2a]) is minimal. However, the difference is significant in the Tropics. This may be due to the fact that the effects of deep convection parameterization in GME are more confined to the Tropics as the associated KE dissipations (for e.g., see Fig. (3.3: Top). Therefore the overall contribution from the SKEB scheme is relatively stronger in the Tropics, and hence is the relative improvement in the forecast. This can also be seen in the

SPREAD and RMSE/SPREAD ratios in the respective regions. For example, in the experiment [oCON\_2a], only the KE dissipation from deep convection contributes to the backscatter forcing, and it has a larger SPREAD and lower RMSE/SPREAD ratio in the Tropics compared to the extra-tropics, as shown in Fig. (3.7).

One of the main purposes of introducing the SKEB scheme is to incorporate the model uncertainty in the GME forecast model, thereby increasing the ensemble spread such that the observations (or truth) are more likely to fall within the ensemble range. This can be verified using the ranked histogram (or Talagrand diagram). Figure (3.9) show the percentage of outliers in the ranked histogram for the 850 hPa temperature field over the forecast range, for the Northern extra-tropics, the Tropics, and the Southern extra-tropics respectively (from left to right). It can be seen from the figure that the experiment [oALL\_2a], which incorporates all the KE dissipations has the lowest percentage of outliers. It should also be noted that incorporating the dissipation from convection in SKEB significantly reduces the outliers in the Tropics. This is consistent with the conclusions from CRPS and RMSE/SPREAD ratio of the same. Thus

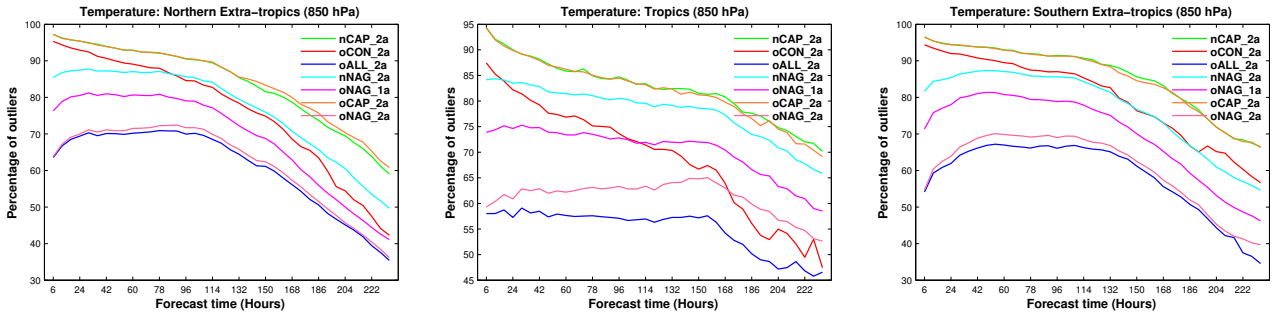


**Figure 3.9:** *Percentage of outliers in the ranked histogram (Talagrand diagram): 850 hPa temperature, ten days forecast.*

in terms of CRPS and RMSE/SPREAD scores, the experiment [oALL\_2a] where the SKEB scheme accounts for all the KE dissipation components, gave the best forecast result for the 850 hPa temperature in all regions. Figure (3.10), shows the CRPS and the corresponding confidence interval for the same. The confidence interval shown in Fig. (3.10: Bottom-row), is below the zero line threshold for all the forecast hours, which clearly indicates that the improvement due to the SKEB scheme is significant throughout the forecast range.

The zonal average of the SPREAD and RMSE of the 850 hPa temperature, for the forecast time steps, 6 hours, 3<sup>rd</sup>, and 5<sup>th</sup> day, is shown in Fig. (3.11: Top-row). The SPREAD is shown in dashed lines and the RMSE is shown in solid lines. The SPREAD is highest for the experiment [oALL\_2a], which accounts for all the KE dissipation component. Overall, the zonal average figures also show improvement in the forecast, i.e., lower RMSE values for the experiments with the SKEB scheme. However, there are some exceptional latitudes where the RMSE is higher. For example, the RMSE around 60°-80° south shows a spike at 6 hours and on the 3<sup>rd</sup> day but it disappears on the 5<sup>th</sup> day. By looking at the spatial structure of the spread from the experiment

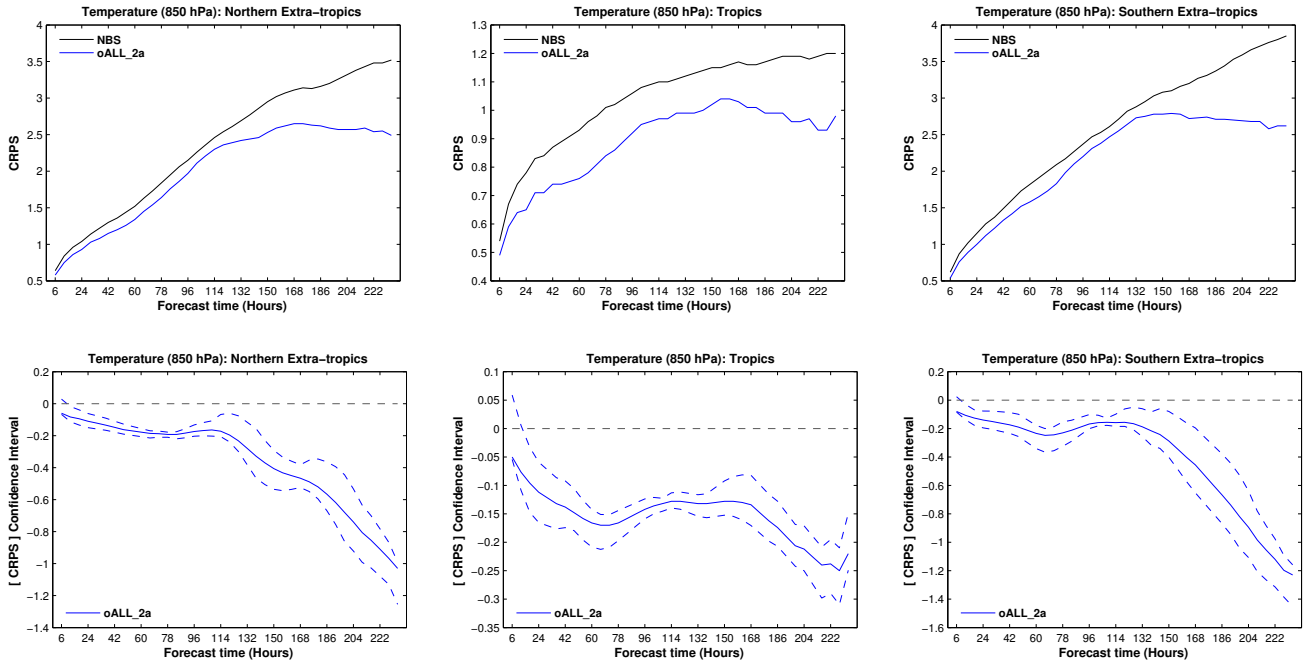


**Figure 3.10:** Continuous Ranked Probability Score (CRPS) and confidence interval for 850 hPa temperature, for the experiment [oALL\_2a]: the Northern extra-tropics (left), the Tropics (middle), and the Southern extra-tropics (right)

[oALL\_2a], shown in Fig. (3.11: bottom-row), it can be seen that those spikes in RMSE are associated with excess/anomalous spread values at few grid-points. Also, the spatial distribution of the SPREAD at 6 hours is quasi-uniform, with exceptions around Europe. On the other hand, by looking at the SPREAD distribution on the 3<sup>rd</sup>, and 5<sup>th</sup> day, we can see that the SPREAD developed quickly and is much higher at both extra-tropics compared to the Tropics. The reason for this can be explained by comparing this feature with the spatial distribution of the KE dissipation from numerical diffusion, shown in Fig. (3.2). From Fig. (3.2), it can be seen that most of the dissipations are around the extra-tropics. Since the backscatter forcing is proportional to the total KE dissipation, a larger dissipation will cause a larger backscatter forcing, producing large SPREAD. Also, since there is no systematic way of estimating the actual KE dissipation, any under or over estimation of the KE dissipation will cause the backscatter scheme to produce under/over SPREAD, and this may create larger errors (RMSE).

The spatial pattern of the RMSE distribution is shown in Fig. (3.12): the top-row shows the RMSE from [No BS] experiment, the middle-row shows the RMSE from the experiment [oALL\_2a], and the bottom-row shows the RMSE/SPREAD Ratio from [oALL\_2a]; for the forecast time at 6 hours, 3<sup>rd</sup>, and 5<sup>th</sup> day respectively (from left to right). From the spatial pattern it is obvious that the RMSE is higher for the experiment without SKEB scheme. The errors are more pronounced in the extra-tropics, especially on the 3<sup>rd</sup>, and 5<sup>th</sup> day. Comparing the RMSE distribution from [No BS], and [oALL\_2a], it is clear that the SKEB scheme in fact helps to reduce the

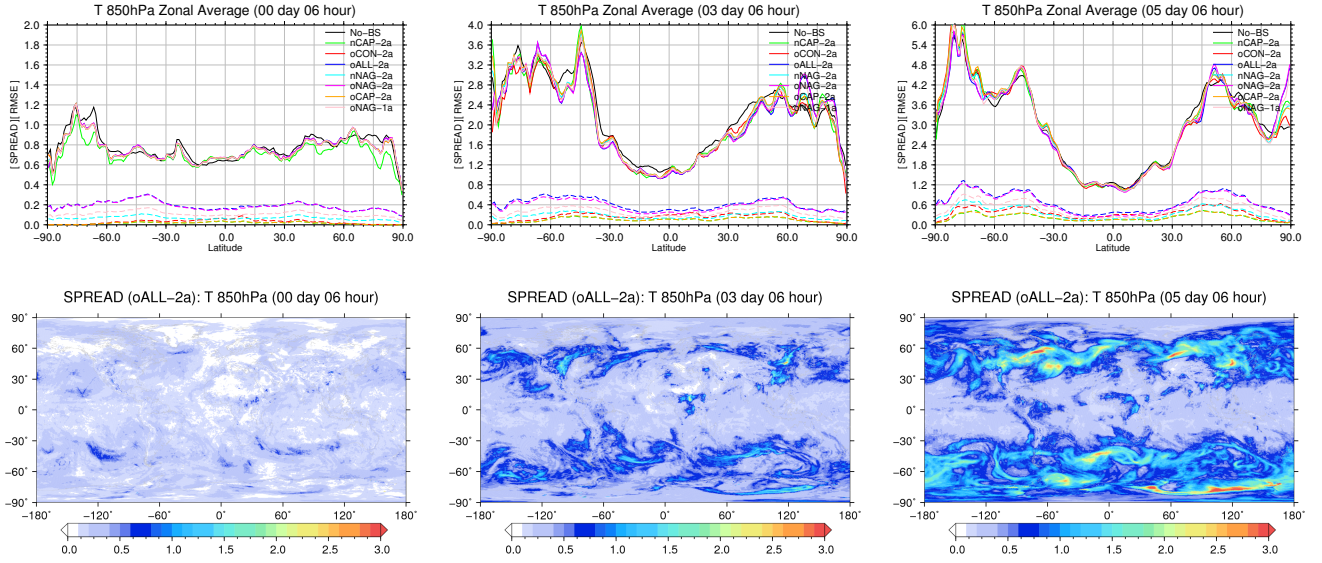


**Figure 3.11:** *Top-row: Zonal average RMSE (solid lines) and SPREAD (dashed lines). Bottom-row: Spatial pattern of the SPREAD from [oALL\_2a]; for the forecast time at 6 hours, 3<sup>rd</sup>, and 5<sup>th</sup> day respectively (from left to right).*

forecast errors or, in other words, by incorporating model uncertainty into the forecast model through a stochastic backscatter we can significantly reduce the forecast error. The RMSE/SPREAD ratio does not show any particular pattern, except few grid-point which shows high ratio, which in fact associated anomalous SPREAD as shown in Fig. (3.11: Bottom-row).

So far, we have looked only at the temperature at a particular pressure level (850 hPa) which is one of the most widely used pressure level for forecast verification. However, the impact of the SKEB scheme may be different at different vertical levels and different forecast time, since the KE dissipation is also different for the same. In the following we will show the vertical profiles of the verification scores for the Northern extra-tropics, the Tropics and the Southern extra-tropics. Figure (3.13) shows the CRPS vertical profiles for temperature for the Northern extra-tropics. The top-row shows the CRPS for all experiments, the middle-row shows the CRPS for the experiment [oALL\_2a], and the bottom-row shows the corresponding confidence interval, for the forecast time at 6 hours, 3<sup>rd</sup>, and 5<sup>th</sup> day, respectively (from left to right). From the figure, it is clear that the temperature forecast improved throughout the entire vertical levels especially for the experiment [oALL\_2a]. The confidence interval is below the zero line threshold which indicates that the improvement in the CRPS is significant. The results are consistent at different forecast steps.

The vertical profile of the SPREAD and RMSE scores for the temperature field for the the Northern extra-tropics is shown in Fig. (3.14). The top-row of Fig. (3.14) shows the SPREAD (dashed lines) and RMSE of the mean (solid lines). The middle-row of Fig. (3.14) shows the RMSE/SPREAD ratio, and the bottom-row shows the normalized RMSE against the deterministic forecast [No BS]. Although the overall

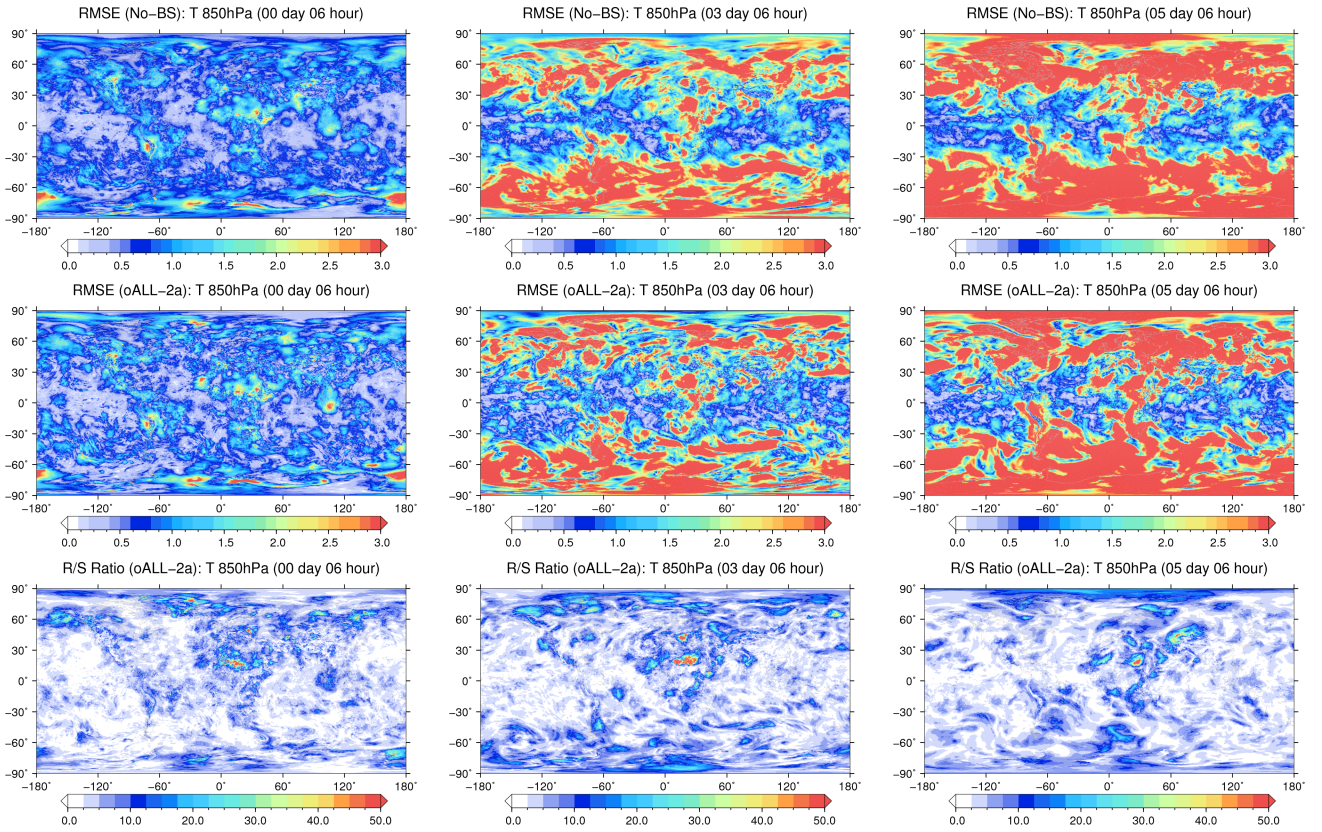


**Figure 3.12:** *Top-row: RMSE from [No BS] experiment. Middle-row: RMSE of the mean from [oALL\_2a], and Bottom-row: RMSE/SPRED Ratio from [oALL\_2a]; for the forecast time at 6 hours, 3<sup>rd</sup>, and 5<sup>th</sup> day respectively (from left to right).*

conclusion is consistent with the CRPS scores, the RMSE score gives us a different outlook. Similar to Fig. (3.7), the lowest RMSE is for experiment [nCAP\_2a], which uses only the random cellular automation pattern and does not incorporate any dissipation component. On the contrary, the CRPS for the same is larger. The disagreement between the absolute RMSE score and the CRPS arise from non-normal probability density distribution (similar to the case shown in Fig. (3.8)). The SPREAD is highest for the experiment [oALL\_2a], hence the RMSE/SPREAD ratio is closer to unity than others. Since the CRPS is smallest for experiment [oALL\_2a], the conclusion from the SPREAD and RMSE/SPREAD ratios are in well agreement with the CRPS. From the vertical profile shown in Fig. (3.14), we can see that the SPREAD is relatively much larger at higher levels, especially for experiments which incorporate KE dissipation from numerical dissipation in the SKEB scheme. This is due to the fact the numerical diffusion is much larger at higher levels in GME making it the largest contributor to the KE dissipation in the SKEB scheme. Since the total KE dissipation is proportional to the backscatter forcing, an increase in the dissipation causes an increase in the backscatter forcing which gives rise to a higher SPREAD.

Analogously, Figure (3.15) shows vertical profiles of skill scores for the Tropics, for the forecast temperature. Overall the CRPS profile shows that the SKEB scheme

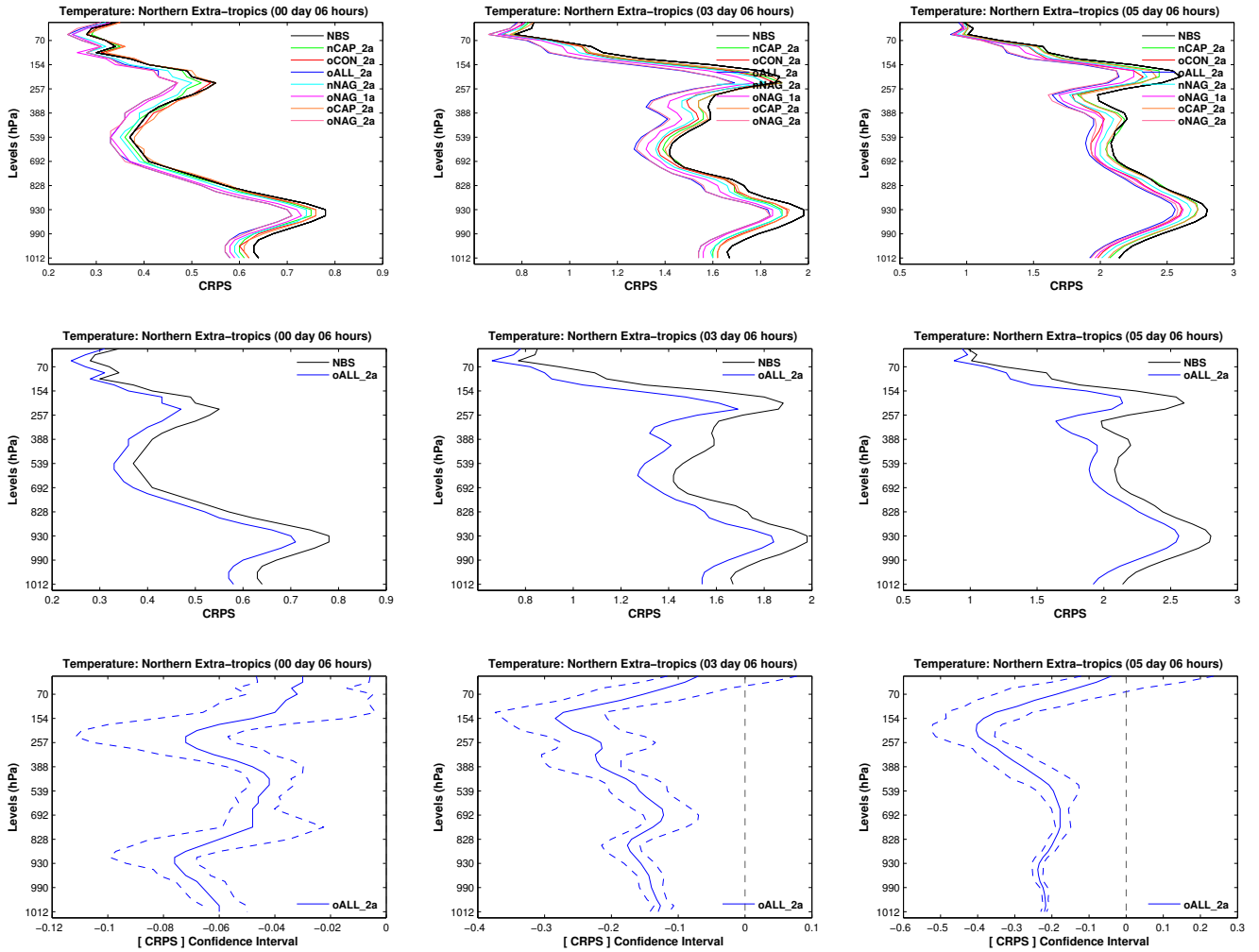


**Figure 3.13:** *Continuous Ranked Probability Score (CRPS) vertical profiles for temperature for the Northern extra-tropics. Top-row: for all experiments, Middle-row: for the experiment [oALL\_2a], and Bottom-row: corresponding confidence interval; for 6 hours, 3<sup>rd</sup>, and 5<sup>th</sup> day respectively (from left to right).*

has a significant positive impact on all levels on the forecast. The impact is more pronounced in the later forecast hours. The RMSE scores of the mean also agree with the conclusion from CRPS, although at higher levels there is some mismatch between the scores. Overall, the SKEB scheme [oALL\_2a] has the highest SPREAD and lowest CRPS.

Similarly, Fig. (3.16) shows the vertical profile for the Southern extra-tropics. Although the CRPS shows significant improvement for most SKEB schemes at 6<sup>th</sup> hour and 3<sup>rd</sup> day, schemes involving correlated stochastic pattern and numerical dissipation show better results on the 5<sup>th</sup> day, and the rest of the schemes show higher CRPS values especially at upper levels. Also the scheme implemented in experiment [oALL\_2a] shows the highest SPREAD.

Another most common physical quantity used for evaluating the forecast quality is

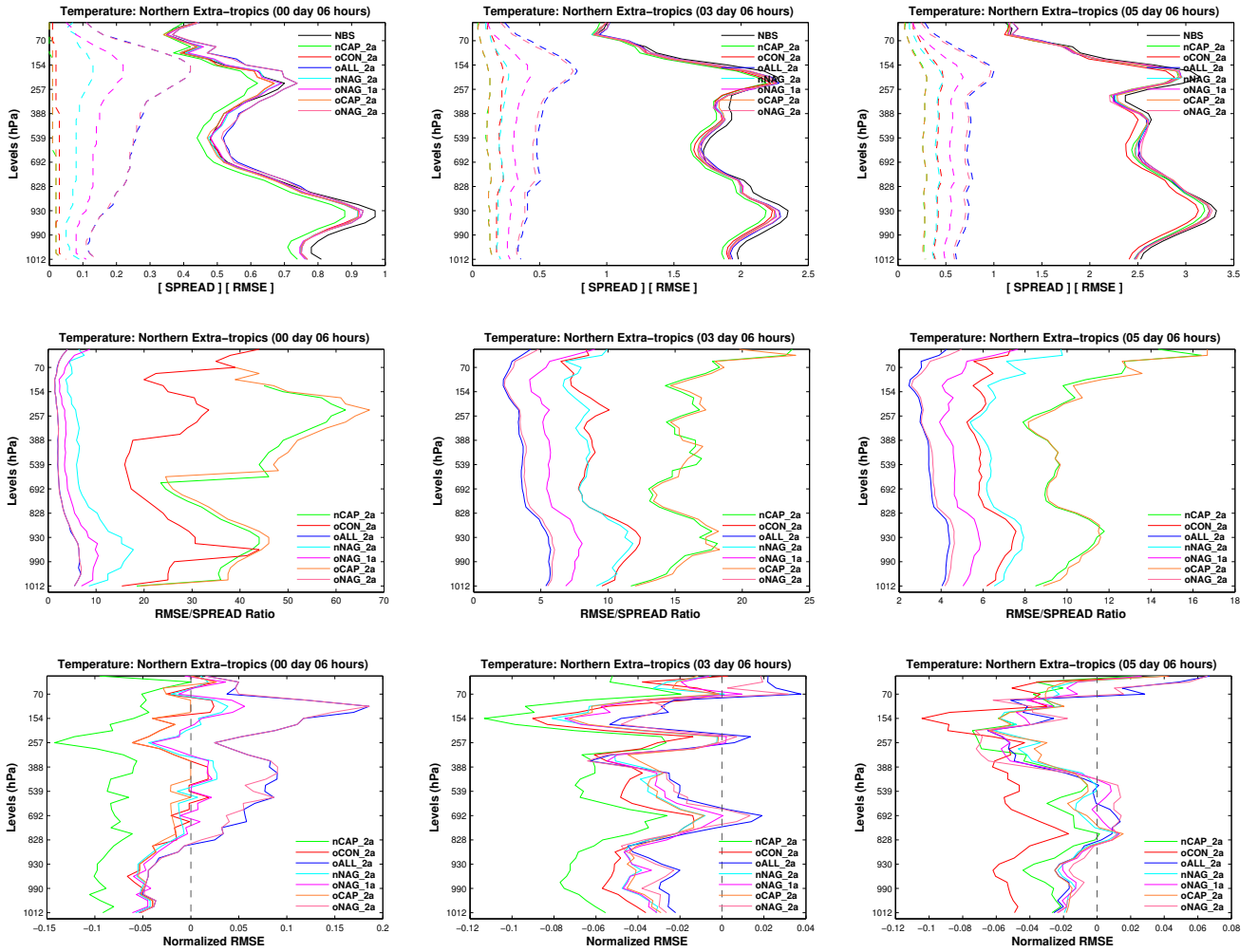


**Figure 3.14:** Vertical profiles of skill scores for temperature for the Northern extra-tropics. Top-row: RMSE and SPREAD, Middle-row: RMSE/SPREAD Ratio, and Bottom-row: Normalized RMSE; for the forecast time 6 hours, 3<sup>rd</sup>, and 5<sup>th</sup> day respectively (from left to right).

the 500 hPa geopotential height. Figure (3.17) shows the RMSE, SPREAD, their ratio, and the Normalized RMSE scores with respect to the [No BS] experiment. The top-row shows the absolute RMSE (solid lines) and SPREAD (dashed lines), the middle-row shows the RMSE/SPREAD Ratio and the bottom row shows the Normalized RMSE with reference to the [No BS] experiment. From the figure, we can see that the response of geopotential height to the backscatter is quite different from that of the temperature. By looking at the Normalized RMSE scores, we can see that in the Northern extra-tropics, the first 24 hour forecast shows significant positive impact for all the case studies. Subsequent forecast steps show negative impact on the forecast for experiments [oALL\_2a] and [oNAG\_2a]. Similar is the case for the Southern extra-tropics, i.e., for the first 50-60 forecast hours all experiments show significant improvement in the forecast, and afterwards the forecasts get worse. On the contrary, forecasts in the Tropics show significant improvement up to seven days for all cases except [oCON\_2a], which is in fact the case where the KE dissipation contribution is only from deep convection. The

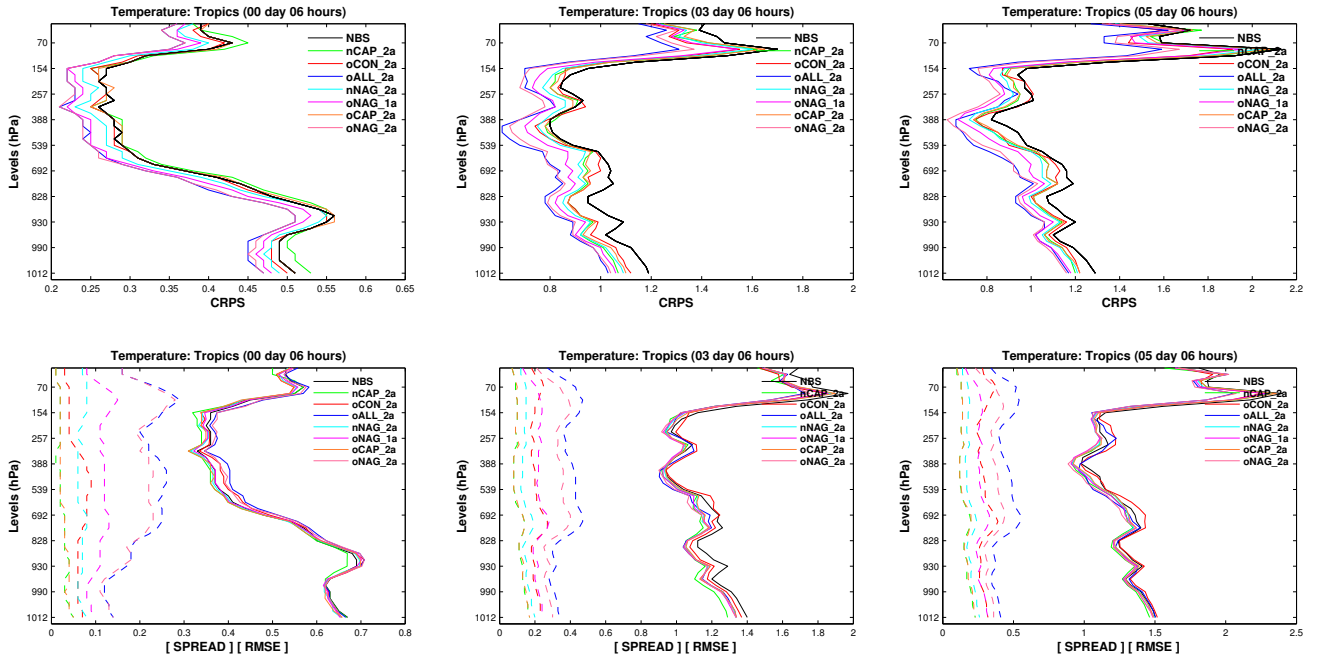


**Figure 3.15:** Vertical profiles of skill scores for temperature for the Tropics. Top-row: CRPS, Bottom-row: SPREAD and RMSE; for the forecast time 6 hours, 3<sup>rd</sup>, and 5<sup>th</sup> day respectively (from left to right).

negative impact of the case [oCON\_2a] can be explained by looking at the SPREAD of the same. The SPREAD for [oCON\_2a] increased almost exponentially in the Tropics. Since the KE dissipation associated with the deep convection case is mostly centered in the Tropics (see Fig. (3.3: Top), the SPREAD in [oCON\_2a] is not spatially uniform and is indeed concentrated in the Tropics. This non-uniformity can create anomalous gradients in the backscatter forcing which cause large errors. In fact we have found that few grid-points cause this anomalous values which is associated with the calculation of the KE dissipation from the deep convection parameterization scheme in the model.

Now we compare the skill scores of the experiment [oALL\_2a] which was found to perform the best in the case of 850 hPa temperature forecast. Since RMSE scores alone cannot be used to judge the forecast performance, we analyze and compare the case using the CRPS score as well. Figure (3.18) shows the CRPS and the corresponding confidence interval for the 500 hPa geopotential height ten days forecast, for the the Northern extra-tropics, the Tropics, and the Southern extra-tropics respectively. The CRPS score for the Northern extra-tropics is consistent with the RMSE, showing significant improvement during the first 24 hours and slightly worsening afterwards for a short period. The Southern extra-tropics also show significant improvement for the first 24-36 hours but slightly worsen afterwards. In contrast to the extra-tropics, the improvement in the Tropics is significant throughout the entire forecast period.

Apart from the temperature and the geopotential height, specific humidity is also another common forecast variable used to evaluate the forecast quality. Figure (3.19) shows the forecast statistics from the GME-ENS experiments for specific humidity, for

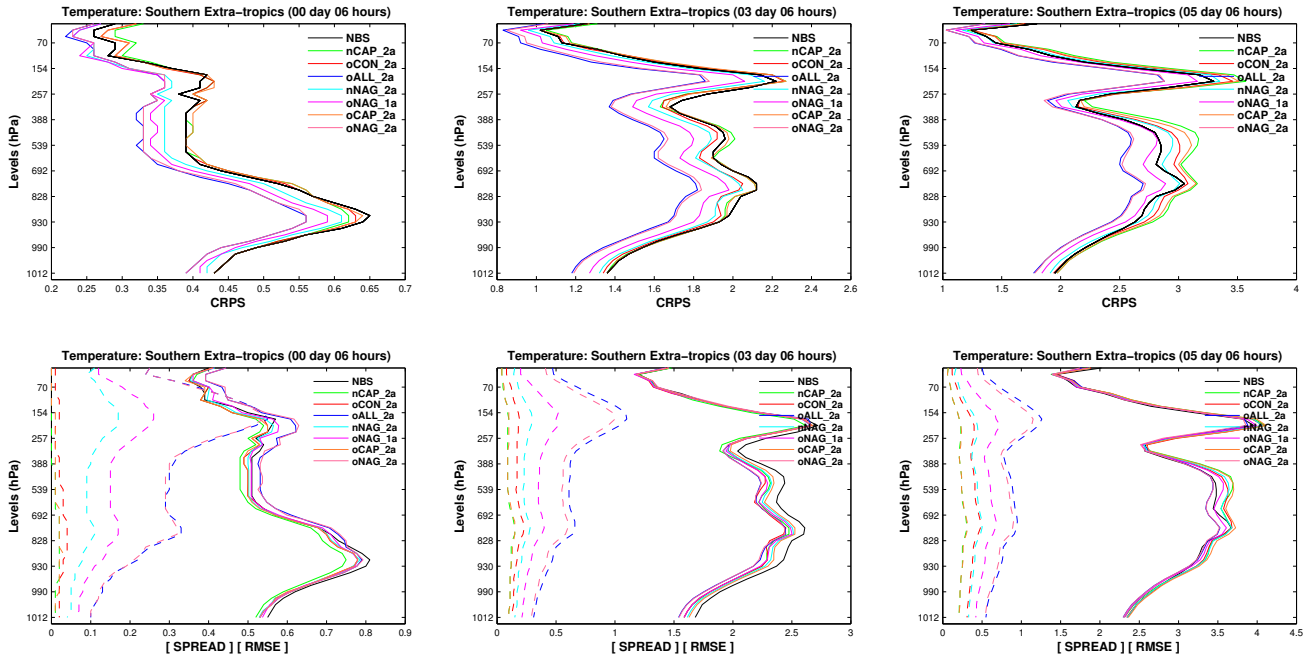


**Figure 3.16:** Vertical profiles of skill scores for temperature for the Southern extra-tropics. Top-row: CRPS, Bottom-row: SPREAD and RMSE; for the forecast time 6 hours, 3<sup>rd</sup>, and 5<sup>th</sup> day respectively (from left to right).

the Northern extra-tropics, the Tropics, and the Southern extra-tropics (from left to right). The top-row shows the ten days forecast SPREAD (dashed lines), and RMSE (solid lines), and the bottom-row of the figure shows the CRPS vertical profiles for the first 6 hours forecast. From the figure, it can be seen that the forecast error reduced significantly over the whole ten days forecast period, for all case studies. Figures showing statistical significance can be found in Appendix-C. Also here, the highest SPREAD is for experiment [oALL\_2a], and the lowest for the case where no dissipation is incorporated in the SKEB scheme. The CRPS vertical profile from experiment [oALL\_2a] also confirms the improvement due to the SKEB scheme. It is also very clear that the improvement is not just confined to one specific pressure level but it is apparent and significant throughout the entire vertical levels.

So far, we have analyzed the impact of the SKEB scheme on multilevel variables such as the temperature, the geopotential height, and the specific humidity, and found that the SKEB scheme has a significant positive impact on the forecast quality overall. Now we will analyze the impact of SKEB scheme on the surface pressure. In general the surface pressure can exhibit large variations over a large area and a short period of time especially in the extra-tropics. Such large variations in surface pressure are directly linked to the strong gradients in the wind components. Since the SKEB scheme directly perturbs the wind components, the variations or perturbations in the wind can cause large variations in surface pressure. Figure (3.20) shows the RMSE scores for surface pressure for ten days forecast, for the Northern extra-tropics, the Tropics, and the Southern extra-tropics (from left to right). The top-row shows the absolute RMSE

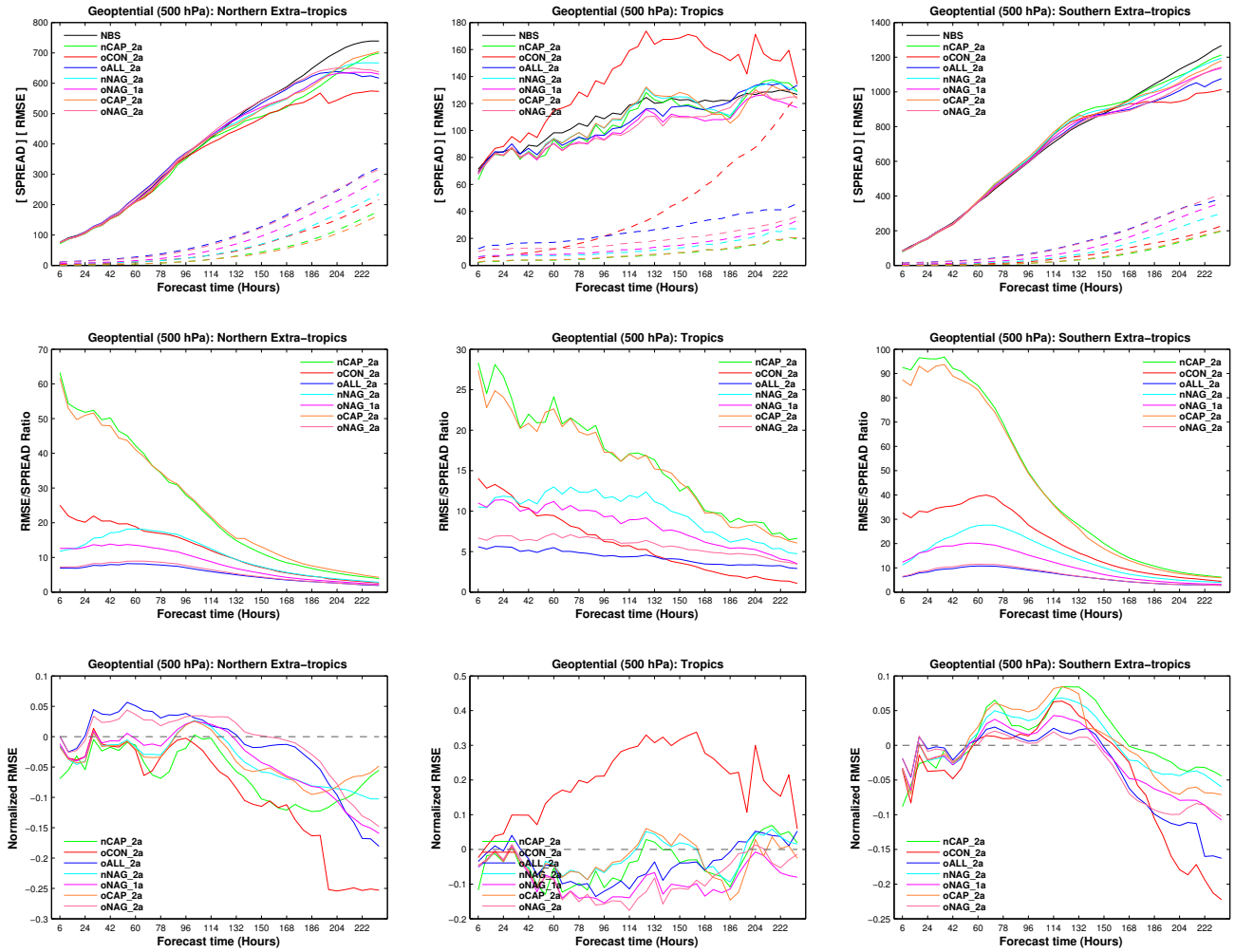


**Figure 3.17:** Ten days forecast statistics for 500 hPa geopotential height. Top-row: RMSE (solid) and SPREAD (dashed), Middle-row: RMSE/SPREAD Ratio, and Bottom row: Normalized RMSE; for the Northern extra-tropics, the Tropics and the Southern extra-tropics (from left to right).

(solid lines) and SPREAD (dashed lines), the middle-row shows its Ratio, and the bottom-row shows the Normalized RMSE with reference to the [No BS] experiment. It is clear from the figure that the SKEB impact on the surface pressure is quite different in the three regions. In the Northern extra-tropics, the improvement is significant throughout the entire forecast period, for all the SKEB cases. For the first 30-40 hours, experiment [oALL\_2a] is the best and afterwards it becomes relatively worse. In the Tropics, all the cases except [oCON\_2a] show significant positive impact for the first 30-40 hours. In the Southern extra-tropics, only experiment [oCON\_2a] shows significant positive impact over the entire forecast period. All other cases have a significant impact only for first 12-24 hours. It should be noted that although [oCON\_2a] shows better results in the extra-tropics, its response or behavior is more erratic, similar to the case for geopotential height shown in Fig. (3.17). Since experiment [oALL\_2a] contains the KE contribution from convection, it is plausible that any issues associated with

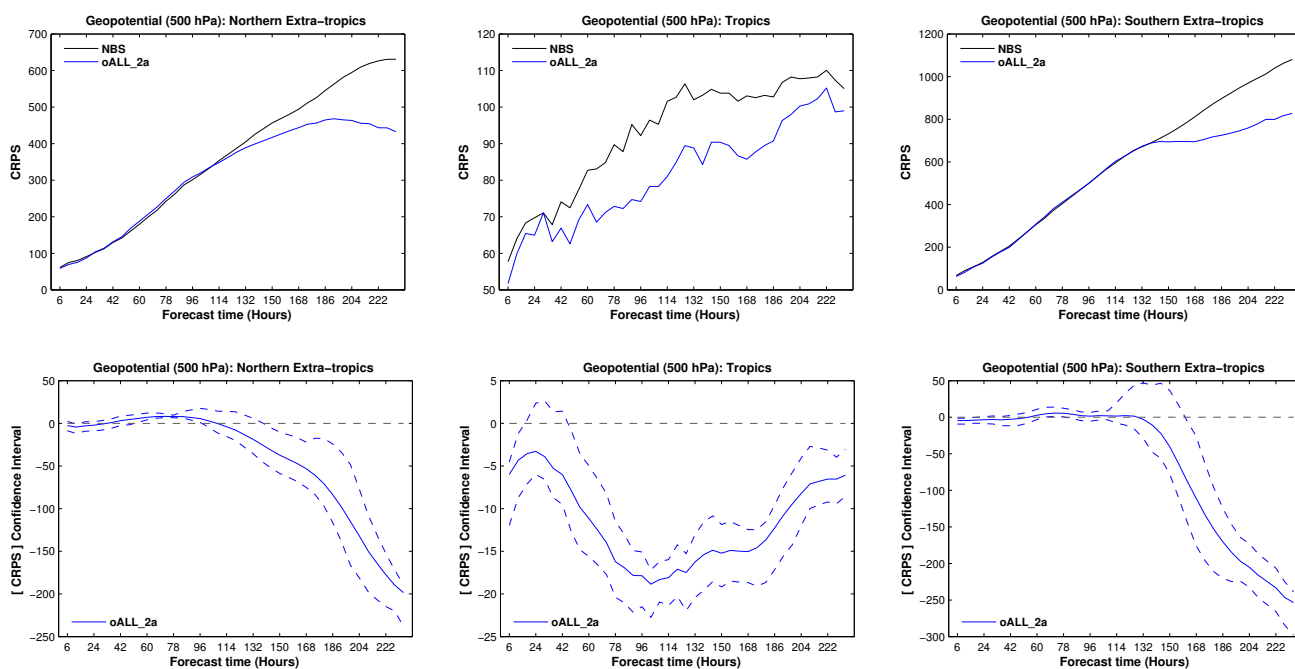


**Figure 3.18:** Continuous Ranked Probability Score (CRPS) and confidence interval for 500 hPa geopotential height, for the experiment [oALL\_2a]: the Northern extra-tropics (left), the Tropics (middle), and the Southern extra-tropics (right)

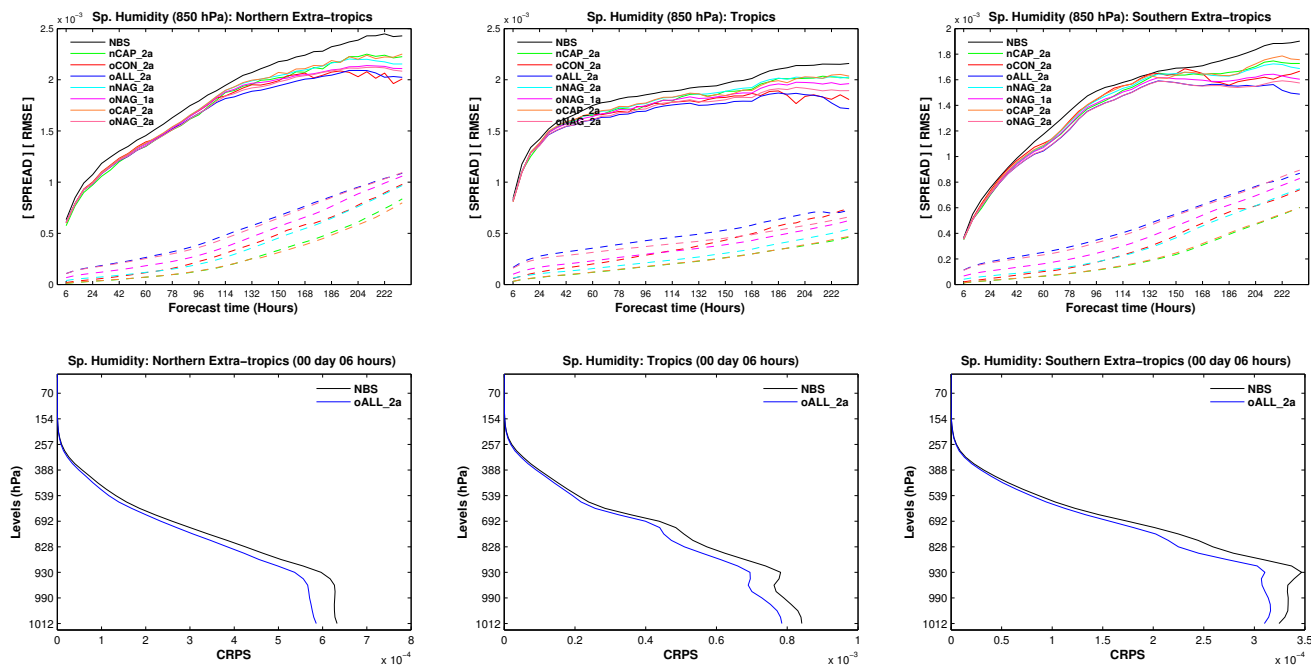


**Figure 3.19:** Specific humidity profiles. Top-row: ten days forecast RMSE, and SPREAD at 850 hPa; Bottom-row: 6 hour forecast CRPS for the experiment [oALL\_2a]

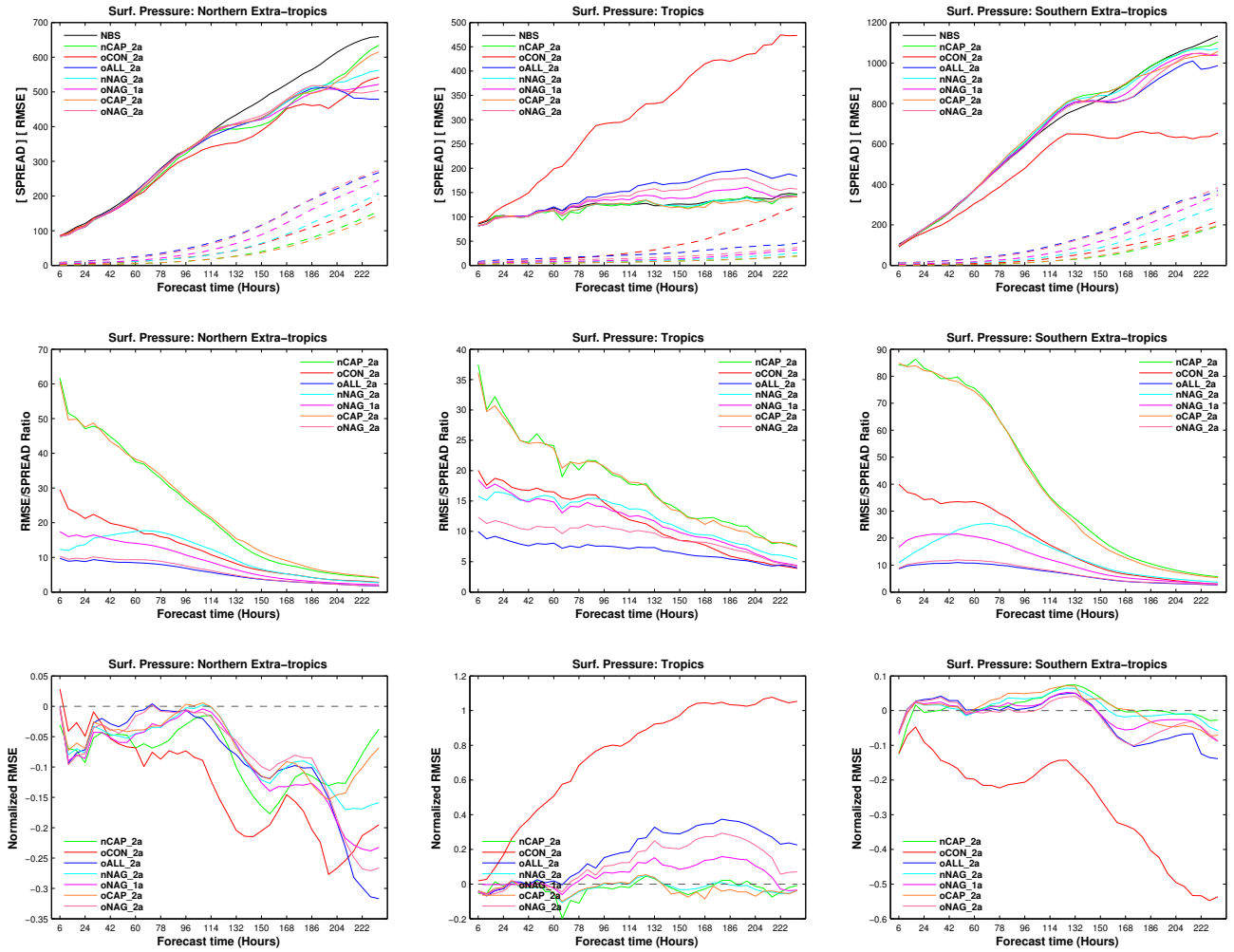


**Figure 3.20:** Ten days forecast statistics for surface pressure: RMSE (solid) and Ensemble SPREAD (dashed) on the top-row, RMSE/SPREAD Ratio (middle-row), and Normalized RMSE (bottom-row), for the Northern extra-tropics, the Tropics and the Southern extra-tropics respectively (from left to right).

[oCON\_2a], which is more evident in the Tropics, will also appear in [oALL\_2a].

The CRPS of the surface pressure forecast for experiment [oALL\_2a] is shown in Fig. (3.21). In general the CRPS agree with the RMSE scores, indicating significant improvement in the forecast during the first 60 hours of the forecast in the Northern extra-tropics, and in the Tropics, and marginal improvement in the Southern extra-tropics. The deterioration of the long-term forecast in the Tropics is due to the inaccuracies in estimating the KE dissipation from deep convection.

### 3.3.4 Conclusion: Impact of SKEB on the GME-ENS Forecast

The following are the main conclusions concerning the impact of SKEB on the short and medium-range forecasts in GME:

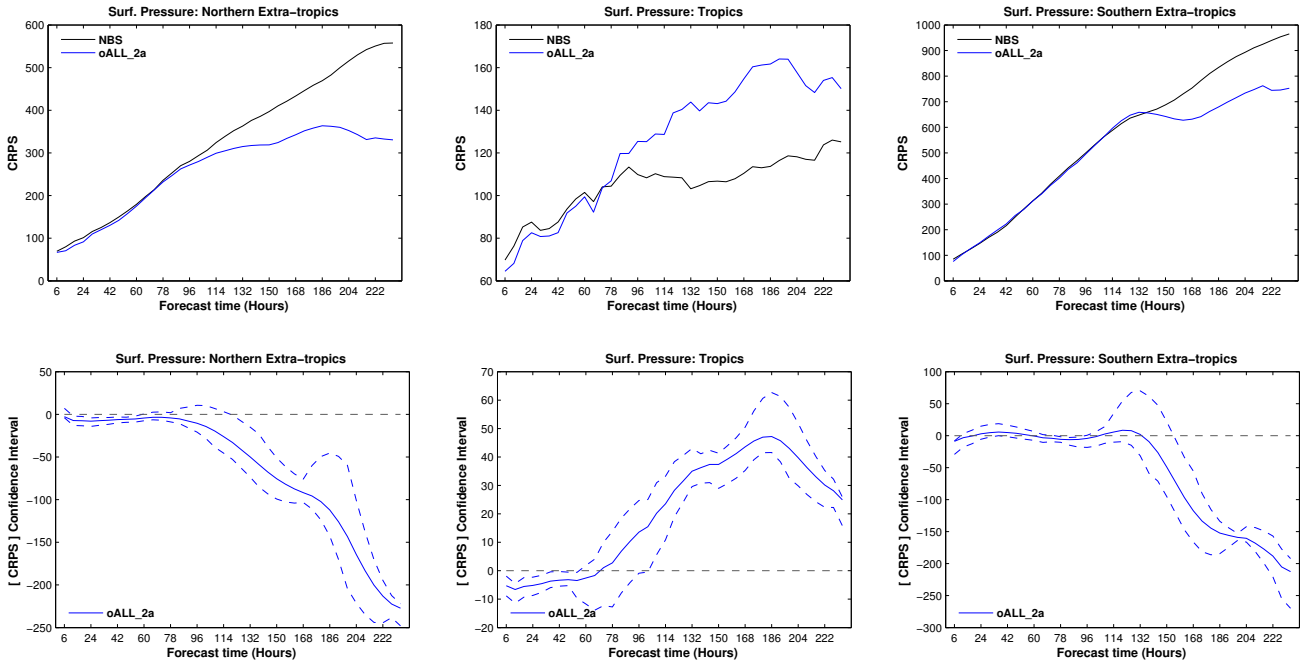


**Figure 3.21:** *Continuous Ranked Probability Score (CRPS) and confidence interval for surface pressure, for the experiment [oALL\_2a]: the Northern extra-tropics (left), the Tropics (middle), and the Southern extra-tropics (right)*

1. The SKEB scheme significantly improved the probabilistic temperature forecast at all pressure levels, i.e. it gives valuable information on the probability distribution in addition to the deterministic forecast.
2. Incorporating a stochastic backscatter scheme produces significantly better results compared to random perturbations (e.g. [oALL\_2a] vs [nCAP\_2a]). The experiment [oALL\_2a], which incorporates all the dissipation components, performs best in most cases, and generates the highest SPREAD,
3. These experiments generally show too less SPREAD over the full forecast range due to the lack of SPREAD in the initial perturbations. This cannot be compensated by the backscatter scheme adding noise during the model integration only.
4. Uncorrelated perturbations have less effect than vertically correlated perturbations. Uncorrelated noise does not correspond to a meaningful (balanced) model state and will be damped out. This especially applies to the extra-tropics.
5. Forecast results of geopotential height, specific humidity and surface pressure show significant improvement over short-range (up to 60 hours) but show mixed results for longer forecast.

In short, we have proved that the KE backscatter can significantly improve the forecast. The most important message is that this improvement is achieved solely by

tapping the model uncertainty since there is no initial uncertainty as each forecast ensemble member starts from same initial state. In other words the forecast improvement is achieved by incorporating the model uncertainty through a stochastic kinetic energy backscatter scheme. Now the question is: How good is this improvement compared to the improvement using an ensemble prediction system (EPS) which in fact incorporates initial uncertainty? In the following, we will try to answer the above question.

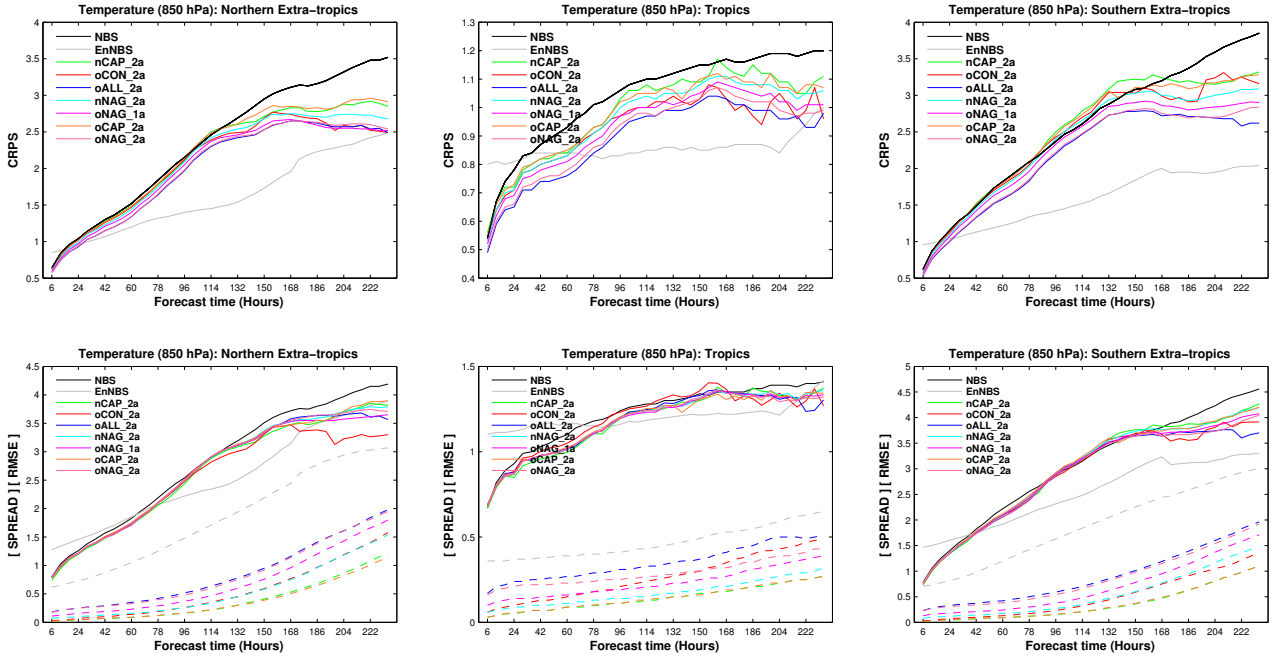


**Figure 3.22:** Ten days forecast statistics of GME-ENS compared to GME-EPS experiments for 850 hPa temperature. Top-row: CRPS; Bottom-row: RMSE (solid), SPREAD (dashed); for the Northern extra-tropics, the Tropics, and the Southern extra-tropics (from left to right).

Figure (3.22) shows a comparison of 850 hPa temperature forecast statistics from the GME-ENS experiments and a GME-EPS experiment [EnNBS], of same resolution (without using any stochastic backscatter scheme). The top-row shows the CRPS statistics over ten days forecast period and the bottom-row shows the RMSE (solid lines) and SPREAD (dashed lines). In general, Figure (3.22) gives two main messages:

1. the importance of incorporating the initial uncertainty, and
2. the importance of data assimilation (or EPS in general) for medium or long-range forecast.

From the CRPS it can be seen that the experiment [oALL.2a] is better for the first 24 hours (1 day) forecast in the extra-tropics and about 72 hours (3 days) in the Tropics. The RMSE in general also agrees with the CRPS results although the range of forecast hours (showing improvement in the skill scores) slightly differ. Both from the CRPS and the RMSE, it is in fact surprising to see that the GME-ENS outperforms

the GME-EPS experiment for the short-range forecast, although for medium and long range forecast the EPS systems are always better. Two main reasons for the under-performance of GME-EPS are: i) no model uncertainty is incorporated in the forecast model although it is implicitly represented in the LETKF data assimilation system through additive inflation; and ii) the initial ensemble members for the EPS are not as good as that from the operational 3D VAR (it is an experimental system under development) On the contrary the GME-ENS forecasts are initialized using the best possible analysis (from the DWD operational data). Therefore, during the first two-to-five days (depending on verification skill score and the region) the forecasts from GME-ENS outperform that from GME-EPS as they initialized from a more accurate forecast. After that time the GME-EPS is better as it leads to higher ensemble spread due to the initial disturbances.

Figure (3.22) compares the forecast improvements achieved by two different forms of uncertainty: i) model uncertainty (through stochastic KE backscatter), and ii) initial uncertainty (through a set of possible initial states or ensemble). Naturally, the next step would be to combine these two methods, which leads to the next research question: would incorporating stochastic backscatter in GME-EPS give better results? Combining these two seems to be straight forward and one would expect a better forecasting system. In the following section we will show the results from GME-EPS experiments which incorporate the SKEB scheme. In fact our experiments results do not follow the logic, and we will try to explain why they do not in the following sub-sections.

### 3.3.4.1 SKEB: Impact on the GME-EPS Forecasts

In this subsection, we will describe the details regarding the GME-EPS experiments, followed by a detailed analysis of the results. A summary of the GME-EPS experiments, the SKEB forcing fraction and LETKF inflation parameters used is given in table (3.2). A total of seven EPS experiments were performed: two experiments (with and without SKEB) with no additive or multiplicative inflation (NBS\_NAI and WBS\_NAI), two experiments with additive inflation but no multiplicative inflation (NBS\_WAI, and WBS\_WAI), two experiments with multiplicative inflation but no additive inflation (NBS\_WMI, WBS\_WMI), and one experiment with additive inflation and with doubled backscatter forcing (WBS\_WDF). Theoretical details regarding the covariance inflation techniques and its effects on analysis can be found in Chapter (4). Here we will focus more on the impact of the SKEB scheme on the EPS forecast. Details regarding the impact of the SKEB scheme on the LETKF analysis can also be found in Chapter (4).

Figure (3.23) shows the ten days forecast statistics for 850 hPa temperature, for all the experiments listed in table (3.2), for the Northern extra-tropics, the Tropics and the Southern extra-tropics (left to right). Top-row shows the CRPS and the bottom-row shows the RMSE (solid lines) and SPREAD (dashed lines). The thin-lines (both solid and dashed lines) represent the experiments with the SKEB scheme, and the thick lines represent the experiments without the backscatter.

First we will analyze the twin experiments [NBS\_NAI] and [WBS\_NAI] (gray color), where there is no contribution from additive or multiplicative covariance inflation during the assimilation cycle. These experiments were designed to evaluate the actual

| <b>GME-EPS<br/>Exp. ID</b> | <b>SKEB scheme<br/>(Yes/No)</b> | <b>Backscatter<br/>forcing</b> | <b>Additive<br/>Inflation</b> | <b>Multiplicative<br/>Inflation</b> |
|----------------------------|---------------------------------|--------------------------------|-------------------------------|-------------------------------------|
| NBS_NAI                    | No                              | $\alpha = 0.0$                 | 0.00                          | 0.00                                |
| WBS_NAI                    | Yes                             | $\alpha = 2.0$                 | 0.00                          | 0.00                                |
| NBS_WAI                    | No                              | $\alpha = 0.0$                 | 0.25                          | 0.00                                |
| WBS_WAI                    | Yes                             | $\alpha = 2.0$                 | 0.25                          | 0.00                                |
| WBS_WDF                    | Yes                             | $\alpha = 4.0$                 | 0.25                          | 0.00                                |
| NBS_WMI                    | No                              | $\alpha = 0.0$                 | 0.00                          | 1.10                                |
| WBS_WMI                    | Yes                             | $\alpha = 2.0$                 | 0.00                          | 1.10                                |

**Table 3.2:** *Summary of GME-EPS sensitivity experiments.*

contribution of backscatter in the EPS or, in other words, to study the response of the initial uncertainty in the presence of backscatter. From the figure, it can be seen that the effects of SKEB or the response of the EPS due to the backscatter is quite different in all the three regions. From the CRPS of the extra-tropics (both Northern and the Southern), it can be seen that the EPS with backscatter [WBS\_NAI] has higher CRPS than [NBS\_NAI], throughout the entire forecast period or, in other words, that the SKEB scheme in fact deteriorates the EPS forecast in the extra-tropics. On the contrary, the CRPS of the Tropics shows significant improvement in the forecast up to five-to-six days but it quickly deteriorate afterwards. The RMSE scores shown in Fig. (3.23: Bottom-row) agree with the results from the CRPS. The Normalized RMSE scores in Fig. (3.24: bottom-row) show the significance of [WBS\_NAI] with respect to [NBS\_NAI]. The figure shows that, in the extra-tropics [WBS\_NAI] is significantly worse than [NBS\_NAI] but it is significantly better in the Tropics. However, we can see an increase in the SPREAD in all three regions, which was also one of the primary goals of incorporating the SKEB scheme into the EPS. The SPREAD for [WBS\_NAI] in the Northern extra-tropics is around ten percent more than for [NBS\_NAI] in the beginning of the forecast and it slightly increases over the forecast period. The Southern extra-tropics also show an increase in the SPREAD for [WBS\_NAI] in the beginning but the SPREAD decreases over the forecast period and is almost equal to [NBS\_NAI] towards the end. The Tropics also show a relatively higher SPREAD for [WBS\_NAI] for almost four-to-five days, but also in this case the SPREAD starts decreasing afterwards. Nevertheless, it can be seen that overall the RMSE and the CRPS results are not very promising, especially in the extra-tropics. Before answering the question: why the SKEB scheme has a negative impact, we will analyze and compare the remaining GME-EPS sensitivity experiments, which implicitly incorporate the model error through covariance inflation in addition to the SKEB scheme.

One of the main purposes of incorporating an additive or multiplicative covariance inflation is to compensate the underestimated background error covariance. In other

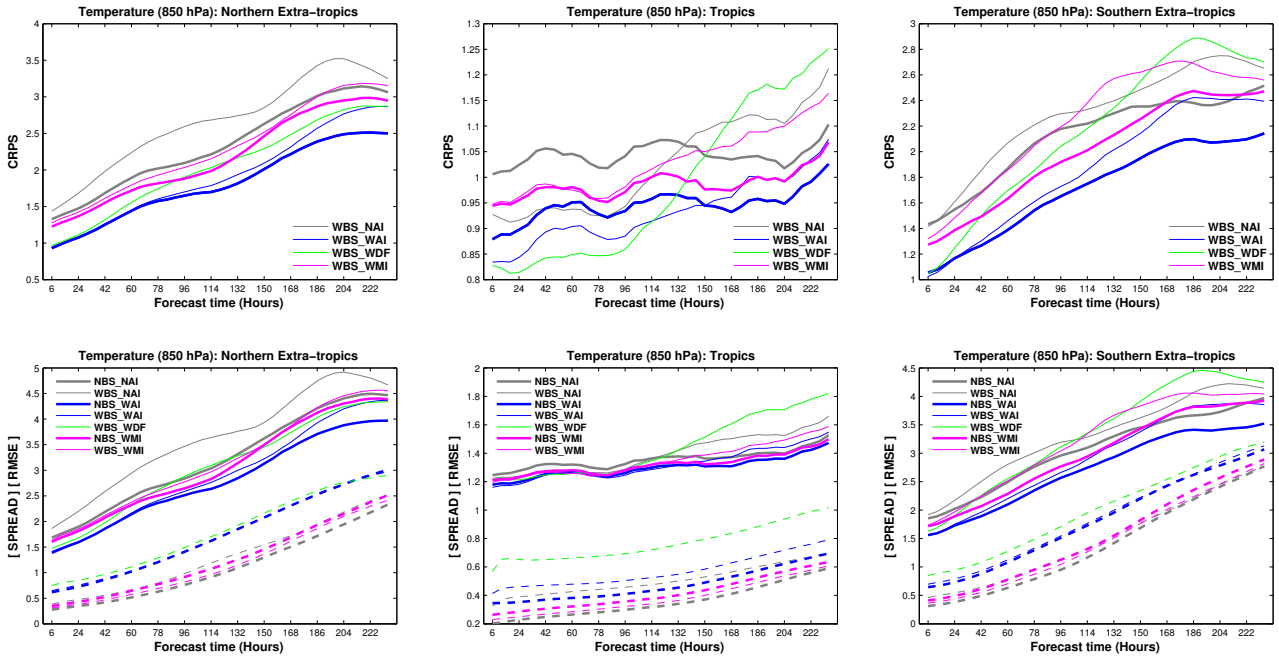


**Figure 3.23:** Ten days forecast statistics for the 850 hPa temperature. Top-row: CRPS, Bottom-row: RMSE (solid lines), and SPREAD (dashed lines); for the Northern extra-tropics, the Tropics, and the Southern extra-tropics (left to right).

words, to compensate the loss of first-guess spread during the assimilation cycle. In general, most of the covariance inflation is achieved using ad-hoc procedures. By using a stochastic backscatter scheme, we expect to increase the ensemble SPREAD dynamically, thereby inflating the background covariance to some extent. More details regarding the same can be found in Chapter (4). Now, we will compare the response of the EPS with covariance inflation, to the one incorporating the backscatter scheme.

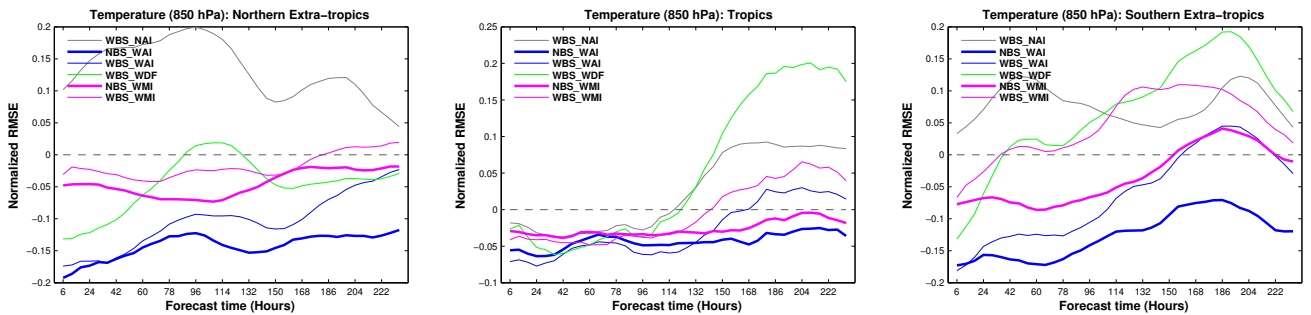


**Figure 3.24:** Ten days forecast statistics for the 850 hPa temperature. Normalized RMSE for the Northern extra-tropics, the Tropics, and the Southern extra-tropics (left to right).

Figure (3.23) also shows the CRPS (Top-row), and RMSE and SPREAD (Bottom-

row) for the additive inflation EPS experiments [NBS\_WAI] and [WBS\_WAI] (blue lines). From the CRPS and RMSE scores we can see that there is no significant improvement in the forecast in the Northern extra-tropics. In fact by looking at the normalized RMSE for [WBS\_WAI] shown in Fig. (3.24), we can see that it is in fact slightly worse than [NBS\_WAI] for the first 36 hours, then almost the same for about 48 hours and then it becomes worse again. In the Southern extra-tropics we can see a slight but significant improvement for the first 6-12 hours for experiment [WBS\_WAI] and a worsening afterwards. We can also see that the relative increase in the SPREAD is very small in the extra-tropics, compared to the SPREAD of the EPS with no inflation (gray lines). This suggests that the inflation and the backscatter are in fact counteracting each other. In contrast to the extra-tropics, the Tropics show (see the Normalized RMSE) significant improvement up to six days. Although the counteracting effects are visible in the Tropics, they are not so strong compared to the extra-tropics. We will come back to the counteracting effects of SKEB and additive inflation in the later part of this section.

In order to study the effects of backscatter forcing, we have performed an EPS experiment [WBS\_WDF] (green line in Fig. (3.23) and (3.24)), which is similar to experiment [WBS\_WAI] but with twice the backscatter forcing. From the CRPS and RMSE score, it is very clear that it has a negative impact on the extra-tropics, and the forecast is worse than [WBS\_WAI]. On the Tropics, [WBS\_WDF] has a significant positive impact compared to [WBS\_WAI]. The SPREAD also increases dramatically in the Tropics. On the contrary, the increase in the SPREAD due to the doubled backscatter forcing weakens in the extra-tropics, which again suggests the fact that the additive inflation and the backscatter forcing are opposite. However, although there is a significant improvement in the Tropics, this lasts up to around four days, and afterwards the scores show a steep increase in the CRPS and the RMSE. The cause of this sudden deterioration of the forecast is unclear at the moment. One possible explanation is the inaccurate estimation of the KE dissipation from deep convection, which was also visible in the CRPS/RMSE for the Tropics in the GME-ENS experiment [oCON\_2a].

Compared to the additive inflation experiments, the performance of the multiplicative inflation experiments ([NBS\_WMI] and [WBS\_WMI]) with backscatter is worse. In some cases it is even worse than experiments with no inflation factors. One of the surprising fact is that the multiplicative inflation experiment with backscatter [WBS\_WMI] has comparatively lower SPREAD than the one without backscatter [NBS\_WMI] in all the three geographical regions.

Now we will analyze the zonal average and spatial distribution of the RMSE and SPREAD statistics, which will give more insights into the EPS response to the backscatter scheme. The spatial patterns shown in Fig. (3.25) give an overview of the geographical distribution of the backscatter contribution to the ensemble SPREAD. It can be seen that the SPREAD for the 6 hour forecast is almost uniform compared to [NBS\_NAI]. On the 3<sup>rd</sup> and 5<sup>th</sup> days, the SPREAD is much higher in the extra-tropics in both experiments. One of the main differences in the spatial patterns of the two experiments is the distribution of the SPREAD in the Tropics. The spatial pattern of [WBS\_NAI] shows uniform, and relatively larger SPREAD, which indicates that the

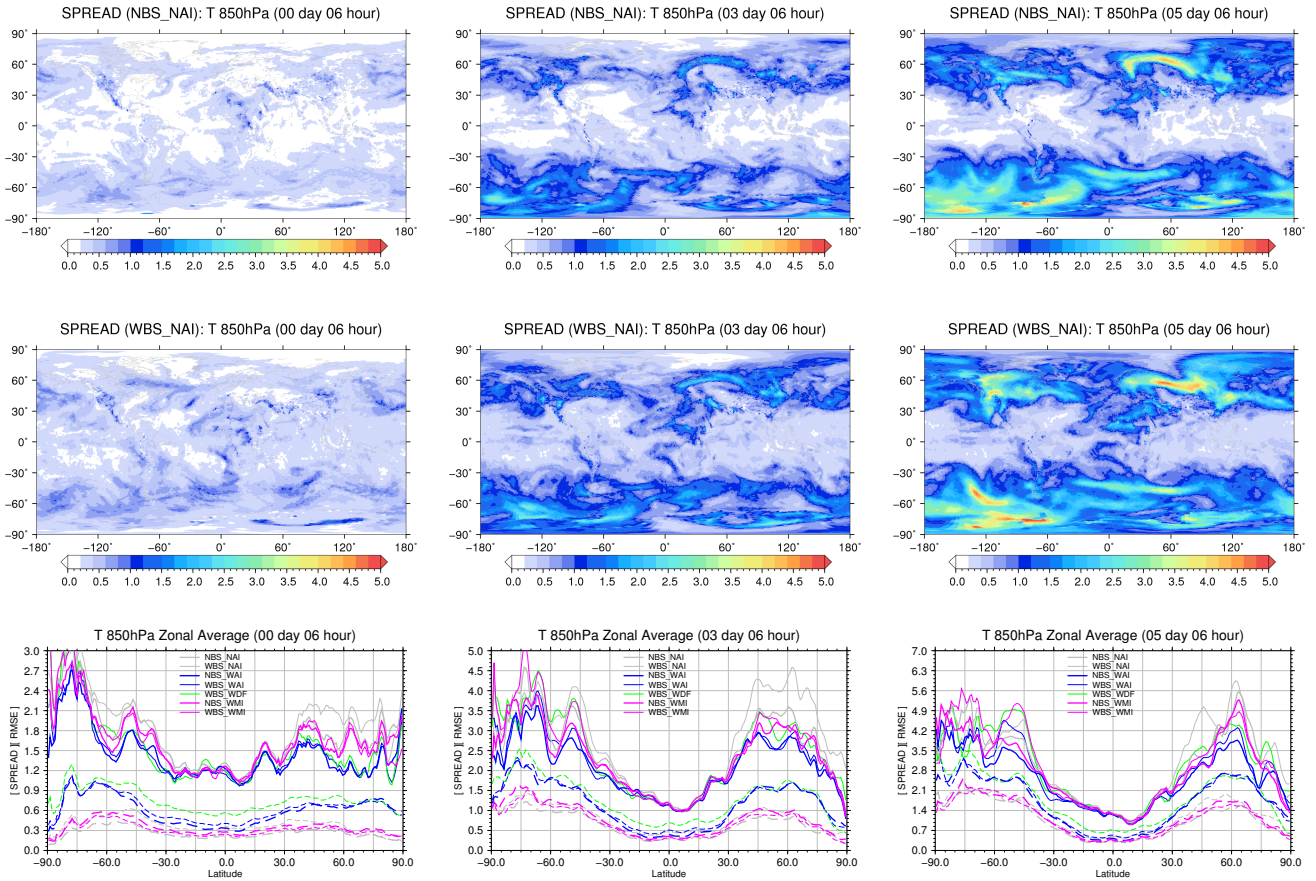


**Figure 3.25:** 850 hPa temperature statistics. Top-row: Spatial distribution of the SPREAD for [NBS\_NAI], Middle-row: Spatial distribution of the SPREAD for [WBS\_NAI]; Bottom-row: Zonal average RMSE (solid lines) and SPREAD (dashed lines). for the forecast time at 6 hours, 3<sup>rd</sup>, and 5<sup>th</sup> day respectively (from left to right).

backscatter is very effective, and in fact confirms the results from CRPS and RMSE scores.

Figure (3.25: Bottom-row) compares the zonal average of the 850 hPa temperature field, for all EPS experiments. From the figure it can be seen that [WBS\_NAI], which is the experiment with backscatter and no inflation, has much lower SPREAD in the extra-tropics compared to [NBS\_WAI], although [WBS\_NAI] shows relatively higher SPREAD than [NBS\_NAI]. This is consistent for the 6 hour, 3<sup>rd</sup>, and 5<sup>th</sup> day. This means that although the backscatter was able to generate a higher SPREAD the amplitude is much less compared to the SPREAD due to the additive inflation. Among the EPS experiments with inflation, multiplicative inflation with backscatter [WBS\_WMI] produces the worst result, which in general agrees with our earlier conclusion.

In the EPS experiments, the SPREAD of the zonal wind fields from the backscatter experiments are relatively larger compared to those for the temperature since the backscatter forcing is applied directly on the wind components and there is no explicit backscatter forcing on the temperature fields. This can be seen in the spatial patterns shown in Fig. (3.26), which gives an overview of the geographical distribution of

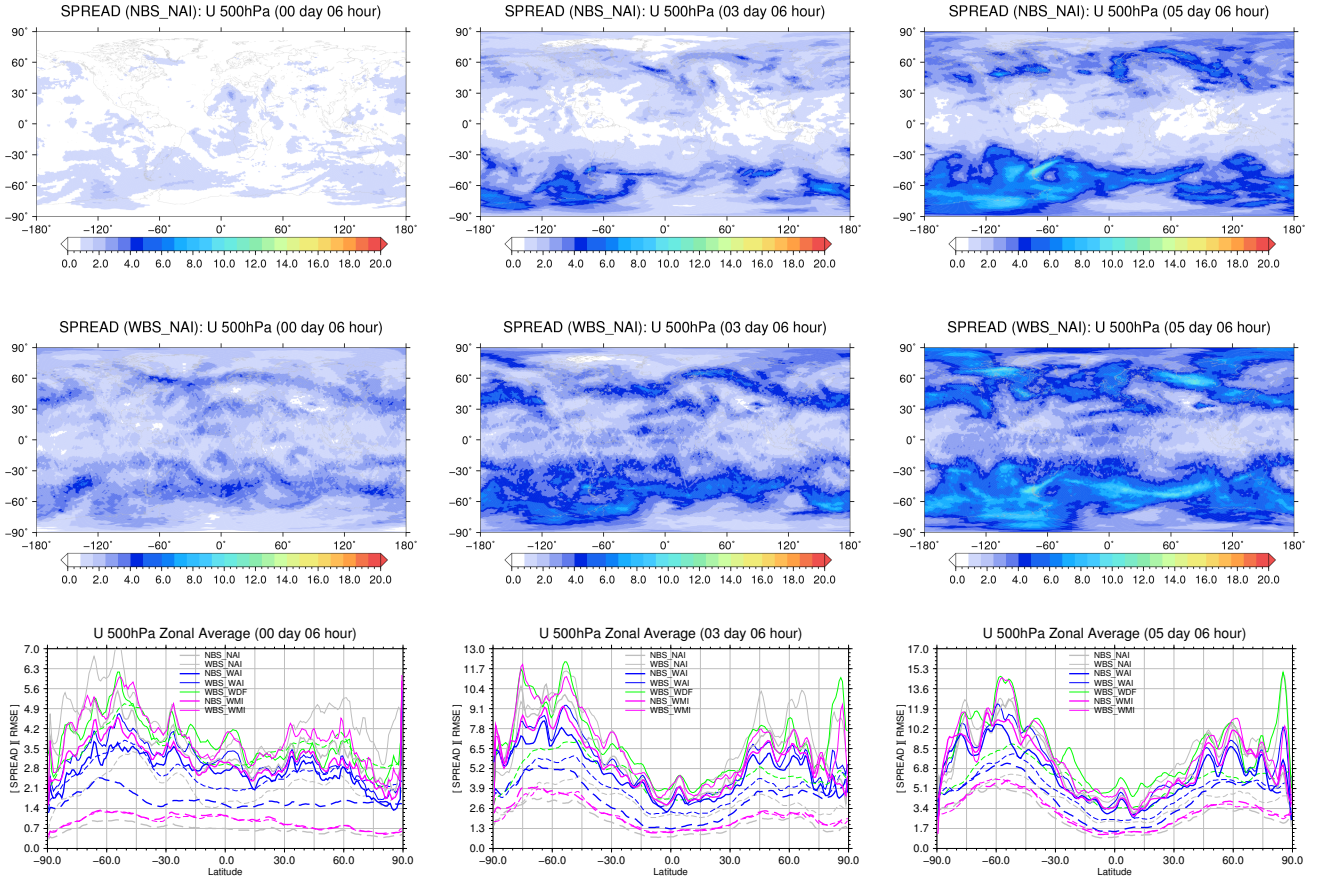


**Figure 3.26:** 500 hPa zonal wind statistics. Top-row: Spatial distribution of the SPREAD for [NBS\_NAI], Middle-row: Spatial distribution of the SPREAD for [WBS\_NAI]; Bottom-row: Zonal average RMSE (solid lines) and SPREAD (dashed lines). for the forecast time at 6 hours, 3<sup>rd</sup>, and 5<sup>th</sup> day respectively (from left to right).

the backscatter contributions to the ensemble SPREAD. Similar to the temperature field, it can be seen that the SPREAD for the 6 hour forecast is almost uniform with slightly larger SPREAD in the extra-tropics. On the 3<sup>rd</sup> and 5<sup>th</sup> day, the SPREAD is much higher in the extra-tropics. The higher spread in the extra-tropics is due to the fact that the KE dissipation due to numerical diffusion is relatively higher in the extra-tropics, and is proportional to the backscatter forcing.

Figure (3.26: Bottom-row) also shows the zonal average of the RMSE (solid lines) and SPREAD (dashed lines) of the 500 hPa zonal wind (top-row), at 6 hours, 3<sup>rd</sup>, and 5<sup>th</sup> day respectively (from left to right). From the zonal average figure it can be seen that the 500 hPa zonal wind SPREAD of the experiment [NBS\_NAI], at 6 hour forecast, is quite different from the 3<sup>rd</sup>, and 5<sup>th</sup> day. The main difference is that at 6 hours, the 500 hPa zonal wind SPREAD of [WBS\_NAI] at the extra-tropics are much larger compared to [NBS\_WAI]. On the other hand the SPREAD of [NBS\_NAI] is much lower on the 3<sup>rd</sup>, and 5<sup>th</sup> day forecast, which indicate that in the extra-tropics, the SKEB scheme was unable to generate enough SPREAD comparable to the additive inflation. In the Tropics the difference is just the opposite with the exception that at 6 hour fore-

cast, the SPREAD is almost the same for both [WBS\_NAI] and [NBS\_WAI]. Here also, [WBS\_WMI], which is the experiment with multiplicative inflation and backscatter, has the worst result among all EPS.

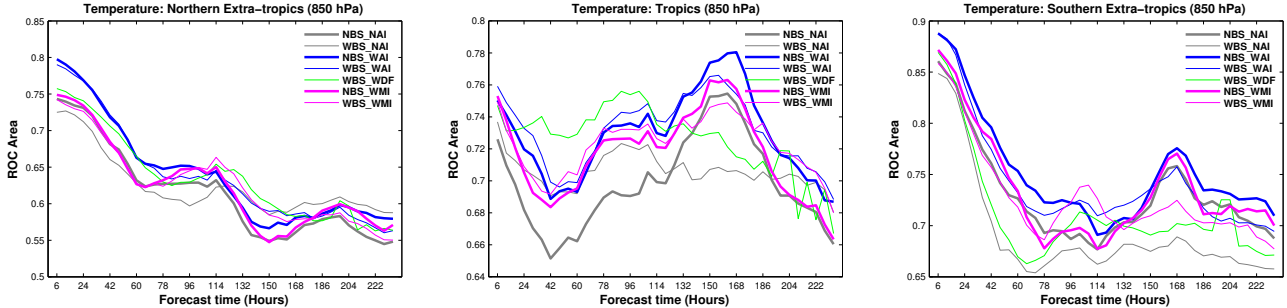


**Figure 3.27:** ROC Area for 850 hPa temperature: GME-EPS experiments with and without SKEB scheme, w.r.t ECMWF forecast; for Northern extra-tropics, the Tropics, and the Southern extra-tropics (from left to right)

In all the results shown previously, we have compared the GME-EPS forecasts with the DWD operational high-resolution deterministic analysis from the same period assuming that it provides the best data. However, this comparison may create a biased conclusion since we compare results from the same model but within different frameworks. In order to ensure unbiasedness in our conclusion we have compared our GME-EPS results and the DWD operational data with the ECMWF operational analysis. Among all the operational weather forecasts, ECMWF operational forecasting system is considered to be the best. To compare our results, we use the Receiver Operating Characteristic (ROC) statistics, which is a plot of hit-rate versus false-alarm rate. The ROC measures the ability of the forecast to discriminate between two alternative outcomes. Here the two possible alternative outcomes are the DWD operational forecast and the ECMWF operational forecast, where the ECMWF data is the reference or truth. Figure (3.27) shows the ROC Area plot for the 850 hPa temperature for the 10-day forecast. Maximum area represents maximum hit-rate, which means that the forecast is closer to the reference. The statistics gives only a relative performance of different GME-EPS experiments. From the figure it can be seen that, for both the Northern and the Southern extra-tropics, the experiment [WBS\_NAI] which is the experiment with SKEB scheme and no inflation, has the lowest area. In the Tropics, we can see that [WBS\_NAI] has a higher area than [WBS\_NAI] for about four days, which indicates the positive impact of the backscatter. For the experiments with additive inflation, the backscatter has a negative impact on the extra-tropics and a significant positive impact on the Tropics. Among all EPS, [NBS\_WAI] has the maximum area in the extra-tropics, but in the Tropics the results with backscatter are the best. Overall the ROC results reaffirm our earlier conclusions regarding the impact of the backscatter scheme on the GME-EPS forecasts.

The vertical profile of the RMSE statistics of temperature, shown in Fig. (3.28), gives an overview of the response of the EPS to the backscatter at all pressure levels at 6 hours, 3<sup>rd</sup>, and 5<sup>th</sup> day. The conclusion from the vertical profile is not different from the

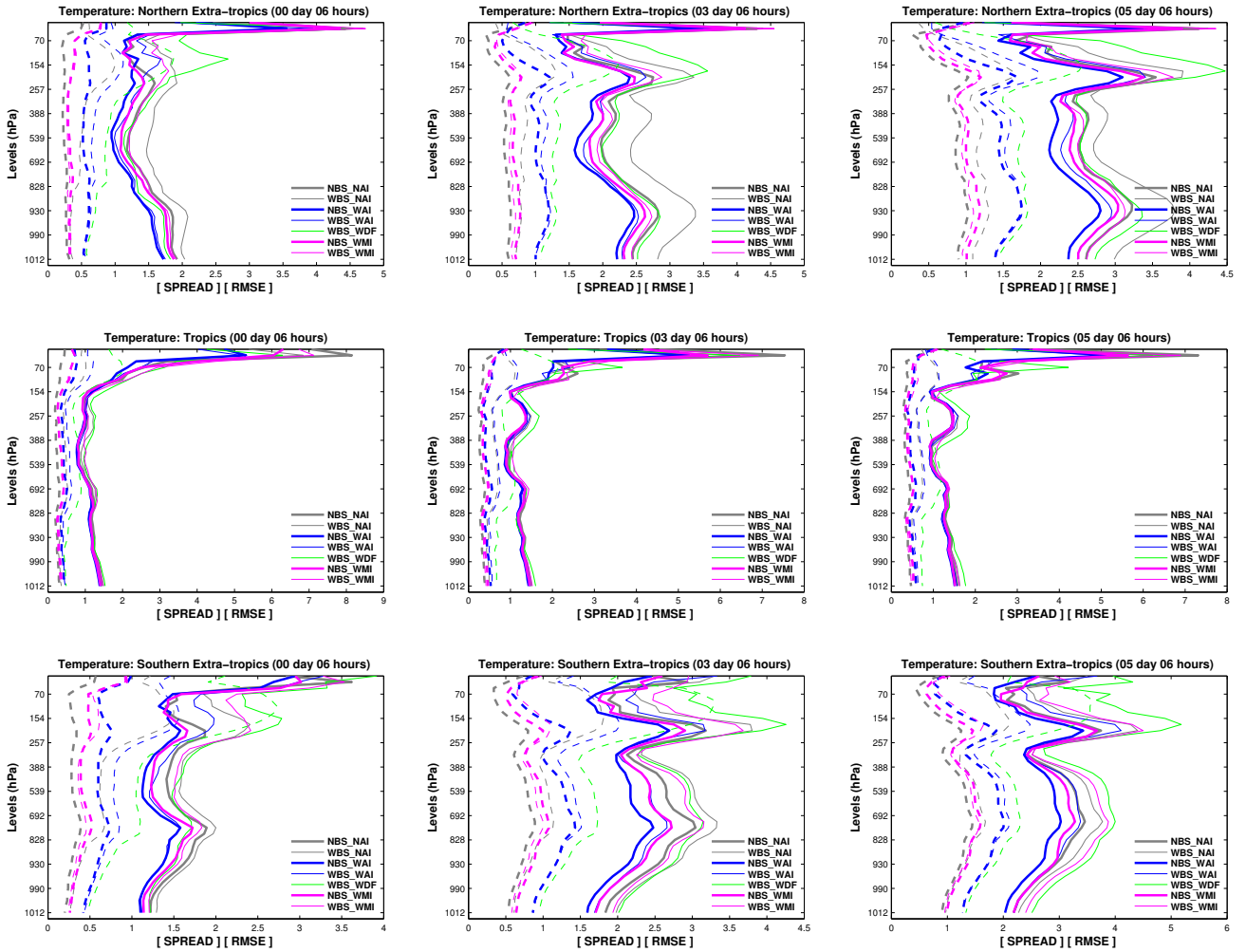


**Figure 3.28:** Vertical profiles for temperature, RMSE (solid lines) and SPREAD (dashed lines). Top-row: the Northern extra-tropics, Middle-row: the Tropics, and Bottom-row: the Southern extra-tropics; for the forecast time 6 hours, 3<sup>rd</sup>, and 5<sup>th</sup> day respectively (from left to right).

conclusion from the 850 hPa temperature results shown previously, i.e., the backscatter has a negative impact (higher RMSE) in the extra-tropics although it generates a relatively larger SPREAD. The CRPS vertical profile, shown in the Appendix-(C), confirms the results from the RMSE scores.

So far we have analyzed only the temperature field, and concluded that the backscatter has a negative impact on the GME-EPS forecast on the extra-tropics and a positive impact on the Tropics. However, this conclusion may not be the same for other variables such as geopotential height and surface pressure. Figure (3.29) shows the ten days forecast CRPS for the 500 hPa geopotential height (top-row) and the surface pressure (bottom-row). The figure shows that the SKEB scheme has a strong negative impact on both the geopotential height and the surface pressure. The impact is quite different from the temperature response in all the three geographic regions. From the

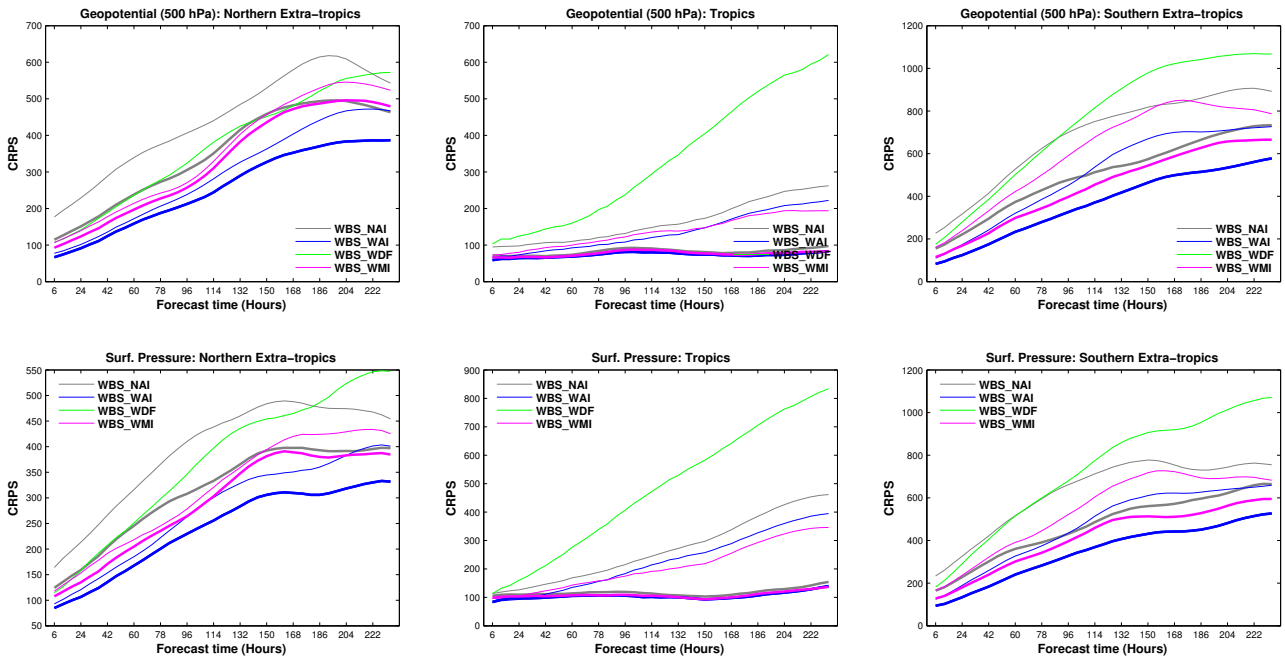


**Figure 3.29:** Ten days forecast CRPS statistics. 500 hPa geopotential height (top-row), surface Pressure (bottom-row); for the Northern extra-tropics, the Tropics, and the Southern extra-tropics (from left to right).

figure it is also clear that both variables are very sensitive to backscatter forcing, which is particularly evident from the results of experiment [WBS\_WDF] (green line).

Now, the question which remains to be answered is: why does the SKEB scheme have a negative impact on the GME-EPS forecast? In the next subsection we will describe the possible causes and try to formulate an answer to this question.

### 3.3.4.2 The SKEB does not have a positive impact on GME-EPS - Why?

In the first part of subsection (3.3.3), we have shown that the backscatter scheme significantly improves the GME-ENS forecast quality in all the three geographical regions. Later in section (3.3.3), we have shown that the backscatter scheme has a negative impact on the GME-EPS. The main differences between those two experiments are: 1) GME-ENS does not account for initial perturbations and takes the initial conditions from a deterministic analysis whereas GME-EPS uses an ensemble of perturbed initial conditions. 2) GME-ENS and GME-EPS take their initial conditions from different data assimilation systems: GME-ENS takes its initial conditions from the operational 3D VAR data assimilation cycle whereas GME-EPS takes them from the experimental LETKF suite which is not very well tuned so far. Thus the analysis (or mean analysis) compared to the deterministic analysis will be considerably different. Therefore possible factors which might influence the backscatter to cause the negative impact in GME-EPS are: the LETKF data assimilation cycle, the initial ensemble distribution, and a combination of both, which would effectively change the statistical distribution of the

assimilated variables. In order to test whether the LETKF assimilation influences the

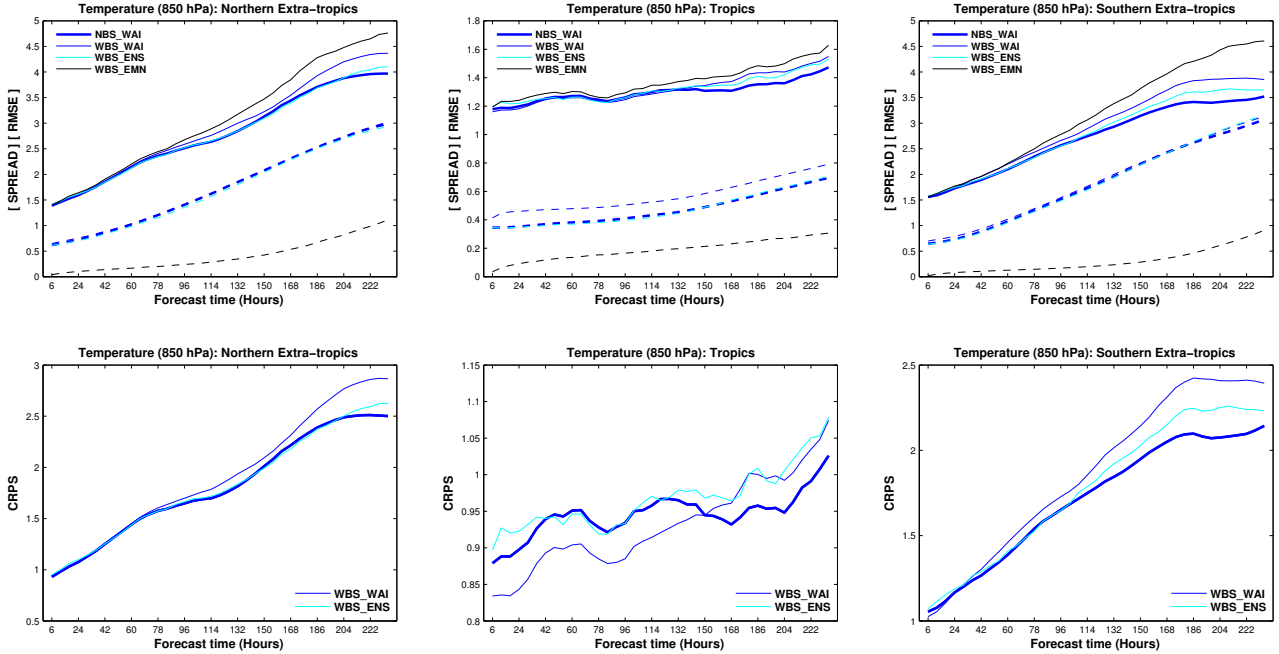


**Figure 3.30:** Ten days forecast statistics for 850 hPa temperature. Top-row: RMSE (solid) and SPREAD (dashed), Bottom-row: CRPS, for the Northern extra-tropics, the Tropics, and the Southern extra-tropics (from left to right).

backscatter, we have designed two experiments named [WBS\_ENS], and [WBS\_EMN]. The experiment [WBS\_ENS] is equivalent to the experiment [NBS\_WAI] but without using the LETKF data assimilation cycle<sup>2</sup>. This experiment will in fact show how the initial uncertainty evolves under the influence of backscatter forcing. The experiment will also reveal how the assimilation cycle affects the backscatter contribution on the forecast. Experiment [WBS\_EMN] is equivalent to the GME-ENS experiment [oALL\_2a], where there is no initial uncertainty is involved, i.e., the forecast is initialized with the forecast ensemble mean of [NBS\_WAI]. The experiment [WBS\_EMN] will show the model uncertainty component of the ensemble SPREAD.

Figure (3.30) shows the ten days forecast statistics for the 850 hPa temperature for the experiments described above. The top-row shows the SPREAD and the RMSE scores and the bottom-row show the CRPS, for the Northern extra-tropics, the Tropics and the Southern extra-tropics (left to right). One of the striking features in Fig. (3.30) is that, in the extra-tropics, the RMSE of experiment [WBS\_ENS] (shown in cyan color) is relatively smaller than the one with assimilation cycle [WBS\_WAI] (thin blue line), and is almost the same as [NBS\_WAI]. This means that the assimilation cycle in fact negatively affects the backscatter contributions resulting in a deterioration of the forecast quality. In the Tropics, the assimilation has a positive effect resulting in a better forecast. Also, the relative contribution of model uncertainty to the SPREAD, is

<sup>2</sup>There is no data assimilation cycle; for each forecast cycle the initial ensemble is taken from [NBS\_WAI] analysis

very small in the extra-tropics but significant in the Tropics. Another striking feature is the forecast RMSE of experiment [WBS\_EMN] (the black line), which is almost the same as the RMSE of experiment [NBS\_WAI], particularly in the extra-tropics and for the first 48-72 hours. It means that tapping the model uncertainty alone is sufficient to get a good short-range forecast. This is also consistent with the GME-ENS experiments. Experiment [WBS\_EMN] also suggests that the effects of model and initial uncertainty are somewhat the same for the short-range forecasts. But for the medium and long range forecasts the initial uncertainty plays a major role, and contributions from the model uncertainty can be significant especially in the Tropics.

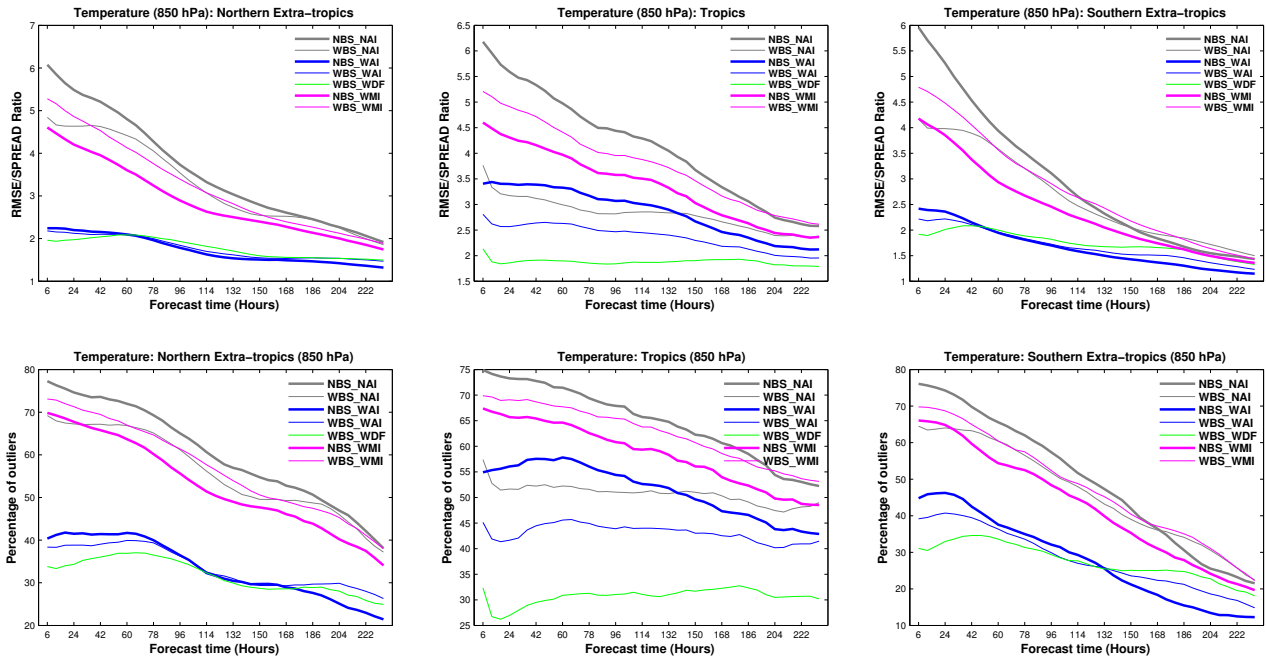


**Figure 3.31:** Ten days forecast statistics for 850 hPa temperature. Top-row: RMSE/SPREAD Ratio, Bottom-row: Percentage of outliers from ranked histogram (Tala-grand diagram); for the Northern extra-tropics, the Tropics, and the Southern extra-tropics (from left to right).

Now we will analyze the third factor: the possibility of a change in the statistical distribution due to the combined effects of assimilation, backscatter, and initial uncertainty. As mentioned in the previous subsection, one of the main tasks of the SKEB scheme is to increase the ensemble SPREAD, which in turn increases the variability of the data variable. This should in turn inflate the error covariance matrices implicitly in the data assimilation scheme. In theory, a perfect EPS should have the SPREAD equal to the RMSE (assuming a normally distributed data). In practice, the RMSE (which is the expected SPREAD) is always higher than the actual SPREAD. An increase in the SPREAD should give a better performance of the data assimilation system and also help to reduce the RMSE. However this works only if we assume the distribution is (to some extent) identical before and after the application of the SKEB scheme, so that the deviation of the mean is minimal from its actual value. If the distribution is

the same and the deviation of the mean is minimal then the smaller RMSE/SPREAD Ratio implies a smaller error hence a better result. We will show that our GME-EPS experiment results suggest that this is not the case.

Figure (3.31: Top-row) shows the RMSE/SPREAD Ratio from the GME-EPS experiments for the 850 hPa temperature. From the figure it is clear that the ratio is relatively smaller for all the experiments with the SKEB scheme except for the experiment with multiplicative inflation [WBS\_WMI]. Comparing these with Fig. (3.23: Bottom-row), we can see that in the Northern extra-tropics the experiments with backscatter such as [WBS\_NAI], have a relatively larger ensemble SPREAD compared to their counterparts (e.g., [NBS\_NAI]), but also have a larger RMSE. This suggests a larger deviation of the forecast mean from the actual mean. Also, we can see that the increase in the SPREAD in fact helps to reduce the outliers in the ranked histogram as shown in Fig. (3.31: Bottom-row). However this does not mean that the EPS becomes better since a parabolic-shaped histogram may still create a lesser number of outliers. In general, a perfect ranked histogram should be flat, which means that the probability that the observation falls within range of forecasted values by the EPS is equal for all ensemble members. Thus it is possible that the SKEB scheme creates a bias in the EPS (e.g., shape is parabolic or skewed parabolic in the ranked histogram). Combining the information from RMSE, SPREAD, their ratio, and the ranked histogram outlier plot suggests that the backscatter causes a change in the statistical distribution of the EPS forecast. If there is a change in the distribution and in the mean due to the backscatter forcing, it will be evident in the probability density plot of the EPS.

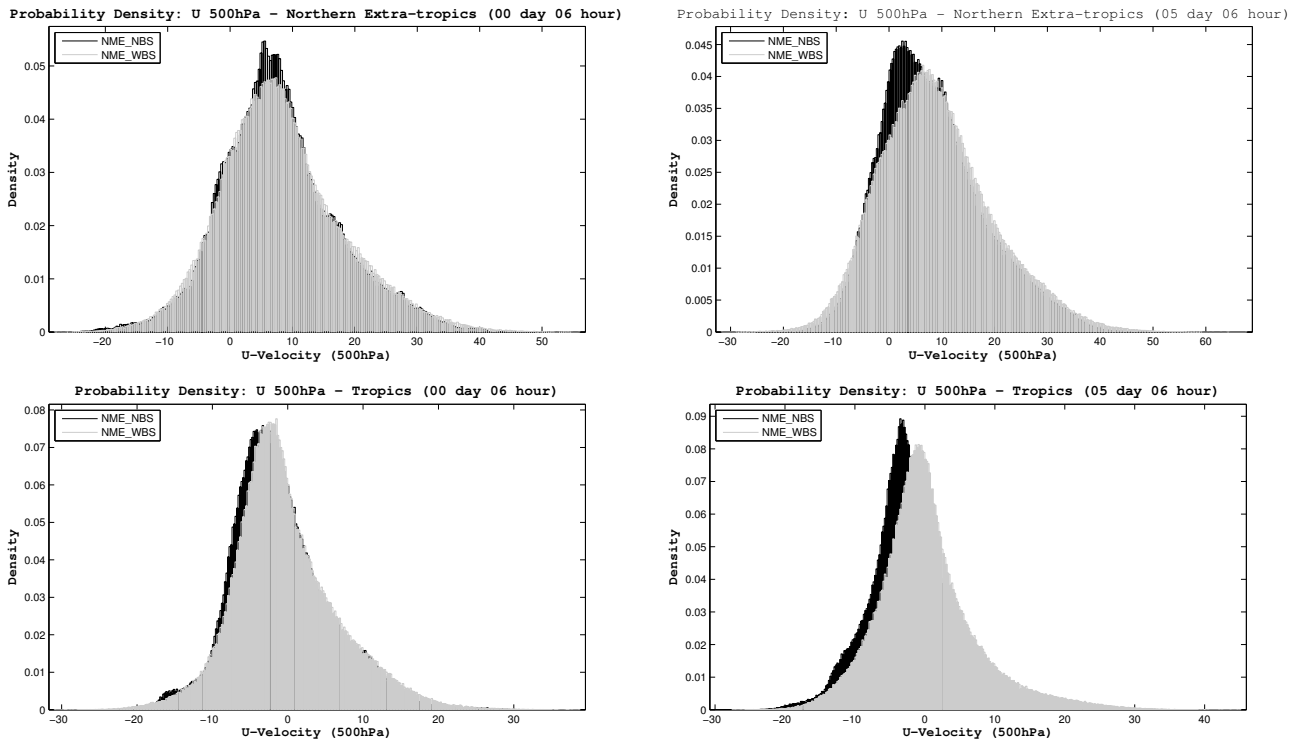


**Figure 3.32:** Probability density plot for 500 hPa U-velocity. Top-row: the Northern extra-tropics, Bottom-row: the Tropics; for the forecast times 6 hours (left), and 5<sup>th</sup> day (right).

Figure (3.32) shows the probability density plot of the 500 hPa zonal wind component for the Northern extra-tropics (top-row), and the Tropics (bottom-row), for the forecast times 6 hours (left), and 5<sup>th</sup> day (right). The black color represents [NBS\_NAI], which is the experiment with no backscatter and no inflation, and the gray color represents [WBS\_NAI], which is the experiment with the backscatter scheme and no inflation. From the figure it is evident that there is in fact a change in the statistical distribution due to the backscatter forcing. The change in the distribution and in the mean is more clearly evident in the 5<sup>th</sup> day forecast probability density plot.

In short, the main reason for the negative impact of SKEB on GME-EPS is the combined negative effects of the LETKF assimilation cycle and of the initial uncertainty on the backscatter contribution, which effectively change the statistical distribution. More details on the impact of SKEB on assimilation can be found in Chapter (4)

### 3.3.5 SKEB: Impact on the Precipitation Forecast

In this subsection we will analyze the impact of the SKEB scheme on the precipitation forecast. We will analyze the GME-ENS precipitation results followed by the GME-EPS results. The main statistics used for the precipitation analysis are CRPS, BRIER score, and ROC. Since the GME-ENS and GME-EPS spatial resolutions are relatively coarse, it is statistically meaningless to compare the global precipitation forecast with station data. On the other hand there is no standard global station data for 6 hourly or daily precipitation. Therefore the reference (i.e., observations) data used for the forecast verification is the satellite-derived 3-hourly precipitation data from the NOAA Climate Prediction Center (CPC) Morphing Technique (a.k.a CMORPH) [Joyce et al., 2004, and references therein]. Although the CMORPH data set is not the best, it will give an overall idea about the forecast performance of the EPS. The original CMORPH data has high temporal and spatial resolution. For our purpose, we have used a coarse resolution version of the data matching the GME-EPS resolution by nearest neighbor remapping.

Figure (3.33) shows the ten days CRPS (top-row) and Brier score (bottom-row) for the daily accumulated precipitation forecast for Europe (left column), and the Tropics (right column), from the GME-ENS experiments. For the deterministic forecast [NBS] (black line) the mean absolute error (MAE), which is equivalent to CRPS, used as the reference. In general, the CRPS is equal to the integral of the Brier score for all forecast thresholds. The CRPS for Europe shows that the GME-ENS experiments, except [oALL\_2a] and [oNAG\_2a], are no better than that of the deterministic forecast for the first two days, but later on GME-ENS results show better forecasts. Experiments [oALL\_2a] and [oNAG\_2a] are only slightly better than the deterministic forecast, for the first two days. Although the medium-to-long-range forecasts (in most cases, longer than three days) for precipitations are not very trustworthy, the overall CRPS shows a relative improvement due to the stochastic backscatter scheme. The CRPS for the Tropics also shows similar improvements in the forecast with the lowest CRPS (which implies best forecast) for [oALL\_2a]. In contrast to the CRPS for Europe, all the GME-ENS experiments have a better forecast skill than the deterministic forecast. It should also be noted that although experiment [nCAP\_2a], which does not account for any KE dissipation, has a better forecast skill in the Tropics, it is in fact worse in Europe.

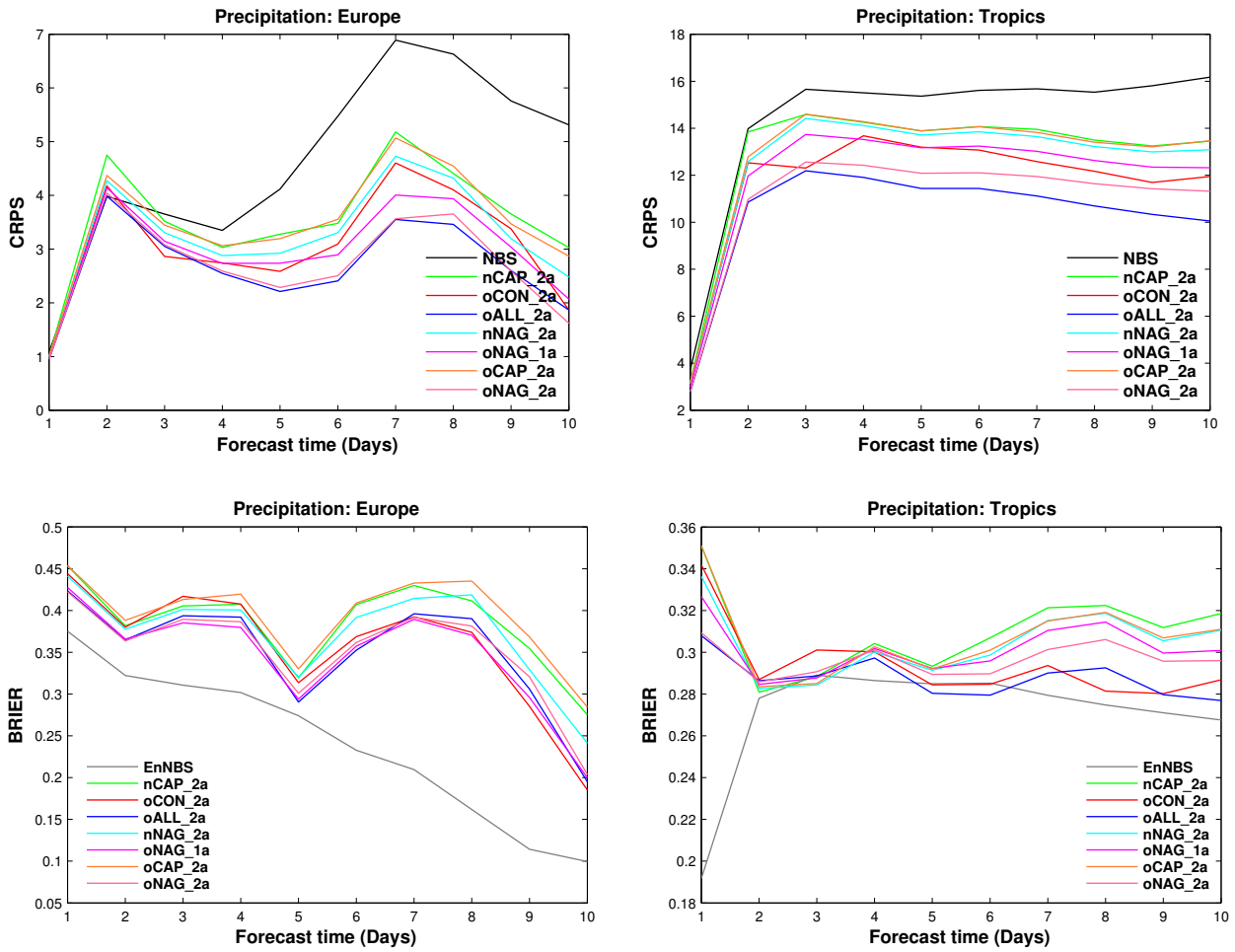


**Figure 3.33:** Precipitation statistics from the GME-ENS experiments. Top-row: CRPS for Europe (left), and the Tropics (right); Bottom-row: Brier score, 2 mm/day for Europe (left) and 5 mm/day for the Tropics (right)

Nevertheless, experiment [oALL\_2a] found to be the best in both regions, which also shows the importance of stochastic backscatter instead of random perturbations. This is in fact consistent with our earlier conclusion regarding other forecast variables such as the 850 hPa temperature.

The Brier score shown in Fig. (3.33: Bottom-row) also agrees with the CRPS in general. The employed threshold for Europe is 2 mm/day, i.e., the Brier score is calculated from the probabilities of the events where the daily accumulated precipitation is 2 mm. For the Tropics the threshold is set to 5 mm/day. Figure (3.33: Bottom-row) also includes the Brier score from the high resolution GME-EPS experiment [EnNBS] which includes the LETKF data assimilation cycle but does not include any backscatter scheme. From the figure it can be seen that among all GME-ENS experiments, [oALL\_2a] is the best (lowest score) for both Europe and the Tropics. One of the striking features in the Tropics is that the skill of GME-ENS, especially the forecast skill of [oALL\_2a], from day 2 onward is almost the same as the [EnNBS]. It should also

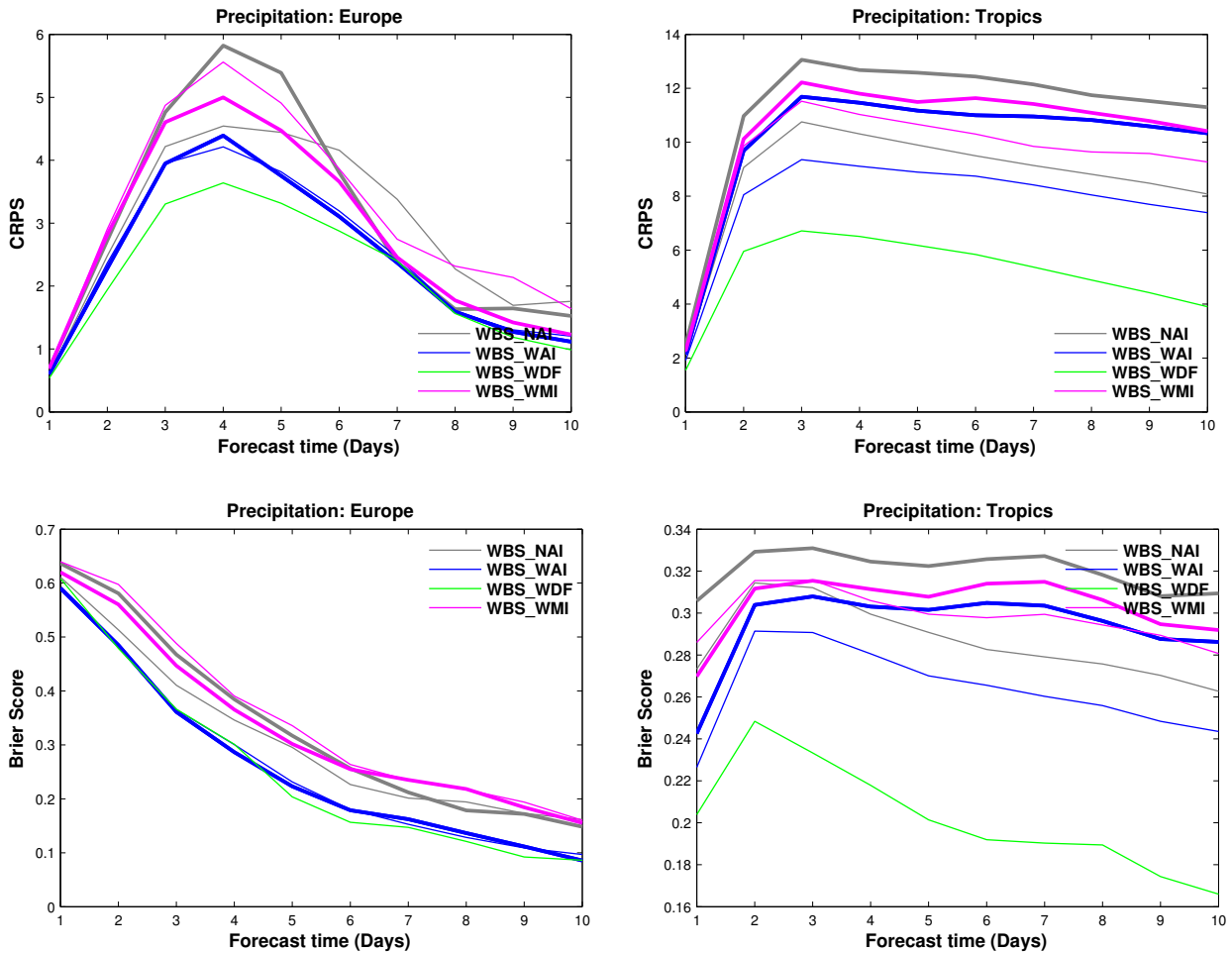


**Figure 3.34:** *Precipitation statistics from GME-EPS experiments. Top-row: CRPS for Europe (left), and the Tropics (right); Bottom-row: Brier score, 2 mm/day for Europe (left) and 5 mm/day for the Tropics (right)*

be noted that this relative improvement is solely achieved by incorporating the model uncertainty through backscatter. Thus in theory we should be able to improve the EPS precipitation forecast by incorporating model uncertainty via the SKEB scheme along with the initial uncertainty via a set of ensemble.

Now we will analyze the precipitation forecast results from the GME-EPS experiments (see Table (3.2)). Figure (3.34) shows the CRPS (top-row) and the Brier score (bottom-row) for the ten days forecast daily accumulated precipitation for Europe (left-column) and the Tropics (right-column). The Brier score thresholds are the same as those of the GME-ENS case discussed above. The first message from the CRPS and BRIER scores is that the backscatter in fact significantly improved the precipitation forecast without any additive or multiplicative inflation. This is clearly from visible from experiments [WBS\_NAI] and [NBS\_NAI] (grey lines). For the experiment with backscatter and additive inflation [WBS\_WAI] there is only a slight improvement in Europe but in the Tropics the improvement is remarkable throughout the entire fore-

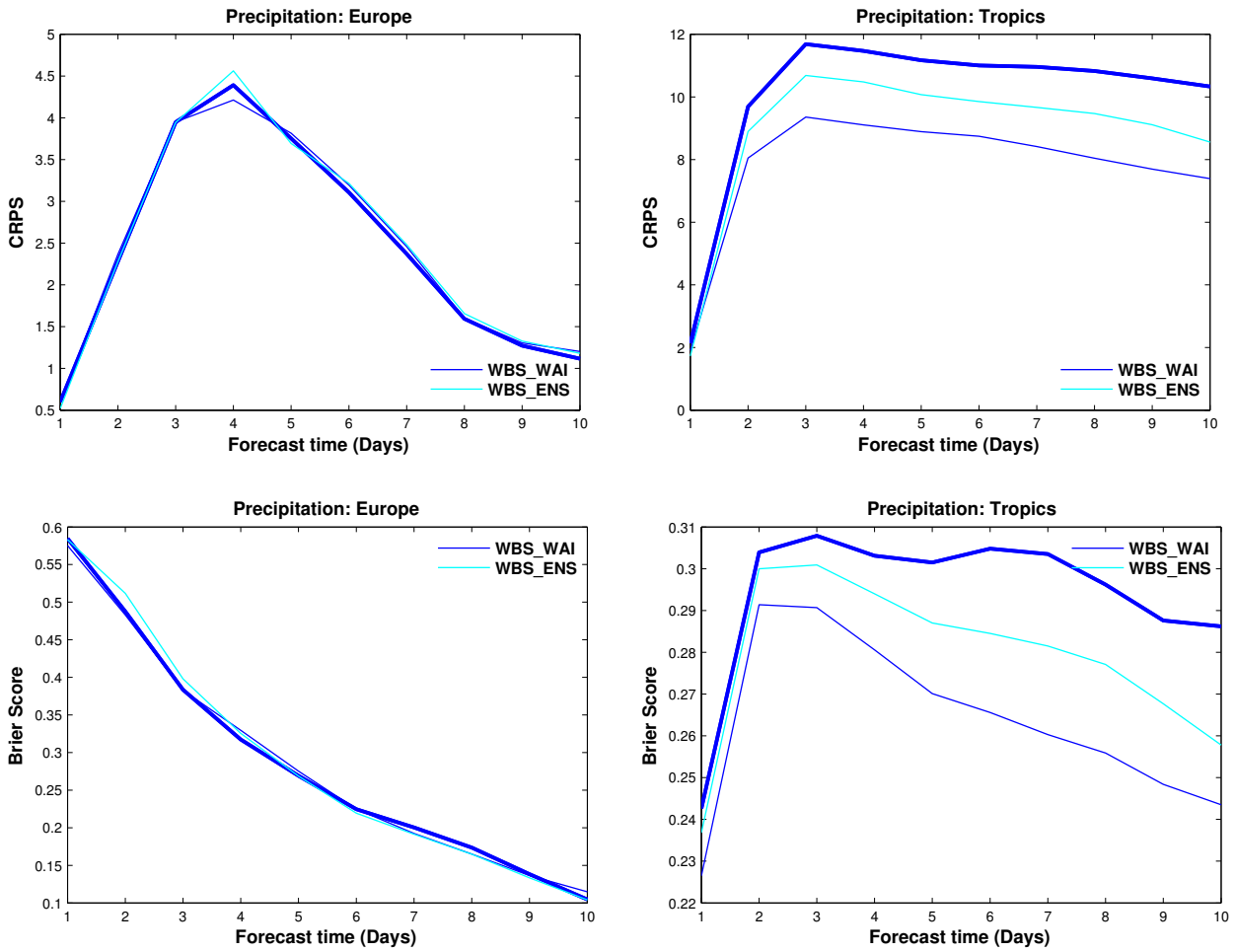


**Figure 3.35:** Precipitation statistics from the GME-EPS experiments. Top-row: CRPS for Europe (left), and the Tropics (right); Bottom-row: Brier score, 2 mm/day for Europe (left) and 5 mm/day for the Tropics (right)

cast period. On the other hand, the Brier score indicates that, for the experiment with backscatter with multiplicative inflation [WBS\_WMI], the forecast is worse for the first four-to-six days in Europe as well as for the first two days in the Tropics. The negative response of backscatter in the presence of multiplicative inflation is in agreement with our earlier conclusion regarding the same for temperature and geopotential height.

We have also analyzed the precipitation forecast from [WBS\_ENS], which is the GME-EPS experiment where there is no assimilation cycle, i.e., each forecast cycle is initialized with the ensemble from [NBS\_NAI]. As mentioned in the previous subsection, this experiment is designed to study the impact of the LETKF assimilation cycle on the backscatter. Figure (3.35) shows the CRPS and the Brier score for Europe. From the scores, it can be seen that there is no big difference in the forecast skill for Europe. Compared to the experiment without backscatter [NBS\_WAI] it is slightly better on day one. On the other hand, in the Tropics we can see a clear improvement (i.e., lower score). This clearly indicates the positive effects incorporating the model

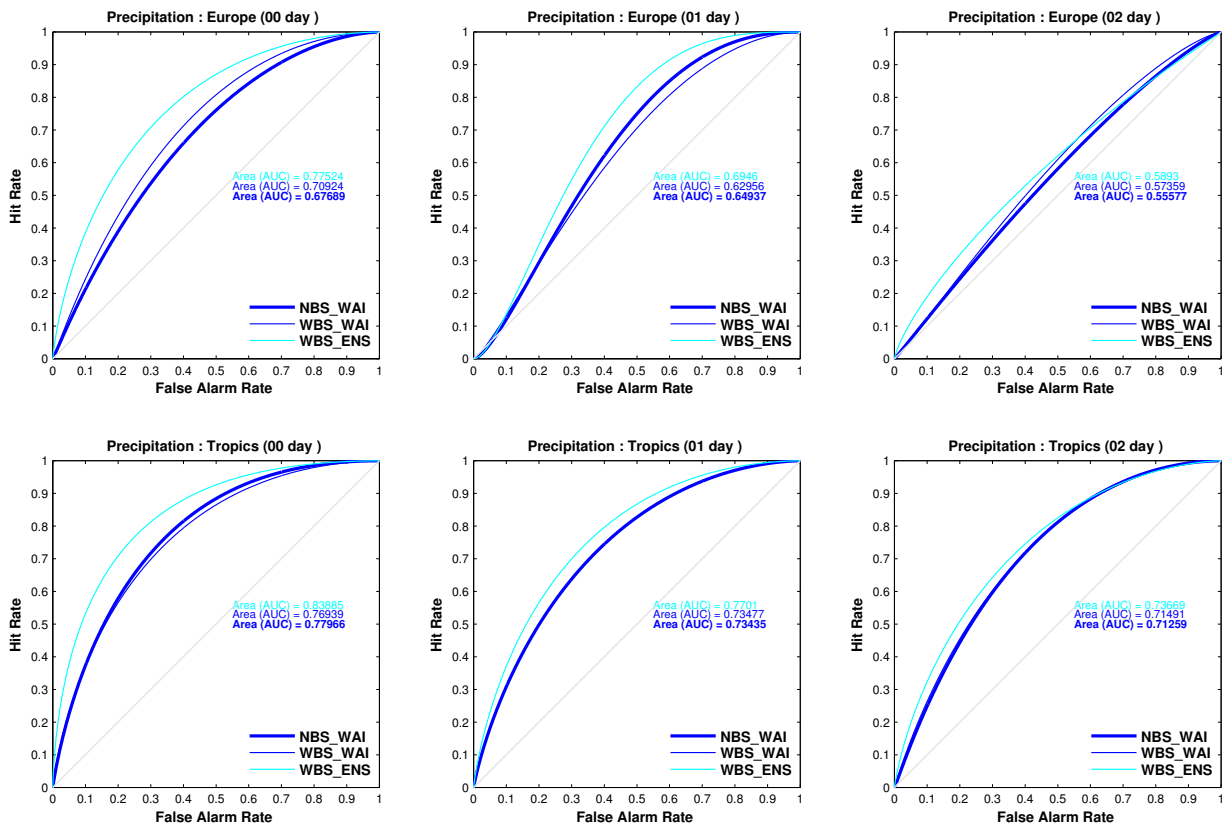


**Figure 3.36:** ROC statistics from the GME-EPS experiments. Top-row: Europe (with threshold=2 mm/day); Bottom-row: the Tropics (with threshold=5 mm/day); for the first three forecast days (left to right)

uncertainty along with initial uncertainty in the precipitation forecast. We can also

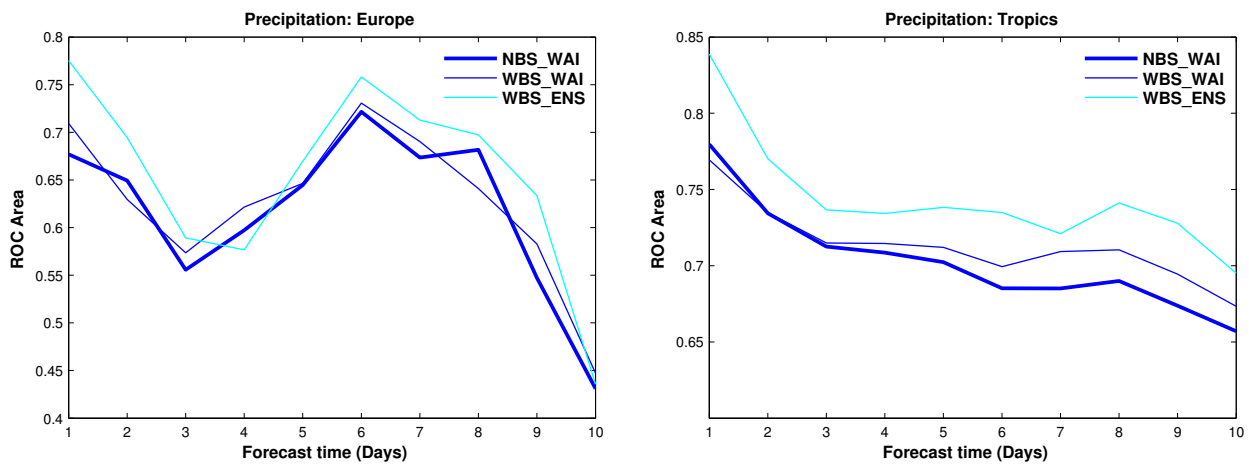


**Figure 3.37:** ROC Area from GME-EPS experiments. Left panel: Europe (for threshold 2 mm/day); Right panel: the Tropics (for threshold 5 mm/day)

come to the same conclusion from the ROC shown in Fig. (3.36): the top-row shows the ROC for precipitation over Europe for the first 3-day forecast, with a threshold of 2 *mm/day*; bottom-row show the same for the Tropics with a threshold set at 5 *mm/day*. One of the important messages from the figure is that the precipitation forecast for Europe is not trustable from 2<sup>nd</sup> day onwards since the false alarm rate is higher than the hit-rate. On day one, we can see the clear positive impact due to the SKEB scheme. Also, experiment [WBS\_NAI] shows worse results from the 2<sup>nd</sup> day onwards compared to [NBS\_WAI], which indicates that the assimilation in fact negatively affects the backscatter contribution. On the contrary, the precipitation forecast over the Tropics is relatively trustable up to three days, and we can see there is also a significant positive impact of the backscatter. On the other hand, the backscatter experiment with the assimilation cycle [WBS\_NAI] shows no improvement, which again points to the negative effects of LETKF assimilation on the backscatter contribution. The ROC area shown in Fig. (3.37) summarizes the superior performance of the SKEB scheme on the precipitation forecast: the larger area indicates better forecast quality, which is clearly visible in the Tropics.

### 3.3.6 Conclusion: Impact of SKEB on the GME-EPS Forecast

The following are the main conclusions concerning the impact of SKEB on the GME-EPS forecasts.

1. Overall the SKEB scheme has a negative impact on the forecast for most of the prognostic variables especially on the extra-tropics. However, some variables such as the temperature and the specific humidity, show a significant improvement in the Tropics as well.
2. Almost all of the GME-EPS experiments with the SKEB scheme except [WBS\_WMI], which is the experiment with the backscatter with multiplicative inflation, show an increase in the ensemble SPREAD
3. All inflation mechanisms in the LETKF assimilation have negative effects on the backscatter contribution, thereby deteriorating the forecast quality
4. The main cause of the negative impact of the backscatter mechanism on GME-EPS is the combined effect of the LETKF assimilation and initial uncertainty, which effectively changes the probability density distribution
5. Incorporating the model uncertainty alone (i.e. even without initial set of ensemble) can produce good short-range forecasts, which show the positive impact of the backscatter scheme on the forecast without the assimilation system.
6. The backscatter has a significant positive effect on the precipitation forecast, especially in the Tropics

# Stochastic Backscatter in the LETKF

## 4.1 Covariance Inflation in LETKF

As the name implies, one of the distinct features of the Local Ensemble Transform Kalman Filter (LETKF) is its ability to perform local analysis at every grid-point spanned in the ensemble sub-space, and use only the local observations within the prescribed distance. The weights of the observations approaches zero at the bounds of the localization volume. In the GME-EPS we follow the LETKF algorithm of Hunt et al. [2007]. The basic theoretical formulation of the LETKF can be found in section (2.2).

Unlike most ensemble Kalman filters (EnKFs), the LETKF does not explicitly calculate either the background error covariance or the Kalman gain matrix. Instead, the LETKF directly obtains the analysis (in a broad sense, the LETKF actually calculate the analysis increments.). For the purpose of presentation, here we repeat the LETKF analysis equations from section (2.2):

$$\bar{\boldsymbol{\theta}}_k^a = \bar{\boldsymbol{\theta}}_k^b + \boldsymbol{\Theta}_k \mathbf{w}^a \quad (4.1)$$

where,

$$\mathbf{w}^a = \tilde{\mathbf{P}}_k^a (\boldsymbol{\Psi}_k)^T \mathbf{R}^{-1} (\boldsymbol{\psi}_k - \bar{\boldsymbol{\psi}}_k) \quad (4.2)$$

$$\tilde{\mathbf{P}}_k^a = \left[ (N-1) \mathbf{I} + (\boldsymbol{\Psi}_k)^T \mathbf{R}^{-1} \boldsymbol{\Psi}_k \right]^T \quad (4.3)$$

Here the analysis error covariance  $\tilde{\mathbf{P}}_k^a$  is often underestimated due to finite ensemble size, sampling errors, errors in representing the model error, and nonlinearities (for example, associated with observation operators). This underestimation of the covariance matrix causes filter divergence, i.e., the filter systematically favor the observations over the model in the assimilation cycle, which eventually generates a sub-optimal analysis ensemble [Hamill, 2006].

In order to compensate for the underestimation of the covariance matrix, a covariance inflation method was proposed, independently by Anderson and Anderson [1999] in Meteorology, and Guivant and Nebot [2001] in control theory (specifically within the Simultaneous Localization And Map building (SLAM) framework) engi-

neering. In general, covariance inflation is an ad-hoc procedure of adding a positive semi-definite matrix to a covariance matrix [Julier, 2003]. Anderson and Anderson [1999] proposed a multiplicative variance inflation scheme, where the background error covariance in EnKF was multiplied by a small number greater than unity. Guivant and Nebot [2001] proposed covariance inflation techniques to de-correlate the off-diagonal elements of the covariance matrix. The latter approach is based on the intuition that most of the computational and storage costs arise from the maintenance and correlation of cross-correlation terms. Since it has been shown that the correlation terms cannot be simply set to zero [Castellanos et al., 1997], covariances must be increased by a sufficient amount to compensate for the neglected correlation, which eventually leads to the idea of covariance inflation. One of the main advantages of de-correlation through covariance inflation is that it can significantly reduce the computational and storage costs. However, it has been shown that the covariance inflation also raises the risk that the covariance increases without bounds thus degrading the performance of the filter. In general, de-correlation through additive inflation is equivalent to the ‘‘Schmidt-Kalman’’ filter [Julier, 2003].

As mentioned above, in all inflation methods, a positive semi-definite matrix is added to the state covariance matrix. Several strategies to choose the positive semidefinite matrix for the covariance inflation in Kalman filters in the context of data assimilation have been proposed. However, there is no systematic way of doing so, and the procedure is considered as a part of model tuning [e.g., Hunt et al., 2007]. Most common strategies are 1) Additive inflation, 2) Multiplicative inflation, and 3) Hybrid methods. 1) In the so called *additive inflation* (although the name has nothing to do with the concept of additive inflation), a small multiple of the identity matrix is added to the covariance matrix during each assimilation cycle, i.e, the covariance matrix given by Eq. (4.3) can be re-written as:

$$\tilde{\mathbb{P}}_k^a = \tilde{\mathbf{P}}_k^a + \gamma \mathbf{I} \quad (4.4)$$

where  $\gamma$  is a real random vector). In *multiplicative inflation*, the covariance is multiplied by a small number, which is greater than one, being equivalent to adding a fraction of the covariance matrix to itself, given by,

$$\tilde{\mathbb{P}}_k^a = \tilde{\mathbf{P}}_k^a + \rho \tilde{\mathbf{P}}_k^a \quad (4.5)$$

where  $\rho$  is a small number (say 0.2). In practice, multiplicative inflation can be easily achieved by multiplying the factor  $\sqrt{1 + \rho}$  to the background deviations  $\Theta_{k,n}$ , and  $\Psi_{k,n}$  [see Chapter (2)]. In the *hybrid approach*, a fraction of the 3D VAR  $\mathbf{B}$  matrix is added to the covariance matrix. However this can only be performed in the model space since  $\mathbf{B}$  cannot be formulated in the ensemble space. In the following subsection we will discuss more on the covariance inflation procedure specific to the GME-EPS implementation of LETKF and about the ways in which the flow-dependent model error is incorporated into the covariance inflation process.

### 4.1.1 Incorporating Flow-Dependent Model Errors in LETKF

As described in the previous subsection, one of the major factors which contributes to the underestimation of the covariance is the inappropriate representation of model error. Conventional additive inflation using random vectors may in fact add more noise to the covariance matrix and destroy its correlation structure. Therefore one of the desired properties of the inflating matrix is that it should be flow-dependent, i.e., it should reflect the dynamical and correlation features of the model. Another desired property of the inflation matrix is that the spatial and temporal correlation structure should not strongly vary with the forecast time as otherwise it may create biases. This in fact cannot be fully achieved by Eq. (4.4). On the other hand, the multiplicative inflation given by Eq. (4.5) has the flow-dependency nature but it is not truly stochastic and completely depends on the analysis covariance matrix (rather than on the background), which anyway may not always reflect the true dynamical features of the model. Thus in order to meet the desired properties, the GME-EPS implementation of LETKF uses a modified version of the hybrid approach for additive inflation, i.e., instead of adding a constant fraction of the  $\mathbf{B}$  matrix to the covariance matrix, a stochastically perturbed  $\sqrt{\mathbf{B}}$  matrix is used to inflate the background ensemble, given by:

$$\boldsymbol{\theta}_{k,n} = \boldsymbol{\theta}_{k,n} + \sqrt{\mathbf{B}} \mathbb{N}(0, \sqrt{\sigma}) \quad (4.6)$$

where  $\mathbb{N}(0, \sqrt{\sigma})$  is the normally distributed random vector with mean zero and variance  $\sigma$ . Although the hybrid additive inflation approach produces better results than Eq. (4.4) and Eq. (4.5), it still has some limitations. One of the main limitations is that it is highly depended on the 3D VAR  $\mathbf{B}$  matrix, which is derived using the NMC method and is therefore not truly flow-dependent. Another limitation is that it cannot represent the model errors effectively, in particular the model errors due to KE dissipations.

In theory, it is possible to overcome the aforementioned limitations of the inflation scheme by using a SKEB scheme. We have used a stochastic KE backscatter (SKEB) scheme as an alternative to the above mentioned inflation schemes in LETKF. The experimental setup can be expressed in terms of Eq. (2.27) where the initial background ensemble at the next analysis time is generated by integrating the model forward with the backscatter scheme:

$$\boldsymbol{\theta}_k^b = \mathbf{f}_{\text{SKEB}}(\boldsymbol{\theta}_{k-1,n}^a + \boldsymbol{\epsilon}) \quad (4.7)$$

where  $\mathbf{f}_{\text{SKEB}}$  is the GME integration with the backscatter scheme, and  $\boldsymbol{\epsilon}$  is the additional model error or inflation using 3D VAR  $\mathbf{B}$  matrix which is optional (ON/OFF).

In Chapter (3), we have shown that the SKEB scheme has a positive impact on the ensemble spread, which implies inflation of covariance. Although the backscatter has a significant positive impact on the forecast quality of the GME model (in the GME-ENS experiments), the combined effect of the initial uncertainty and the LETKF assimilation has a negative impact on the backscatter contributions, which results in a deterioration of the forecast quality in GME-EPS. In the following subsections, we will analyze the impact of the SKEB scheme on the LETKF analysis.

## 4.2 Impact of the SKEB Scheme on the LETKF Assimilation

A brief summary of all the GME-EPS sensitivity experiments is given in Table (3.2). Altogether there are seven assimilation variables namely: 1) temperature, 2) U-velocity, 3) V-velocity, 4) specific humidity, 5) specific cloud-water content, 6) specific cloud-ice content, and 7) surface Pressure. First we will describe in details the LETKF analysis and illustrate the first-guess RMSE and SPREAD scores of 850 hPa temperature, and 500 hPa zonal wind fields, followed by other assimilated variables. The RMSE and SPREAD scores are calculated within the data assimilation cycles and not within a free forecast. In principle the statistics should converge after a few days, otherwise the assimilation will be unreliable (too less spread in general). Also, the initial spin-up/spin-down stems from the initial start of the system. Thus we only started free forecasts after a few days (or few assimilation cycle).

Figure (4.1) shows the statistics for the 850 hPa temperature: the top-row shows the LETKF analysis RMSE (solid lines) and SPREAD (dashed lines), the middle-row gives a comparison between the RMSE of the LETKF first-guess (solid lines) and the LETKF analysis (dashed lines) and the bottom-row gives a comparison between the ensemble SPREAD of the LETKF first-guess (solid-lines) and the LETKF analysis (dashed-lines).

The most noticeable feature in Fig. (4.1: Top-row) is that, the ensemble SPREAD decreases exponentially, especially for the experiment [NBS\_NAI] which does not incorporate either the SKEB scheme or any inflation scheme. This decrease of SPREAD is apparent in all the three geographical regions. The rapid decrease of SPREAD is due to the fact that in most cases the observation error covariances are much smaller than the model errors, causing the LETKF assimilation system to force the forecast towards the observations very quickly. However, this creates a systematic underestimation of the error covariance in the subsequent assimilation cycle and causes the filter divergence as mentioned in the previous subsection. The RMSE of the analysis is comparable among all the experiments for the first few cycles, but it later diverges quite rapidly for the experiments with backscatter. Although the experiment [WBS\_NAI] shows a relative increase in the spread in the extra-tropics compared to [NBS\_NAI], the corresponding RMSE is also quite high.

Among the experiments with inflation schemes, multiplicative inflation has the worst performance and is distinctive in the sense that the ensemble SPREAD of [WBS\_WMI] is relatively smaller than [NBS\_WMI] in all the three regions. In other words, the backscatter forcing and the multiplicative forcing are acting opposite to each other. One possible reason for this counteractive effect is that the multiplicative inflation is unidirectional, i.e., since the inflation factor  $\rho$  in Eq. (4.5) is not stochastic, the inflation which is applied to the background deviations  $\Theta_{k,n}$  and  $\Psi_{k,n}$  will both increase the SPREAD only in the same direction. Since the backscatter forcing is stochastic, this effectively reduces the probability of increase in the SPREAD. On the other hand, [WBS\_WAI], which is the experiment with additive inflation and backscatter, has a relatively larger SPREAD compared to its counter-part [NBS\_NAI]. This increase in SPREAD in fact supports our earlier hypothesis regarding the counteracting effects, since the additive inflation given by Eq. (4.6) has a stochastic component. In summary, it is clear that the SKEB scheme has a negative impact on the LETKF

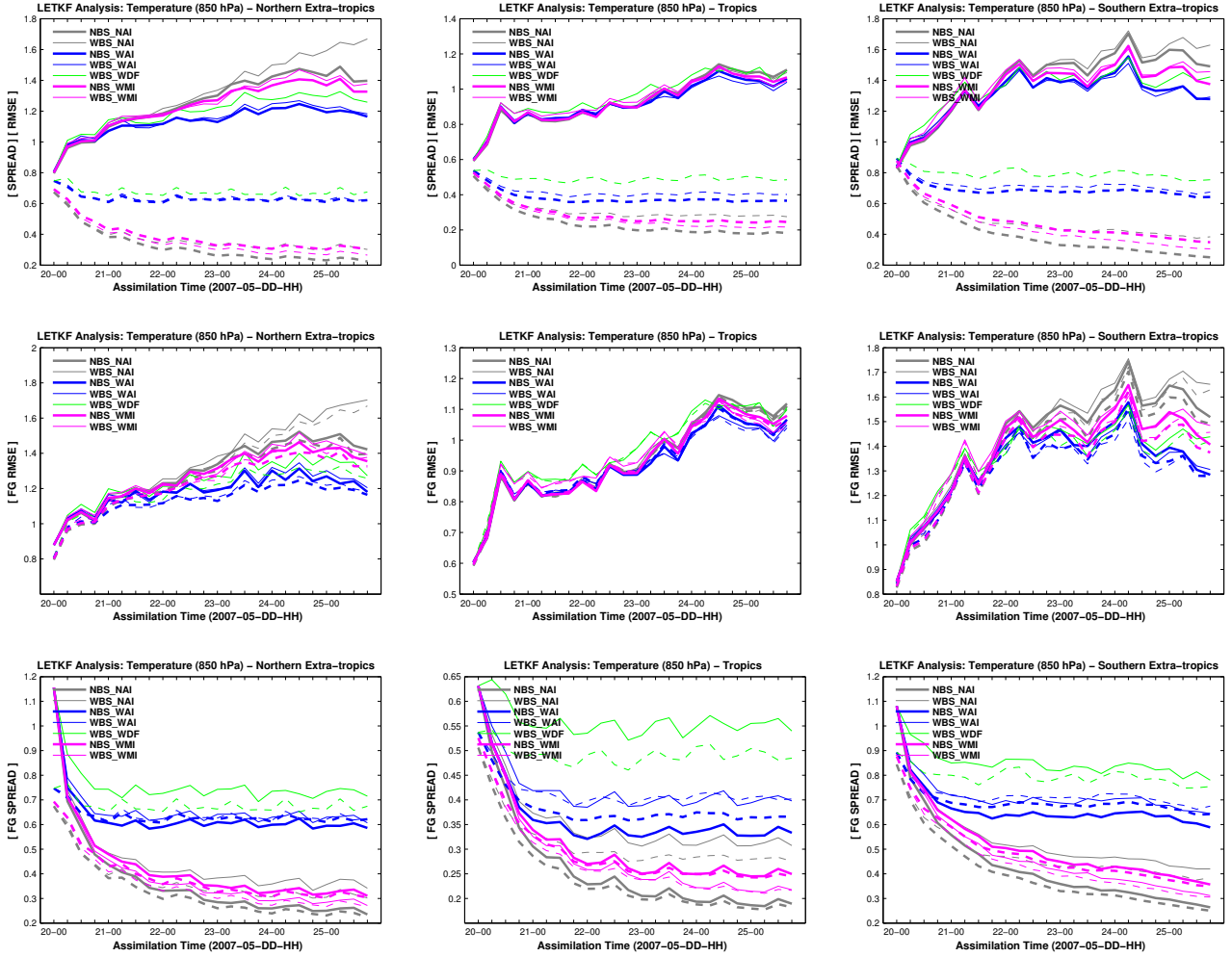


**Figure 4.1:** *LETKF analysis and the First-Guess statistics for 850 hPa temperature, for the Northern extra-tropics, the Tropics, and the Southern extra-tropics (left to right). Top-row: RMSE (solid), and SPREAD (dashed) from the LETKF analysis; Middle-row: First-guess RMSE (solid), and analysis RMSE (dashed); Bottom-row: First-guess SPREAD (solid), and analysis SPREAD (dashed)*

analysis especially on the extra-tropics. In the Tropics, although there is a slightly positive improvement in the analysis, it is not significant. In order to study the causes of the negative impact of the backscatter on the analysis, we will first compare the LETKF first-guess statistics with the corresponding LETKF analysis.

In doing so, it becomes very clear that the backscatter forcing has a large positive effect on the SPREAD. In the Tropics, the SPREAD of [WBS\_NAI] is comparable to that of [NBS\_NAI], which indicates that the backscatter was able to generate a SPREAD comparable to the additive inflation scheme. In general, the first-guess SPREAD is always larger than the analysis. However, [NBS\_WAI], which is the experiment with additive inflation and no backscatter, shows relatively higher SPREAD for the analysis than the first-guess. The main reason for this surprising feature is the additive inflation mechanism in LETKF. In this experiment, the ensemble members are inflated after the

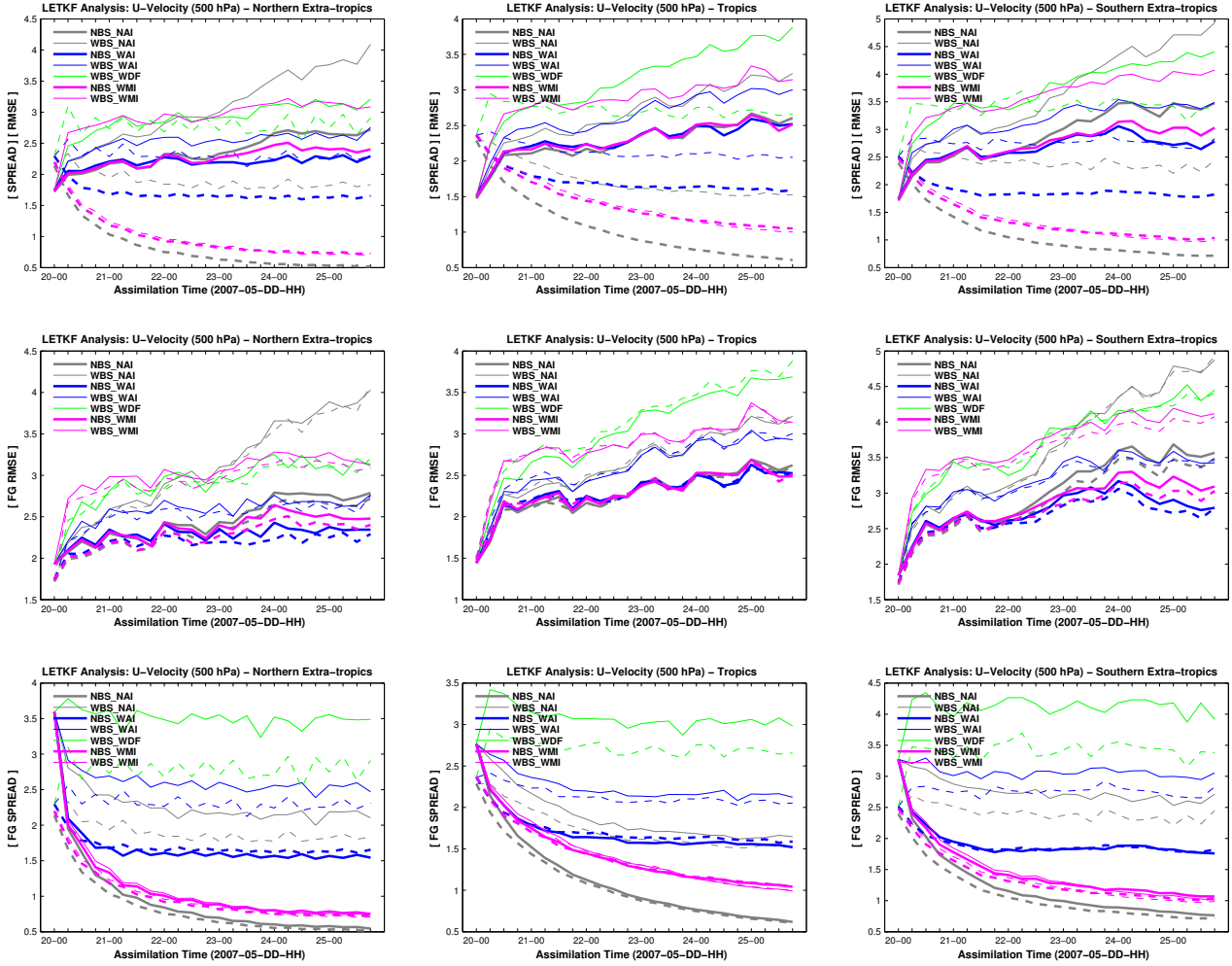


**Figure 4.2:** LETKF analysis and First-Guess statistics for 500 hPa zonal wind, for Northern extra-tropics, the Tropics, and the Southern extra-tropics (left to right). Top-row: RMSE (solid), and SPREAD (dashed) from the LETKF analysis; Middle-row: Comparison of First-guess RMSE (solid), and analysis RMSE (dashed); Bottom-row: Comparison of First-guess SPREAD (solid), and analysis SPREAD (dashed)

LETKF analysis (which helps to increase the first-guess (FG) SPREAD in subsequent cycles). Overall there is no large difference between the RMSE of the first-guess and of the analysis for the first few assimilation cycles. Later, the difference is more visible especially in the extra-tropics.

The RMSE and SPREAD statistics for the 500 hPa zonal wind are shown in Fig. (4.2). The overall conclusion is not different from that of the temperature analysis shown in Fig. (4.1). Since the backscatter forcing directly acts on the wind components, we can see a substantial increase in the SPREAD for all the experiments with backscatter in all three regions. At the same time, the RMSE is also very large, as a consequence of the negative impact of the backscatter on the ensemble SPREAD. One possible reason for this negative impact is due to the large initial ensemble SPREAD. In most assimilation systems, the initial first-guess ensemble SPREAD is usually kept

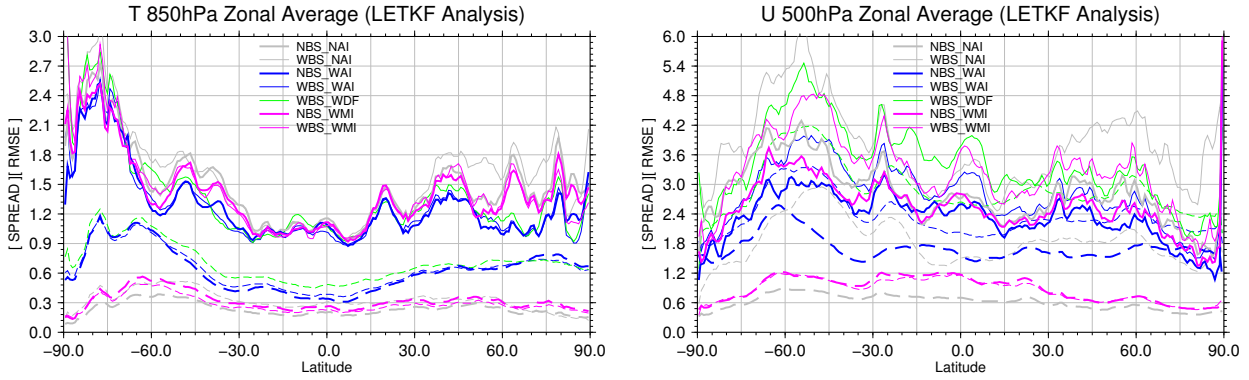


**Figure 4.3:** Zonal RMSE (solid) and SPREAD (dashed) from the LETKF analysis and the first-guess, for 850 hPa temperature (left), and 500 hPa zonal wind (right).

substantially high in order to compensate the sudden decrease of SPREAD due to the assimilation cycle. Comparing the first-guess ensemble SPREAD of experiments [NBS.NAI] and [WBS.NAI], it is very clear that the SPREAD decreases at much lower rate for the experiment with backscatter. It is therefore very likely that the backscatter gives a better result if we start from a lower initial first-guess SPREAD - a case study, which we leave for future work.

The zonal average RMSE statistics for the 850 hPa temperature and the 500 hPa zonal wind are shown in Fig. (4.3). For all the experiments with backscatter, except that with multiplicative inflation, the statistics for the wind show relatively higher SPREAD especially in the extra-tropics, with the highest SPREAD in the Southern extra-tropics. For the temperature field, although the SPREAD is higher for the experiments with the backscatter scheme, the statistics are relatively small compared to the wind. Also the SPREAD is lowest in the Northern extra-tropics, for the temperature. However, the experiment with multiplicative inflation and backscatter show relatively lower SPREAD for both temperature and wind fields. The reason is the same one we described previously, i.e, the unidirectional multiplicative inflation and the bi-directional backscatter forcings are acting opposite.

Figure (4.4) and (4.5) show the spatial patterns of the RMSE and SPREAD distribution of the temperature and wind fields from the LETKF analysis, for experiments [NBS.NAI] and [WBS.NAI]. For the temperature field, the spatial pattern shows that the ensemble SPREAD is not uniformly distributed over the globe. In fact it shows a bias in the Southern extra-tropics. In the Tropics and the Northern extra-tropics, we can see patterns where the SPREAD is very small. This is clearly visible also in the RMSE/SPREAD Ratio pattern of the temperature field. Also, the RMSE patterns of temperature does not show any apparent difference. There we assume that the higher errors (RMSE) of [WBS.NAI] are due to the anomalous values of a few grid-points. On the other hand the zonal wind RMSE pattern shows large differences in the extra-tropics, with higher RMSE values for [WBS.NAI]. However, the RMSE/SPREAD ratio pattern for the same variable is close to unity, which indicates that although the actual SPREAD is high enough to match the RMSE (expected SPREAD), there is an ap-

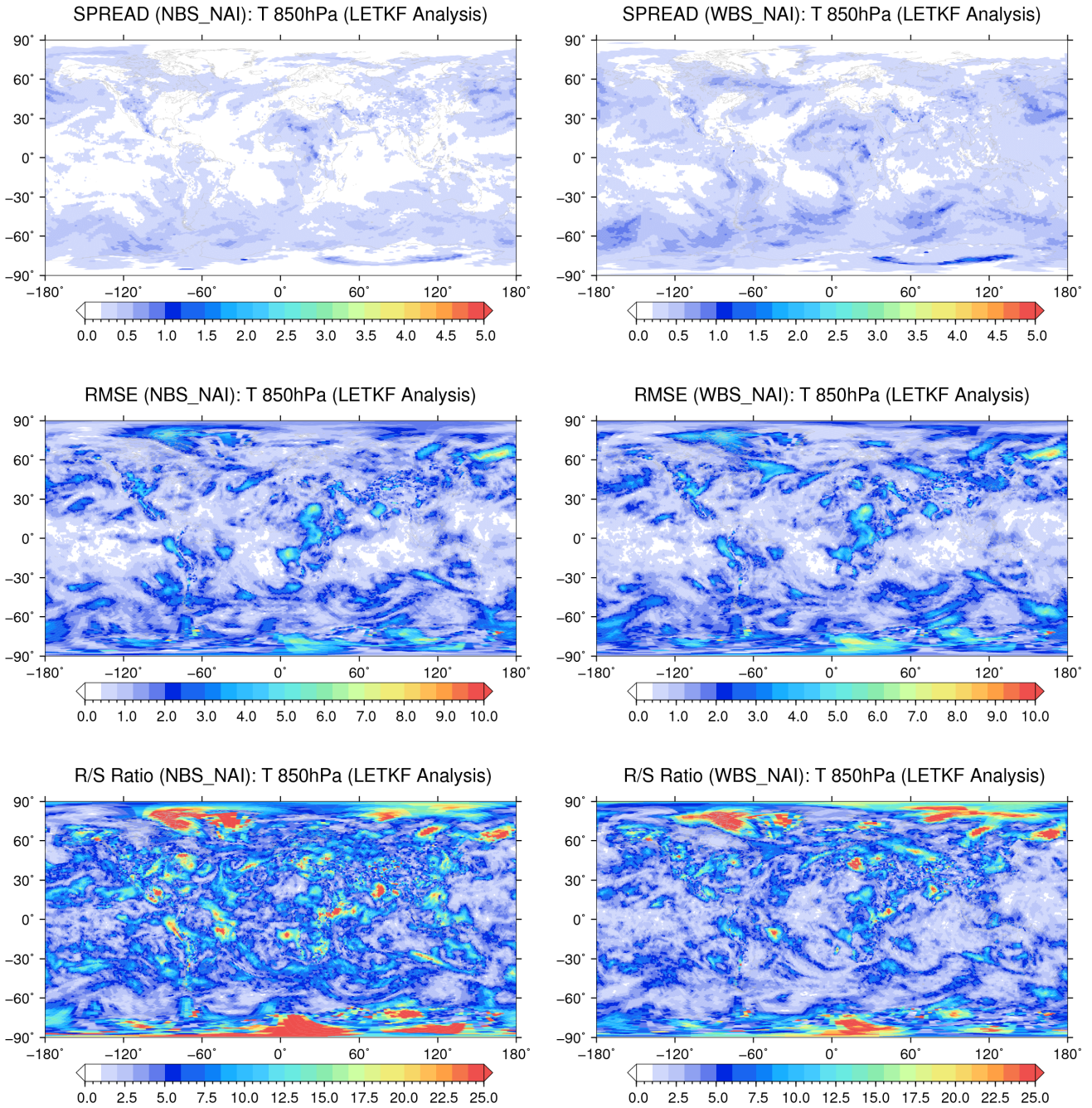


**Figure 4.4:** *LETKF analysis SPREAD and RMSE spatial distribution for 850 hPa temperature, from the experiments [NBS\_NAI] (left) and [WBS\_NAI] (right). Top-row: SPREAD; Middle-row: RMSE; Bottom-row: RMSE/SPREAD Ratio.*

parent difference in the ensemble mean values between experiments with and without backscatter. This explains the overall negative impact of the backscatter scheme. We will discuss more details regarding the same in a later part of this section.

So far we have only looked at the statistics of temperature and zonal wind at a certain pressure level. Figure (4.6: top-row) shows the vertical CRPS, RMSE and

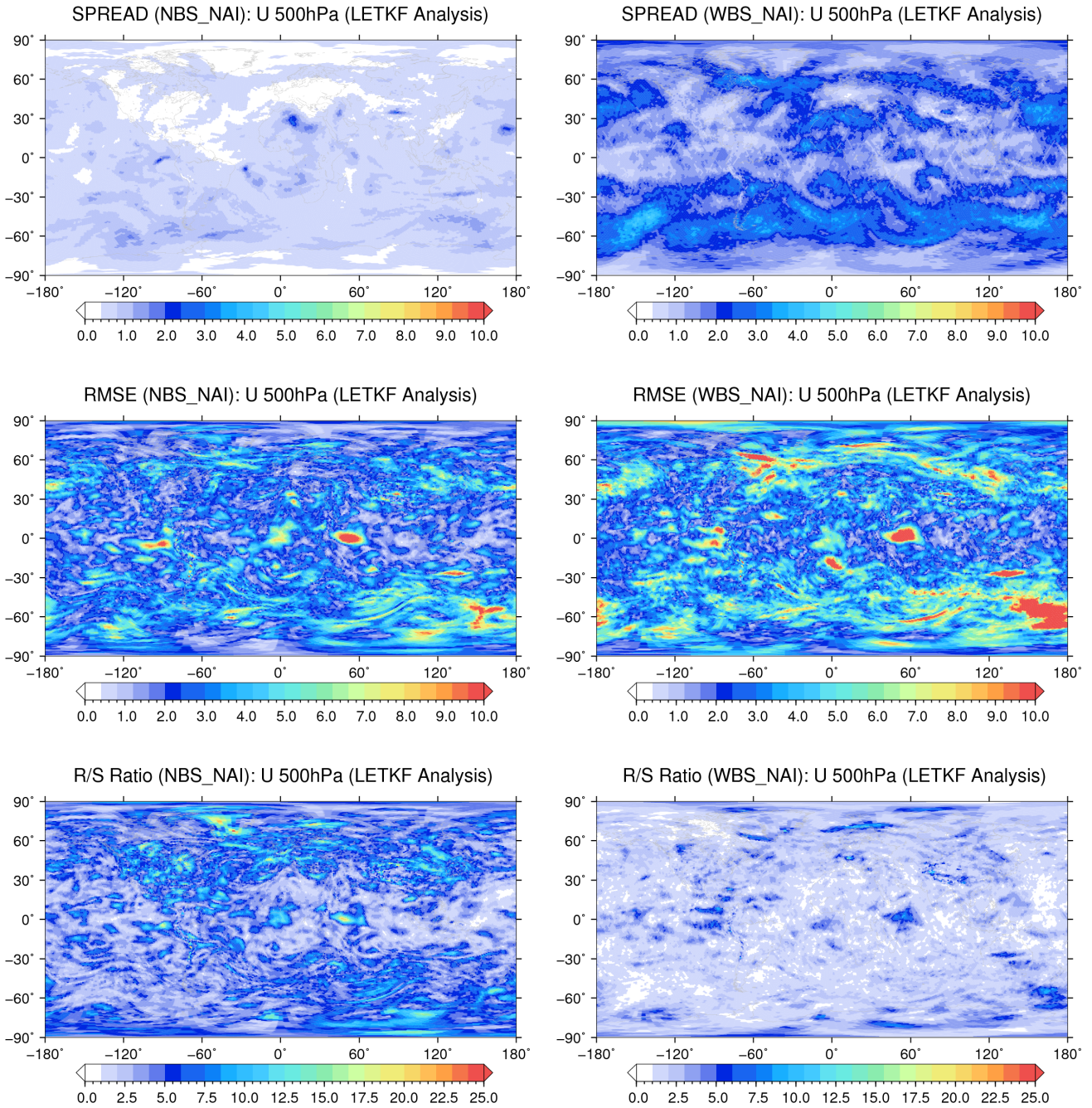


**Figure 4.5:** *LETKF analysis SPREAD and RMSE spatial distribution for 500 hPa temperature, from the experiments [NBS\_NAI] (left) and [WBS\_NAI] (right). Top-row: SPREAD; Middle-row: RMSE; Bottom-row: RMSE/SPREAD Ratio.*

SPREAD profiles for temperature. For the Northern extra-tropics, [WBS\_NAI], the experiment with SKEB scheme and no inflation, shows a higher CRPS which indicates that the negative impact of backscatter is effective throughout the entire vertical extent. For the Tropics and the Southern extra-tropics the CRPS shows mixed results. In the Tropics, [WBS\_NAI], shows significant improvement in the upper levels, although the improvements at the lower levels are not very significant. The Southern extra-tropics

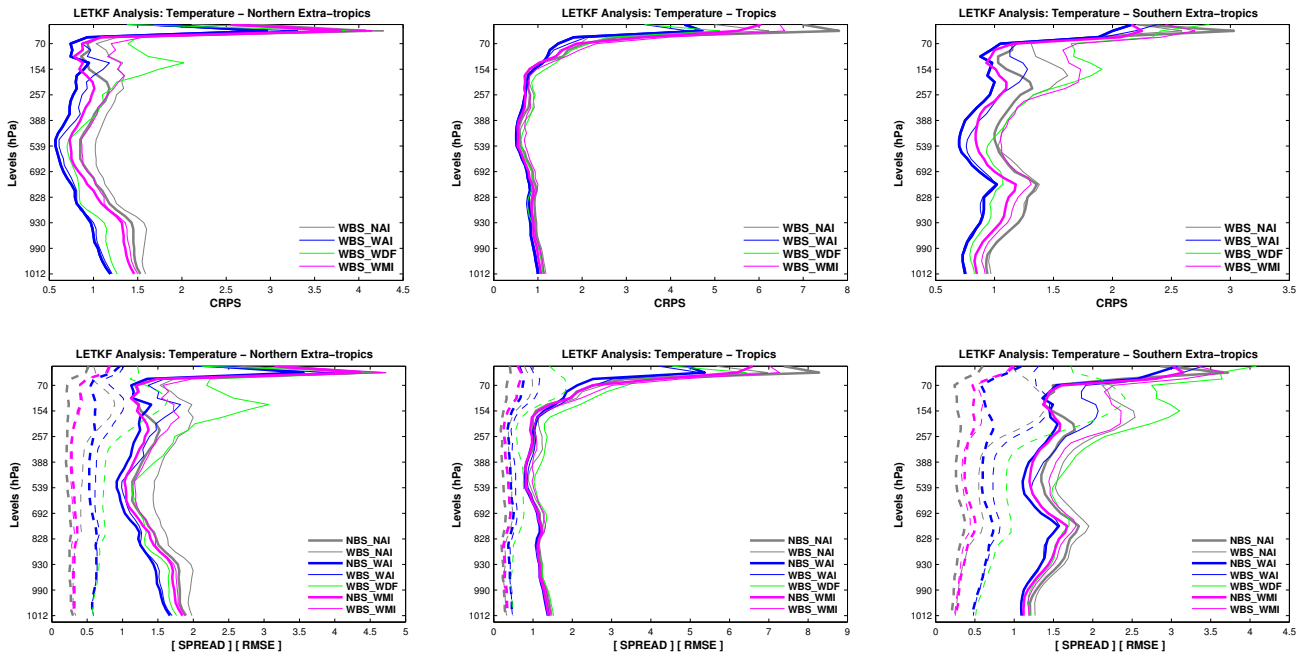


**Figure 4.6:** Vertical profiles for the 850 hPa temperature. CRPS (top-row) and RMSE (bottom-row), for the Northern extra-tropics, the Tropics, and the Southern extra-tropics (left to right).

shows no improvements at lower levels while the upper level results are worse. For the experiment with additive inflation and backscatter [WBS\_WAI], the results for the extra-tropics show no improvements at lower levels and a negative impact at the upper levels. In the Tropics the results are slightly better. The vertical profiles of RMSE and SPREAD shown in Fig. (4.6: bottom-row) also generally agree with the above conclusions gained from the CRPS profiles.

The vertical statistics of the zonal wind are shown in Fig. (4.6). The statistics show that the experiments with backscatter have large negative impacts on the analysis at all levels, for all the three regions. Possible reasons for this negative impacts are discussed in section (4.2). Compared to the statistics for temperature one noticeable difference is the magnitude of the SPREAD at higher levels (above 850 hPa). It is very likely that this “over spread”, which is due to the higher backscatter forcing, contributed to the higher errors (RMSE, CRPS).

The RMSE statistics of specific humidity, specific cloud-water content, and specific cloud-ice content are shown in Fig. (4.8). In the case of specific humidity, all experiments with backscatter show a slight improvement in the Tropics, limited at lower levels. In the extra-tropics, the backscatter has a significant negative impact on the analysis. The RMSE of specific cloud-water content, shows significant improvement in all the three regions, for experiments [WBS\_NAI] and [WBS\_WAI]. On the contrary the specific cloud-ice RMSE shows worse results with backscatter, although the ensemble spread is relatively high.

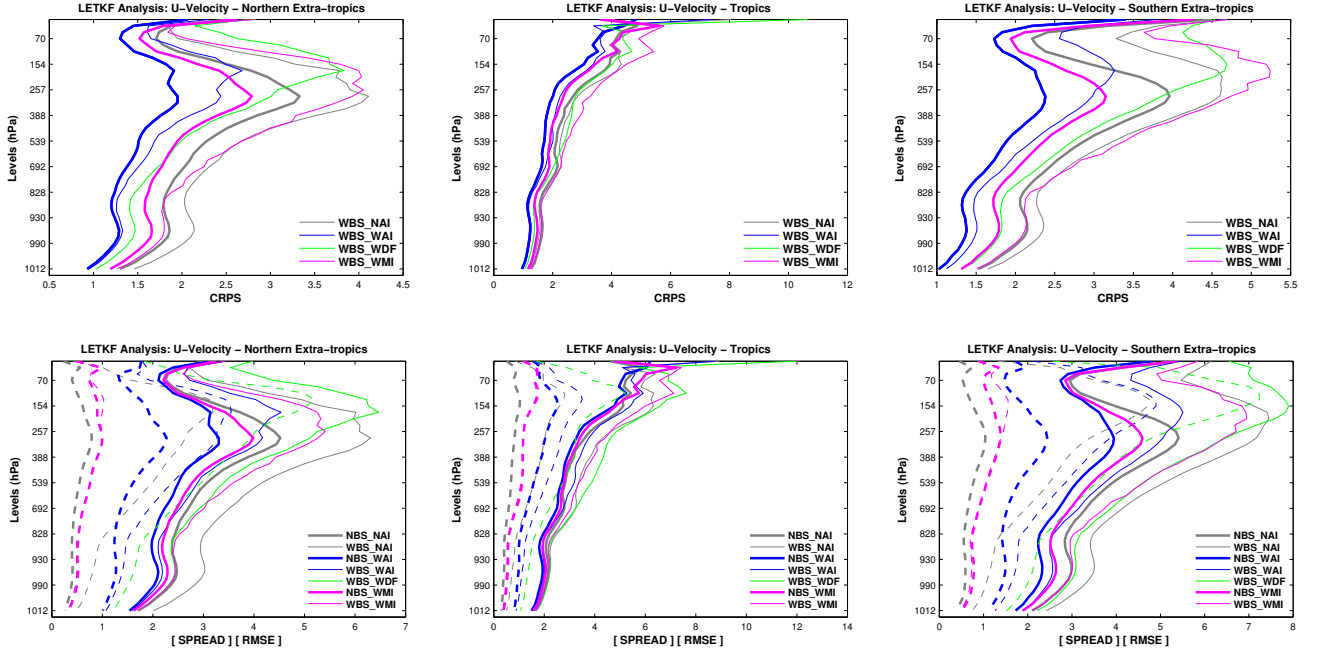


**Figure 4.7:** Vertical profiles for the 500 hPa zonal wind. CRPS (top-row) and RMSE (bottom-row), for the Northern extra-tropics, the Tropics, and the Southern extra-tropics (left to right).

In the next subsection, we will discuss possible causes of the negative impacts of the backscatter on the LETKF analysis, and will summarize with concluding remarks.

### 4.2.1 Conclusions: Impact of the SKEB on the LETKF Analysis

In the above subsection, we have seen that the backscatter does not seem to improve the LETKF analysis. The results show a slight improvement in the the Tropics (for some variables), but also a deterioration of the analysis in the in the extra-tropics. In this subsection we will explore the possible causes of this behavior and try to explain the reasons for the negative impact of the backscatter scheme on GME-EPS.

One of the main factors influencing the quality of the LETKF analysis is the number of observations assimilated in the 3D VAR-LETKF system. In most cases, less observations lead to relatively higher errors in the analysis. In our GME-EPS, all observations undergo a number of preprocessing, which include: thinning, blacklisting, quality control, First-Guess (FG) checks etc. Among those preprocessing steps, the First-Guess (FG) checks involve filtering the observations based on their deviation from the first-guess or background forecast, based on the following criterion:

$$\text{if } |FG - OBS| > \gamma \sqrt{\sigma_b^2 + \sigma_o^2}, \quad \text{then reject the } OBS \quad (4.8)$$

where  $FG$  is the First-Guess or the background model forecast,  $OBS$  is the observa-

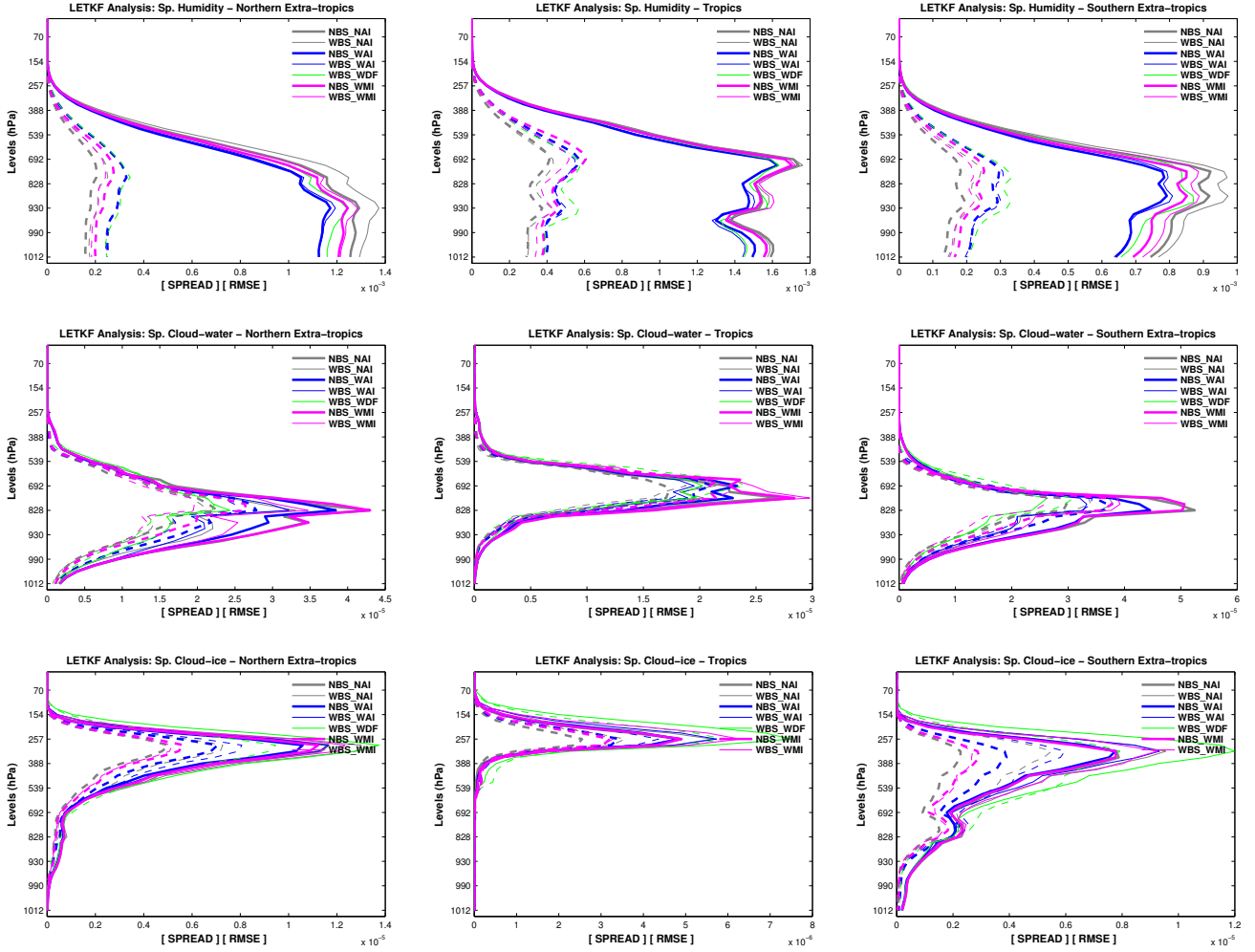


**Figure 4.8:** *RMSE and SPREAD statistics for specific humidity (top-row), specific cloud-water content (middle-row), and specific cloud-ice content (bottom-row), for the Northern extra-tropics, the Tropics, the Southern extra-tropics (left to right).*

tions,  $\sigma_f$  and  $\sigma_o$  are the *expected* standard deviations (or SPREAD) of the background forecast and observations respectively, and  $\gamma$  is a positive integer which controls the amount of deviation. In the DWD assimilation system, conventionally,  $\sigma_f$ ,  $\sigma_o$ , and  $\gamma$  are kept constant. Thus, higher values of  $|FG - OBS|$  will cause the FG check in the 3D VAR preprocessing routine to reject the observations. So these observations will not be assimilated in the LETKF, although it is likely they might be still good enough to assimilate.

In our experiments with the backscatter scheme, for example, a relatively larger number of Atmospheric Motion Vector (AMV) satellite observations, which were used to assimilate the wind components, were rejected based on the FG checks given by Eq. (4.8). This is due to the fact that the deviations  $|FG - OBS|$  were large due to the higher SPREAD in the wind components as shown in Fig. (4.2). Figure (4.9) shows a comparison of the percentage of rejected AMV observations w.r.t the total

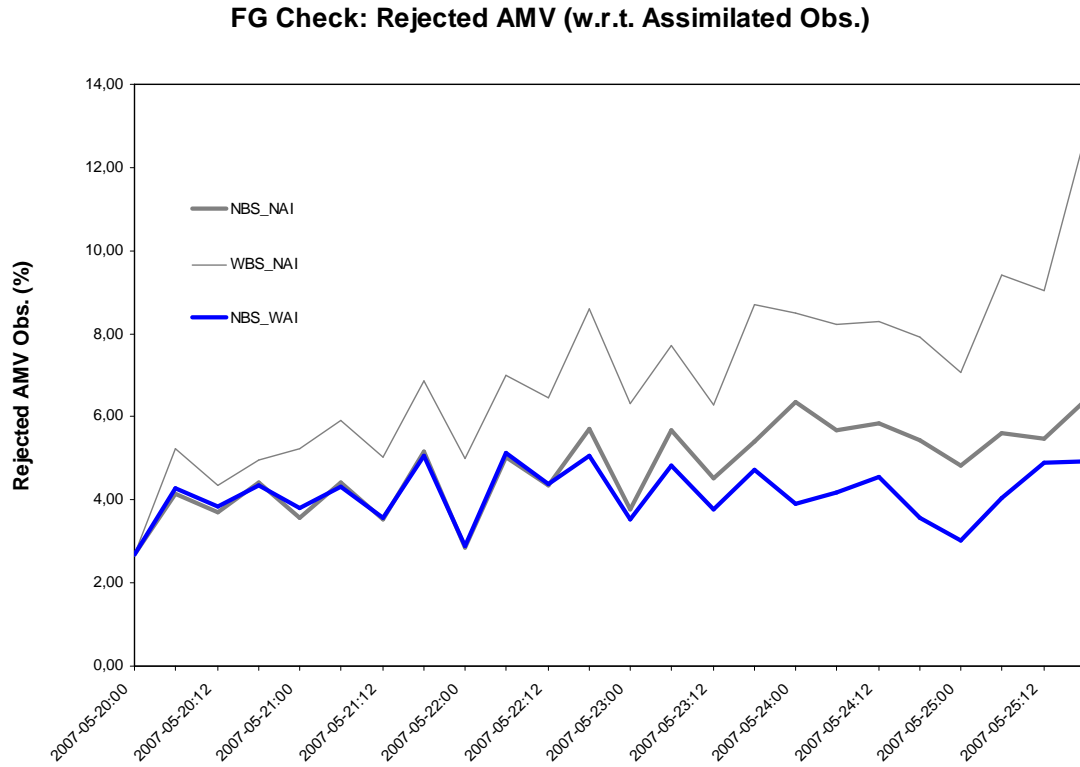


**Figure 4.9:** Percentage of rejected Atmospheric Motion Vectors (AMV) w.r.t. the total assimilated AMVs in the assimilation cycle

assimilated AMVs, from the experiments [NBS\_NAI], [WBS\_NAI], and [NBS\_WAI]. It is very clear from the figure (Fig. (4.2)) that [WBS\_NAI], which is the experiment with SKEB scheme, has the highest percentage of rejected AMVs. Towards the end of the assimilation cycle we can see that the rejection later is almost twice compared to the experiment without the backscatter scheme. On the other hand, [NBS\_WAI], which is the experiment with additive inflation and no backscatter, has the lowest percentage of rejected AMVs. Thus it is highly likely that the rejection of the observations in fact causes the deterioration of the LETKF analysis for all the experiments involving the backscatter scheme. However, this does not necessarily mean that the background forecast by the same experiments were completely wrong. Since the constant  $\sigma_b$  in Eq. (4.8), which is the *expected* FG SPREAD, does not reflect the actual SPREAD, a higher background SPREAD causes the FG check routine to reject the corresponding observations. This is therefore one of the major limitations of the current FG check preprocessing routine in the GME-EPS system. In short, the current FG check observation preprocessing routine in GME-EPS is one of the main causes of the deterioration of LETKF analysis for the experiments with backscatter scheme.

Other possible reasons for the negative impact of the backscatter scheme on the LETKF analysis are: changes in the probability distribution of the forecast w.r.t. observation in the ensemble space, and the changes in the probability density distribution of the analysis variables in the state-space. Figure (4.10) shows the ranked histogram

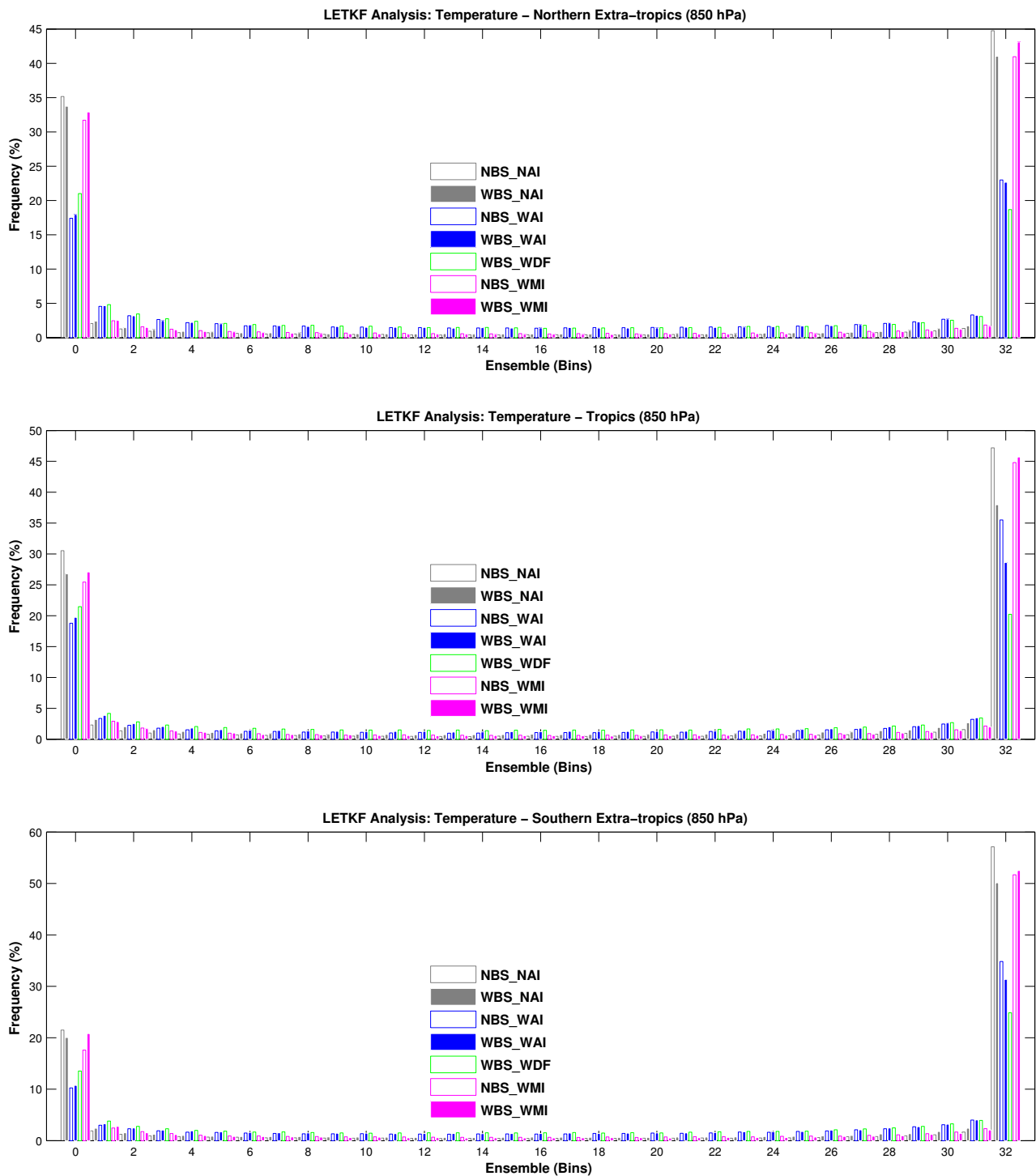


**Figure 4.10:** Ranked histogram (Talagrand diagram) for 850 hPa temperature, for the Northern extra-tropics (top), the Tropics (middle), and the Southern extra-tropics (bottom)

(or Talagrand diagram) of the 850 hPa temperature, for the Northern extra-tropics, the Tropics, and the Southern extra-tropics, and Fig. (4.11) shows the histogram difference between NBS (No Back-Scatter) and WBS (With Back-Scatter) experiments.

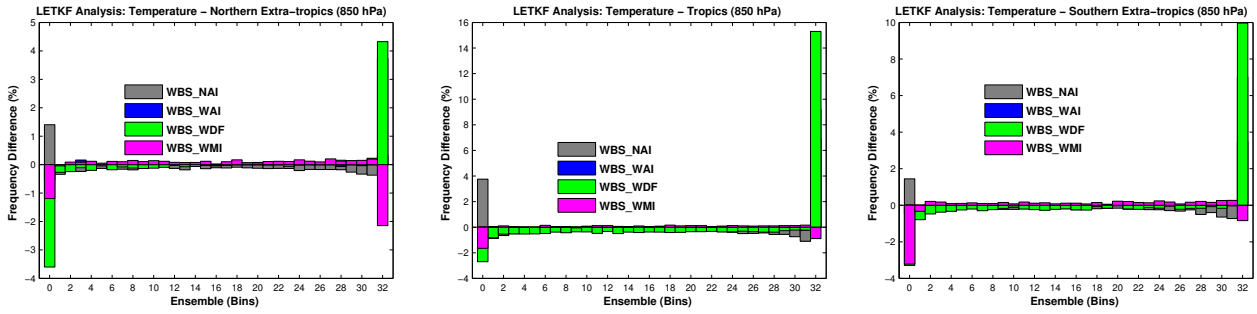


**Figure 4.11:** Ranked histogram difference between NBS (No Back-Scatter) and WBS (With Back-Scatter) experiments for 850 hPa temperature, for the Northern extra-tropics (top), the Tropics (middle), and the Southern extra-tropics (bottom)

It is very well known that, for a perfect EPS, the ranked histogram will be flat, by this means that the probability that the observation falls within the ensemble is equal for all ensemble members. This also implies that the ensemble members are unbiased. However, from the GME-EPS histogram difference, shown in Fig. (4.11), it is obvious that [WBS\_NAI], which is the experiment with backscatter and no inflation, has a bias towards higher bin numbers (except the bin 0 and 32, which are outliers), in all the three regions. This means that, although the probability of capturing higher values of observed temperature for [WBS\_NAI] is higher, compared to [NBS\_NAI], it is relatively lower for lower temperatures. This implicitly means that the temperature analysis of the experiments with backscatter has a positive bias. However, it is also likely that the positive bias is caused by the fewer number of observations used in the assimilation system due to the FG checks. It is also clear from the figures that [WBS\_WMI], which is the experiment with multiplicative inflation and backscatter, has a higher number of outliers in the extra-tropics. Additionally, the relative probability for the ensemble members are relatively lower, which agrees with our earlier conclusions regarding the general under-performance of [WBS\_WMI].

The probability density distribution of the 500 hPa zonal wind from [NBS\_NAI] and [WBS\_NAI], for the Northern extra-tropics and the Tropics are shown in Fig. (4.12). Although there is a noticeable difference in the distribution between experiments with and without backscatter, there is little difference between the FG and LETKF analysis distribution both in the Northern extra-tropics and the Tropics. In the Northern extra-tropics, the probability density is much lower for lower velocities and relatively higher for higher velocities. This is in fact consistent with the conclusion from the ranked histogram. On the other hand, for the Tropics the shape and amplitudes of the FG and analysis distributions are almost the same.

In summary, the following are the main conclusions concerning the impact of the SKEB on the LETKF analysis:

1. Overall the backscatter scheme increases the LETKF analysis ensemble SPREAD, thereby inflating the covariance implicitly (which was one of the aims of introducing the backscatter scheme)

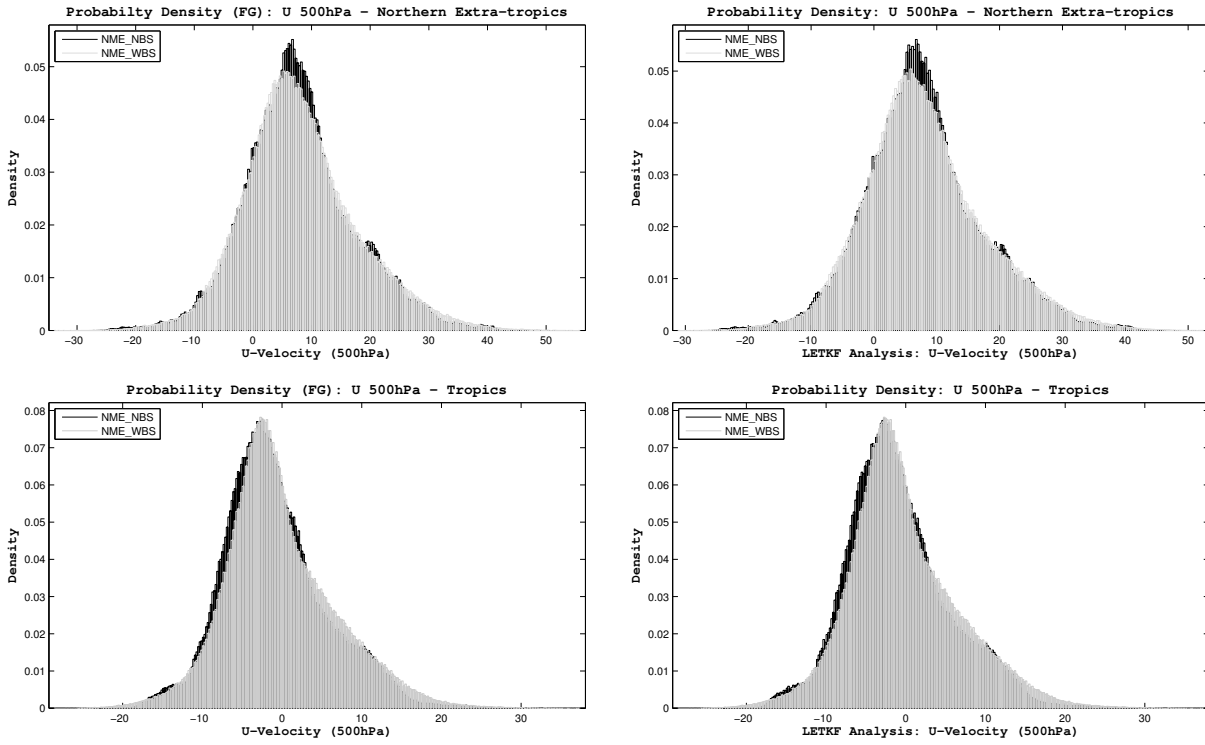


**Figure 4.12:** Probability density distribution of the 500 hPa zonal wind. Top-row: the Northern extra-tropics, and Bottom-row: the Tropics; for the First-Guess (left), and LETKF analysis (right)

2. However, the increase in the SPREAD due to backscatter (without any additional inflation scheme) has an overall negative impact on the analysis.
3. For 850 hPa temperature, the RMSE of the experiments with backscatter (and no inflation) is relatively larger in the extra-tropics but smaller in the Tropics
4. The backscatter scheme has also a significant negative impact on the LETKF analysis for zonal wind, specific humidity, and specific cloud-ice content, although the specific humidity analysis seems to be better in the Tropics at the lower layers of the atmosphere.
5. For experiments with additive inflation and backscatter, the results are not better than the ones without backscatter at the lower levels but they are worse at the upper levels.
6. The LETKF analysis of experiments with multiplicative inflation is one of the worst among all experiments with backscatter scheme.
7. One of the main reason for the deterioration of the LETKF analysis in the experiments with backscatter scheme is the rejection of observations due to the conventional First-Guess (FG) check routine in GME-EPS or, in other words, fewer observations were assimilated in the experiments with the backscatter scheme.

8. Another reason for the negative impact of the backscatter on the LETKF analysis is the positive bias in the ensemble probability distribution (in the ensemble space), i.e., probability densities get lower for lower temperatures (and velocities), and are relatively higher for higher temperature (velocities.), especially in the extra-tropics.



## Non-Gaussianity in Ensemble Kalman Filters

In this chapter, we explore the possibility of a *worst-case scenario* using the backscatter scheme, that violates the basic assumptions in the Kalman filter-based data assimilation, using simple toy models. We consider the backscatter scheme as a multiplicative noise model, and explore the challenges of the multiplicative noise to the current EnKF schemes. The classic Lorenz '63 model and a higher dimensional Lorenz '96 model are used as test beds for the data assimilation experiments. A hybrid Kalman-Particle filter called, Sigma-point Particle Filter (SPPF) is presented as an alternative to solve the issues associated with multiplicative noise.

### 5.1 Multiplicative Noise and Non-Gaussian statistics in EnKFs

Important assumptions involved in the Kalman filter data assimilation methods are: (i) the background (or process) and observation (or measurement) noises are additive, and (ii) the associated probability density functions are Gaussian<sup>1</sup>. However, these assumptions may not hold in reality. For example, the probability density function of daily or weekly averages of many atmospheric variables is non-Gaussian, even though long-term averages tend to follow Gaussian distribution. Recently, several studies have also shown that persistent nonlinear circulation regimes in the atmosphere and associated deviations from the Gaussian probability distributions can be modeled with multiplicative noise [Sura and Sardeshmukh, 2008; Sardeshmukh and Sura, 2009; Sardeshmukh, 2010]. In this case, the multiplicative noise corresponds to the state dependent variations of stochastic feedback from unresolved system components [Sura et al., 2005]. Another interesting example is the stochastic parameterization method such as the stochastic kinetic energy backscatter (SKEB) scheme used in many ensemble prediction systems [Shutts, 2005; Shutts et al., 2008; Berner et al., 2008, 2009; Charron et al., 2010]. The SKEB schemes, which are designed to account for the dissipations in the forecast model, introduce perturbations, which are state-dependent directly or indirectly. These perturbations introduce stochasticity into the model, and are expected to increase the spread of the forecast ensemble. In a broad sense, one may consider these schemes as multiplicative noises models. These stochastic schemes can create non-Gaussian statistics, and may cause the forecast model to deviate from Gaussian-

---

<sup>1</sup>under those assumptions, the estimate will be “globally optimal”

ity. The representativeness errors due to the unresolved scales may also be considered as multiplicative noise since they are state dependent and correlated in time [Janjic and Cohn, 2006]. In general, the multiplicative process noise is attributed to the internally evolving dynamical and numerical errors and the observation or measurement noise corresponds to external noise. If the noise is multiplicative (state dependent) and the model is nonlinear, both the internal and external noises play an important role in the estimation statistics.

Non-Gaussianity and controlling noise have been recently an extensive research topic in the data assimilation community [e.g., Peña et al., 2010]. Data assimilation methods based on conditional mean estimate such as the iterated Kalman filter [Jazwinsky, 1970; Cohn, 1997] have yielded limited success in non-Gaussian scenarios. In variational assimilation methods such as 4D VAR, an asymmetric cost function might be useful for assimilating non-Gaussian variables as shown by some studies [Tsuyuki et al., 2003; Koizumi et al., 2005; Honda et al., 2005]. Fletcher and Zupanski [2006a,b, 2007] proposed two different approaches to deal with non-Gaussian variables in a 3D variational data assimilation framework. The first approach uses a transform to make the log-normal random variable into a normal random variable and the second one uses the correct distribution for a collection of normal and log-normal random variables through a hybrid distribution which gives a different cost function to minimize. However, this approach may not be effective in all cases as shown by Fletcher and Zupanski [2007]. Zupanski [2005] developed the Maximum-Likelihood Ensemble Filter (MLEF), a hybrid filter based on variational assimilation method and the EnKF. The MLEF uses a nonlinear cost-function similar to the 3D-var and could be useful in some cases where observations are log-normally distributed since the preferred estimator is the *Mode*. Jardak et al. [2010] gives a comparison of the assimilation performances of MLEF, EnKF and PF under additive noise and Gaussian assumptions. Theoretically the MLEF method could be used for assimilating non-Gaussian variables. However, its performance may be different if the random variable cannot be transformed to a Gaussian Random Variable (GRV) and the corresponding noises are multiplicative. The motivation of this work is to explore the EnKF based methods in the presence of multiplicative noise, and in particular, the effects of multiplicative noise on them. A Sigma-point particle filter (SPPF) will be presented and its applicability to multiplicative noise models and non-Gaussian systems will be explored.

Section (5.1) gives a general overview of parameter estimation using ensemble based Kalman filters. Section (5.2) introduces the Sigma-Point Particle Filter approach, while Section (5.3) describes experimental and implementation details of the schemes in the highly nonlinear Lorenz '63 and Lorenz '96 models. The last section summarizes the conclusion.

### 5.1.1 Overview of EnKF Parameter estimation

One of the main objectives of data assimilation is to tune the parameters of a dynamical model by deterministically using observations such that they can perform more accurate simulations or predictions. Recursive parameter estimation using EnKF has garnered modelers attention and made considerable progress [Annan and Hargreaves,

2004; Annan, 2005; Annan et al., 2005a,b; Hacker and Snyder, 2005; Aksoy et al., 2005b,a, 2006; Tong and Xue, 2008a,b]. Annan [2005] and Annan and Hargreaves [2004] estimated the parameters of various models using EnKF, where they introduced a preconditioning procedure and scaling to improve the error covariance matrix, which may introduce additional computational burden. Aksoy et al. [2005b,a, 2006] and Tong and Xue [2008a,b] used the EnSRKF formulation where they estimated the model parameters from noisy observations. In their approach, the Kalman gain term is replaced by a scaling parameter in the state update equation, which acts as an alternative to perturbing observations in the analysis step of standard EnKF. However, there are reports that the standard EnKF generates poor parameter estimates, especially for high nonlinear systems [e.g., Kivman, 2003]. Recently, Ambadan and Tang [2009] estimated the parameters of the Lorenz '63 model using Sigma-point Kalman filters (SPKF), which use deterministic sampling of ensemble for calculating the error statistics [Julier et al., 1995; Nørgård Magnus et al., 2000; Ito and Xiong, 2000; Lefebvre et al., 2002; Wan and Van Der Merve, 2000; Haykin, 2001; Van der Merwe et al., 2004]. All the above mentioned experiments were performed under the assumption that the state and observation noises are additive, and follow Gaussian distribution. In the following sections, we will introduce a recently developed hybrid particle filter data assimilation method, called Sigma-Point Particle Filter (SPPF), which use existing SPKF techniques for resampling [Van der Merwe et al., 2000]. We will also show that the SPPF scheme is more suitable in such situations where multiplicative noise is inherent in the model.

## 5.2 The Sigma-Point Particle Filter

The theory and derivations presented in this section are mainly based on the works by Doucet et al. [2000], Van der Merwe et al. [2000], Haykin [2001], Arulampalam et al. [2002], Van der Merwe and Wan [2001a,b], Schon [2006], and Simon [2006].

Consider a stochastic process defined by a nonlinear differential equation of first order in time:

$$\dot{\boldsymbol{\theta}}_k = \mathbf{f}(\boldsymbol{\theta}_k) + \mathbf{g}(\boldsymbol{\theta}_k) \mathbf{q}_k \quad (5.1)$$

where  $\mathbf{f}(\cdot)$  and  $\mathbf{g}(\cdot)$  are in general nonlinear functions of the state  $\boldsymbol{\theta}_k$ , and  $\mathbf{q}_k$  is the random force. The random force is generally considered as a zero-mean Gaussian process or white noise. In the case of additive noise  $\mathbf{g}(\cdot)$  is a constant (e.g., 1.0), i.e. independent of the state  $\boldsymbol{\theta}_k$ , and the stochastic process given by (5.1) is Markovian<sup>2</sup>. On the other hand, in the case of multiplicative process noise,  $\mathbf{g}(\cdot)$  is a linear or nonlinear function of  $\boldsymbol{\theta}_k$ , and the process is no longer Markovian.

For the purpose of presentation, the standard state space equations for an  $L$  di-

---

<sup>2</sup>In recursive estimation, the states evolve in time according to a Markov process. The Markovian property implies that given the present state, the future states are independent of the past states, which is one of the primary properties of recursive Bayesian estimators such as KF

mensional model are given by,

$$\boldsymbol{\theta}_k = \mathbf{f}(\boldsymbol{\theta}_{k-1}, \mathbf{q}_{k-1}) \quad (5.2)$$

$$\boldsymbol{\psi}_k = \mathbf{h}(\boldsymbol{\theta}_k, \mathbf{r}_k) \quad (5.3)$$

Here  $\boldsymbol{\theta}_k$  is the state vector at time  $k$ ,  $\mathbf{f}(\cdot)$  is the forecast model,  $\boldsymbol{\psi}_k$  is the observed state,  $\mathbf{h}(\cdot)$  is the observation function, and  $\mathbf{q}_k$  and  $\mathbf{r}_k$  are the zero-mean random noises corresponding to the background and observations respectively. Given the imperfection of model states and observations, the recursive Bayesian estimation of the state space model given by Eq. (5.2)-(5.3) is actually the Kalman Filter (KF), Extended Kalman Filter (EKF), EnKF, SPKF etc., under Gaussian assumption. Appendix A summarizes the least square formulation of Kalman gain, which is the core of the SPKF approach. A pre-requisite for KF is the Gaussian distribution of background and observation errors, under which the KF provides the globally optimal estimate for state-space equations. The Gaussian assumption reflects the fact that the KF is designed based on the minimization of the analysis error variance (i.e., the trace of error covariance), which ignores the higher order moments. For a non-Gaussian system, the solution by KF may not be optimal, and it could be even erroneous. In his seminal paper, Kalman [1960] confined the filter to linear systems and linear measurement functions. In fact, it has been shown that the standard Kalman gain used in KF, EKF and EnKF is the special case of Eq. (B.15) when the measurement function is linear or locally linearized, and the noise is additive [Ambadan and Tang, 2009]. The EnKF and SPKF algorithms use the same optimality criterion in their algorithms. In the following sections, we will show that the EnKF and the SPKF failed to estimate the model parameters accurately in the presence of multiplicative noise and underlying non-Gaussian probability distribution, and in such case the SPPF assimilation scheme is found to be more accurate.

The basic idea behind the particle filter is to represent the underlying probability distribution by a set of samples known as particles, and associated weights. Van Leeuwen [2009] provided a clear overview of generic particle filters and of their role in geophysical estimation problems. In a broad sense the particles are similar to the ensembles in the EnKF. In a particle filter the probability density function is fully propagated in time whereas in the Kalman filter only the first and second moments are propagated in time. The probability density is approximated using an empirical function given by,

$$p(\boldsymbol{\theta}_k | \boldsymbol{\psi}_{1:k}) \approx \sum_{m=1}^M \tilde{q}_k^{(m)} \delta(\boldsymbol{\theta}_k - \boldsymbol{\theta}_k^{(m)}), \quad \sum_{m=1}^M \tilde{q}_k^{(m)} = 1, \quad \tilde{q}_k^{(m)} \geq 0, \quad \forall m \quad (5.4)$$

where  $\boldsymbol{\theta}_k^{(m)}$ ;  $m = 1, \dots, M$  are the independent and identically distributed (i.i.d.) particles, at time step  $k$ , with corresponding weights  $\tilde{q}_k^{(m)}$ , and  $\delta(\cdot)$  is the Dirac-delta function. Here  $m$  represents the particle index. Practically, it is almost impossible to get i.i.d. samples at any time  $k$  from the posterior density function (5.4), but this limitation can be circumvented by using importance sampling from a *proposal distribution*. The choice of the *proposal distribution* is one of the most important factor in importance sampling schemes. Several strategies for choosing *proposal distribution* have been

proposed in the literature. The most popular schemes include the Sampling Importance Re-sampling (SIR), the Residual sampling, and the minimum variance sampling. For further details and references, see Gordon et al. [1993], Kitagawa [1996], Isard and Blake [1998], Liu and Chen [1998], Doucet et al. [2000], Doucet et al. [2001], Haykin [2001], Arulampalam et al. [2002], and Schon [2006].

The SPPF, first introduced by Van der Merwe et al. [2000], has wide applications in robotics, and artificial intelligence. Van der Merwe et al. [2000] suggested that significant improvement on the particle resampling can be accomplished by using a Kalman filter for the proposal distribution. By using more advanced Kalman filters such as the square-root EnKF, or the SPKFs one can generate a better proposal distribution for the particle filter thereby propagating the statistics more accurately. The family of SPKF algorithms includes the Sigma-Point Unscented Kalman Filter (SP-UKF) [Julier et al., 1995; Wan and Van Der Merve, 2000], Sigma-Point Central Difference Kalman Filter (SP-CDKF) [Nørgård Magnus et al., 2000; Ito and Xiong, 2000] and their square root versions [Haykin, 2001; Van der Merwe and Wan, 2001a,b]. Julier et al. [1995] have shown that for the nonlinear model given by (5.2), the number of sigma-points needed to compute precisely the mean and covariance of the model state at time  $k$  is  $2L + 1$ , where  $L$  is the number of degrees of freedom. The selection scheme for the sigma-points for SP-UKF is based on the scaled unscented transformation, and that for the SP-CDKF is based on the *sterling's interpolation* formula [Press et al., 1992; Ito and Xiong, 2000; Nørgård Magnus et al., 2000]. In our experiments we have used the square-root SP-CDKF for generating the proposal distribution because of its well known numerical stability [Van der Merwe, 2004].

In SP-CDKF the analytical derivatives in EKF are replaced by numerically evaluated *central divided differences*. For implementing the SP-CDKF, augmented state vectors are constructed by concatenating the original model state, and the background and observation error vectors. The augmented *sigma-point state vectors* are calculated using the following selection scheme:

$$x_{k,0} = \bar{\theta}_k \qquad w_0^{(m)} = \frac{\delta^2 - L}{\delta^2} \qquad (5.5)$$

$$x_{k,i}^+ = \bar{\theta}_k + \left( \sqrt{\delta^2 \mathbf{P}_{\theta_k}} \right)_i \quad i = 1, \dots, L \qquad w_i^{(m)} = \frac{1}{2\delta^2} \quad i = 1, \dots, 2L \qquad (5.6)$$

$$x_{k,i}^- = \bar{\theta}_k - \left( \sqrt{\delta^2 \mathbf{P}_{\theta_k}} \right)_i \quad i = (L+1), \dots, 2L \qquad w_i^{(c1)} = \frac{1}{4\delta^2} \quad i = 1, \dots, 2L \qquad (5.7)$$

$$w_i^{(c2)} = \frac{\delta^2 - 1}{4\delta^4} \quad i = 1, \dots, 2L \qquad (5.8)$$

where  $\delta$  is the central difference step size, and  $w_i^{(m)}$  is the weighting term corresponding to the  $i^{\text{th}}$  sigma-point for computing the mean, and  $w_i^{(c)}$  that for the covariance. The sigma-points are then propagated through the forecast model, and the approximated mean, covariance and cross-covariance for the calculation of Kalman gain are computed

as follows:

$$\hat{\boldsymbol{\theta}}_k^- \approx \sum_{i=0}^{2L} w_i^{(m)} \boldsymbol{x}_{k,i}^\theta \quad (5.9)$$

$$\hat{\boldsymbol{\psi}}_k^- \approx \sum_{i=0}^{2L} w_i^{(m)} \mathcal{Y}_{k,i}^\theta \quad (5.10)$$

$$\mathbf{P}_{\theta_k}^- \approx \sum_{i=1}^L \left[ w_i^{(c1)} (\boldsymbol{x}_{k,i}^\theta - \boldsymbol{x}_{k,L+i}^\theta)^2 + w_i^{(c2)} (\boldsymbol{x}_{k,i}^\theta + \boldsymbol{x}_{k,L+i}^\theta - 2\boldsymbol{x}_{k,0}^\theta)^2 \right] \quad (5.11)$$

$$\mathbf{P}_{\tilde{\psi}_k}^- \approx \sum_{i=1}^L \left[ w_i^{(c1)} (\mathcal{Y}_{k,i}^\theta - \mathcal{Y}_{k,L+i}^\theta)^2 + w_i^{(c2)} (\mathcal{Y}_{k,i}^\theta + \mathcal{Y}_{k,L+i}^\theta - 2\mathcal{Y}_{k,0}^\theta)^2 \right] \quad (5.12)$$

$$\mathbf{P}_{\theta_k \tilde{\psi}_k}^- \approx \sum_{i=0}^L w_i^{(m)} \left( \boldsymbol{x}_{k,i}^\theta - \hat{\boldsymbol{\theta}}_k^- \right) \left( \mathcal{Y}_{k,i}^\theta - \hat{\boldsymbol{\psi}}_k^- \right)^\top \quad (5.13)$$

Equations (5.9)-(5.13) form the core part for generating the proposal distribution (Sigma-point particles) for SPPF. The SP-CDKF generated proposal distribution in SPPF may be Gaussian approximate. However, it has been shown that as long as the Kalman filter generated distribution overlaps with the proposal distribution, this approximation results in a better particle filter implementation [Van der Merwe et al., 2004]. One of the advantages of using the SP-CDKF for generating the proposal distribution is that it uses only one ‘‘control parameter’’ ( $\delta$ ) compared to three in SP-UKF. The SPPF algorithm is summarized as follows.<sup>3</sup>

I. Initialization :  $k = 0$

For  $i = 1 \dots N$  draw particles  $\boldsymbol{\theta}_0^i$  from the prior  $p(\boldsymbol{\theta}_0)$

II. For time  $k = 1, 2 \dots$

1. Importance sampling step :

For  $i = 1 \dots N$  :

(a) Update the prior distribution for each particle with the SPKF

(i) Calculate the sigma points for the particle,  $\boldsymbol{x}_{k,i} = [\boldsymbol{x}_{k,0} \quad \boldsymbol{x}_{k,j}^+ \quad \boldsymbol{x}_{k,j}^-]$

where  $\boldsymbol{x}_{k,0}$ ,  $\boldsymbol{x}_{k,j}^+$ , and  $\boldsymbol{x}_{k,j}^-$  are the sigma point vectors given by

$$\boldsymbol{x}_{k,0} = \boldsymbol{\theta}_k \quad (5.14)$$

$$\boldsymbol{x}_{k,j}^+ = \bar{\boldsymbol{\theta}}_k + \left( \sqrt{\delta^2 \mathbf{P}_{\theta_k}} \right)_i \quad (5.15)$$

$$\boldsymbol{x}_{k,j}^- = \bar{\boldsymbol{\theta}}_k - \left( \sqrt{\delta^2 \mathbf{P}_{\theta_k}} \right)_i \quad (5.16)$$

---

<sup>3</sup>Here we repeat the SPPF algorithm derived by Van der Merwe [2004]

(ii) Propagate sigma points in time (forecast step of SPKF) :

$$\mathbf{x}_k^f = \mathbf{f}(\mathbf{x}_{k-1}, \mathbf{x}_{k-1}^q) \quad (5.17)$$

$$\hat{\boldsymbol{\theta}}_k^- = \mathbf{w}^{(m)} \sum_{m=1}^M \mathbf{x}_{k,m}^f \quad (5.18)$$

$$\mathbf{P}_{\hat{\boldsymbol{\theta}}_k^-} = \sum_{i=1}^L \left[ \mathbf{w}_i^{(c_1)} \left( \mathbf{x}_{k,i}^f - \mathbf{x}_{k,L+i}^f \right)^2 + \mathbf{w}_i^{(c_2)} \left( \mathbf{x}_{k,i}^f + \mathbf{x}_{k,L+i}^f - 2\mathbf{x}_{k,0}^f \right)^2 \right] \quad (5.19)$$

(iii) Measurement update (analysis step of SPKF) :

$$\mathcal{Y}_k^f = \mathbf{h}(\mathbf{x}_k^f, \mathbf{x}_k^r) \quad (5.20)$$

$$\hat{\boldsymbol{\psi}}_k^- = \mathbf{w}^{(m)} \sum_{m=1}^M \mathcal{Y}_{k,m}^f \quad (5.21)$$

$$\mathbf{P}_{\hat{\boldsymbol{\psi}}_k^-} = \sum_{i=1}^L \left[ \mathbf{w}_i^{(c_1)} \left( \mathcal{Y}_{k,i}^f - \mathcal{Y}_{k,L+i}^f \right)^2 + \mathbf{w}_i^{(c_2)} \left( \mathcal{Y}_{k,i}^f + \mathcal{Y}_{k,L+i}^f - 2\mathcal{Y}_{k,0}^f \right)^2 \right] \quad (5.22)$$

$$\mathbf{P}_{\theta_k, \hat{\boldsymbol{\psi}}_k^-} = \sum_{i=0}^L \mathbf{w}_i^{(m)} \left( \mathbf{x}_{k,i}^f - \hat{\boldsymbol{\theta}}_k^- \right) \left( \mathcal{Y}_{k,i}^f - \hat{\boldsymbol{\psi}}_k^- \right)^T \quad (5.23)$$

$$\mathbf{K}_k = \mathbf{P}_{\theta_k, \hat{\boldsymbol{\psi}}_k^-} \mathbf{P}_{\hat{\boldsymbol{\psi}}_k^-}^{-1} \quad (5.24)$$

$$\hat{\boldsymbol{\theta}}_{k,i} = \hat{\boldsymbol{\theta}}_k^- + \mathbf{K}_k (\boldsymbol{\psi}_k - \hat{\boldsymbol{\psi}}_k^-) \quad (5.25)$$

$$\mathbf{P}_{\hat{\boldsymbol{\theta}}_{k,i}} = \mathbf{P}_{\hat{\boldsymbol{\theta}}_k^-} - \mathbf{K}_k \mathbf{P}_{\hat{\boldsymbol{\psi}}_k^-} \mathbf{K}_k^T \quad (5.26)$$

(b) Sample  $\mathbf{x}_{k,i} \sim \mathcal{N}(\hat{\boldsymbol{\theta}}_{k,i}; \mathbf{P}_{\hat{\boldsymbol{\theta}}_{k,i}})$  (SPKF analysis distribution)

For  $i = 1 \dots N$ , evaluate the important weights, and normalize the weights :

$$w_{k,i} = w_{k-1,i} \frac{\text{likelihood}_{k,i} \times \text{prior}_{k,i}}{\text{proposal}_{k,i}} \quad (5.27)$$

$$= w_{k-1,i} \frac{p(\boldsymbol{\psi}_k | \boldsymbol{\theta}_{k,i}) p(\boldsymbol{\theta}_{k,i} | \boldsymbol{\theta}_{k-1,i})}{p(\boldsymbol{\theta}_{k,i} | \boldsymbol{\psi}_{1:k,i})} \quad (5.28)$$

$$\tilde{w}_{k,i} = \frac{w_{k,i}}{\sum_{j=0}^N w_{k,i}} \quad (5.29)$$

2. Resample the particles using the above weights (by multiplying with important weights)

3. Approximate the posterior distribution, and the estimate

$$\hat{\boldsymbol{\theta}}_k \approx \frac{1}{N} \sum_{i=1}^N \hat{\boldsymbol{\theta}}_{k,i} \quad (5.30)$$

A more detailed interpretation and derivation of the above expression can be found in Van der Merwe [2004].

## 5.3 Parameter estimation experiments

In general the parameter estimation involves a nonlinear mapping given by

$$\mathbf{Y}_k = \mathcal{N}(\boldsymbol{\theta}_k, \boldsymbol{\Lambda}) \quad (5.31)$$

where the nonlinear map<sup>4</sup>  $\mathcal{N}(\cdot)$  may be the dynamical model  $\mathbf{f}(\cdot)$  or an empirical model such as a neural network, parameterized by the vector  $\boldsymbol{\Lambda}$ .

The state space model for the parameter estimation problem can be written as,

$$\boldsymbol{\Lambda}_k = \boldsymbol{\Lambda}_{k-1} + \mathbf{q}(\boldsymbol{\Lambda}_k) \mathbf{W}_k^\theta \quad (5.32)$$

$$\boldsymbol{\psi}_k = \mathbf{f}(\boldsymbol{\theta}_k, \boldsymbol{\Lambda}_k) + \mathbf{r}(\boldsymbol{\psi}_k) \mathbf{W}_k^\psi \quad (5.33)$$

where  $\mathbf{f}(\cdot)$  is the nonlinear model,  $\boldsymbol{\Lambda}$  is the parameter vector which constitutes the dynamical parameters (or empirical parameters in the case of empirical model),  $\mathbf{q}(\cdot)$  and  $\mathbf{r}(\cdot)$  represent the multiplicative noise models corresponding to the model states and observations, and  $\mathbf{W}^\theta$ , and  $\mathbf{W}^\psi$  are random white noises corresponding to the respective noise models. The state space model for the parameter estimation is similar to the state estimation except for the fact that the state (here states are parameters) time evolution is linear (Eq. 5.32) and the measurement function is nonlinear (Eq. 5.33). In this particular situation Eq. (5.32) may be considered as a linear stochastic system with multiplicative forcing. In the following subsection we will use the Lorenz [1963], and Lorenz [1996] models as test beds for our parameter estimation experiments. In all the experiments the state observations are related to the model parameters through the nonlinear dynamical model.

### 5.3.1 Experiments with Lorenz '63 Model

In the data assimilation community, the Lorenz [1963] model has served as a test bed for examining the properties of various data assimilation methods as the model shares many common features with the atmospheric circulation and the climate system in terms of variability and predictability [Gauthier, 1992; Palmer, 1993; Miller et al., 1994; Evensen, 1997]. The model can be used to simulate nearly-regular oscillations or irregular chaotic variations by adjusting the model parameters that control the non-linearity of the system. In our experiments, we used a modified version of the standard Lorenz [1963] model with additional noise terms, given by

$$\frac{dx}{dt} = \sigma(y - x) + q(x)w^x \quad (5.34)$$

$$\frac{dy}{dt} = \rho x - y - xz + q(y)w^y \quad (5.35)$$

$$\frac{dz}{dt} = xy - \beta z + q(z)w^z \quad (5.36)$$

---

<sup>4</sup>In general  $Y_k$  refers to the mapped vector (e.g. temperature) from the state vector  $\theta_k$ , (e.g. radiance), and  $\mathcal{N}$  is the nonlinear function which is the mapping function (e.g. radiative transfer model).

where variables  $x$ ,  $y$ , and  $z$  are related to the intensity of convective motion and to the temperature gradients in the horizontal and vertical directions, and the parameters  $\sigma$ ,  $\rho$ , and  $\beta$  will be referred to as dynamical parameters.  $q(\cdot)$  represents the state dependent (multiplicative) background errors, and  $w$  is the Gaussian white noise. The true data are created by integrating the model using the fourth-order Runge-Kutta scheme [Press et al., 1992], with parameters  $\sigma$ ,  $\rho$ , and  $\beta$  set to 10.0, 28.0, and 8/3 respectively, and initial conditions set to 1.508870,  $-1.531271$ , and 25.46091 as in Miller et al. [1994] and Evensen [1997].

To apply the assimilation algorithms, we discretize the nonlinear Lorenz model (5.34)-(5.36) using the fourth-order Runge-Kutta method and write it in the form of state space equations given by (5.32) and (5.33), where  $\boldsymbol{\theta}_k$  represents the system state vector (a column vector composed of  $x$ ,  $y$  and  $z$ ),  $\mathbf{f}(\cdot)$  is the Lorenz model and  $\mathbf{q}_k$  is the random (white) process noise vector (column vector composed of  $q^x$ ,  $q^y$  and  $q^z$ ). The measurement function  $\boldsymbol{\psi}_k$ , required for the application of the EnKF parameter estimation, is the nonlinear model itself, connecting the state observations and model parameters.

For all the experimental cases (involving multiplicative noise) to be discussed, the observation data sets are generated by setting:

$$\mathbf{q}(\boldsymbol{\theta}_k) \mathbf{w}_k^\theta = C_m \boldsymbol{\theta}_k \mathbf{w}^\theta \quad (5.37)$$

where  $C_m$  is a constant<sup>5</sup>, called the multiplicity factor, which determines the strength of the state influence in the multiplicative noise.  $\boldsymbol{\theta}$  is the system state vector, and  $w^\theta$  is the normally distributed white noise  $N(0, \sqrt{2})$ . This white noise distribution is similar to that in the additive noise experiments in Miller et al. [1994] and Evensen [1997]. The observation interval is set to 25, i.e., the observations are assimilated to the model at every 25 steps.

Two particular cases were studied. Case 1: the background noise (or internal noise) is additive and the observation noise (or external noise) is multiplicative. Case 2: both the background and the observation noises are multiplicative.

We assume that the parameter  $\rho$  is uncertain. Our task is to estimate the correct value of  $\rho$  from infrequent noisy observations using a noisy model. In Case 1 the observations are generated using the multiplicative noise model given by Eq. (5.37), where the multiplicity factor  $C_m$  is set to 0.02. Figure (5.1-a) shows the distribution of the variables  $X$  and  $Z$ , and Fig. (5.1-b) shows the distribution of the corresponding additive and multiplicative noises used in the experiments. It is clear from the probability plot that the observations (Fig. (5.1-a)) are non-Gaussian. The multiplicative noise shown in Fig. (5.1-b) also shows non-Gaussian features, and is symmetric. However, the symmetric nature may not be the case for real observations. In all our experiments, we set the initial parameter to zero.

Figure (5.2-a) shows the parameter estimation results using the EnKF scheme. The number of ensemble members used in the experiments is 100. Similarly, Fig. (5.2-b)

---

<sup>5</sup>In our study we focus only on linear multiplicative noise model where  $C_m$  is a constant. However in many real situations such as the stochastic kinetic energy backscatter (SKEB) schemes, the multiplicative noise models are nonlinear in general.

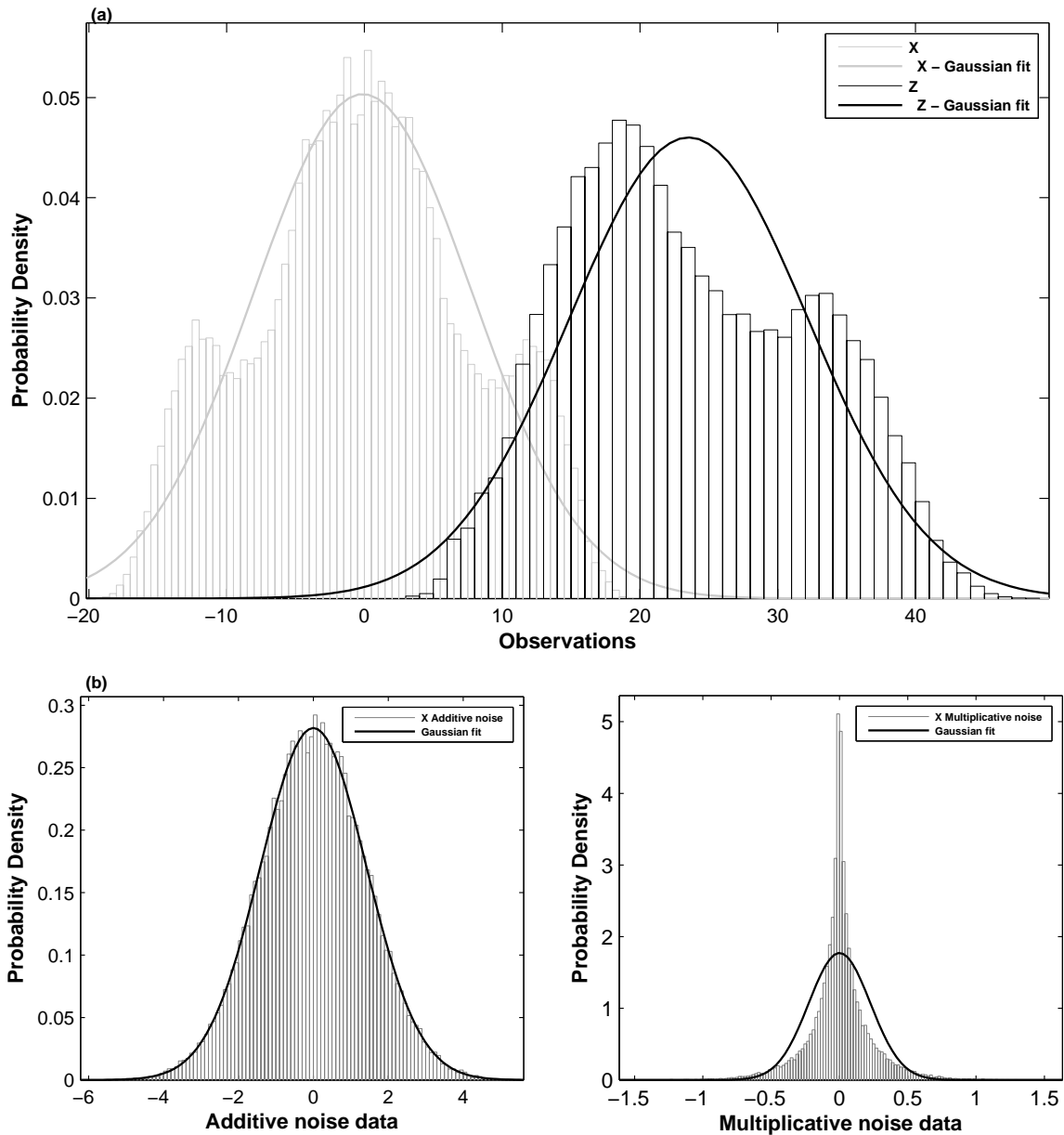


**Figure 5.1:** (a) Observation distribution: Gray -  $X$ , and Black - Variable  $Z$ ; (b) Noise Distributions for  $X$ : Left panel - Additive Noise, Right panel - Multiplicative noise; solid curves represent corresponding Gaussian fits

shows the results using the square-root SP-CDKF, which uses  $2L + 1$  sigma-points for the estimation. As can be seen in Fig. (5.2-a) the EnKF scheme failed to estimate the parameter. On the other hand the performance of the square-root SP-CDKF is better but the parameter is still slightly overestimated as shown in Fig. (5.2-b). It should be noted that the estimate might be sensitive to the initial guess. In fact the performance of the SP-CDKF can be adjusted by tuning the central difference parameter. However in all our trial experiments the SP-CDKF either underestimates or overestimates the true parameter even though it converges very fast compared to

other Kalman filter schemes. We repeated the experiment with the SPPF scheme, which is a hybrid Particle filter-Kalman filter. The results are shown in Fig. (5.2-c), and they are remarkably better compared to any of the Kalman filter based assimilation schemes including the advanced square-root filters.

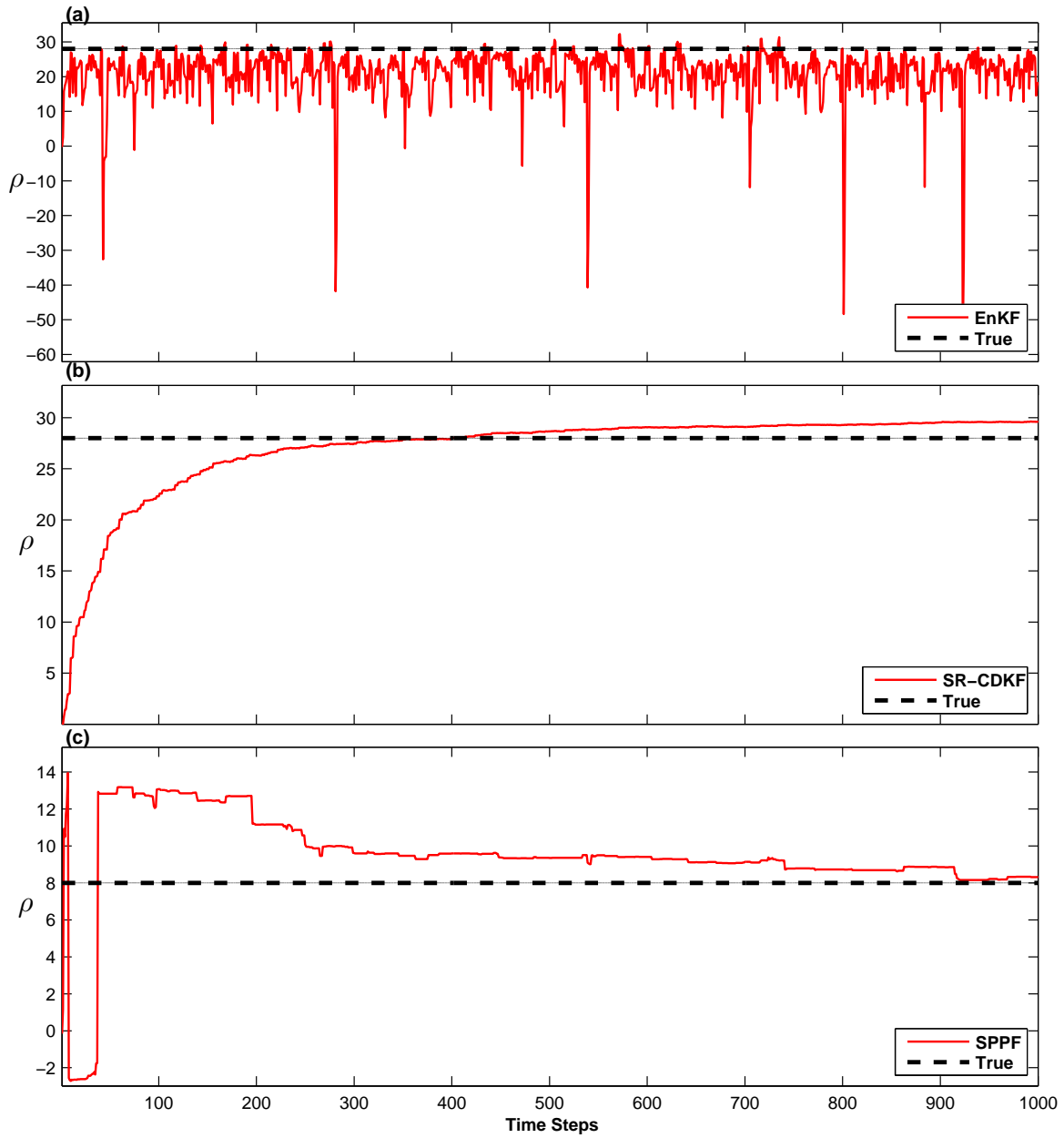


**Figure 5.2:** Lorenz '63 model: (a) EnKF (b) SR-CDKF (c) SPPF with 100 particles. True  $\rho$  - dashed line, estimated  $\rho$  - solid red line.

In Case 2, the situation is much more realistic and may give rise to complex non-Gaussian distribution. Here we focus only on the performances of the advanced square root SP-CDKF and the SPPF since the role of generic EnKF methods are in this case irrelevant. Figure (5.3-a & b) shows the results of the experiments, which are similar

to Case 1 where the square root SP-CDKF overestimates/underestimates the model parameter, and the SPPF scheme estimates the parameter with better accuracy. To study the effect of the multiplicity factor on the SPPF assimilation scheme, we have increased  $C_m$  from 0.02 to 0.2. The results of the experiments are shown in Fig. (5.3-c). From the figure it can be concluded that irrespective of the strength of the multiplicative noise, the SPPF scheme was able to estimate the parameter accurately. Table (5.1) gives the Root Mean Squared Error (RMSE) values of all the above experiments, which in general confirms the results from the figures.

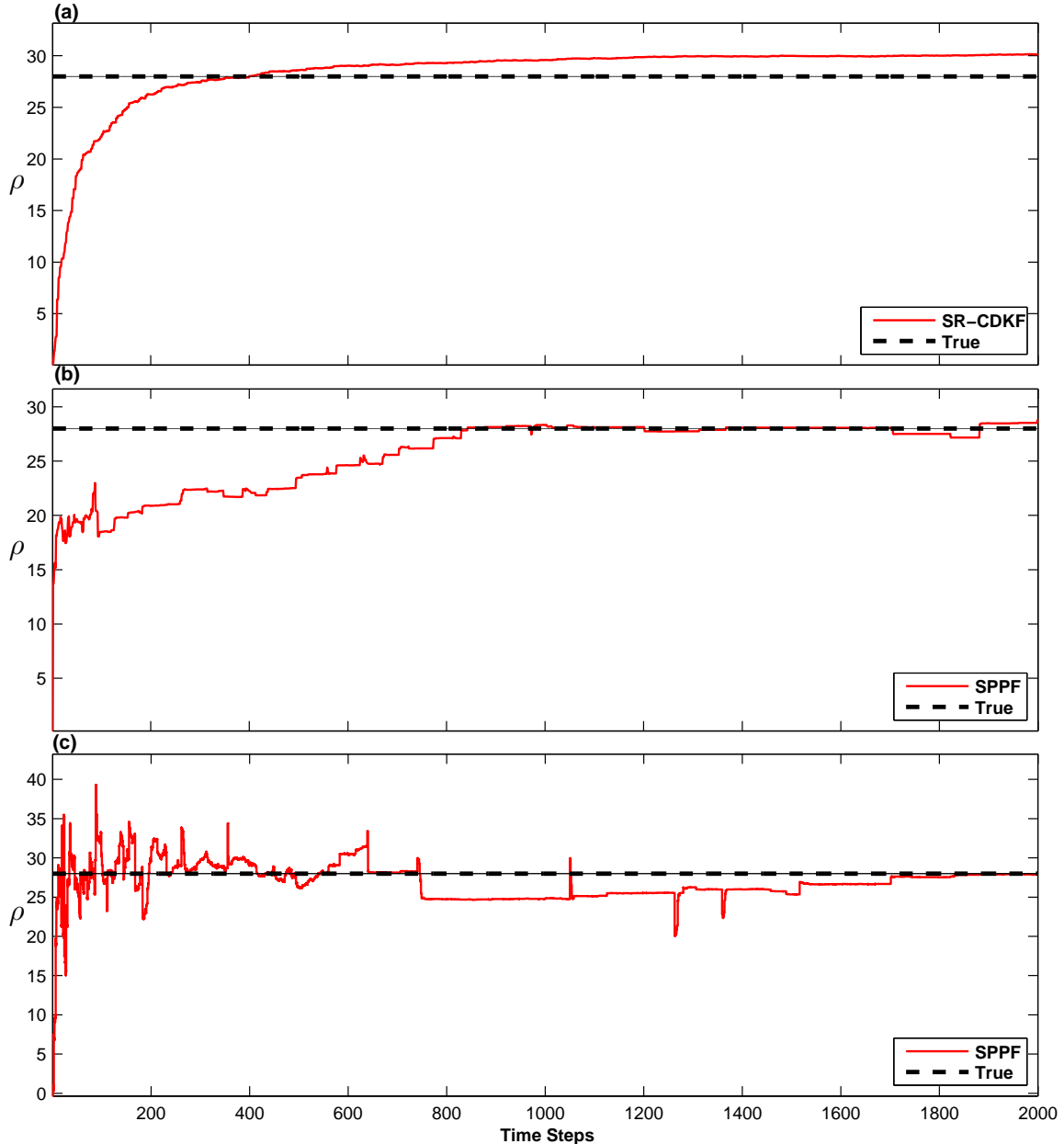


**Figure 5.3:** Lorenz '63 model: (a) SR-CDKF (b) SPPF using 100 particles. (c) SPPF with a higher multiplicity factor of 0.2. True  $\rho$  - dashed line, estimated  $\rho$  - solid red line.

In summary, we have investigated the merits and de-merits of different Kalman filter based ensemble data assimilation schemes in a multiplicative model noise environment, using the low-dimensional Lorenz '63 model. Important features in evaluating the performance of a data assimilation algorithm are its robustness and computational expense as they can become issues when it is applied to higher dimensional models. In the following section we will further explore the above mentioned schemes using the higher dimensional Lorenz '96 model.

### 5.3.2 Experiments with Lorenz '96 Model

To explain the dynamics of weather at a fixed latitude, Lorenz [1996] introduced a one dimensional atmosphere that shares similar error growth characteristics as full Numerical Weather Prediction (NWP) models. In our experiments, we used a modified version of the model containing  $K$  variables  $X_1, \dots, X_k$ , which may be thought of as atmospheric variables in  $K$  sectors of a latitude circle, governed by,

$$\frac{dX_k}{dt} = -X_{k-1}(X_{k-2} - X_{k+1}) - X_k + F + \underbrace{q(X_k)}_{w^{X_k}} \quad (5.38)$$

where the constant  $F$  is called the forcing term. The last term (under-bracketed expression) in Eq. (5.38) forms the noise model, which is given by Eq. (5.37). By using cyclic boundary conditions, the definition of  $X_k$  is extended to all values of  $k$ ; i.e.  $X_{k-K}$  and  $X_{k+K}$  equal to  $X_k$ . It is assumed that a unit time  $\Delta t = 1$  corresponds to five days.

The experimental setup is similar to that of Lorenz and Emmanuel [1998], where  $K = 40$  and the magnitude of the forcing term is set to 8 for which the system is chaotic. The system was integrated using fourth-order Runge-Kutta scheme, with an integration step  $\Delta t = 0.05$  (i.e. 6 hours). The experiments were carried out with random initial conditions, and the observations were generated by applying the noise model to the true model. For different case studies the strength of the multiplicative noise was controlled by setting the multiplicity factor either to 0.02 (weak case) or 0.2 (strong case). Also the observation interval was set to 5, i.e., the observed states are assimilated to the nonlinear model at every 5 steps. A complete discussion of the Lorenz '96 model can be found in Lorenz [1996]; Lorenz and Emmanuel [1998]; Lorenz [2005, 2006a], and [Lorenz, 2006b]. Here we focus on a case study where both the model and measurement noises are multiplicative, which is similar to the second case study using the Lorenz '63 model described in the previous subsection. In all experiments in this section, we assume that observations of all the states are available, and the forcing term  $F$  is uncertain. Initially we set the forcing term  $F$  to zero, and our aim is to estimate the actual forcing term  $F$  accurately from the observed state variables so that we will be able to tune the dynamical model for a more accurate prediction.

Estimation results are shown in Fig. (5.4-a & b) respectively. These results imply that the pure Kalman filter based methods either underestimate or over-estimate the parameter. It is due to the fact that pure Kalman filter based optimal estimation methods rely only on the first two moments, which are insufficient for estimating non-Gaussian statistics. In all the cases described above the SPPF scheme is very successful in estimating the parameters with reasonable accuracy. The results of experiments

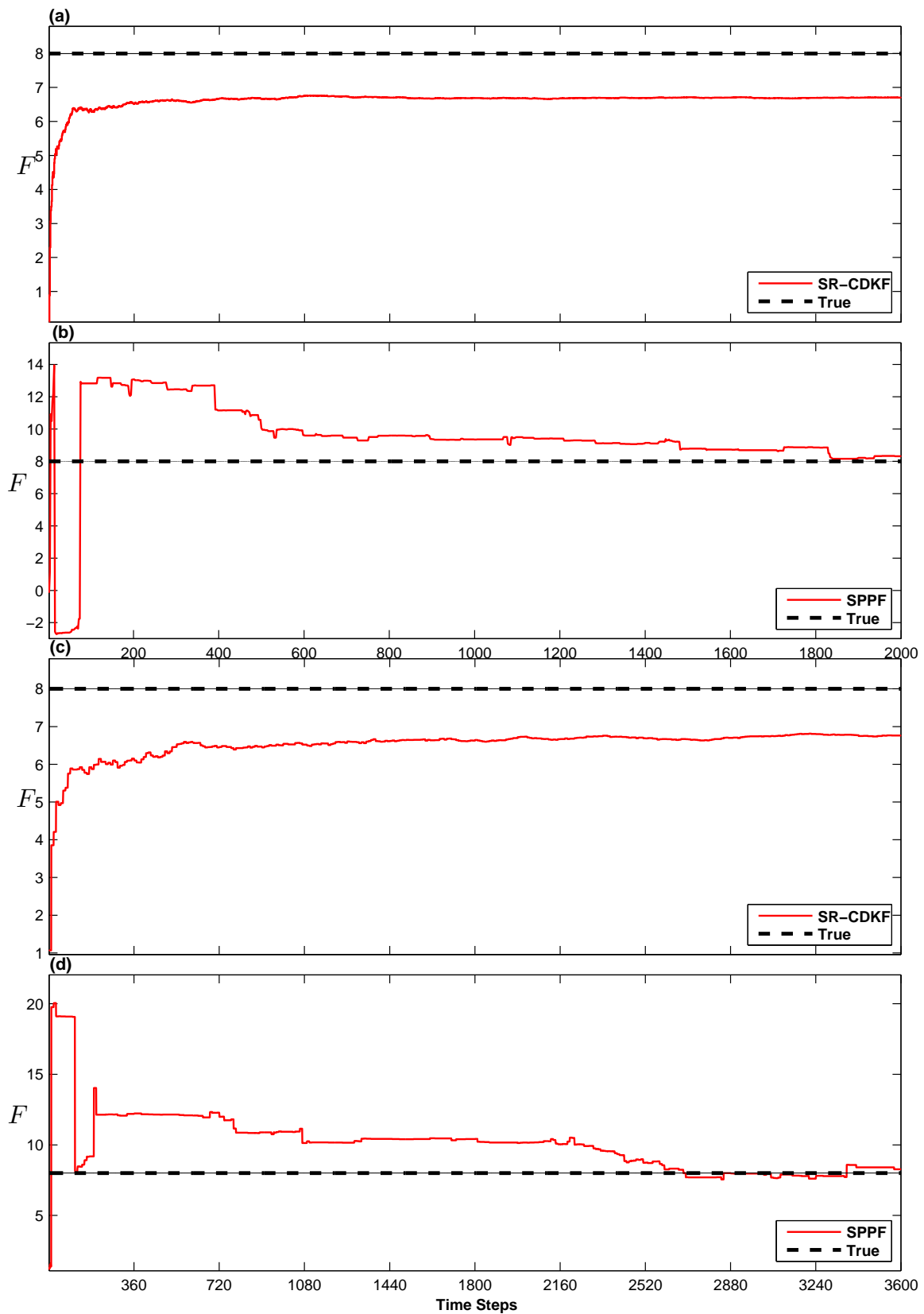


**Figure 5.4:** Lorenz '96 model: (a) SR-CDKF (b) SPPF (c) SR-CDKF with a higher multiplicity factor of 0.2. (d) SPPF with a higher multiplicity factor of 0.2 True  $F$  - dashed line, estimated  $F$  - solid red line.

using a higher multiplicity factor are shown in Fig. (5.4-c & d). The results once again re-iterate the fact that pure Kalman filter methods fail in non-Gaussian scenarios whereas the hybrid SPPF scheme estimates the parameter accurately. However, the RMSE values corresponding to the Lorenz '96 model experiments are relatively higher than those of the square-root SP-CDKF. This is due to an initial fluctuation in SPPF estimate. The RMSE values may get smaller for SPPF if one takes a longer assimilation period, since the SP-CDKF converges to an under-estimated value (almost constant) after a certain assimilation steps.

| Assimilation Method       | Observation error | Background error | Multiplicity factor, $C_m$ | RMSE    |
|---------------------------|-------------------|------------------|----------------------------|---------|
| EnKF (L63, Fig. 5.2-a)    | Multiplicative    | Additive         | 0.02                       | 10.2340 |
| SR-CDKF (L63, Fig. 5.2-b) | Multiplicative    | Additive         | 0.02                       | 4.5692  |
| SPPF (L63, Fig. 5.2-c)    | Multiplicative    | Additive         | 0.02                       | 3.4762  |
| SR-CDKF (L63, Fig. 5.3-a) | Multiplicative    | Multiplicative   | 0.02                       | 3.5363  |
| SPPF (L63, Fig. 5.3-b)    | Multiplicative    | Multiplicative   | 0.02                       | 3.8475  |
| SPPF (L63, Fig. 5.3-c)    | Multiplicative    | Multiplicative   | 0.2                        | 2.6334  |
| SR-CDKF (L96, Fig. 5.4-a) | Multiplicative    | Multiplicative   | 0.02                       | 1.4193  |
| SPPF (L96, Fig. 5.4-b)    | Multiplicative    | Multiplicative   | 0.02                       | 2.9593  |
| SR-CDKF (L96, Fig. 5.4-c) | Multiplicative    | Multiplicative   | 0.2                        | 1.5403  |
| SPPF (L96, Fig. 5.4-d)    | Multiplicative    | Multiplicative   | 0.2                        | 3.0108  |

**Table 5.1:** *Parameter estimation: Root Mean Squared Error*

## 5.4 Discussion and Conclusions

Over the last decade, the data assimilation community made significant progresses towards the development and application of ensemble based Kalman filter data assimilation schemes. The EnKF and its derivatives have been widely applied to various fields, in particular atmosphere and ocean sciences. However, a preliminary limit imposed in carrying out all the above mentioned Kalman filters is that the states, observations and associated noise models should follow a Gaussian distribution. On the other hand, the multiplicative noise typically introduced in nonlinear dynamical systems may cause non-Gaussianity, which is a major concern for the Kalman filter based ensemble data assimilation, and has not been well addressed in the literature. Recently, Anderson [2010] introduced the Ranked Histogram Filter (RHF), which is a promising workaround to deal with non-Gaussian observation space. Notwithstanding

those improvements, the Kalman filter based methods still lacks the ability to handle non-Gaussian statistics. In such cases, hybrid methods may be more useful.

We have explored the impacts of multiplicative noise on ensemble based Kalman filter data assimilation methods in the context of parameter estimation problems. In parameter estimation in the presence of multiplicative noise, the nonlinearity of the measurement function also plays an important role. Our experiments show that all ensemble based Kalman filters, including EnKF, SPKF and square root SPKFs, either underestimate or overestimate the parameter, sometimes even diverging from the true value. The main reason for their poor performance is the fact that the multiplicative noise causes the system to deviate from Gaussianity. In such situations, it is difficult to approximate the statistical moments in a closed form, which is the necessary and sufficient condition for global optimality of the EnKFs.

Further, we introduced the recently developed SPPF scheme to the assimilation problem involving multiplicative noise. In the SPPF scheme, the particles are resampled using the SPKF scheme. Using a three-variable Lorenz '63, and a forty-variable Lorenz '96 model, we explored the merits and properties of SPPF. The results showed that the SPPF scheme can estimate the model parameters with reasonable accuracy and most importantly better than ensemble Kalman filters. The main advantages of using the hybrid method are that the number of particles is significantly reduced compared to the SIR particle filter, and the method works well in a multiplicative noise environment.

In our experiments, we assume that the dynamical parameters are stationary, and do not change with time. It is a common approach in parameter estimation using the Kalman filters [Annan and Hargreaves, 2004; Annan, 2005; Annan et al., 2005a,b; Hacker and Snyder, 2005; Aksoy et al., 2005b,a, 2006; Tong and Xue, 2008a,b]. Other researchers have noted that the time series defined by Eq. (5.32) may not be stationary [Dee, 1995; Evensen et al., 1998]. This lack of stationarity may add further complexity into the estimation problem. Besides, it may be possible that large differences in the initial parameter value may place the system in qualitatively different regimes. In fact, in such models, the original state has stable equilibriums (or stable limit cycles) while the true state was chaotic. We would imagine such cases would present a special challenge to any state-of-the art data assimilation technique.

Another interesting issue is the computational expense of the SPPF algorithm. In a broad sense, one may consider the SPPF scheme as a super-ensemble technique, where each sample is estimated through a subset of sigma-points and resampled accordingly. Compared to EnKFs and SPKFs, the computational requirement of SPPF is larger. However, the super-ensemble structure of the SPPF algorithm is highly parallelizable, and one can manage the computing time with the expense of more computing resources. On the other hand, the hybrid approach may help many researchers to use the existing EnKF based assimilation packages such as the Data Assimilation Research Test bed (DART), [Anderson et al., 2009], which is optimized for many GCMs. There is no doubt that much additional research is required before applying the SPPF technique to highly dimensional systems like GCMs.

In conclusion, we have demonstrated that hybrid methods such as the SPPF can overcome the drawbacks of pure Kalman filter bases ensemble data assimilation meth-

ods in the presence of multiplicative noise, and associated deviations from Gaussianity. Issues related to SPPF do not seem to impede their applications to high complexity models.

---

This Chapter has been published in the *Journal of Advances in Modelling the Earth System* (JAMES), as Ambadan and Tang [2011], and reproduced here with editorial modifications

Part of the work described in this chapter was partially supported by a NSERC (Natural Sciences and Engineering Research Council of Canada) Discovery Grant, British Columbia-China Innovation and Commercialization Strategic Development Program (ICSD-2007-Tang-Y) and an open grant of the State Key Laboratory of Satellite Ocean Environment Dynamics, Second Institute of Oceanography, P. R. China. The main work was completed during the period that Mr. Ambadan's visit Dr. Youmin Tang in summer 2010. Mr. Ambadan would like to acknowledge and thank the International Max-Planck Research School on Earth System Modelling (IMPRS-ESM), Max-Planck Institute for Meteorology (MPI-M), and Dr. Luis Kornbluh for making this visit possible, and for their continued support. Mr. Ambadan would also like to acknowledge and thank the Oregon Graduate Institute, Dr. Eric A. Wan and Dr. Rudolph Van der Merwe for providing the ReBEL [Van der Merwe and Wan, 2003] tool kit, part of which has been used in for the research work described in this Chapter.



# Conclusions

## 6.1 Summary of Results and Conclusions

This thesis primarily addressed the importance of estimating the model uncertainties associated with kinetic energy (KE) dissipations in a Numerical Weather Prediction (NWP) model and of incorporating the same in an ensemble data assimilation system. The operational global weather forecast model GME of the *Deutscher Wetterdienst* (DWD) and the hybrid 3D VAR - Local Ensemble Transform Kalman Filter (LETKF) are used as the test-bed for this study. This thesis work is unique in the following aspects: 1) it gave an independent evaluation of model uncertainty associated with KE dissipation in GME compared to other operational weather forecast models (ECMWF, NCEP, CMC); 2) it led to the development of the first stochastic parameterization (or stochastic physics) scheme based on kinetic energy backscatter for the operational global weather forecast model GME of DWD; 3) it gave a comprehensive study of different KE dissipation component in the backscatter scheme and its impacts on the GME-EPS medium range forecast as well as on the 3D VAR - LETKF assimilation system; and 4) it substantially contributed towards the development of an operational GME-EPS.

### 6.1.1 Impact of the SKEB on the KE Spectra and on the GME forecast

In summary, we have proved that: 1) the stochastic kinetic energy backscatter (SKEB) scheme is very effective in tapping the model error and associated uncertainties in the GME model, and 2) the quantified (approximated) model uncertainty can later be used to provide dynamical feedbacks through the backscatter scheme, improving the model forecast significantly. The following are the specific results concerning the impact of SKEB on the GME model forecast.

1. As shown by the KE spectra of the horizontal wind of the GME forecast, the backscatter injects the energy back into the model near the meso-scales, effectively contributing to the  $k^{-5/3}$  part of the spectrum.
2. The reason for the dampening of the tail of the GME KE spectrum is due to the lack of proper divergent components in the backscatter scheme.

3. Incorporating KE dissipation through the stochastic backscatter scheme produces significantly better forecast results compared to random perturbations.
4. Forecast experiments which incorporate KE dissipation due to numerical diffusion, deep convection and small-scale orographic gravity wave drag are the best for generating a large ensemble spread.
5. Regarding the GME forecast: the SKEB scheme significantly improves the temperature forecast over ten-days, at all pressure levels.
6. Forecast results of geopotential height, specific humidity and surface pressure show significant improvement over short to medium-range (up to 60 hours) but show mixed results for long-range forecast.
7. The backscatter scheme has a significant positive effect on the precipitation forecast, especially in the Tropics

### **6.1.2 Impacts of SKEB on the LETKF Analysis and on the GME-EPS Forecast**

We have proposed and implemented a stochastic KE backscatter (SKEB) scheme as an alternative to the current additive and multiplicative covariance inflation schemes in the LETKF assimilation system for the GME-EPS. Since the SKEB scheme has a positive impact on the ensemble spread, which implies inflation of covariance, we expected a significant positive impact on the LETKF analysis and EPS forecast. However, the combined effect of the initial uncertainty and of other mechanisms in the LETKF assimilation resulted in negative impacts on the backscatter contributions, hence in a deterioration of the analysis and EPS forecast quality. The following are the main conclusions concerning the impact of SKEB on the LETKF analysis and on the GME-EPS forecasts.

#### **6.1.2.1 Impacts of SKEB on the LETKF Analysis**

1. Overall the backscatter scheme found has a negative impact on the LETKF analysis although the backscatter has a positive impact on the background covariance inflation
2. For 850 hPa temperature, the analysis RMSE is relatively larger in the extratropics but smaller in the Tropics, which indicates slight improvement in the Tropics.
3. The SKEB scheme has significant negative impacts on the zonal wind, specific humidity, and specific cloud-ice content analysis, although specific humidity analysis is better in the Tropics at lower layers.
4. For experiments with additive inflation and backscatter the results are no better than the one without backscatter at the lower levels but they are worse at the upper levels.

5. Experiments with multiplicative inflation are the worst among all experiments with the backscatter scheme.
6. The main reason for the deterioration of LETKF analysis in the experiments with backscatter scheme is the rejection of observations due to the conventional First-Guess check routine in GME-EPS. Or, in other words, fewer observations were assimilated for experiments with backscatter scheme.
7. Another reason for the negative impact of the backscatter on the LETKF analysis is the positive bias in the ensemble probability distribution (in the ensemble space), i.e., probability densities get lower for lower temperatures (and velocities), and are relatively higher for higher temperature (and velocities.), especially in the extra-tropics.

### 6.1.2.2 Impacts of SKEB on the GME-EPS Forecast

1. In GME-EPS, the SKEB scheme has negative impacts on the forecast for most of the prognostic variables in the extra-tropics. However, some variables such as temperature and specific humidity show significant improvement in the Tropics.
2. Almost all GME-EPS experiments with the SKEB scheme, except the experiment with backscatter with multiplicative inflation, show an increase in the ensemble spread
3. The main cause of the negative impact of backscatter mechanism on GME-EPS is the combined effects of the LETKF assimilation (which generates sub-optimal analysis) and of initial uncertainty, which effectively changes the probability density distribution.
4. Incorporating the model uncertainty alone (i.e. without in initial set of ensemble) can produce good short-range forecasts, proving the positive impact of the backscatter scheme on the GME forecast (without the assimilation system).
5. The current inflation mechanism in the GME-EPS assimilation system has negative effects on the backscatter contribution of the ensemble spread.
6. The GME-EPS with the backscatter shows a significant improvement on the precipitation forecast, especially in the Tropics

## 6.2 Outlook

A couple of key issues related to the SKEB scheme have been identified that must be addressed in the near future. A first issue is related to the computational problems associated with the cellular automated stochastic pattern generator in the SKEB scheme. In the following subsection we briefly describe a new approach for generating stochastic pattern, which is relatively simple compared to the CA scheme. The second issue concerns the covariance inflation in 3D VAR - LETKF assimilation using the backscatter scheme including first-guess (FG) filtering during the observation preprocessing. In

the current implementation, unlike other covariance inflation schemes, the assimilation system has no direct information regarding the contribution of the backscatter. It is possible to formulate a covariance inflation factor (such  $\rho$  in the multiplicative inflation scheme) from the backscatter scheme which can be later used in the LETKF to adjust the covariance matrix. Also, it would be interesting to determine whether incorporating the first-guess (FG) spread information in the FG check criteria given by Eq.(4.8) reduces the number of rejected observations.

### 6.2.1 Stochastic Pattern Generators

The main disadvantages of the cellular automation (CA) scheme are: i) the difficulties in the design of appropriate automation rules for the model, and ii) the excessive computing time needed for the CA spin-up. These issues motivated us to design a simple scheme for generating the random spatial pattern for GME. The kinetic energy spectra of the streamfunction forcing from the cellular automated SKEB scheme (shown in Fig. (3.5)) indicate that the backscatter forcing may be considered as a *blue noise* which has roughly a  $5/3$  dependence. This leads to the development of a much simple stochastic pattern generator for the GME-SKEB scheme based on a power-law. The basic idea is to generate a *blue noise* field which has a spectral slope of  $k^{5/3}$  (contrary to  $k^{-5/3}$  cascade) and then modulate the *blue noise* with the total dissipation to form the backscatter fraction. The main advantage of using such a scheme is that there is only one tuning parameter compared to the CA, and there is no need of complicated automation rules. The scheme is computationally simpler as it does not require any spin-up runs. An example of the random stream-function forcing patterns using the power-law scheme is shown in Fig. (6.1: left). Fig. (6.1: right) also shows the KE

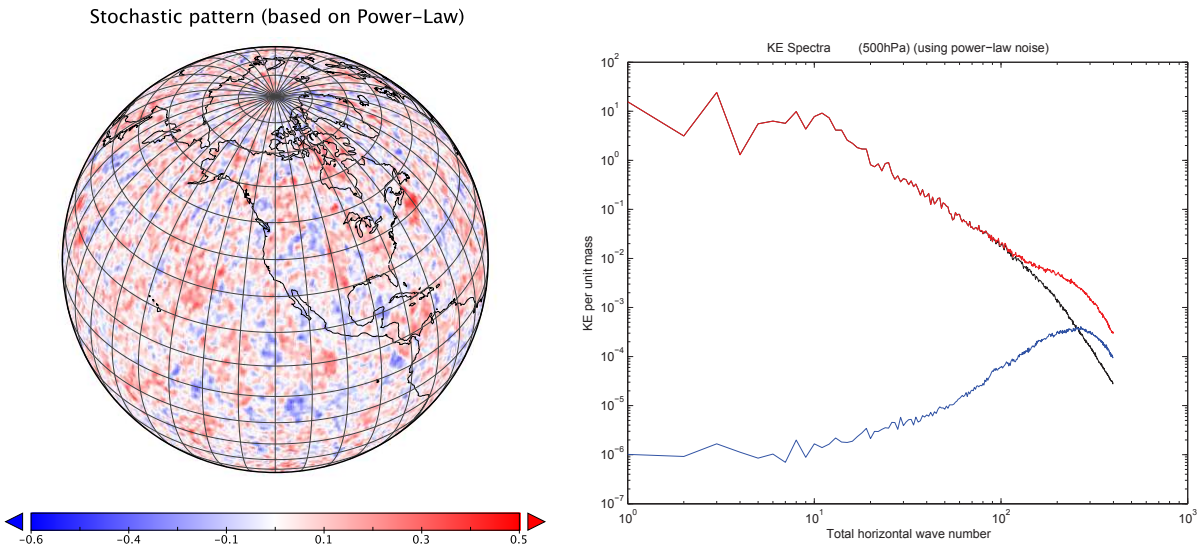


**Figure 6.1:** *Stochastic stream-function forcing pattern (left) and corresponding GME Kinetic energy spectra at 500 hPa*

spectra of the horizontal wind at 500 hPa from the GME 6 hour forecast using the power-law scheme. The black curve is the KE spectrum without the SKEB scheme;

the red curve is that with the power-law scheme, and the blue curve represents the KE spectrum of the backscatter energy. The spectra shows the effectiveness of this new scheme which can backscatter the energy back into model partially contributing to the  $k^{-5/3}$  part of the spectrum. Here also, the quick dampening of the tail of the KE spectrum (red line) is due to the lack of proper divergent component in the backscatter forcing.

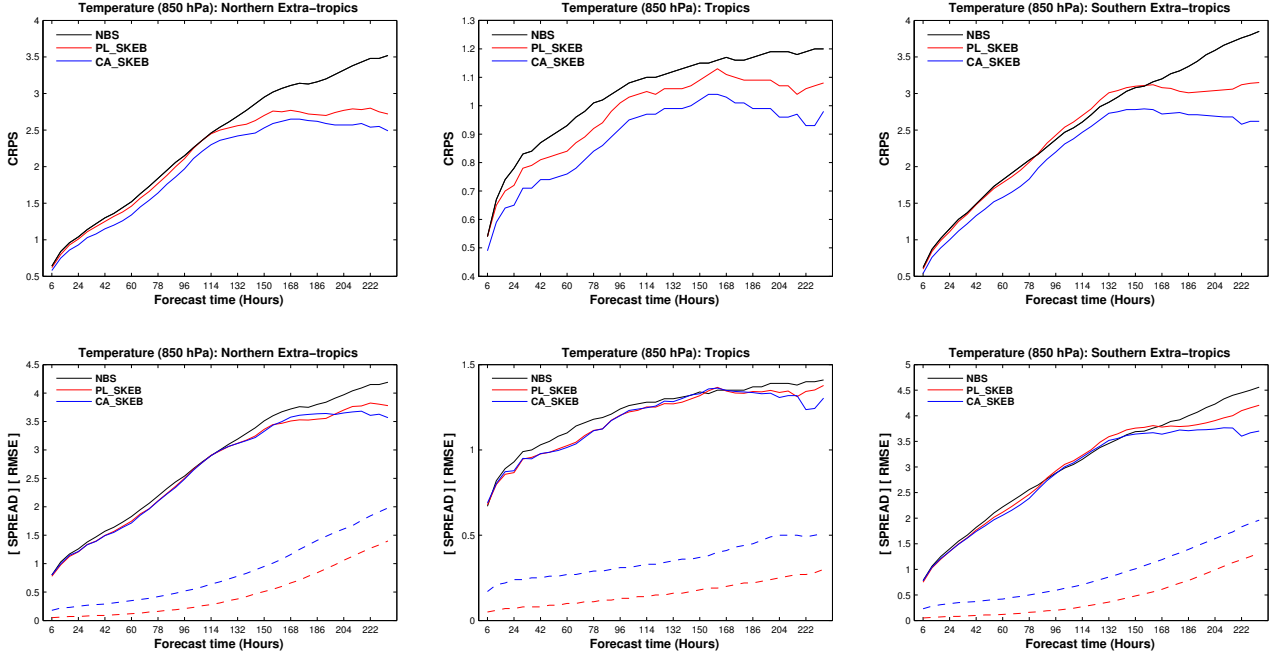


**Figure 6.2:** Ten days forecast statistics for 850 hPa temperature. Top-row: CRPS, Bottom-row: RMSE (solid lines), and SPREAD (dashed lines); for Northern extra-tropics, the Tropics, and the Southern extra-tropics (left to right).

Figure (6.2) shows some of the initial results of the GME 10-day forecast for the 850 hPa temperature field using the new power-law scheme (red line). The top-row of Fig. (6.2) shows the Continuous Ranked Probability Scores (CRPS) and the bottom-row shows the RMSE (solid line) and the ensemble SPREAD (dashed line) for the Northern extra-tropics, the Tropics, and the Southern extra-tropics (left to right). From the results it is clear that although the power-law scheme [PL\_SKEB] is not better than the cellular automated scheme [CA\_SKEB], it is still better than the forecast without any backscatter scheme [NBS]. It should also be noted that this initial experiment setup [PL\_SKEB] was not very well tuned compared to [CA\_SKEB]. Nevertheless, our results are promising and it may be possible to achieve equivalent or relatively better performances by appropriately tuning the scheme. There is no doubt that much additional research is needed to applying these techniques in the 3D VAR - LETKF assimilation systems. It is left for future research.

As a final remark, in this thesis work, we explored the possibilities of quantifying the model uncertainty associated with the KE dissipation and also the ways to incorporate it in an ensemble Kalman filter-based data assimilation system. Although limitations

were found, the present study represents a step forward in developing robust ensemble prediction systems (EPS) for short-to-medium range weather forecast.

## The LETKF Algorithm

I. Ensemble initialization: for each ensemble member,  $m = 1 \dots M$

$$\boldsymbol{\theta}_{0,m}^a = \mathbb{E}(\boldsymbol{\theta}_{0,m}) \quad (\text{A.1})$$

II. For time  $k = 1, 2 \dots$

1. Time update equations:

$$\boldsymbol{\theta}_{k,m}^b = \mathbf{f}(\boldsymbol{\theta}_{k-1,m}^a) \quad (\text{A.2})$$

$$\bar{\boldsymbol{\theta}}_k^b = \frac{1}{M} \sum_{m=1}^M \boldsymbol{\theta}_{k,m}^b \quad (\text{A.3})$$

$$\mathbf{P}_k^b = \frac{1}{M-1} \sum_{m=1}^M \left[ (\boldsymbol{\theta}_{k,m}^b - \bar{\boldsymbol{\theta}}_k^b) (\boldsymbol{\theta}_{k,m}^b - \bar{\boldsymbol{\theta}}_k^b)^\top \right] \quad (\text{A.4})$$

$$= \frac{1}{M-1} \sum_{m=1}^M \boldsymbol{\Theta}_k (\boldsymbol{\Theta}_k)^\top \quad (\text{A.5})$$

2. Measurement update equations:

(a) Apply  $\mathbf{h}$  operator to the background ensemble,  $\boldsymbol{\theta}_{k,m}^b$

$$\boldsymbol{\psi}_{k,m}^b = \mathbf{h}(\boldsymbol{\theta}_{k,m}^b) \quad (\text{A.6})$$

$$\bar{\boldsymbol{\psi}}_k^b = \frac{1}{N} \sum_{n=1}^N \boldsymbol{\psi}_{k,m}^b \quad (\text{A.7})$$

$$\boldsymbol{\Psi}_k = \boldsymbol{\psi}_k^o - \bar{\boldsymbol{\psi}}_k^b \quad (\text{A.8})$$

(b) Compute the weight matrix:

$$\tilde{\mathbf{P}}_k^a = \left[ (N-1) \mathbf{I} + (\boldsymbol{\Psi}_k)^\top \mathbf{R}^{-1} \boldsymbol{\Psi}_k \right]^\top \quad (\text{A.9})$$

$$\mathbf{w}^a = \tilde{\mathbf{P}}_k^a (\boldsymbol{\Psi}_k)^\top \mathbf{R}^{-1} (\boldsymbol{\psi}_k^o - \bar{\boldsymbol{\psi}}_k^b) \quad (\text{A.10})$$

(c) Calculate the analysis:

$$\bar{\boldsymbol{\theta}}_k^a = \bar{\boldsymbol{\theta}}_k^b + \boldsymbol{\Theta}_k \mathbf{w}^a \quad (\text{A.11})$$

In the LETKF the computation of the background error covariance given by Eq.(A.4) is not necessary since it is not used for the calculation of analysis.

## Least square formulation of Kalman gain

The state update equation for the state space model (2.1)-(2.2) is given by,

$$\hat{\boldsymbol{\theta}}_k = \hat{\boldsymbol{\theta}}_k^- + \mathbf{K}_k(\boldsymbol{\psi}_k - \hat{\boldsymbol{\psi}}_k^-) \quad (\text{B.1})$$

where  $\mathbf{K}_k$  is the Kalman gain. The superscript “-” represents the prior states given by the following equations:

$$\hat{\boldsymbol{\theta}}_k^- = \mathbf{E}[\mathbf{f}(\boldsymbol{\theta}_{k-1}, \mathbf{q}_{k-1})] \quad (\text{B.2})$$

$$\hat{\boldsymbol{\psi}}_k^- = \mathbf{E}[\mathbf{h}(\boldsymbol{\theta}_k^-, \mathbf{r}_k)] \quad (\text{B.3})$$

where  $\mathbf{E}[\cdot]$  represents the mathematical expectation or the expected value. In general, the estimation error is defined as,

$$\tilde{\boldsymbol{\theta}}_k = \boldsymbol{\theta}_k - \hat{\boldsymbol{\theta}}_k \quad (\text{B.4})$$

Similarly the error between the noisy observation  $\boldsymbol{\psi}_k$  and its prediction  $\hat{\boldsymbol{\psi}}_k^-$ , is given by

$$\tilde{\boldsymbol{\psi}}_k = \boldsymbol{\psi}_k - \hat{\boldsymbol{\psi}}_k^- \quad (\text{B.5})$$

Substituting (B.4) into the state update equation (B.1), we can rewrite the estimation error as

$$\begin{aligned} \tilde{\boldsymbol{\theta}}_k &= \boldsymbol{\theta}_k - \hat{\boldsymbol{\theta}}_k^- - \mathbf{K}_k(\boldsymbol{\psi}_k - \hat{\boldsymbol{\psi}}_k^-) \\ &= \tilde{\boldsymbol{\theta}}_k^- - \mathbf{K}_k \tilde{\boldsymbol{\psi}}_k \end{aligned} \quad (\text{B.6})$$

Here we made use of the fact that the estimator is unbiased:

$$\begin{aligned} \mathbf{E}[\tilde{\boldsymbol{\psi}}_k] &= 0 \\ \mathbf{E}[\tilde{\boldsymbol{\theta}}_k] &= 0 \end{aligned} \quad (\text{B.7})$$

Now, the state error covariance,  $\mathbf{P}_{\boldsymbol{\theta}_k}$  and the cross covariance,  $\mathbf{P}_{\boldsymbol{\theta}_k \tilde{\boldsymbol{\psi}}_k}$  between the state

and observation error can be rewritten in terms of equations (B.4) and (B.5) and are given by

$$\mathbf{P}_{\theta_k} = \mathbf{E} \left[ \tilde{\boldsymbol{\theta}}_k \tilde{\boldsymbol{\theta}}_k^{\text{T}} \right] \quad (\text{B.8})$$

$$\mathbf{P}_{\theta_k \tilde{\boldsymbol{\psi}}_k} = \mathbf{E} \left[ \tilde{\boldsymbol{\theta}}_k \tilde{\boldsymbol{\psi}}_k^{\text{T}} \right] \quad (\text{B.9})$$

Taking the outer products and expectation of (B.6) produces

$$\begin{aligned} \mathbf{E} \left[ \tilde{\boldsymbol{\theta}}_k \tilde{\boldsymbol{\theta}}_k^{\text{T}} \right] &= \mathbf{E} \left[ \left( \tilde{\boldsymbol{\theta}}_k^- - \mathbf{K}_k \tilde{\boldsymbol{\psi}}_k \right) \left( \tilde{\boldsymbol{\theta}}_k^- - \mathbf{K}_k \tilde{\boldsymbol{\psi}}_k \right)^{\text{T}} \right] \\ &= \mathbf{E} \left[ \tilde{\boldsymbol{\theta}}_k^- \tilde{\boldsymbol{\theta}}_{k^-}^{\text{T}} \right] - \mathbf{E} \left[ \tilde{\boldsymbol{\theta}}_k^- \tilde{\boldsymbol{\psi}}_k^{\text{T}} \mathbf{K}_k^{\text{T}} \right] - \mathbf{E} \left[ \mathbf{K}_k \tilde{\boldsymbol{\psi}}_k \tilde{\boldsymbol{\theta}}_{k^-}^{\text{T}} \right] + \mathbf{E} \left[ \mathbf{K}_k \tilde{\boldsymbol{\psi}}_k \tilde{\boldsymbol{\psi}}_k^{\text{T}} \mathbf{K}_k^{\text{T}} \right] \end{aligned} \quad (\text{B.10})$$

Using equations (B.8) and (B.9), equation (B.10) can be rewritten as

$$\mathbf{P}_{\theta_k} = \mathbf{P}_{\theta_k}^- - \mathbf{P}_{\theta_k \tilde{\boldsymbol{\psi}}_k} \mathbf{K}_k^{\text{T}} - \mathbf{K}_k \mathbf{P}_{\tilde{\boldsymbol{\psi}}_k \theta_k} + \mathbf{K}_k \mathbf{P}_{\tilde{\boldsymbol{\psi}}_k} \mathbf{K}_k^{\text{T}} \quad (\text{B.11})$$

Our aim is to minimize the trace of  $\mathbf{P}_{\theta_k}$  for the unbiased estimator, i.e.

$$\frac{\partial}{\partial \mathbf{K}_k} (\text{Tr}(\mathbf{P}_{\theta_k})) = 0 \quad (\text{B.12})$$

We have

$$\text{Tr}(\mathbf{P}_{\theta_k}) = \text{Tr}(\mathbf{P}_{\theta_k}^- - \mathbf{P}_{\theta_k \tilde{\boldsymbol{\psi}}_k} \mathbf{K}_k^{\text{T}} - \mathbf{K}_k \mathbf{P}_{\tilde{\boldsymbol{\psi}}_k \theta_k} + \mathbf{K}_k \mathbf{P}_{\tilde{\boldsymbol{\psi}}_k} \mathbf{K}_k^{\text{T}}) \quad (\text{B.13})$$

$$= \text{Tr} \left[ \left( \mathbf{K}_k - \mathbf{P}_{\theta_k \tilde{\boldsymbol{\psi}}_k} \mathbf{P}_{\tilde{\boldsymbol{\psi}}_k}^{-1} \right) \mathbf{P}_{\tilde{\boldsymbol{\psi}}_k} \left( \mathbf{K}_k - \mathbf{P}_{\theta_k \tilde{\boldsymbol{\psi}}_k} \mathbf{P}_{\tilde{\boldsymbol{\psi}}_k}^{-1} \right)^{\text{T}} \right] + \text{Tr} \left( \mathbf{P}_{\theta_k}^- - \mathbf{P}_{\theta_k \tilde{\boldsymbol{\psi}}_k} \mathbf{P}_{\tilde{\boldsymbol{\psi}}_k}^{-1} \mathbf{P}_{\theta_k \tilde{\boldsymbol{\psi}}_k}^{\text{T}} \right) \quad (\text{B.14})$$

We want to choose  $\mathbf{K}_k$  in order to minimize (B.11). It can be easily verified that the above expression<sup>1</sup> (B.11) is minimum when

$$\mathbf{K}_k = \mathbf{P}_{\theta_k \tilde{\boldsymbol{\psi}}_k} \mathbf{P}_{\tilde{\boldsymbol{\psi}}_k}^{-1} \quad (\text{B.15})$$

Here we have used the following identities,

$$\frac{\partial}{\partial \mathbf{A}} (\text{Tr}(\mathbf{A} \mathbf{B} \mathbf{A}^{\text{T}})) = 2 \mathbf{A} \mathbf{B} \quad (\text{B.16})$$

where  $\mathbf{B}$  is symmetric, and

$$\frac{\partial}{\partial \mathbf{A}} (\text{Tr}(\mathbf{A} \mathbf{C}^{\text{T}})) = \frac{\partial}{\partial \mathbf{A}} (\text{Tr}(\mathbf{C}^{\text{T}} \mathbf{A})) = \mathbf{C} \quad (\text{B.17})$$

Substituting the expression for Kalman gain, given by equation (B.15) back into the

---

<sup>1</sup>Here we have used the principle  $\text{Tr}(\mathbf{A} \mathbf{B}) = \text{Tr}(\mathbf{B} \mathbf{A})$

expression for the error covariance (B.11), the covariance update equation is given by

$$\mathbf{P}_{\theta_k} = \mathbf{P}_{\theta_k}^- - \mathbf{K}_k \mathbf{P}_{\tilde{\psi}_k} \mathbf{K}_k^T \quad (\text{B.18})$$

It has been shown that the standard Kalman gain used in KF, EKF and EnKF is a special case of Eq. (B.15) when the measurement function is linear or locally linearized, and the noise is additive [Ambadan and Tang, 2009].



# Additional Supporting Figures

## C.1 SKEB: Impact on the GME-ENS Forecast

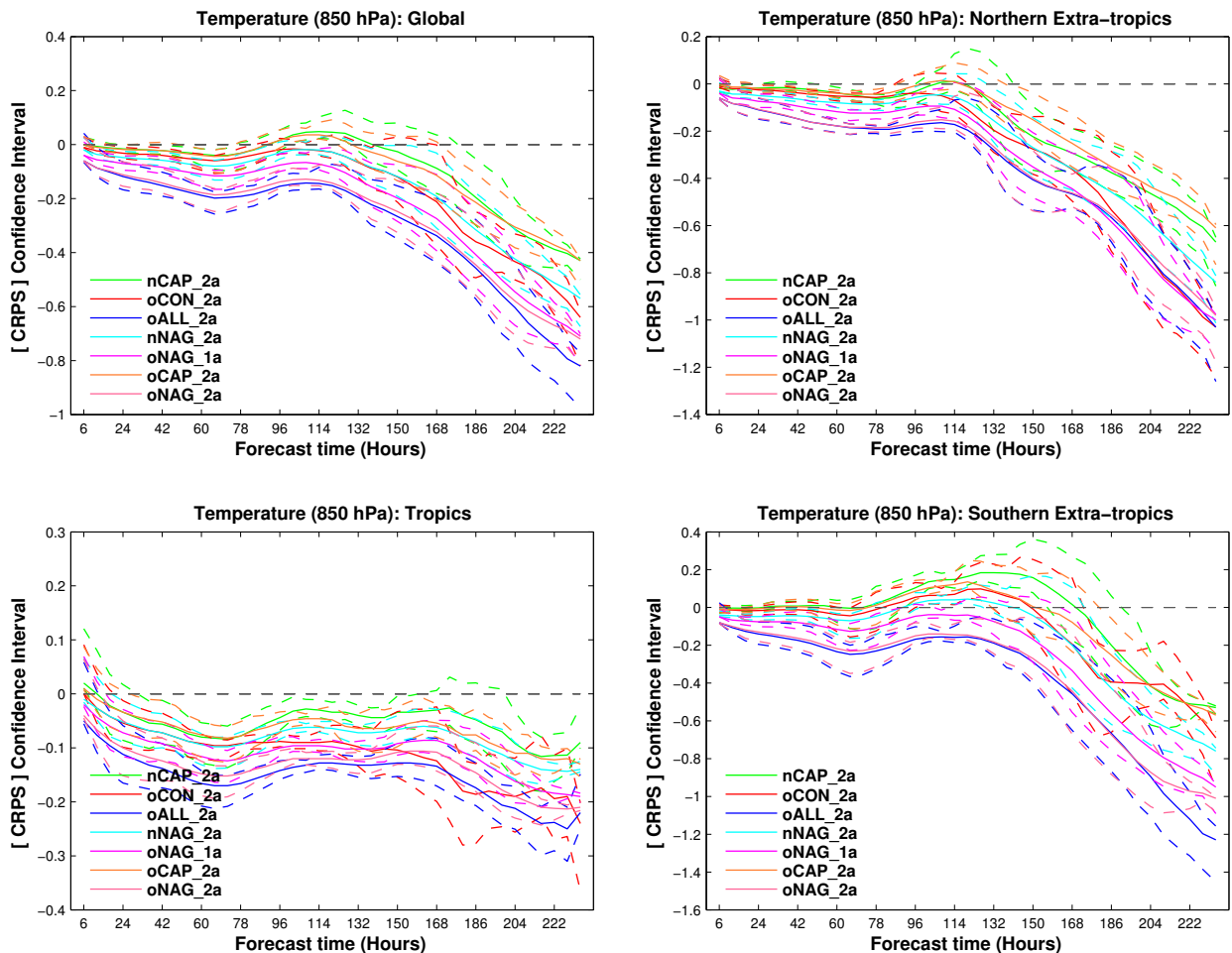


**Figure C.1:** CRPS confidence intervals for 850 hPa temperature, for ten days forecast: Global (Top-Left), the Northern extra-tropics (Top-Right), the Tropics (Bottom-Left), and the Southern extra-tropics (Bottom-Right).

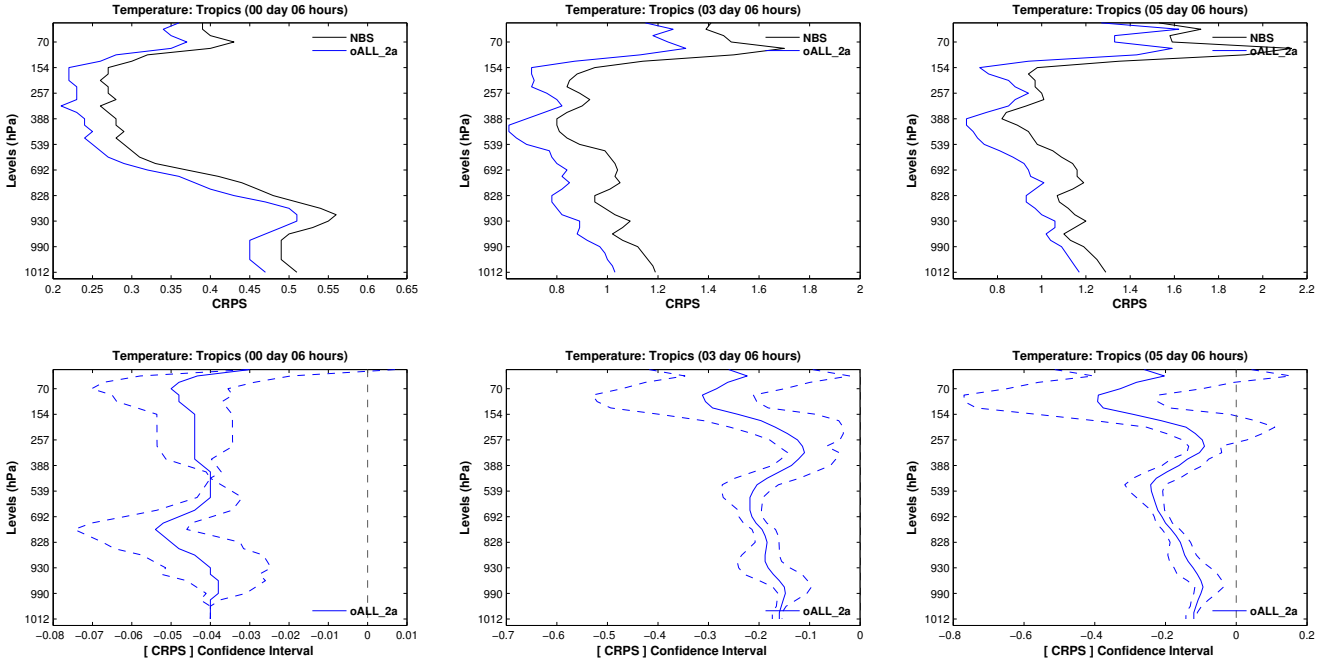


**Figure C.2:** CRPS vertical profile statistics for temperature, for the experiment [oALL\_2a], for the Tropics. Top-row: CRPS, and Bottom-row: corresponding confidence interval; for 6 hours, 3<sup>rd</sup>, and 5<sup>th</sup> day respectively (from left to right).

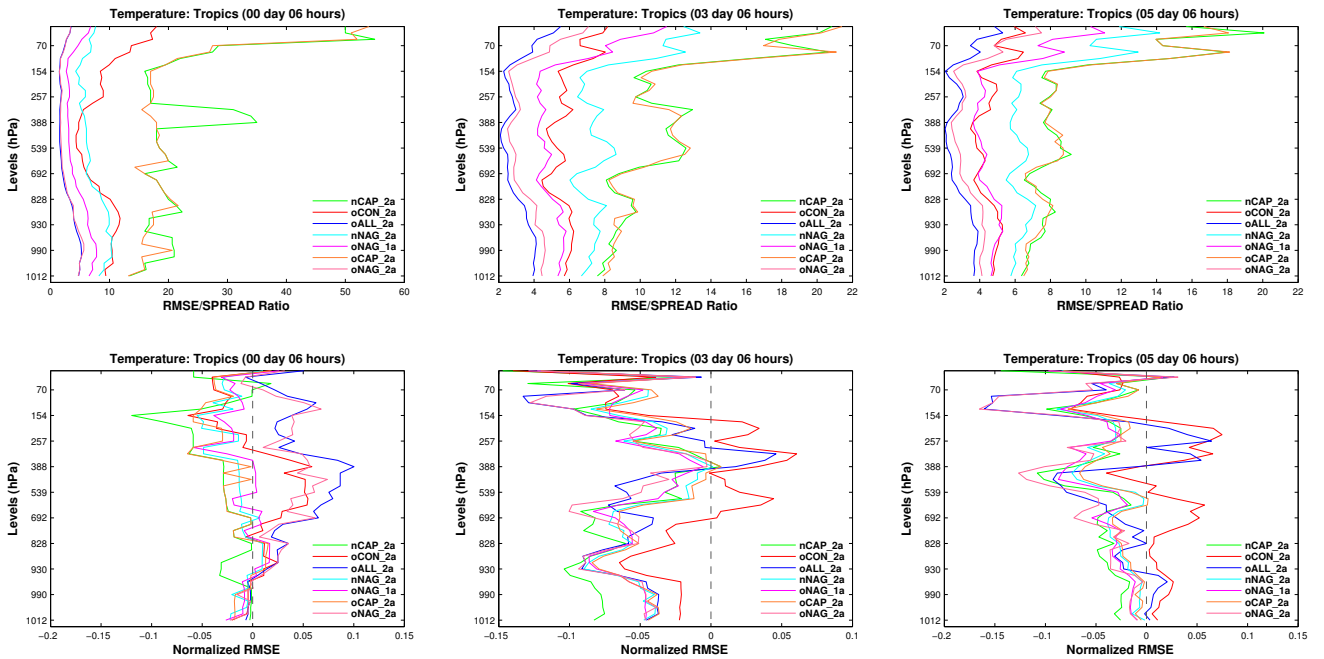


**Figure C.3:** Vertical profiles of RMSE statistics for temperature for the Tropics. Top-row: RMSE/SPREAD ratio; and Bottom-row: Normalized RMSE, for 6 hours, 3<sup>rd</sup>, and 5<sup>th</sup> day (from left to right).

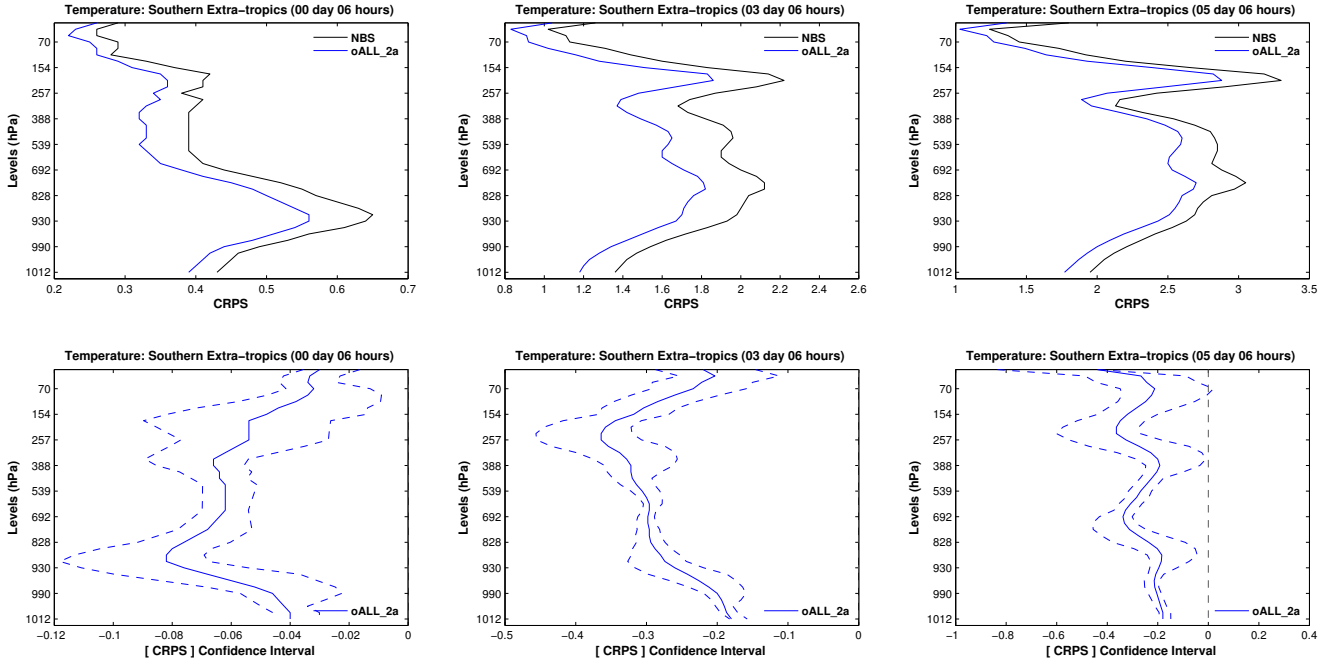


**Figure C.4:** CRPS vertical profile statistics for temperature, for the experiment [oALL\_2a], for the Southern extra-tropics. Top-row: CRPS, and Bottom-row: corresponding confidence interval; for 6 hours, 3<sup>rd</sup>, and 5<sup>th</sup> day respectively (from left to right).

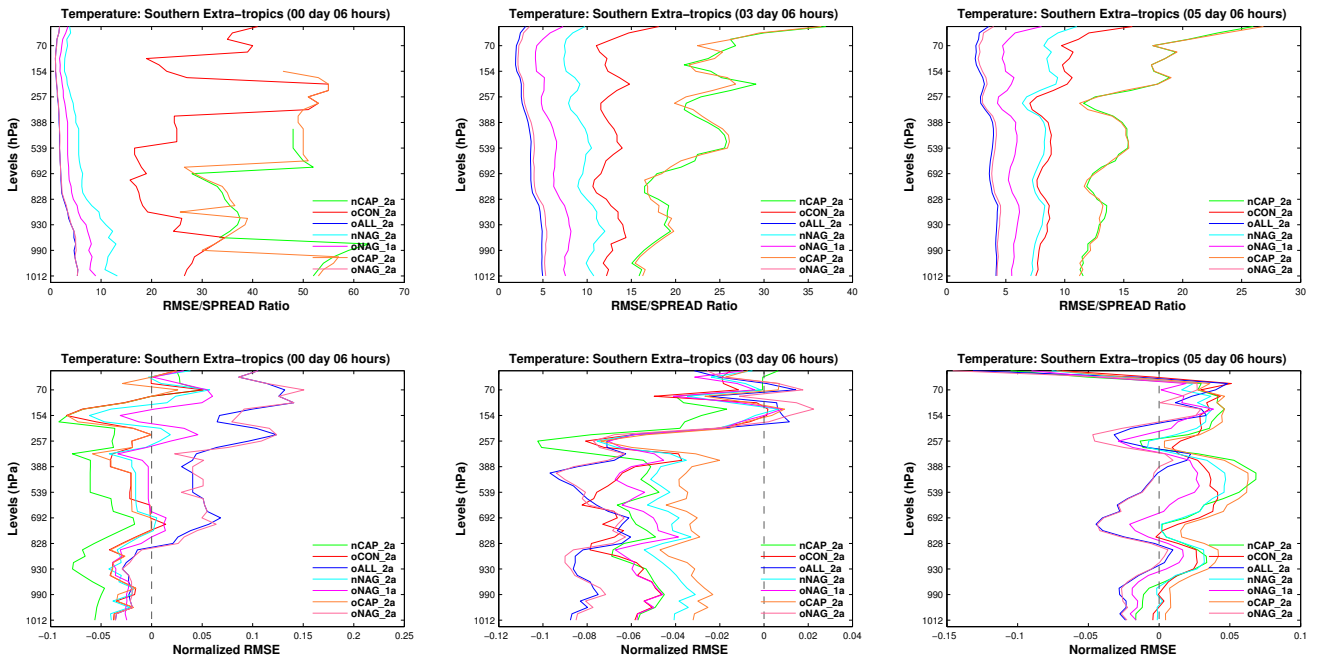


**Figure C.5:** Vertical profiles of RMSE statistics for temperature for the Southern extra-tropics. Top-row: RMSE/SPREAD ratio; and Bottom-row: Normalized RMSE, for 6 hours, 3<sup>rd</sup>, and 5<sup>th</sup> day (from left to right).

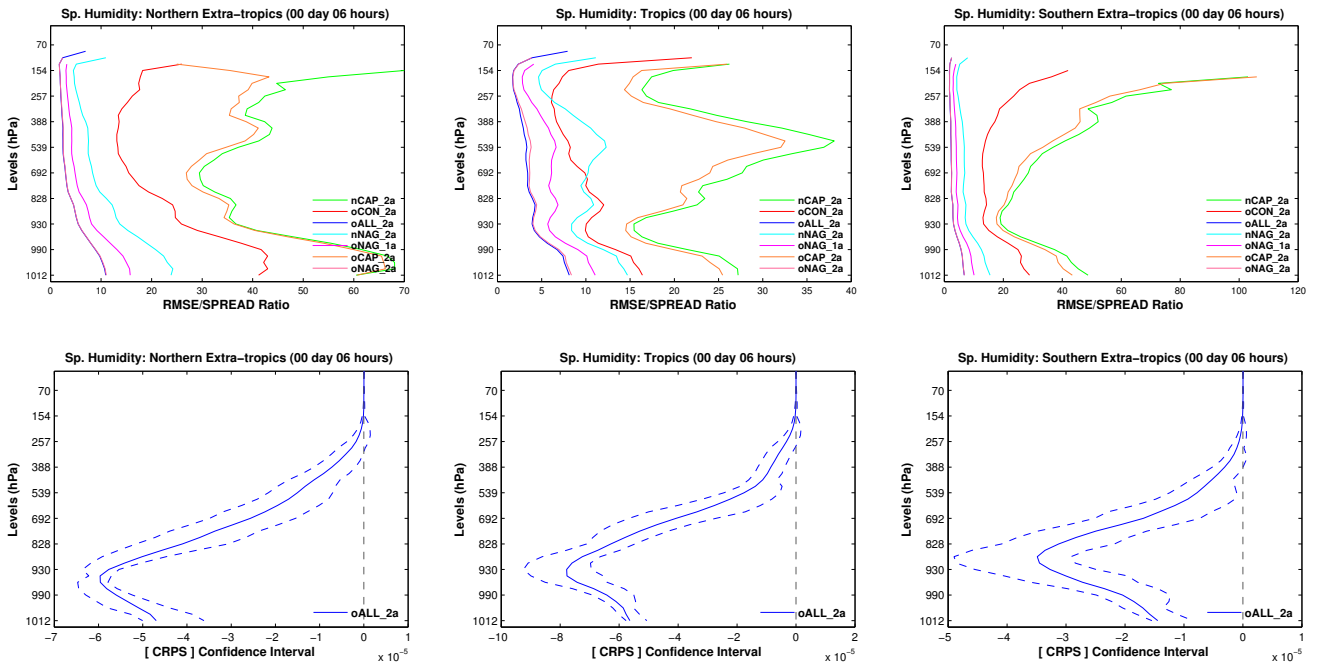


**Figure C.6:** *Specific humidity profiles. Top-row: ten days forecast RMSE, and SPREAD at 850 hPa; Bottom-row: 6 hour forecast CRPS confidence interval for the experiment [oALL\_2a]*

## C.2 SKEB: Impact on the GME-EPS Forecast

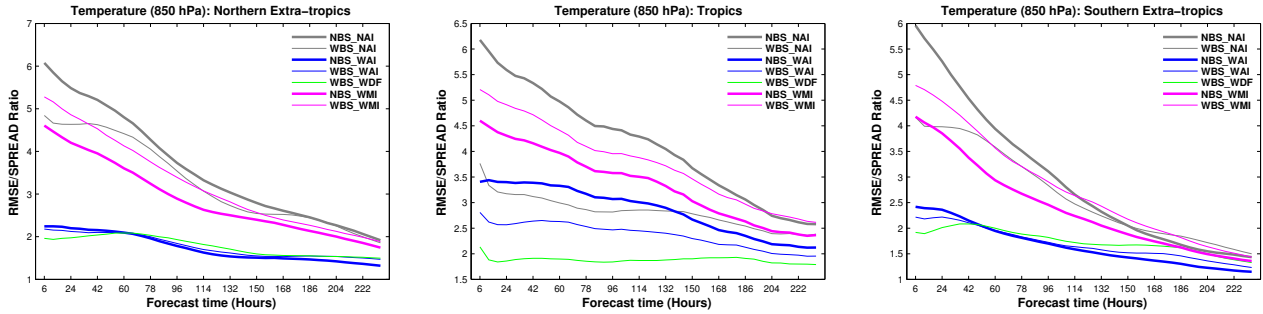


**Figure C.7:** *RMSE/SPREAD ratio statistics for the 850 hPa temperature, ten days forecast; for the the Northern extra-tropics, the Tropics, and the Southern extra-tropics (left to right).*

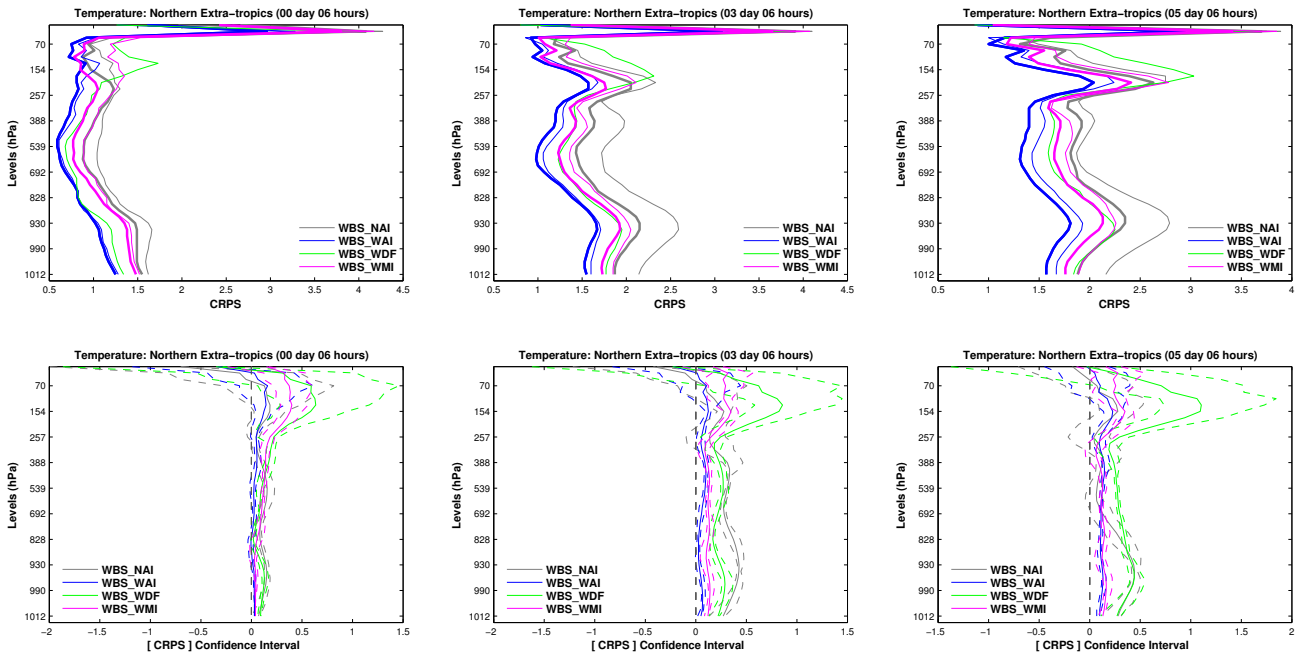


**Figure C.8:** *CRPS vertical profile statistics for temperature, for the Northern extra-tropics. Top-row: CRPS, and Bottom-row: corresponding confidence interval; for 6 hours, 3<sup>rd</sup>, and 5<sup>th</sup> day respectively (from left to right).*

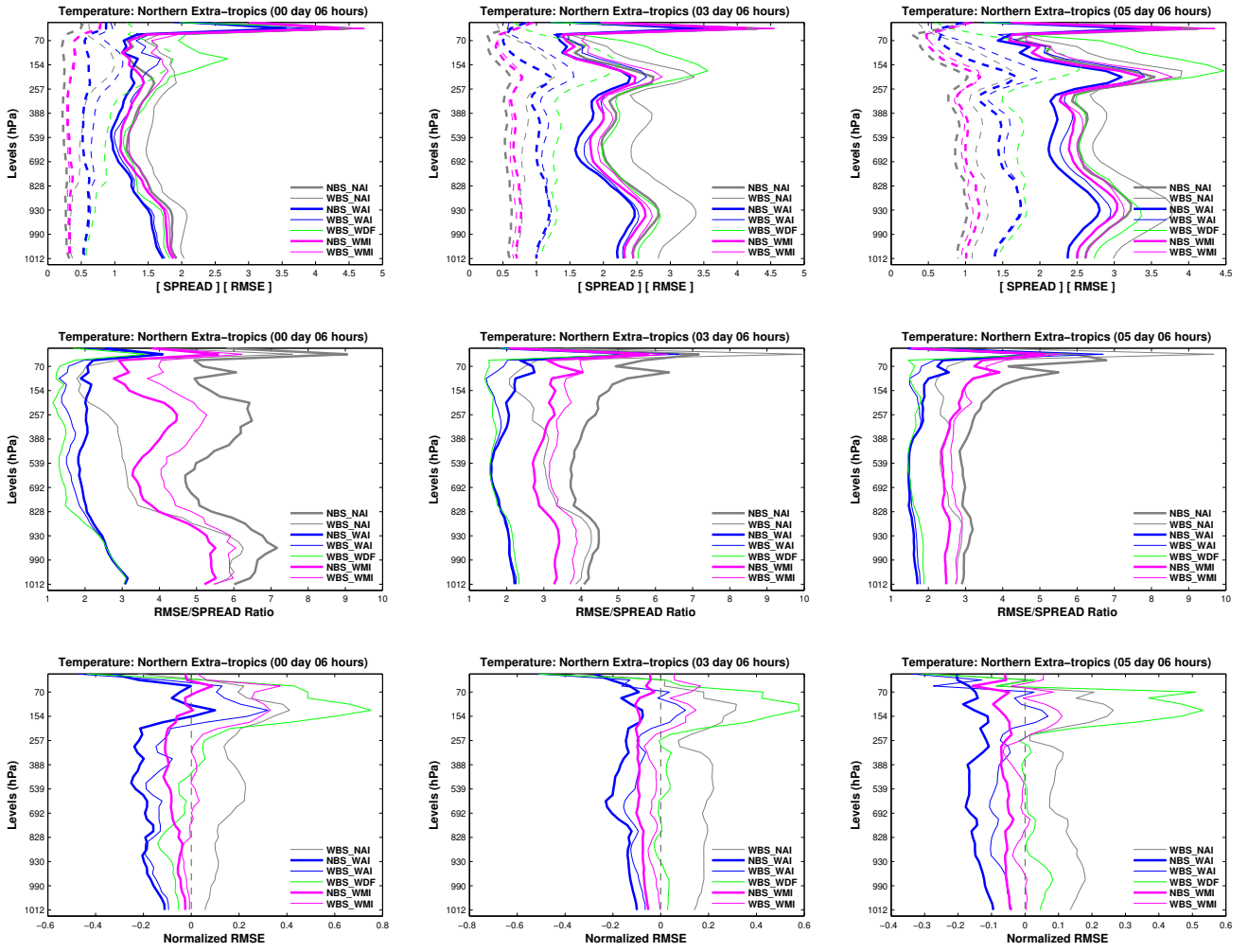


**Figure C.9:** Vertical profiles of RMSE statistics for temperature, for the Northern extra-tropics. Top-row: RMSE and SPREAD, Middle-row: RMSE/SPREAD Ratio, and Bottom-row: Normalized RMSE; for the forecast time 6 hours, 3<sup>rd</sup>, and 5<sup>th</sup> day respectively (from left to right).

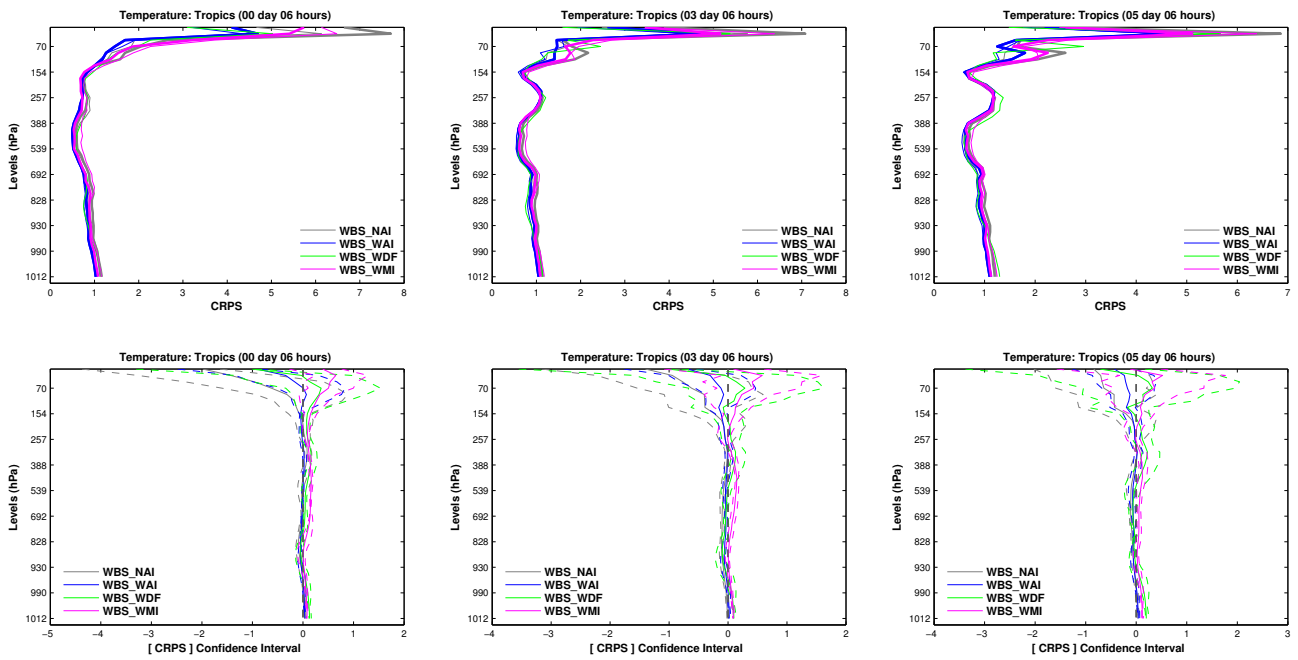


**Figure C.10:** CRPS vertical profile statistics for temperature, for the Tropics. Top-row: CRPS, and Bottom-row: corresponding confidence interval; for 6 hours, 3<sup>rd</sup>, and 5<sup>th</sup> day respectively (from left to right).

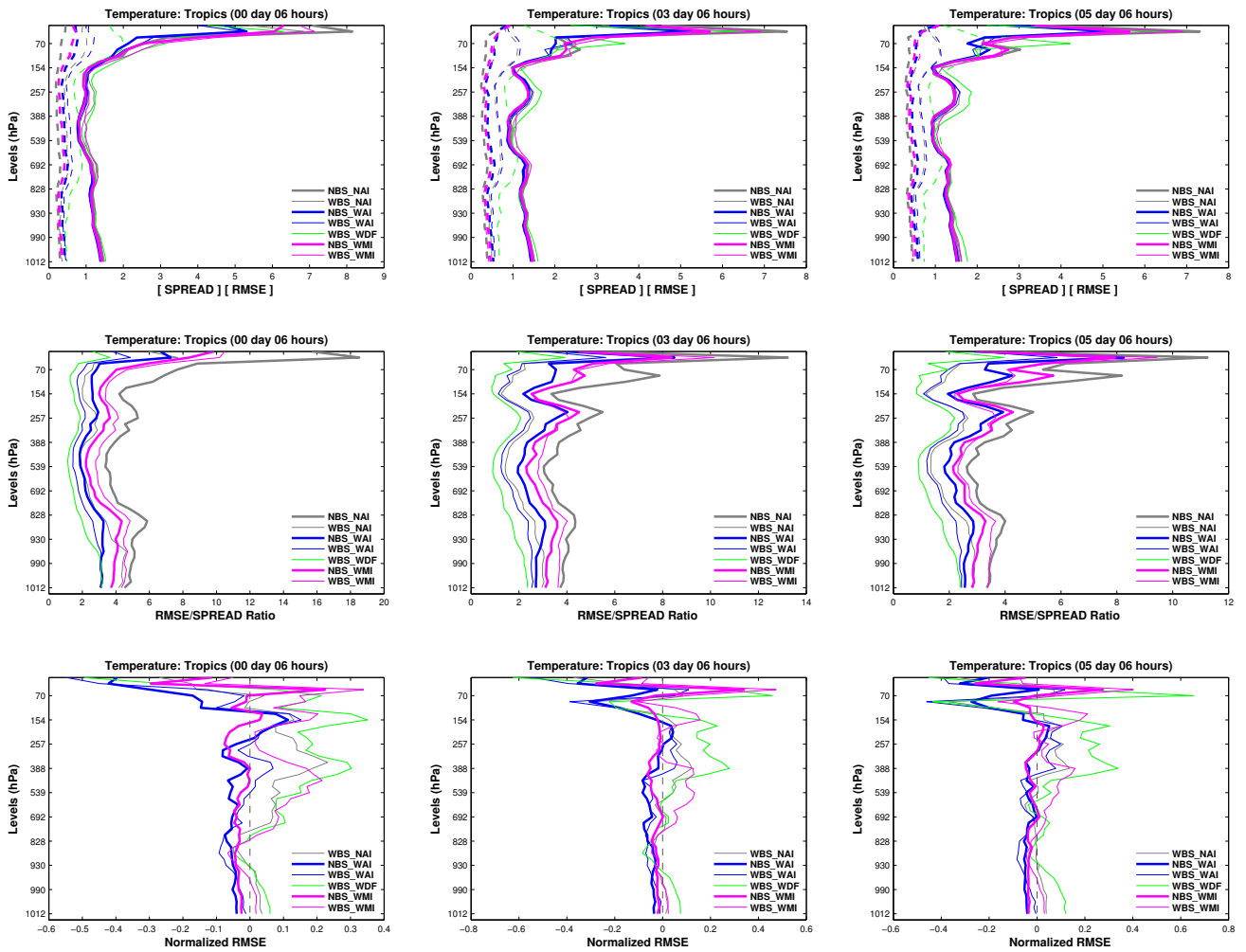


**Figure C.11:** Vertical profiles of RMSE statistics for temperature, for the Tropics. Top-row: RMSE and SPREAD, Middle-row: RMSE/SPREAD Ratio, and Bottom-row: Normalized RMSE; for the forecast time 6 hours, 3<sup>rd</sup>, and 5<sup>th</sup> day respectively (from left to right).

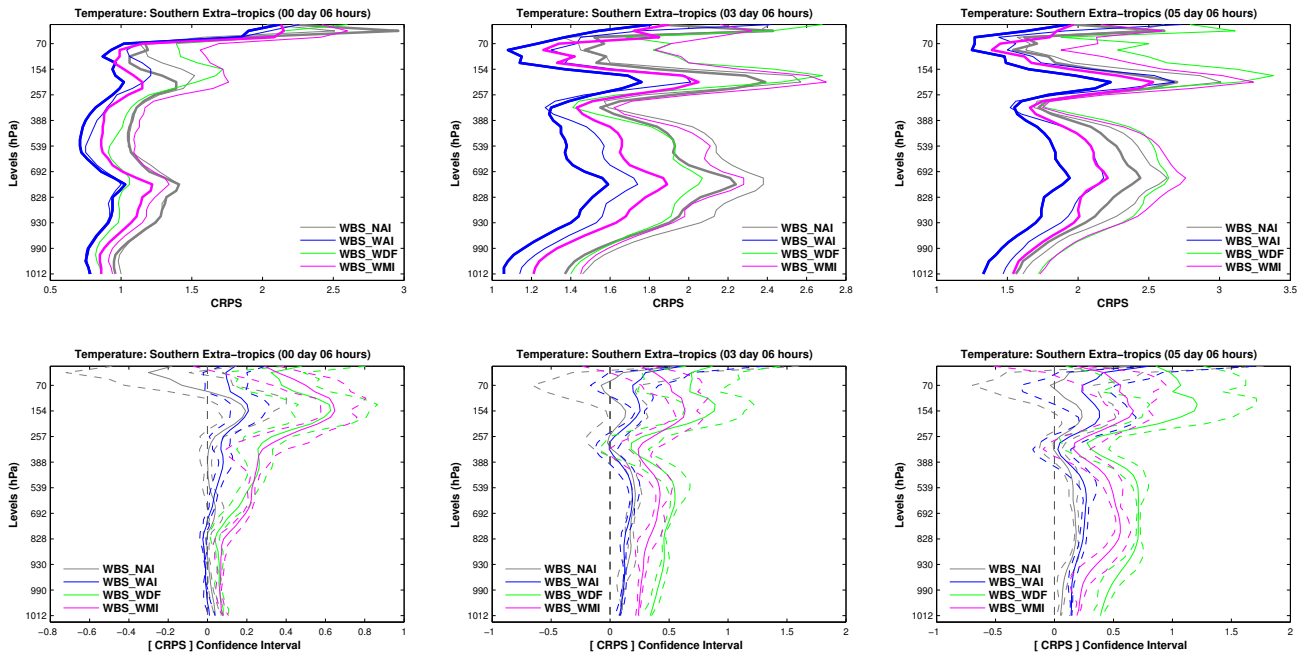


**Figure C.12:** CRPS vertical profile statistics for temperature, for the Southern extra-tropics. Top-row: CRPS, and Bottom-row: corresponding confidence interval; for 6 hours, 3<sup>rd</sup>, and 5<sup>th</sup> day respectively (from left to right).

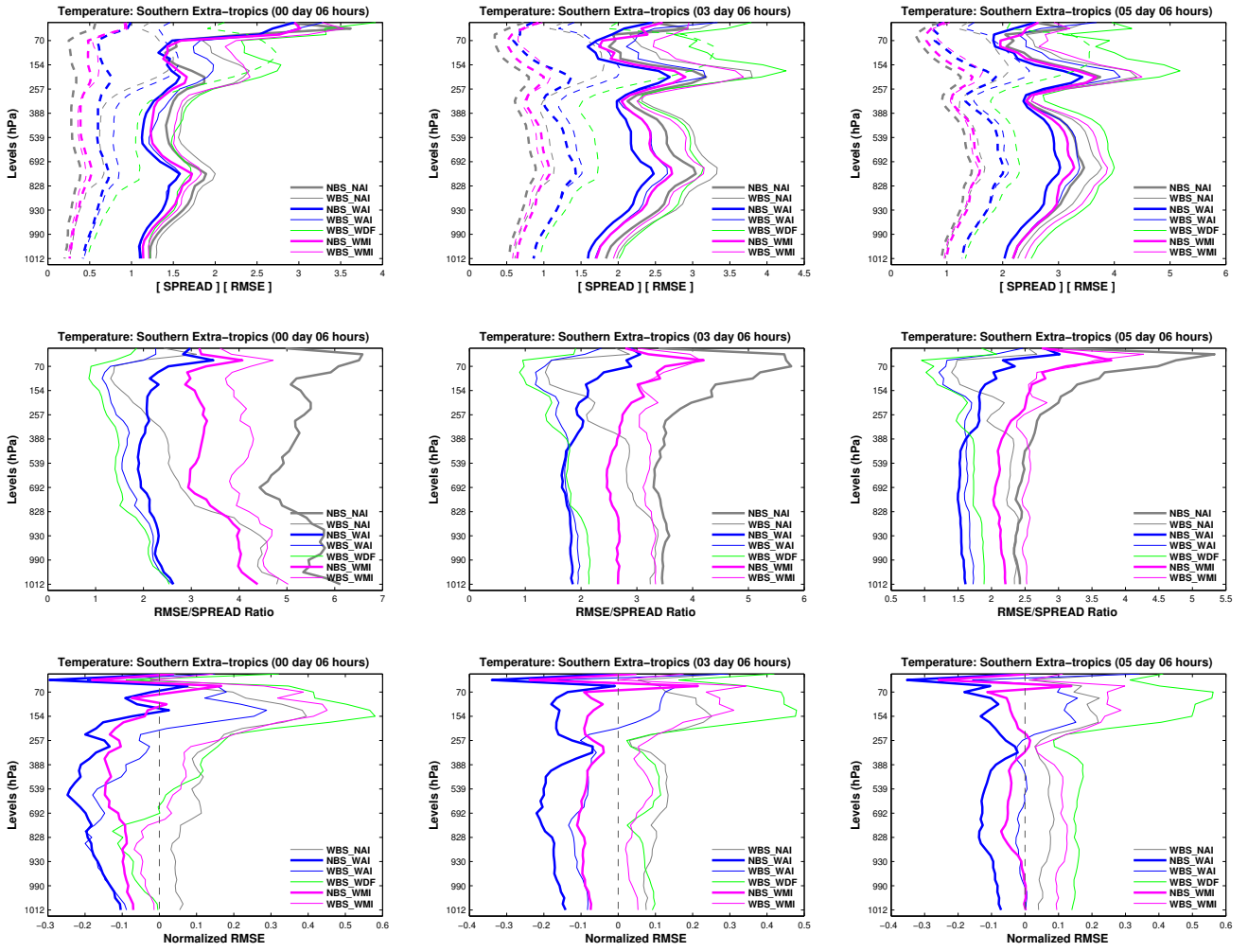


**Figure C.13:** Vertical profiles of RMSE statistics for temperature, for the Southern extra-tropics. Top-row: RMSE and SPREAD, Middle-row: RMSE/SPREAD Ratio, and Bottom-row: Normalized RMSE; for the forecast time 6 hours, 3<sup>rd</sup>, and 5<sup>th</sup> day respectively (from left to right).

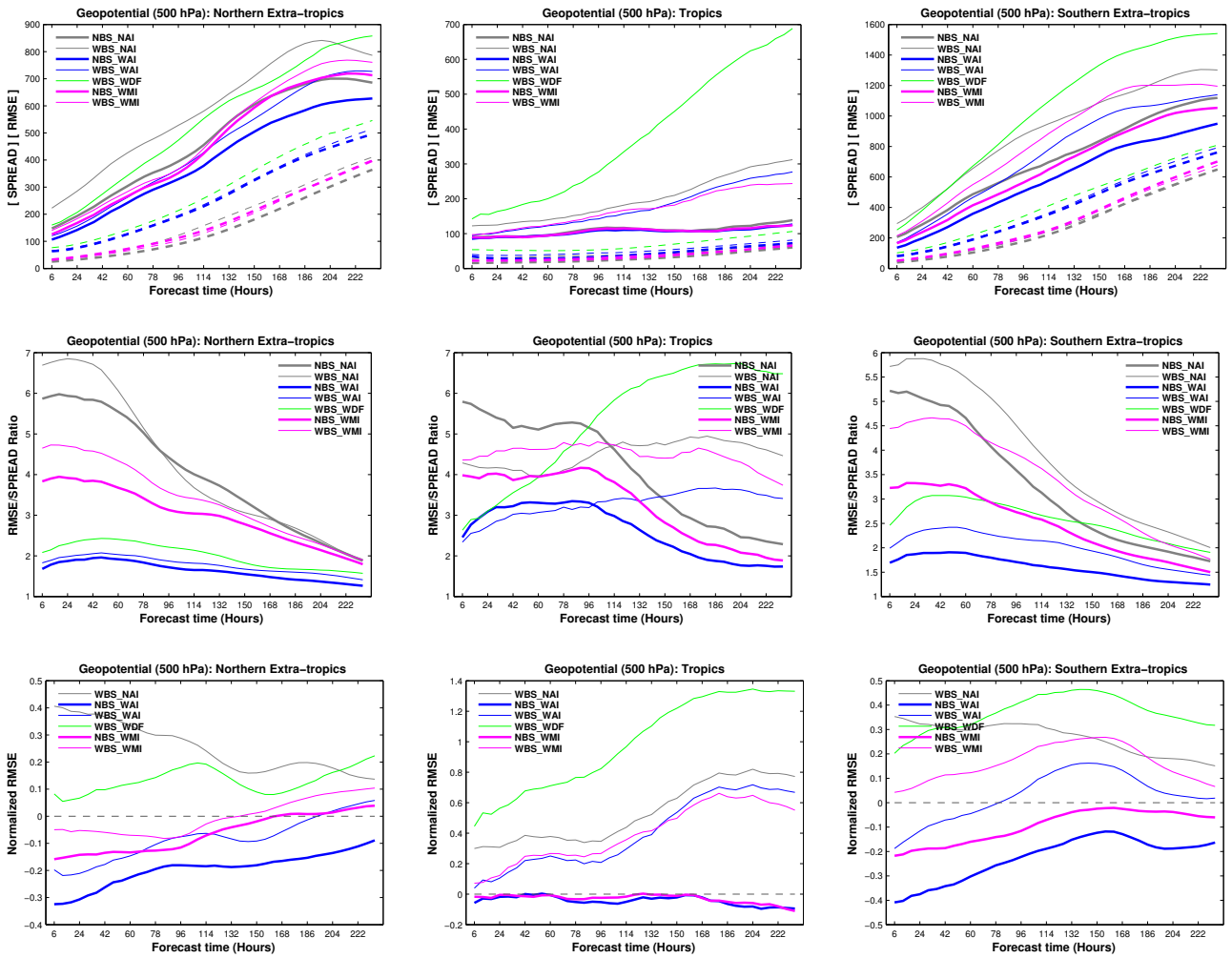


**Figure C.14:** Ten days forecast RMSE statistics for 500 hPa geopotential height. Top row: RMSE (solid) and Ensemble SPREAD; Middle-row: RMSE/SPREAD Ratio; and Bottom-row: Normalized RMSE, for the the Northern extra-tropics, the Tropics and the Southern extra-tropics respectively (from left to right).

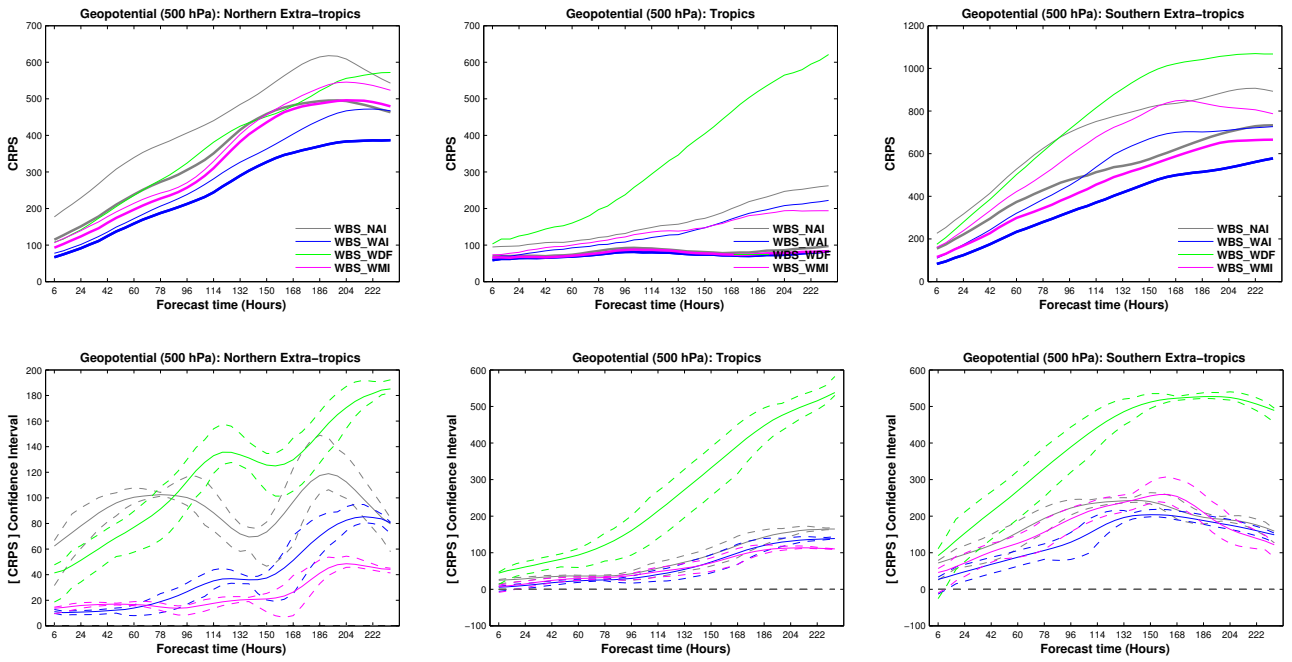


**Figure C.15:** CRPS and confidence interval for 500 hPa geopotential height, for the Northern extra-tropics (left), the Tropics (middle), and the Southern extra-tropics (right)

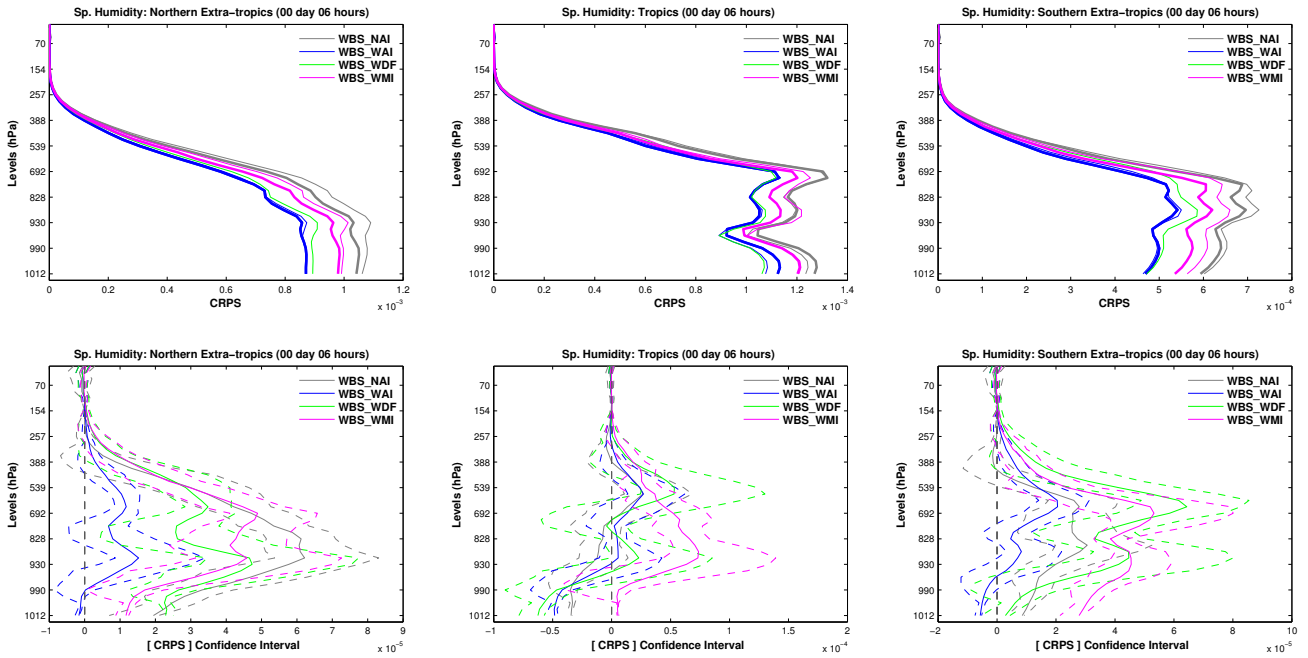


**Figure C.16:** CRPS vertical profiles for specific humidity, for 6 hour forecast. Top-row: CRPS; Bottom-row: corresponding CRPS confidence interval.

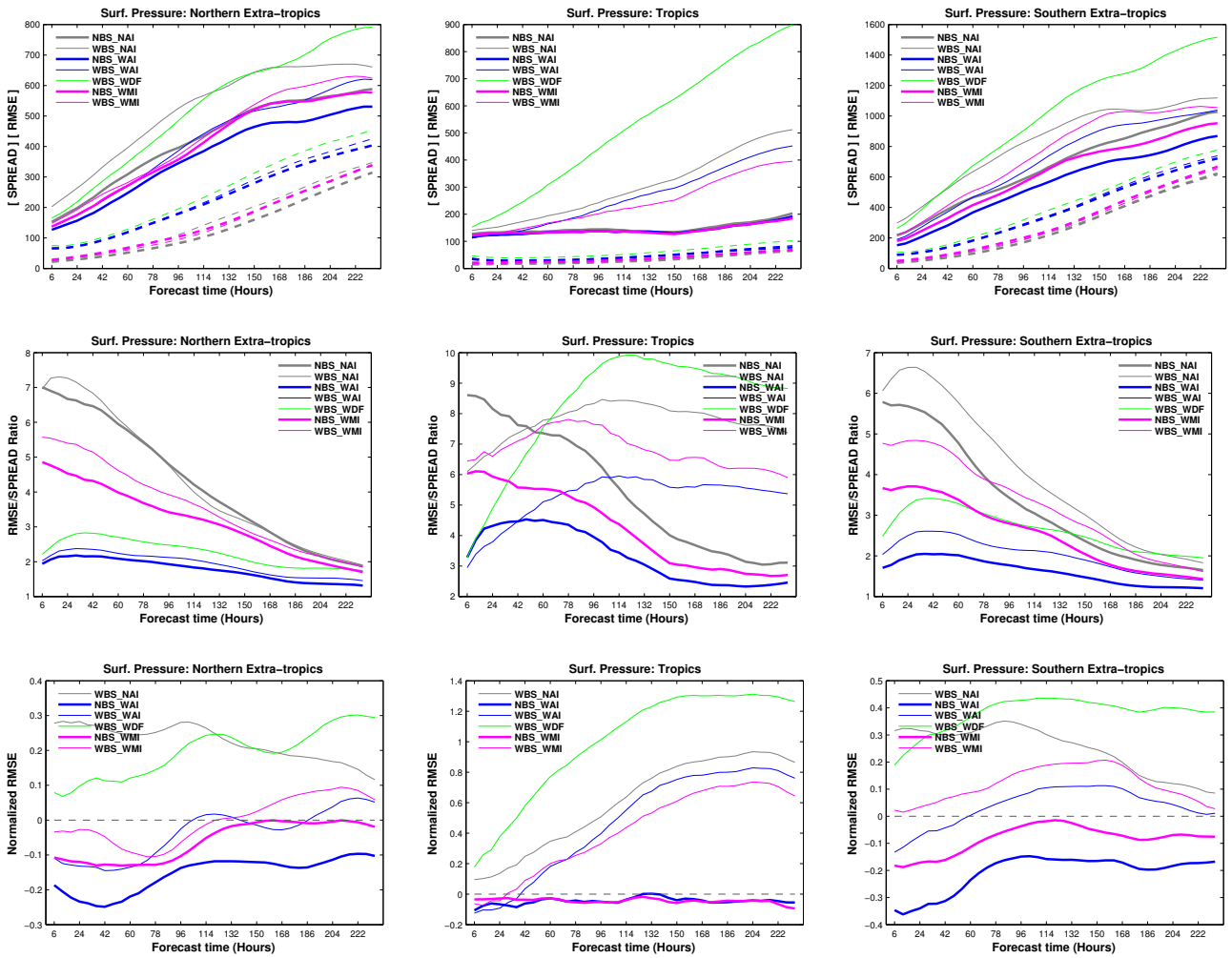


**Figure C.17:** Ten days forecast statistics for surface pressure: RMSE (solid) and Ensemble SPREAD (dashed) on the top-row, RMSE/SPREAD Ratio (middle-row), and Normalized RMSE (bottom-row), for the Northern extra-tropics, the Tropics and the Southern extra-tropics respectively (from left to right).

### C.3 SKEB: Impact on the LETKF Analysis

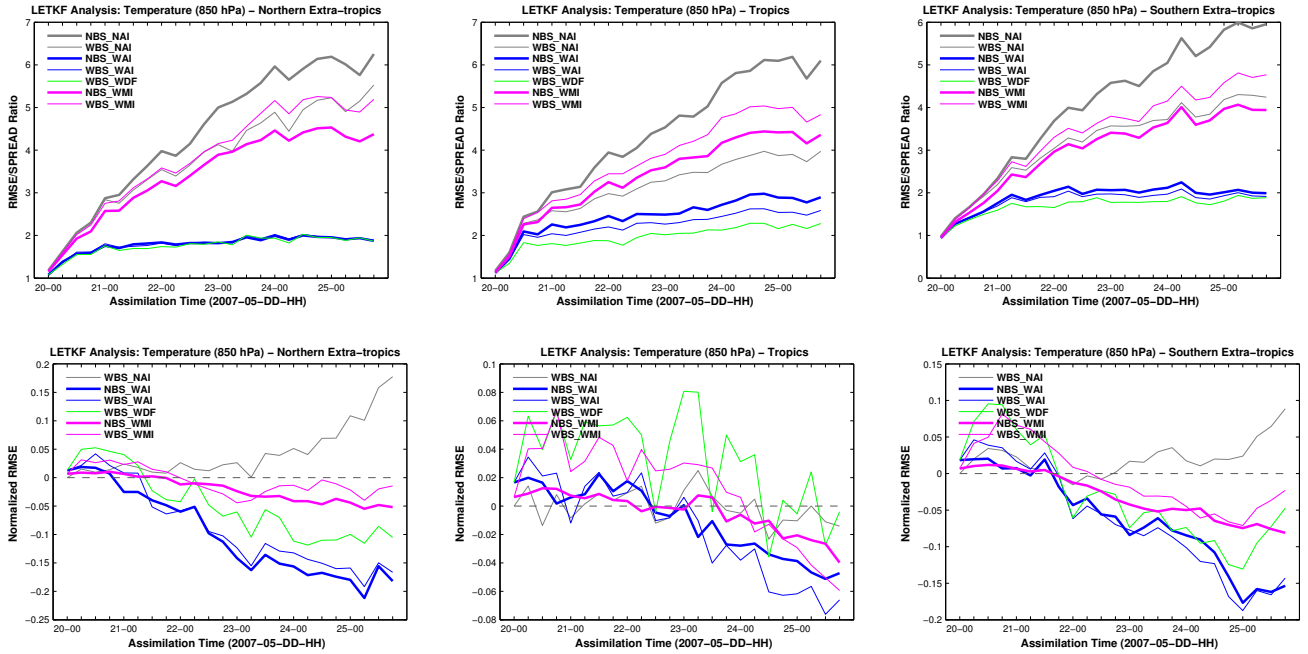
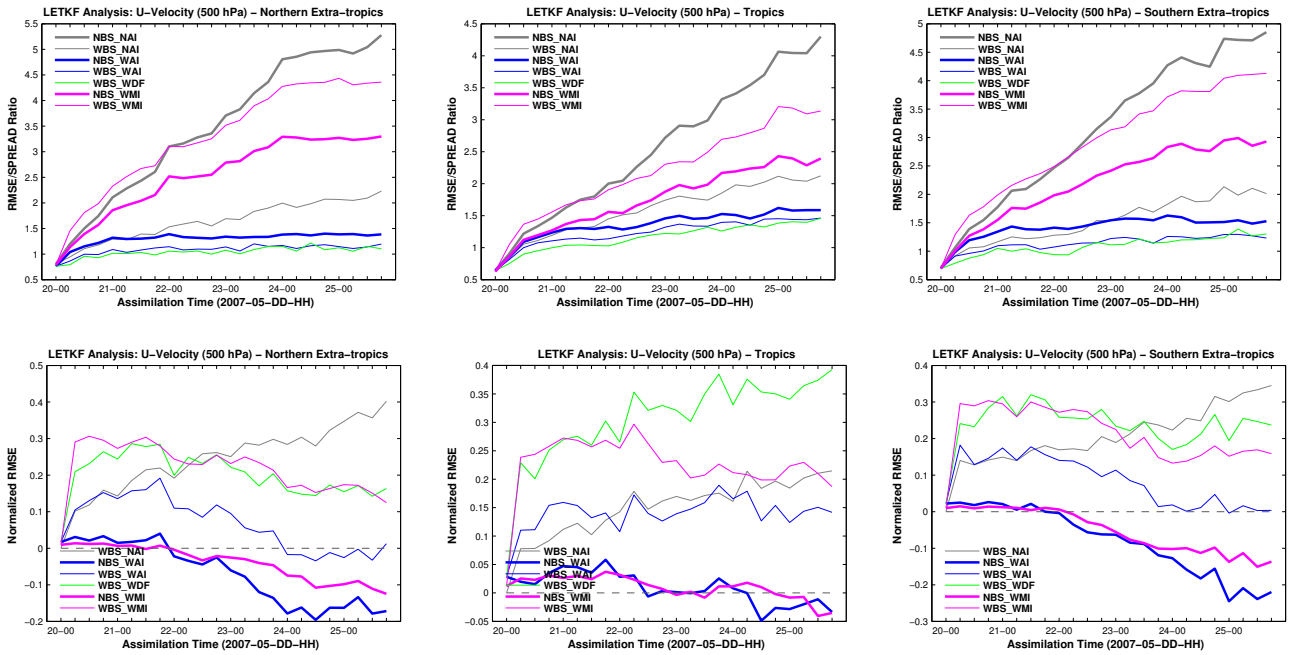
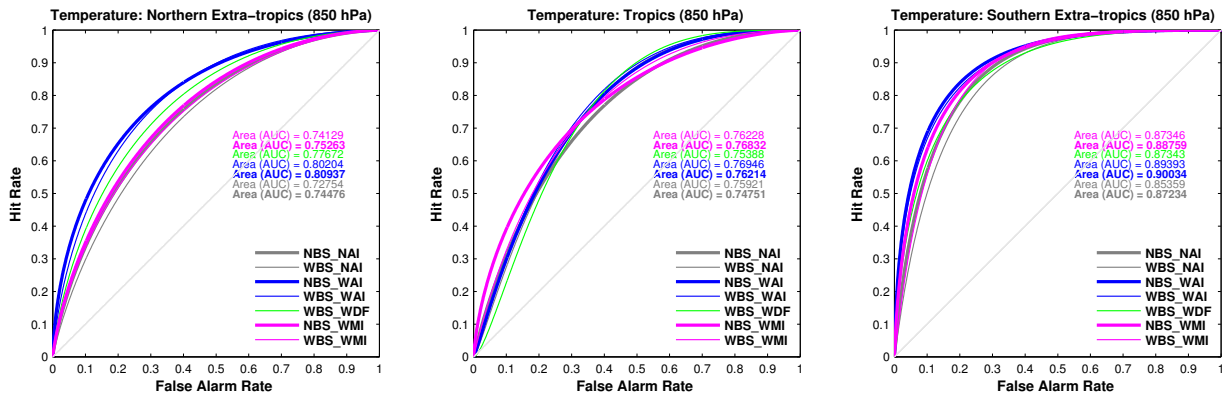


Figure C.18: *RMSE statistics for LETKF analysis for 850 hPa temperature. Top-row: RMSE/SPREAD ratio; Bottom-row: Normalized RMSE; for the Northern extra-tropics, the Tropics, and the Southern extra-tropics (from left to right).*



**Figure C.19:** RMSE statistics for LETKF analysis for 500 hPa zonal wind. Top-row: RMSE/SPREAD ratio; Bottom-row: Normalized RMSE; for the Northern extra-tropics, the Tropics, and the Southern extra-tropics (from left to right).



**Figure C.20:** ROC statistics for 850 hPa temperature against ECMWF deterministic analysis, for the Northern extra-tropics, the Tropics, and the Southern extra-tropics (left to right).



## List of Acronyms

|        |   |
|--------|---|
| 3D VAR | 3 Dimensional VARiational                                     |
| 4D VAR | 4 Dimensional VARiational                                     |
| AMSU   | Advanced Microwave Sounding Unit                              |
| AMV    | Atmospheric Motion Vectors                                    |
| AUC    | Area Under the Curve  |
| BS     | Brier Score   |
| BV     | Breeding Vector   |
| CA     | Cellular Automation   |
| CMC    | Canadian Meteorological Center                                |
| COSMO  | COnsortium for Small scale MOdelling (also name of the model) |
| CRPS   | Continuous Ranked Probability Score                           |
| DFI    | Digital Filter Initialization                                 |
| DWD    | Deutscher Wetterdienst  |
| EAKF   | Ensemble Adjustment Kalman Filter                             |
| ECMWF  | European Center for Medium-range Weather Forecasting          |
| EDA    | Ensemble Data Assimilation                                    |
| EnKF   | Ensemble Kalman Filter  |
| EnSRKF | Ensemble Square-Root Kalman Filter                            |
| EPS    | Ensemble Prediction System                                    |
| FAR    | False Alarm Rate  |
| FN     | False Negative  |
| FP     | False Positive  |
| FPE    | Fokker-Planck Equation  |
| GCM    | General Circulation Model                                     |
| GEM    | Global Environmental Multiscale                               |
| GOES   | Geostationary Operational Environmental Satellite             |
| GRV    | Gaussian Random Variable                                      |
| HR     | Hit Rate  |
| JAMES  | Journal of Advances in Modeling Earth System                  |
| KE     | Kinetic Energy  |
| KEB    | Kinetic Energy Backscatter                                    |
| KF     | Kalman Filter   |
| LAF    | Lagged Average Forecasting                                    |

|            |  |
|------------|--|
| LE         | Louville Equation  |
| LETKF      | Local Ensemble Transform Kalman Filter                         |
| LM         | Local Model (regional model of DWD, now renamed to COSMO)      |
| MAE        | Mean Absolute Error  |
| MC         | Monte-Carlo  |
| MLE        | Maximum Likelihood Estimation                                  |
| MLEF       | Maximum Likelihood Ensemble Filter                             |
| MMSE       | Minimum Mean Squared Error                                     |
| MODIS      | MODERate resolution Imaging Spectrometer                       |
| MOGREPS    | Met. Office Global and Regional Ensemble Prediction System     |
| MPI        | Message Passing Interface                                      |
| NCEP       | National Center for Environmental Prediction                   |
| NESDIS     | National Environmental Satellite, Data and Information Service |
| NMC        | National Meteorological Center                                 |
| NOAA       | National Oceanic and Atmospheric Administration                |
| NWP        | Numerical Weather Prediction                                   |
| <i>pdf</i> | Probability Density Function                                   |
| PDF        | Probability Distribution Function                              |
| PF         | Particle Filter  |
| PSAS       | Physical Space Assimilation System                             |
| QPF        | Quantitative Precipitation Forecast                            |
| RMSE       | Root Mean-Squared Error  |
| ROC        | Receiver (or Relative) Operating Characteristics               |
| SIR        | Sequential Importance Sampling                                 |
| SKEB       | Stochastic Kinetic Energy Backscatter                          |
| SLAM       | Simultaneous Localization And Map                              |
| SP-CDKF    | Sigma-Point Central Difference Kalman Filter                   |
| SP-UKF     | Sigma-Point Unscented Kalman Filter                            |
| SPKF       | Sigma-Point Kalman Filter                                      |
| SPPF       | Sigma-Point Particle Filter                                    |
| SSO        | Subgrid-Scale Orography  |
| SV         | Singular Vector  |
| TN         | True Negative  |
| TP         | True Positive  |
| UKMO       | United Kingdom Meteorological Office                           |

## Bibliography

- Aksoy, A., F. Zhang, and J. Neilsen-Gammon, 2005a: Ensemble based simultaneous state and parameter estimation with MM5. *Geophys. Res. Lett.*, **33**, L12 801, doi:10.1029/2006GL026 186.
- Aksoy, A., F. Zhang, and J. Neilsen-Gammon, 2006: Ensemble based simultaneous state and parameter estimation in a two-dimensional sea-breeze model. *Mon. Wea. Rev.*, **134**, 2951–2970.
- Aksoy, A., F. Zhang, J. Neilsen-Gammon, and C. Epifanio, 2005b: Ensemble based data assimilation for thermally forced circulations. *J. Geophys. Res.*, **110**, D16 105, doi:10.1029/2004JD005 718.
- Ambadan, J. and Y. Tang, 2009: Sigma-point Kalman filter data assimilation methods for strongly nonlinear systems. *J. Atmos. Sci.*, **66**, 261–285.
- Ambadan, J. and Y. Tang, 2011: Sigma-point particle filter for parameter estimation in a multiplicative noise environment. *J. Adv. Model. Earth Syst.*, **3**, M12 005.
- Anderson, J., 2010: A non-Gaussian ensemble filter update for data assimilation. *Mon. Wea. Rev.*, **138**, 4186–4198.
- Anderson, J., T. Hoar, K. Raeder, H. Liu, N. Collins, R. Torn, and A. Avellano, 2009: The data assimilation research testbed: A community facility. *Bull. Amer. Meteor. Soc.*, **90** (9), 1283–1296.
- Anderson, J. L., 2001: An ensemble adjustment Kalman filter for data assimilation. *Mon. Wea. Rev.*, **129**, 2884–2903.
- Anderson, J. L., 2002: A local least square framework for ensemble filtering. *Mon. Wea. Rev.*, **131**, 634–642.
- Anderson, J. L. and S. L. Anderson, 1999: A Monte Carlo implementation of the nonlinear filtering problem to produce ensemble assimilations and forecasts. *Mon. Wea. Rev.*, **127**, 2741–2758.
- Annan, J., 2005: Parameter estimation using chaotic time series. *Tellus*, **57A**, 709–714.

- Annan, J. and J. Hargreaves, 2004: Efficient parameter estimation for a highly chaotic system. *Tellus*, **56A**, 520–526.
- Annan, J., J. Hargreaves, N. Edwards, and R. Marsh, 2005a: Parameter estimation in an intermediate complexity earth system model using an ensemble kalman filter. *Ocean Modell*, **8**, 135–154.
- Annan, J., D. Lunt, J. Hargreaves, and P. Valdes, 2005b: Parameter estimation in an atmospheric GCM using the ensemble Kalman filter. *Nonlinear Proc. Geoph.*, **12**, 363–371.
- Arulampalam, M., S. Maskell, N. Gordon, and T. Clapp, 2002: A tutorial on particle filter for online nonlinear/non-Gaussian Bayesian tracking. *IEEE T. Signal Proces.*, **50 (2)**, 188–197.
- Berner, J., F. Doblas-Reyes, T. Palmer, G. Shutts, and A. Weisheimer, 2008: Impact of a quasi-stochastic cellular automaton backscatter scheme on the systematic error and seasonal prediction skill of a global climate model. *Philos. Trans. Roy. Soc. London A*, **366**, 12 559–2577.
- Berner, J., S. Ha, J. Hacker, A. Fournier, and C. Snyder, 2011: Model uncertainty in a mesoscale ensemble prediction system: Stochastic versus multiphysics representations. *Mon. Wea. Rev.*, **139 (6)**, 1972–1995.
- Berner, J., G. Shutts, M. Leutbecher, and T. Palmer, 2009: A spectral stochastic kinetic energy backscatter scheme and its impact on flow-dependent predictability in the ECMWF ensemble prediction system. *J. Atmos. Sci.*, **66**, 603–626.
- Birgé, L. and Y. Rozenholc, 2006: How many bins should be put in a regular histogram. *ESAIM: Probability and Statistics*, **10 (1)**, 24–45.
- Bonavita, M., L. Isaksen, and E. Hólm, 2012: On the use of EDA background error variances in the ECMWF 4D-Var. *Quart. J. Roy. Meteor. Soc.*
- Brier, G., 1950: Verification of forecasts expressed in terms of probability. *Mon. Wea. Rev.*, **78 (1)**, 1–3.
- Buehner, M., 2005: Ensemble-derived stationary and flow-dependent background-error covariances: Evaluation in a quasi-operational NWP setting. *Quart. J. Roy. Meteor. Soc.*, **131 (607)**, 1013–1043.
- Buehner, M. and M. Charron, 2007: Spectral and spatial localization of background-error correlations for data assimilation. *Quart. J. Roy. Meteor. Soc.*, **133 (624)**, 615–630.
- Buizza, R., M. Miller, and T. Palmer, 1999: Stochastic representation of model uncertainties in the ECMWF ensemble prediction system. *Mon. Wea. Rev.*, **125**, 2887–2908.
- Candille, G., C. Côté, P. Houtekamer, and G. Pellerin, 2007: Verification of an ensemble prediction system against observations. *Mon. Wea. Rev.*, **135 (7)**, 2688–2699.

- Casati, B., et al., 2008: Forecast verification: current status and future directions. *Meteor. Appl.*, **15**, 3–18.
- Castellanos, J., J. Tardós, and G. Schmidt, 1997: Building a global map of the environment of a mobile robot: The importance of correlations. *Proc. of the International Conference on Robotics and Automation*, IEEE, Vol. 2, 1053–1059.
- Charney, J., 1971: Geostrophic turbulence. *J. Atmos. Sci.*, **28**, 1087–1094.
- Charron, M., L. Spacek, P. Houtekamer, H. Mitchell, L. Michelin, G. Pellerin, and N. Gagnon, 2010: Towards random sampling of model error in the Canadian ensemble prediction system. *Mon. Wea. Rev.*, **138**, 1877–1901.
- Cho, J., R. Newell, and J. Barrick, 1999: Horizontal wavenumber spectra of winds, temperature, and trace gases during the pacific exploratory missions; 2. Gravity waves, quasi-two-dimensional turbulence, and vertical modes. *J. Geophys. Res.*, **104**, 16–297.
- Cohn, S., 1997: An introduction to estimation theory. *J. Meteor. Soc. Japan*, **75**, 147–178.
- Cohn, S., A. da Silva, J. Guo, M. Sienkiewicz, and D. Lamich, 1998: Assessing the effects of data selection with the DAO physical-space statistical analysis system. *Mon. Wea. Rev.*, **126** (11), 2913–2926.
- Cooke, W., 1906: Forecasts and verifications in western Australia. *Mon. Wea. Rev.*, **34**, 23–24.
- COSMO, 2003: Consortium for small-scale modeling. [<http://www.cosmo-model.org/content/model/documentation/core/default.html>]. COSMO consortium.
- Courtier, P., 1997: Dual formulation of four-dimensional variational assimilation. *Quart. J. Roy. Meteor. Soc.*, **123** (544), 2449–2461.
- Courtier, P., et al., 1998: The ECMWF implementation of three-dimensional variational assimilation (3D-Var). I: Formulation. *Quart. J. Roy. Meteor. Soc.*, **124** (550), 1783–1807.
- Cox, M. and P. Harris, 2006: Software specifications for uncertainty evaluation. NPL Report, PDB: 4662, National Physical Laboratory (Great Britain). Centre for Mathematics and Scientific Computing.
- da Silva, A. and J. Guo, 1996: Documentation of the physical-space statistical analysis system (PSAS) Part I: The conjugate gradient solver version PSAS-1.00. Tech. rep.
- da Silva, A., J. Pfaendtner, J. Guo, M. Sienkiewicz, and S. Cohn, 1995: Assessing the effects of data selection with DAO's physical-space statistical analysis system. *International Symposium on Assimilation of Observations, 13-17 March 1995, Tokyo, Japan*, World Meteorological Organization., 273–278.

- Dalcher, A., E. Kalnay, and R. Hoffman, 1988: Medium range lagged average forecasts. *Mon. Wea. Rev.*, **116**, 402–416.
- Daley, R., 1992: Estimating model-error covariances for application to atmospheric data assimilation. *Mon. Wea. Rev.*, **120** (8), 1735–1746.
- Dee, D. P., 1995: On-line estimation of error covariance parameters for atmospheric data assimilation. *Mon. Wea. Rev.*, **123**, 1128–1145.
- Dewan, E., 1979: Stratospheric wave spectra resembling turbulence. *Science*, **204** (4395), 832–835.
- Doucet, A., N. DeFreitas, and N. Gordon, 2001: *Sequential Monte-Carlo Methods in Practice*. 1st ed., Springer-Verlag, 581 pp.
- Doucet, A., S. Godsil, and C. Andrieu, 2000: On sequential Monte-Carlo sampling methods for Bayesian filtering. *Statist. Comput.*, **10**, 197–208.
- Ehrendorfer, M., 1997: Predicting the uncertainty of numerical weather forecasts: A review. *Meteor. Z.*, **6**, 147–183.
- Ehrendorfer, M. and J. Tribbia, 1997: Optimal prediction of forecast error covariances through singular vectors. *J. Atmos. Sci.*, **54** (2), 286–313.
- Epstein, E., 1969: Stochastic dynamic prediction1. *Tellus*, **21** (6), 739–759.
- Evensen, G., 1992: Using the extended Kalman filter with a multilayer quasi-geostrophic ocean model. *J. Geophys. Res.*, **97** (C11), 17 905–17 924.
- Evensen, G., 1994: Sequential data assimilation with a nonlinear quasi-geostrophic model using Monte Carlo methods to forecast error statistics. *J. Geophys. Res.*, **99** (C5), 10 143–10 162.
- Evensen, G., 1997: Advanced data assimilation for strongly nonlinear dynamics. *Mon. Wea. Rev.*, **125**, 1342–1354.
- Evensen, G., 2003: The ensemble Kalman filter: theoretical formulation and practical implementation. *Ocean Dynam.*, **53**, 343–367.
- Evensen, G., D. Dee, and J. Schröter, 1998: Parameter estimation in dynamical models. *Ocean Modeling and Parameterization*, E. P. Chassignet and J. Verron, Eds., Kluwer Academic Publishers, NATO Science Series C: Mathematical and Physical Sciences, Vol. 516, 373–398.
- Fischer, N., A. Rhodin, D. Pingel, R. Potthast, and O. Schmid, 2012: Documentation of the DWD data assimilation system: Scientific documentation. Tech. rep., Deutscher Wetterdienst, Offenbach, Germany.
- Fleming, R., 1971a: On stochastic dynamic prediction. I-The energetics of uncertainty and the question of closure. *Mon. Wea. Rev.*, **99**, 851–872.

- Fleming, R., 1971b: On stochastic dynamic prediction. II-Predictability and utility. *Mon. Wea. Rev.*, **99** (12), 927–938.
- Fletcher, S. and M. Zupanski, 2006a: A data assimilation method for log-normally distributed observational errors. *Quart. J. Roy. Meteor. Soc.*, **132** (621), 2505–2519.
- Fletcher, S. and M. Zupanski, 2006b: A hybrid multivariate normal and lognormal distribution for data assimilation. *Atmospheric Science Letters*, **7** (2), 43–46.
- Fletcher, S. and M. Zupanski, 2007: Implications and impacts of transforming lognormal variables into normal variables in var. *Meteorologische Zeitschrift*, **16**, 755–765.
- Frederiksen, J. and A. Davies, 1997: Eddy viscosity and stochastic backscatter parameterizations on the sphere for atmospheric circulation models. *J. Atmos. Sci.*, **54** (20), 2475–2492.
- Freedman, D. and P. Diaconis, 1981: On the histogram as a density estimator:  $L_2$  theory. *Probability theory and related fields*, **57** (4), 453–476.
- Gage, K., 1979: Evidence for a  $-5/3$  law inertial range in mesoscale two-dimensional turbulence. *J. Atmos. Sci.*, **36**, 1950–1954.
- Gaspari, G. and S. Cohn, 1999: Construction of correlation functions in two and three dimensions. *Quart. J. Roy. Meteor. Soc.*, **125** (554), 723–757.
- Gaspari, G., S. Cohn, D. Dee, J. Guo, and A. da Silva, 1998: Construction of the PSAS multi-level forecast error covariance models. Technical Report DAO 98-06, NASA, Goddard Space Flight Center, Greenbelt, Maryland, USA. [Available at <http://dao.gsfc.nasa.gov>].
- Gauthier, P., 1992: Chaos and quadric-dimensional data assimilation: A study based on the Lorenz model. *Tellus*, **44A**, 2–17.
- Gauthier, P. and J. Thépaut, 2001: Impact of the digital filter as a weak constraint in the preoperational 4DVAR assimilation system of Météo-France. *Mon. Wea. Rev.*, **129** (8), 2089–2102.
- Gelaro, R., R. Buizza, T. Palmer, and E. Klinker, 1998: Sensitivity analysis of forecast errors and the construction of optimal perturbations using singular vectors. *J. Atmos. Sci.*, **55** (6), 1012–1037.
- Golub, G. H. and C. F. van Loan., 1989: *Matrix Computations*. 2d ed., The John Hopkins University Press, 642 pp.
- Gordon, N. J., D. J. Salmond, and A. F. M. Smith, 1993: Novel approach to nonlinear or non-Gaussian Bayesian filtering. *IEE Proc-FP.*, IEEE, 107–113.
- Guivant, J. and E. Nebot, 2001: Optimization of the simultaneous localization and map-building algorithm for real-time implementation. *IEEE Transactions on Robotics and Automation*, **17** (3), 242–257.

- Hacker, J. and C. Snyder, 2005: Ensemble Kalman filter assimilation of fixed screen-height observations in a parameterized PBL. *Mon. Wea. Rev.*, **133**, 3260–3275.
- Hamill, T., 2001: Interpretation of rank histograms for verifying ensemble forecasts. *Mon. Wea. Rev.*, **129** (3), 550–560.
- Hamill, T. and J. Whitaker, 2005: Accounting for the error due to unresolved scales in ensemble data assimilation: A comparison of different approaches. *Mon. Wea. Rev.*, **133** (11), 3132–3147.
- Hamill, T. M., 2006: Ensemble-based atmospheric data assimilation. *Predictability of Weather and Climate*, T. Palmer and R. Hagedorn, Eds., Cambridge University Press, 124–156.
- Haykin, E., S., 2001: *Kalman Filtering and Neural Networks*. Wiley., 128 pp.
- Hersbach, H., 2000: Decomposition of the continuous ranked probability score for ensemble prediction systems. *Wea. Forecasting*, **15** (5), 559–570.
- Hoffman, R. and E. Kalnay, 1983: Lagged average forecasting, an alternative to Monte Carlo forecasting. *Tellus A*, **35** (2), 100–118.
- Honda, Y., M. Nishijima, K. Koizumi, Y. Ohta, K. Tamiya, T. Kawabata, and T. Tsuyuki, 2005: A pre-operational variational data assimilation system for a non-hydrostatic model at the Japan Meteorological Agency: formulation and preliminary results. *Quart. J. Roy. Meteor. Soc.*, **131** (613), 3465–3475.
- Houtekamer, P. and H. Mitchell, 1998: Data assimilation using an ensemble Kalman filter technique. *Mon. Wea. Rev.*, **126**, 796–811.
- Houtekamer, P. and H. Mitchell, 2001: A sequential ensemble Kalman filter for atmospheric data assimilation. *Mon. Wea. Rev.*, **129**, 123–137.
- Houtekamer, P., H. Mitchell, and X. Deng, 2009: Model error representation in an operational ensemble Kalman filter. *Mon. Wea. Rev.*, **137** (7), 2126–2143.
- Hunt, B., E. Kostelich, and I. Szunyogh, 2007: Efficient data assimilation for spatiotemporal chaos: A local ensemble transform Kalman filter. *Physica D*, **230**, 112–126.
- Isard, M. and A. Blake, 1998: A smoothing filter for condensation. *Proceedings of 5th European Conference on Computer Vision*, Vol. 1, 767–781.
- Ito, K. and K. Xiong, 2000: Gaussian filters for nonlinear filtering problems. *IEEE T. Automat. Contr.*, **45**(5), 910–927.
- Jablonowski, C. and D. Williamson, 2011: The pros and cons of diffusion, filters and fixers in atmospheric general circulation models. *Numerical Techniques for Global Atmospheric Models*, P. Lauritzen, C. Jablonowski, M. Taylor, and R. Nair, Eds., Springer Verlag, Lecture Notes in Computational Science and Engineering, Vol. 80, 381–494.

- Janjic, T. and S. Cohn, 2006: Treatment of observation error due to unresolved scales in atmospheric data assimilation. *Mon. Wea. Rev.*, **134** (10), 2900–2915.
- Jardak, M., I. M. Navon, and M. Zupanski, 2010: Comparison of sequential data assimilation methods for the Kuramoto-Sivashinsky equation. *Int. J. Numer. Meth. Fluids.*, **62** (4), 374–402.
- Jazwinsky, A., 1970: *Stochastic Processes and Filtering Theory*. Academic Press, New York.
- Jolliffe, I. and D. Stephenson, 2003: *Forecast Verification: A Practitioner's Guide in Atmospheric Science*. John Wiley and Sons, 254 pp.
- Joyce, R., J. Janowiak, P. Arkin, and P. Xie, 2004: CMORPH: A method that produces global precipitation estimates from passive microwave and infrared data at high spatial and temporal resolution. *J. Hydrometeor.*, **5** (3), 487–503.
- Julier, S., 2003: The stability of covariance inflation methods for SLAM. *Proc. of the International Conference on Intelligent Robots and Systems, (IROS 2003)*., IEEE, Vol. 3, 2749–2754.
- Julier, S., J. Uhlmann, and H. Durrant-Whyte, 1995: A new approach for filtering nonlinear systems. *Proceedings of the American Control Conference*, Seattle, WA, USA, IEEE, 1628–1632.
- Kalman, R., 1960: A new approach to linear filtering and prediction problems. *Transaction of the ASME, Series D. J. Basic Eng.*, **82**, 35–45.
- Kalnay, E., 2003: *Atmospheric modeling, data assimilation, and predictability*. Cambridge Univ Pr.
- Keller, J., A. Hense, L. Kornblueh, and A. Rhodin, 2010: On the orthogonalization of bred vectors. *Wea. Forecasting*, **25** (4), 1219–1234.
- Keppenne, C. L., 2000: Data assimilation into a primitive-equation model with a parallel ensemble Kalman filter. *Mon. Wea. Rev.*, **128**, 1971–1981.
- Kitagawa, G., 1996: Monte Carlo filter and smoother for non-Gaussian nonlinear state space models. *J. Comput. Graph. Statist.*, **5**, 1–25.
- Kivman, G. A., 2003: Sequential parameter estimation for stochastic systems. *Nonlinear Proc. Geoph.*, **10**, 253–259.
- Koizumi, K., Y. Ishikawa, and T. Tsuyuki, 2005: Assimilation of precipitation data to the JMA mesoscale model with a four-dimensional variational method and its impact on precipitation forecasts. *Sola*, **1** (0), 45–48.
- Koshyk, J. and K. Hamilton, 2001: The horizontal kinetic energy spectrum and spectral budget simulated by a high-resolution troposphere-stratosphere-mesosphere GCM. *J. Atmos. Sci.*, **58** (4), 329–348.

- Koshyk, J., K. Hamilton, and J. Mahlman, 1999: Simulation of the  $k^{-5/3}$  mesoscale spectral regime in the GFDL SKYHI general circulation model. *Geophys. Res. Lett.*, **26** (7), 843–846.
- Kraichnan, R. and S. Nagarajan, 1967: Growth of turbulent magnetic fields. *Phys. Fluids*, **10**, 859.
- Lefebvre, T., H. Bruyninckx, and J. De Schutter, 2002: Comment on - new method for the nonlinear transformation of means and covariances in filters and estimators deterministic non-periodic flow.”. *IEEE T. Automat. Contr.*, **47**(8), 1406–1409.
- Leight, W., 1953: The use of probability statements in extended forecasting. *Mon. Wea. Rev.*, **81** (11), 349–356.
- Leith, C., 1971: Atmospheric predictability and two-dimensional turbulence. *J. Atmos. Sci.*, **28**, 145–161.
- Leith, C., 1974: Theoretical skill of Monte Carlo forecasts (stochastic atmospheric processes). *Mon. Wea. Rev.*, **102**, 409–418.
- Leith, C., 1978: Objective methods for weather prediction. *Annu. Rev. Fluid Mech.*, **10**, 107–128.
- Leith, C., 1980: Nonlinear normal mode initialization and quasi-geostrophic theory. *J. Atmos. Sci.*, **37**, 958–968.
- Leith, C., 1990: Stochastic backscatter in a subgrid-scale model: Plane shear mixing layer. *Phy. Fluids A: Fluid Dynamics*, **2**, 297.
- Lewis, J., 2005: Roots of ensemble forecasting. *Mon. Wea. Rev.*, **133** (7), 1865–1885.
- Lilly, D., 1983: Stratified turbulence and the mesoscale variability of the atmosphere. *J. Atmos. Sci.*, **40**, 749–761.
- Lindborg, E., 1999: Can the atmospheric kinetic energy spectrum be explained by two-dimensional turbulence? *J. Fluid Mech.*, **388**, 259–288.
- Lindborg, E., 2006: The energy cascade in a strongly stratified fluid. *J. Fluid Mech.*, **550**, 207–242.
- Lindborg, E. and K. Alvelius, 2000: The kinetic energy spectrum of the two-dimensional enstrophy turbulence cascade. *Phys. Fluids*, **12**, 945.
- Liu, J. S. and E. Chen, 1998: Sequential Monte Carlo methods for dynamics systems. *J. Amer. Statist. Assoc.*, **93**, 1032–1044.
- Lorenz, E., 1963: Deterministic nonperiodic flow. *J. Atmos. Sci.*, **20**, 13–141.
- Lorenz, E., 1969: The predictability of a flow which possesses many scales of motion. *Tellus*, **21** (3), 289–307.

- Lorenz, E., 1996: Predictability: A problem partly solved. *Proc. Seminar on Predictability*, ECMWF, Reading, Berkshire, Vol. 1, 1–18.
- Lorenz, E., 2005: Designing chaotic models. *J. Atmos. Sci.*, **62**, 1574–1587.
- Lorenz, E., 2006a: Regimes in simple systems. *J. Atmos. Sci.*, **63** (8), 2056–2073.
- Lorenz, E. and K. A. Emanuel, 1998: Optimal sites for supplementary weather observations: Simulations with a small model. *J. Atmos. Sci.*, **55**, 399–414.
- Lorenz, E. N., 2006b: Predictability - a problem partly solved. *Predictability of Weather and Climate*, T. Palmer and R. Hagedorn, Eds., Cambridge University Press, 40–58.
- Lott, F. and M. Miller, 1997: A new subgrid-scale orographic drag parametrization: Its formulation and testing. *Quart. J. Roy. Meteor. Soc.*, **123** (537), 101–127.
- Lynch, P., D. Giard, and V. Ivanovici, 1997: Improving the efficiency of a digital filtering scheme for diabatic initialization. *Mon. Wea. Rev.*, **125** (8), 1976–1982.
- Majewski, D., et al., 2002: The operational global icosahedral-hexagonal gridpoint model GME: Description and high-resolution tests. *Mon. Wea. Rev.*, **130** (2), 319–338.
- Mason, I., 1982: A model for assessment of weather forecasts. *Aust. Meteor. Mag.*, **30** (4), 291–303.
- Mason, P. and D. Thomson, 1992: Stochastic backscatter in large-eddy simulations of boundary layers. *J. Fluid Mech.*, **242** (1), 51–78.
- Miller, R., M. Ghil, and F. Gauthiez, 1994: Advanced data assimilation in strongly nonlinear dynamical systems. *J. Atmos. Sci.*, **51**, 1037–1056.
- Mitchell, H. and P. Houtekamer, 2000: An adaptive ensemble Kalman filter. *Mon. Wea. Rev.*, **128** (2), 416–433.
- Molteni, F., R. Buizza, T. Palmer, and T. Petroliagis, 1996: The ECMWF ensemble prediction system: Methodology and validation. *Quart. J. Roy. Meteor. Soc.*, **122** (529), 73–119.
- Murphy, A., 1973: A new vector partition of the probability score. *J. Appl. Meteor.*, **12**, 595–600.
- Murphy, A., 1998: The early history of probability forecasts: Some extensions and clarifications. *Wea. Forecasting*, **13** (1), 5–15.
- Murphy, A. and R. Winkler, 1971: Forecasters and probability forecasts: some current problems. *Bull. Amer. Meteor. Soc.*, **52**, 239–247.
- Murphy, A. and R. Winkler, 1984: Probability forecasting in meteorology. *J. Amer. Statist. Assoc.*, **79**, 489–500.

- Namias, J., 1947: Characteristics of the general circulation over the northern hemisphere during the abnormal winter 1946-47. *Mon. Wea. Rev.*, **75** (8), 145–152.
- Namias, J. and P. Clapp, 1949: Confluence theory of the high tropospheric jet stream. *J. Atmos. Sci.*, **6**, 330–336.
- Nastrom, G. and K. Gage, 1985: A climatology of atmospheric wavenumber spectra of wind and temperature observed by commercial aircraft. *J. Atmos. Sci.*, **42**, 950–960.
- Nastrom, G., K. Gage, and W. Jasperson, 1984: Kinetic energy spectrum of large- and mesoscale atmospheric processes. *Nature*, **310** (5972), 36–38.
- Nørgård Magnus, P., N. K. Poulsen, and O. Ravn, 2000: New developments in state estimation of nonlinear systems. *Automatica.*, **36**, 1627–1638.
- Palmer, T., 1993: Extended-range atmospheric prediction and the Lorenz model. *Bull. Amer. Meteor. Soc.*, **74**, 49–65.
- Palmer, T., 1997: On parametrizing scales that are only somewhat smaller than the smallest resolved scales, with application to convection and orography. *Proc. of the ECMWF workshop on New insights and approaches to convective parametrization.*, Shinfield Park, Reading RG2-9AX, UK, ECMWF, 328–337.
- Palmer, T., 2001: A nonlinear dynamical perspective on model error: A proposal for non-local stochastic-dynamic parametrization in weather and climate prediction models. *Quart. J. Roy. Meteor. Soc.*, **127**, 279–304.
- Palmer, T., R. Gelaro, J. Barkmeijer, and R. Buizza, 1998: Singular vectors, metrics, and adaptive observations. *J. Atmos. Sci.*, **55** (4), 633–653.
- Palmer, T., B. R., D.-R. F., J. T., L. M., S. G.J., S. M., and W. A., 2009: Stochastic parametrization and model uncertainty. Technical memorandum, 598., European Center for Medium-range Weather Forecast, Shinfield Park, Reading, RG29AX, UK. [Available at <http://www.ecmwf.int/publications>].
- Patil, D., B. Hunt, E. Kalnay, J. Yorke, and E. Ott, 2001: Local low dimensionality of atmospheric dynamics. *Phys. Rev. Lett.*, **86** (26), 5878–5881.
- Peña, M., Z. Toth, and M. Wei, 2010: Controlling noise in ensemble data assimilation schemes. *Mon. Wea. Rev.*, **138**, 1502–1512.
- Press, W. H., S. A. Teukolsky, W. T. Vetterling, and B. P. Flannery, 1992: *Numerical Recipes in C: The Art of Scientific Computing*. Cambridge University Press, 2 Edition.
- Rabier, F., E. Klinker, P. Courtier, and A. Hollingsworth, 1996: Sensitivity of forecast errors to initial condition. *Quart. J. Roy. Meteor. Soc.*, **122**, 121–150.
- Saha, S., 1992: Response of the NMC MRF model to systematic-error correction within integration. *Mon. Wea. Rev.*, **120** (2), 345–360.

- Sanders, F., 1963: On subjective probability forecasting. *J. Appl. Meteor.*, **2** (2), 191–201.
- Sardeshmukh, P. D., 2010: Global climate diagnosis in a linear stochastically forced framework. *Seminar on Diagnosis of Forecasting and Data Assimilation Systems*, 7 - 10 September 2009, Shinfield Park, Reading, ECMWF, 15–24.
- Sardeshmukh, P. D. and P. Sura, 2009: Reconciling non-Gaussian climate statistics with linear dynamics. *J. Climate*, **22**, 1193–1207.
- Schon, T. B., 2006: Estimation of nonlinear dynamic systems - theory and applications. Ph.D. thesis, Linköping Studies in Science and Technology.
- Shutts, G., 2005: A kinetic energy backscatter algorithm for use in ensemble prediction systems. *Quart. J. Roy. Meteor. Soc.*, **612**, 3079–3102.
- Shutts, G., T. Allen, and J. Berner, 2008: Stochastic parametrization of multiscale processes using a dual-grid approach. *Philos. Trans. Roy. Soc. London A*, **366**, 2623–2639.
- Simmons, A. and D. Burridge, 1981: An energy and angular-momentum conserving vertical finite-difference scheme and hybrid vertical coordinates. *Mon. Wea. Rev.*, **109** (4), 758–766.
- Simon, D., 2006: *Optimal State Estimation, Kalman,  $H_\infty$ , and Nonlinear Approaches*. 1st ed., Wiley-Interscience, 318–320 pp.
- Skamarock, W., 2004: Evaluating mesoscale NWP models using kinetic energy spectra. *Mon. Wea. Rev.*, **132** (12), 3019–3032.
- Stensrud, D., J. Bao, and T. Warner, 2000: Using initial condition and model physics perturbations in short-range ensemble simulations of mesoscale convective systems. *Mon. Wea. Rev.*, **128** (7), 2077–2107.
- Sura, P., M. Newman, C. Penland, and P. D. Sardeshmukh, 2005: Multiplicative noise and non-Gaussianity: A paradigm for atmospheric regimes? *J. Atmos. Sci.*, **62**, 1391–1409.
- Sura, P. and P. D. Sardeshmukh, 2008: A global view of non-Gaussian SST variability. *J. Phys. Oceanogr.*, **38**, 639–647.
- Talagrand, O., R. Vautard, and B. Strauss, 1997: Evaluation of probabilistic prediction systems. *Proc. ECMWF Workshop on Predictability*, 1–25.
- Tennant, W., G. Shutts, A. Arribas, and S. Thompson, 2011: Using a stochastic kinetic energy backscatter scheme to improve MOGREPS probabilistic forecast skill. *Mon. Wea. Rev.*, **139** (4), 1190–1206.
- Theis, S., 2005: Deriving probabilistic short-range forecasts from a deterministic high-resolution model. Ph.D. thesis, Mathematisch-Naturwissenschaftlichen Fakultät, University of Bonn.

- Theis, S., A. Hense, and U. Damrath, 2005: Probabilistic precipitation forecasts from a deterministic model: a pragmatic approach. *Meteor. Appl.*, **12** (3), 257–268.
- Thompson, P., 1957: Uncertainty of initial state as a factor in the predictability of large scale atmospheric flow patterns. *Tellus*, **9** (3), 275–295.
- Tiedtke, M., 1989: A comprehensive mass flux scheme for cumulus parameterization in large- scale models. *Mon. Wea. Rev.*, **117** (8), 1779–1800.
- Tippett, M. K., J. Anderson, C. Bishop, T. Hamill, and J. Whitaker, 2003: Ensemble square root filters. *Mon. Wea. Rev.*, **131**, 1485–1490.
- Tong, M. and M. Xue, 2008a: Simultaneous estimation of microphysical parameters and atmospheric state with simulated radar data and ensemble square root Kalman filter. Part I: Sensitivity analysis and parameter identifiability. *Mon. Wea. Rev.*, **136**, 1630–1648.
- Tong, M. and M. Xue, 2008b: Simultaneous estimation of microphysical parameters and atmospheric state with simulated radar data and ensemble square root Kalman filter. Part II: Parameter estimation experiments. *Mon. Wea. Rev.*, **136**, 1630–1648.
- Toth, Z. and E. Kalnay, 1993: Ensemble forecasting at NMC: The generation of perturbations. *Bull. Amer. Meteor. Soc.*, **74** (12), 2317–2330.
- Toth, Z. and E. Kalnay, 1997: Ensemble forecasting at ncep and the breeding method. *Mon. Wea. Rev.*, **125** (12), 3297–3319.
- Trèmolet, Y., 2003: Model error in variational data assimilation. *Proceedings of the annual seminar on recent developments in data assimilation for atmosphere and ocean, 8-12 September 2003*, Shinfield Park, Reading, ECMWF, 361–367.
- Tribbia, J. and D. Baumhefner, 1988: The reliability of improvements in deterministic short-range forecasts in the presence of initial state and modeling deficiencies. *Mon. Wea. Rev.*, **116**, 2276–2288.
- Tsuyuki, T., K. Koizumi, and Y. Ishikawa, 2003: The JMA mesoscale 4D-Var system and assimilation of precipitation and moisture data. *Proc. ECMWF/GEWEX Workshop on Humidity Analysis*, 59–68.
- Tung, K. and W. Orlando, 2003: The  $k^{-3}$  and  $k^{-5/3}$  energy spectrum of atmospheric turbulence: Quasigeostrophic two-level model simulation. *J. Atmos. Sci.*, **60** (6), 824–835.
- Van der Merwe, R., 2004: Sigma-Point Kalman filters for probabilistic inference in dynamic state-space models. Ph.D. thesis, Oregon Health & Science University.
- Van der Merwe, R., A. Doucet, N. de Freitas, and E. Wan, 2000: The unscented particle filter. Tech. rep., Cambridge University Engineering Department, 46 pp. [Available at <http://citeseer.ist.psu.edu/artile/vandermerwe00unscented.html>].

- Van der Merwe, R. and E. A. Wan, 2001a: Efficient derivative-free Kalman filters for online learning. *Proceedings of European Symposium on Artificial Neural Networks (ESANN)*, Bruges, Belgium.
- Van der Merwe, R. and E. A. Wan, 2001b: The square-root unscented Kalman filter for state and parameter estimation. *Proceedings of the International Conference on Acoustics, Speech, and Signal Processing (ICASSP)*., Salt Lake City, Utah, IEEE.
- Van der Merwe, R. and E. A. Wan, 2003: ReBEL: Recursive Bayesian Estimation Library. [Available at <http://choosh.csee.ogi.edu/rebel/index.html>].
- Van der Merwe, R., E. A. Wan, and S. I. Julier, 2004: Sigma-point Kalman filters for nonlinear estimation and sensor fusion: Applications to integrated navigation. *AIAA Guidance, Navigation and Control Conference*, Providence, RI, American Institute of Aeronautics and Astronautics, 5120–5122.
- Van Leeuwen, P., 2009: Particle filtering in geophysical systems. *Mon. Wea. Rev.*, **137** (12), 4089–4114.
- Van Zandt, T., 1982: A universal spectrum of buoyancy waves in the atmosphere. *Geophys. Res. Lett.*, **9**, 575–578.
- Wan, E. and R. Van Der Merve, 2000: The unscented Kalman filter for nonlinear estimation. *Adaptive Systems for Signal Processing, Communications, and Control Symposium ASSPCC 2000*, Lake Louise, Alberta, Canada, IEEE Communications Society, 153–158.
- Weber, R. and P. Talkner, 1993: Some remarks on spatial correlation function models. *Mon. Wea. Rev.*, **121**, 2611–2611.
- Welch, G. and G. Bishop, 1995: An Introduction to the Kalman Filter; Technical Report: TR95-041. Tech. rep., University of North Carolina, Chapel Hill, NC.
- Wilson, L., 2000: Comments on “Probabilistic Predictions of Precipitation Using the ECMWF Ensemble Prediction System”. *Wea. Forecasting*, **15** (3), 361–364.
- Zhang, F. and C. Snyder, 2007: Ensemble-based data assimilation. *Bull. Amer. Meteor. Soc.*, **88**, 565–568.
- Zupanski, D. and M. Zupanski, 2006: Model error estimation employing an ensemble data assimilation approach. *Mon. Wea. Rev.*, **134** (5), 1337–1354.
- Zupanski, M., 2005: Maximum likelihood ensemble filter: Theoretical aspects. *Mon. Wea. Rev.*, **133** (6), 1710–1726.



## Acknowledgments

I would like to express my gratitude to my advisor Dr. Luis Kornblueh for his help and guidance. I also thank my co-advisor Dr. Andreas Rhodin (DWD) for his constant support. This thesis work has certainly benefited from his help and advice. Also, many thanks to my PhD advisory panel chair Dr. Bjorn Stevens, who helped my research with many insightful suggestions especially during the panel meetings.

Thanks to the International Max-Planck Research School (IMPRS), especially our co-ordinator Dr. Antje Weitz, and Cornelia Kampmann for their administrative and moral support as well as to my fellow PhD students for a great working environment.

I also acknowledge and thank CDO developers Uwe Schulzweida and Cedrik Anson for their invaluable help for creating new statistical operators, which I used countless times in this thesis work. Thanks to the German Climate Computing Centre (DKRZ), and also to the Central IT Services (CIS) for their technical support. My thanks also go to Carsten Schmidt (CIS), Christian Schwede (DKRZ), Reinard Budich (MPIM), and also to my supervisor Dr. Luis Kornblueh, for helping me with the computing environment on Tornado, Squall, and the archive.

Further thanks go to Dr. Hendrik Reich (DWD), who helped me to setup the assimilation system on Tornado, and Dr. Helmut Frank (DWD) for providing the code for calculating the kinetic energy spectra from the GME model. I also acknowledge and thank the ECMWF and the DWD for providing the data and satellite observations for my experiments.

I also acknowledge and thank the Oregon Graduate Institute, and Dr. Eric A. Wan and Dr. Rudolph Van der Merwe for providing the ReBEL tool kit, part of which has been used in the research work described in Chapter 5 of this thesis. I also thank the ZEIT Foundation, and the IMPRS-ESM Guest and Exchange Program for funding my visit (2009) to Dr. Youmin Tang's Lab at the University of Northern British Columbia, Canada.

Also, I thank Dr. Davide Zanchettin for proof-reading the first draft of this thesis.

Funding of this PhD was provided by the DFG project, Quantitative Precipitation Forecast (QPF Phase III - SPP 1167).

A special word of gratitude to all my co-workers, group members, and my beloved friends and officemates who have given me companionship, help, and above all their valuable time during the course of my life at MPIM.

I am particularly indebted to my parents, my brother, and my sisters for their monumental, unwavering support and encouragement.

*Hamburg,  
September, 2012*

*Jaison Thomas Ambadan*

---

**Declaration:** Any mirrored or quoted materials and ideas in this document © and full credit to their respective authors, journals, and publications.





